Supported Liquid Metal Membranes for Hydrogen Separation

A Dissertation

Submitted to the faculty of the

Worcester Polytechnic Institute

In partial fulfillment of the requirement for the

Degree of Doctor of Philosophy In Chemical Engineering

By

Pei-Shan Yen

Approved:

Prof. Ravindra Datta, Advisor

Prof. Nikolaos K. Kazantzis
(Committee Member)

Prof. Yan Wang
(Committee Member)

Prof. Susan C. Roberts
(Department Head)

Abstract

Hydrogen (H_2) and fuel cells applications are central to the realization of a global hydrogen economy. In this scenario, H_2 may be produced from renewable biofuels via steam reforming in addition to solar powered water electrolysis. The purification required for fuel cell grade H_2 whether in tandem or *in situ* within a catalytic reformer operating at 500 ºC or above would be greatly facilitated by the availability a cheaper and more robust option to palladium (Pd) dense metal membrane, currently the leading H_2 separation membrane candidate.

Here, we describe our results on the feasibility of a completely novel membrane for hydrogen separation: Sandiwiched Liquid Metal Membrane, or SLiMM. The goal was to develop new dense metal membranes based on supporting thin films of low-melting, non-precious group metals, e.g., tin (Sn), indium (In), or gallium (Ga), to obtain a flux and selectivity of hydrogen that rivals the conventional but substantially more expensive Pd or Pd alloy membranes, which are susceptible to poisoning, and further possess inadequate stability and limited operating temperature range. Gallium was selected for this feasibility study to prove of the concept of SLiMM. Gallium is molten at essentially room temperature, is non-toxic, and is much cheaper and more abundant than Palladium.

The novelty of the concept presented numerous challenges during the course of this project, mainly in the selection of an appropriate support and in the fabrication of a stable supported liquid metal membrane. Based on trial-and-error with several porous sintered metal and ceramic supports coupled with a thermodynamic analysis, we developed an adequate understanding of the reactive interactions of liquid metal films with porous supports at elevated temperatures, so that we were able to finally select appropriate inert but wettable supports, namely, porous SiC and graphite. It was also discovered that the surface tension and wettability of the liquid metal

film is a strong function of the gas composition, rendering a SLiMM with a free liquid surface inadequately stable. This led us to propose a sandwich configuration, i.e., a liquid metal film held between two porous substrates. The tests with SLiMM reported here indicate that the SiC/Ga SLiMM at 550 ºC has a permeability 35 time higher than Pd, and substantial exceeds the 2015 DOE target for dense metal membranes.

To make practical membranes, however, improving the physical stability of the membrane is the next goal. For this, it is important to better understand the change in liquid metal surface tension and contact angle as a function of temperature, pressure and gas-phase composition. A thermodynamic theory was developed that is not only able to explain this change in the liquid-gas surface tension, but also the change in the solid-liquid surface tension and contact angle.

For developing a fundamental understanding of the thermodynamics and hydrogen transport in liquid metals, a Pauling Bond Valence-Modified Morse Potential (PBV-MMP) model, in which the Pauling's relationship between bond-valence (BV) and bond-length (BL) was incorporated within a modified Morse-Potential (MMP), along the lines of the Unity Bond Index-Quadratic Exponential Potential (UBI-QEP) of Shustorovich for catalyst metal surfaces. The new PBV-MMP model extends the UBI-QEP approach per predicting *surface solid* metal energetics to *bulk liquid* metal energetic parameters. This was combined with the free volume theory of Eyring to estimate the corresponding entropy changes to obtain all thermodynamic and kinetic parameters of interest. The calculation only requires density, covalent radius heat of vaporization, and hydrogen binding energy to accurately predict properties of interest, namely, liquid metal self-diffusion, viscosity, surface tension, as well as thermodynamic and energetic properties of hydrogen in liquid metal such as heat of dissociative adsorption, heat of solution and activation energy of diffusion.

Acknowledgements

First I would like to thank my advisor Prof. Ravindra Datta for guiding me throughout the entire PhD study. I really admire his passion, dedication in always trying something new and the courage to take on the challenge. Instead of traveling through the road people less taken, let's go through the direction people have never taken. I am also thankful for his patience for giving me the freedom to try and would always lead me back on the track during research. His sense of humor and timely response helped me go through the time of frustration and showed me that there is light at the end of the tunnel. I found 100 ways to destroy the membrane but his persistent attitude and insightful knowledge taught me to find a way that works. Thank you for everything.

Next I would like to thank my co-advisor Prof. Yi Hua Ma for introducing me to WPI and for giving me the chance in pursuing PhD here. His hard working attitude always brought me back to the earth when I drifted too far. His knowledge of hydrogen separation is amazingly abundant and I am lucky and grateful to be able to learn a tip of the iceberg from him. I would like to thank Prof. Kazantzis and Prof. Wang for serving on my thesis committee and for their time and interest.

I would also like to thank both of my advisors, Chemical Engineering Department, Worcester Polytechnic Institute, and Department of Energy for the financial supports through these years. I couldn't make it without all of them. Thanks to all the faculty members from our department for their advice and lectures. Special thanks to Prof. Sisson for landing me his books and letting me keep them for a very long time.

Thanks to all the staff of our department: Felicia, Tiffany, for helping me on administrative things and Paula for helping out with enormous amount of my purchase orders. Thanks to

Douglas for maintaining XRD, and SEM in the department, electronics in the lab and for showing me some tricks on playing guitar. We had some great conversations on music. Also thanks to Jack and Tom for helping out on constructing lab equipment. Thanks to Ivan for all his great ideas about membrane preparation, testing and cell assembly.

Thanks to all the past and current members in hydrogen separation lab: Engin, Federico, Jacopo, Reyyan, Alex, Mike, Natalie, Stanley and Rei for your companionship and the suggestions. All the days and nights we spent on discussing membrane preparation technique or debating which beer tasted better were fun and invaluable. Thanks to members from fuel cell lab, Neal, Becky, Nick for hydrogen absorption experiment, Drew, Patrick, Jason, Anqi, Yan and Xiangyu. Together we kept the vibe in the basement alive and enjoyable even with the lack of sunshine (and cell phone signal). Thanks to all my friends who I hang out with, Juan, Elli, Qingxiong, Roulin, Feifei, Yu, Lulu, Xiaokong, Yuxian. We had lots of wonderful memories and fun. I will never forget some of the crazy things that we did. Special thanks to one my best friends Ying for her help, support and suffered from my couch potato syndrome sometimes during my study.

Finally, I would also like to thank my family, for letting me do whatever my heart desires and being so supportive with all the decisions that I made. Your selfless devotion gives me all I have and I am truly grateful.

Table of Contents

List of Figures

Lists of Tables

Nomenclature

Symbols

$\mathscr{A}_\rho$	dimensionless reaction affinity of elementary step ρ, $\mathscr{A}_\rho = -\Delta G_\rho / RT$
$\mathscr{A}_{OR}$	dimensionless affinity of the overall reaction (OR), $\mathscr{A}_{OR} = -\Delta G_{OR} / RT$
a	the lattice constant, cm
a_i	activity of species *i* in the liquid
$a_{\mathrm{Ag}}^{\Sigma_L}$	activity of Ag at liquid surface sub-layer
a_{Ag}^{L}	activity of Ag in the bulk liquid
$a_{Al_2O_3}^{\Sigma_S}$	activity of Al_2O_3 at solid surface sub-layer
$a_{\mathrm{Al_2O_3}}^{S}$	activity of Al_2O_3 in bulk solid
$\underline{A}^{\Sigma}$	molar interfacial area
b	Morse Potential structural parameter
c	dimensionless parameter adjustable for each ionocovalent oxide
$c_{\mathrm{S},t}$	total concentration of the surface metal atoms, 2.06×10^{-5} mol Ga $\cdot$ cm^{-2}
d_{H}	covalent diameter of hydrogen
$D_{\mathrm{AM}}^{\mathrm{o}}$	single binding energy of gas atom A with metal M kJ/mol H
D_{H}	interstitial diffusion coefficient of the hydrogen atoms, cm^2/s
$D_{\mathrm{H},0}$	pre-exponential factor of interstitial diffusion coefficient of H, cm^2/s
$D_{\mathrm{H\text{-}H}}^{\mathrm{o}}$	binding energy of H_2 kJ/mol H

E_d	activation energy of interstitial diffusion of H, kJ/mol H
$\vec{E}_r$	activation energy of the forward reaction step ρ, kJ/mol
$\overleftarrow{E}_\rho$	activation energy of the reverse reaction step ρ, kJ/mol
F	the partition functions for the initial state
$F^{\ddagger}$	the partition functions for the transition state
F_{trans}	translational partition function
F_{rot}	rotational partition function
F_{vib}	vibrational partition function
$\underline{G}^{\Sigma}$	Gibbs free energy of system
h	Planck's constant, 6.6260×10^{-34} J·s
K_ρ	equilibrium constant of the elementary reaction step ρ
K_{OR}	equilibrium constant of the overall reaction
K_S	Sieverts' equilibrium constant for the hydrogen solution in metal
$K_O^{\Sigma_L}$	equilibrium constant of oxygen partitioning from the bulk to the surface layer
$K_O^{\Sigma_S}$	equilibrium constant of oxygen partitioning from the bulk to the solid surface layer
K_{ads}^{L}	oxygen dissociative adsorption equilibrium constant from the gas-phase
K_{ads}^{S}	oxygen dissociative adsorption equilibrium constant from the solid-phase

k_B	Boltzmann constant, 1.38064×10^{-23} J / K
$\vec{k}_\rho$	forward rate constant of the elementary reaction ρ
$\overleftarrow{k}_\rho$	reverse rate constant of the elementary reaction ρ
$M_{\mathrm{H_2}}$	molar mass of H_2, g/mol
M_i	molecular weight (mass) of species i
n	mole
N_{Av}	Avogadro's number
n_{M_Σ}	number of metal atoms on metal surface
n_ξ	number of nearest neighbor molecules against the traversing molecule shears
$n^\ddagger$	number of metal atoms at saddle point in a unit cell
$N_{\mathrm{H_2}}$	hydrogen flux, $\mathrm{m^3/m^2h}$
N_{M}	the total number of atoms in a unit cell
$p_{\mathrm{H_2}}$	hydrogen partial pressure, Pa or atm
$P_{\mathrm{H_2}}$	membrane permeance, $\mathrm{m^3/m^2h\,atm^{0.5}}$
p^{o}	standard atmosphere, 101,325 Pa, or 1 atm
p	pressure
$Q_{\mathrm{A\text{-}M}_{n_\Sigma}}$	binding energy for A gas atom on surface metal M
$Q_{\mathrm{HM}n^\ddagger}$	binding energy for H atom on surface metal M in bridge (saddle) position

Q_i	quasi-steady-state relations (QSS), or KFL relations for species *i*
$Q_{\mathrm{H_2}}$	hydrogen membrane permeability $\mathrm{m^3 \mu m/m^2 h\ atm^{0.5}}$
R	gas constant, 8.314 $\mathrm{J/mol\ K}$
R_ρ	resistance of elementary reaction ρ , rate^{-1}
R_{OR}	total resistance of the overall reaction network, rate^{-1}
r_{OR}	net rate of the overall reaction, $\mathrm{mol\ H_2 \cdot cm^{-2} \cdot s^{-1}}$
r_{ij}^{o}	internuclear length between species *i* and *j*
r_{ij}^{I}	empirical bond parameter from Pauling BV-BL correlation of species *i* and *j*
r_ρ	net rate of the elementary reaction ρ $\vec{r}_\rho - \overleftarrow{r}_\rho$, $\mathrm{mol/cm^2\ s}$
$\vec{r}_\rho$	forward rate of elementary reaction ρ, $\mathrm{mol/cm^2\ s}$
$\overleftarrow{r}_\rho$	reverse rate of elementary reaction ρ, $\mathrm{mol/cm^2\ s}$
s_ρ	elementary reaction ρ
T	Temperature, K
v_f	free molecular volume of liquid metal, $\mathrm{cm^3}$
v_0	molecular volume of liquid at absolute zero
v_{void}	maximum molecular free volume of liquid metal
v_l	molecular volume of liquid
V	volume

V_{Me} molar volume of the metal

V_i atomic valence of specie *i*

W_{ad} work of adhesion in J/m^2

$x_{H \cdot M}$ mole fraction of interstitial hydrogen with metal

x_i mole fraction of species *i*

z_i number of nearest neighbor interstitial positions, z = 12 for fcc

z_{OR} reversibility of overall reaction

Greek Symbols

α the jumping distance coefficient in metal lattice

β free volume parameter

ε_{PF} liquid metal packing factor

γ geometric factor in interstitial diffusion coefficient, = 1/12 for the fcc lattice of Pd

$\lambda_{D,k}$ the hydrogen interstitial jump distance in metal in direction *k*

λ_D the *mean* hydrogen interstitial jump distance

λ_t thermal wave-length in Sackur-Tetrode equation

ρ_i density of species *i*

ρ_M density of liquid metal M , kg/m^3

ΔG_S^o standard Gibbs free energy change of hydrogen solution in metal, kJ/mol H

ΔG_ρ Gibbs free energy change of the elementary reaction step ρ, kJ/mol

$\mathrm{D}G_r^{\mathrm{o}}$	standard Gibbs free energy change of the elementary reaction step ρ, kJ/mol
ΔH_{ad}	heat of dissociative adsorption, kJ/mol H
ΔH_d	surface dissociation energy of AB molecular
ΔH_S^{o}	standard enthalpy change of hydrogen solution in metal, kJ/mol H
$\Delta H_\rho^{\mathrm{o}}$	standard enthalpy change of the elementary reaction step ρ, kJ/mol
S	entropy J/mol K
$\Delta S_{ad}^{\mathrm{o}}$	standard entropy of formation of a surface species $\mathrm{A}\cdot\mathrm{S}$, J/mol K
$S_{\mathrm{A}}^{\mathrm{o}}$	standard gas-phase entropy of A, J/mol K
$S_{\mathrm{H}(g)}^{o}$	standard hydrogen atom entropy in gas phase, J/mol K
$S_{\mathrm{H}_2(g)}^{o}$	standard hydrogen molecule entropy in gas phase, J/mol K
S_{HM}^{o}	standard entropy of hydrogen in liquid metal, J/mol K
ΔS_S^{o}	standard entropy change of hydrogen solution in metal, J/mol K
$\Delta S_\rho^{\mathrm{o}}$	standard entropy change of the elementary reaction step ρ, J/mol K
$\Delta S_D^{\ddagger,\mathrm{o}}$	standard entropy change of activation for diffusion, J/mol K
$\Delta \vec{S}_\rho^{\ddagger,\mathrm{o}}$	standard entropy change of activation for the forward step, J/mol K
$\Delta \overleftarrow{S}_\rho^{\ddagger,\mathrm{o}}$	standard entropy change of activation for the reverse step
κ	transmission coefficient

Λ_D	jump attempt frequency factor of diffusion step, s^{-1}
$\vec{\Lambda}_\rho$	forward frequency factor of step s_ρ, s^{-1}
$\overleftarrow{\Lambda}_\rho$	reverse frequency factor of step s_ρ, s^{-1}
μ_i	chemical potential of species *i*
μ_i^o	standard state (unit activity) chemical potential of species *i*
ν_0	frequency of vibration of the solute in an interstitial position, s^{-1}
ν_{ij}	bond valence of species between *i* and *j*
$\nu_{\rho i}$	stoichiometric coefficient of species *i* in an elementary reaction
ω	the correction factor for free volume
σ	symmetry number
σ_ρ	stoichiometric number for step ρ
$\sigma_{\alpha\beta}$	surface tension of α and β phase
σ_α, σ_β	interfacial free energy of the surface sub-layer Σ_α, and Σ_β
σ_α^o	Gibbs free energy of formation of pure component in phase α in unit interfacial area
σ_{LG}	liquid-gas surface tension in J/m^2 or mN/m
σ_{LG}^o	pure liquid-gas surface tension without any oxygen contamination in J/m^2
$\Delta\sigma_{LG}$	change of liquid-gas surface tension due to oxygen partial pressure in J/m^2
σ_{SG}	solid-gas surface tension in J/m^2

σ_{SG}^{o}	pure solid-gas surface tension without any oxygen contamination in J/m^2
σ_{SL}	solid-liquid surface tension in J/m^2
σ_{SL}^{o}	pure solid-liquid surface tension without oxygen contamination in J/m^2
$\Delta\sigma_{SL}$	change of solid-liquid surface tension due to oxygen partial pressure in J/m^2
δ	membrane thickness μm
$\Delta G_i^{\Sigma_\alpha,0}$	standard state Gibbs free energy change for the partitioning step
$\overline{\Delta H}_{O(Me)}^{\infty}$	enthalpies of mixing at infinite dilution of oxygen into liquid metal
$\overline{\Delta H}_{M(Me)}^{\infty}$	enthalpies of mixing at infinite dilution of metal in the oxide into liquid metal
θ	contact angle
Γ_i	saturated oxygen adsorption concentration of species i at the liquid surface mol/m^2
$\log P_{O_2}$	logarithm oxygen partial pressure
Σ	interface phase
Σ_α, Σ_β	sublayers of α and β phase
$\tilde{\mu}_i$	electrochemical potential of species i
ψ_i^{Σ}	physicochemical potential
$\theta_i^{\Sigma_\alpha}$	the coverage fraction of species i at α phase

$\theta_j^{\Sigma_\beta}$	the coverage fraction of species j at β phase

Sub- and super-scripts

f	feed side of membrane
p	permeate side of membrane
ρ	elementary reaction step
S	unoccupied surface site
M	unoccupied interstitial site

Abbreviations

DFT	density functional theory
KFL	Kirchhoff's flux law, or Kirchhoff's current law
KPL	Kirchhoff's potential law
OR	overall reaction
QSS	quasi-steady state
QE	quasi-equilibrium
RDS	rate-determining step
TST	transition-state theory

Chapter I

Introduction

1.1 Background

In 2010, CO_2 accounted for about 84% of all U.S. greenhouse gas emissions resulting from human activities. The main source of this CO_2 is the combustion of fossil fuels (coal, natural gas, and oil) for electricity, transportation, industry, residential and commercial, applications. There were about 6.7 Gton of CO_2 emissions in U.S. at 2010, increasing by 10 percent from 1990 to 2010 (U.S. Greenhouse Gas Inventory Report, 2012). Globally 35.7 Gton of CO_2 were added to the atmosphere through the combustion of fossil fuels in 2014, of which the U.S. accounted for about 15% (Friedlingstein, et al., 2010; Olivier, et al., 2015). To reduce CO_2 emissions and alleviate the climate change concerns, it is inevitable to reduce the dependence on fossil fuels and develop clean energy technologies. Hydrogen economy may be one of the potential routes (Bockris, 1999) torward a sustainable energy future, as shown schematically in Figure 1.1.

But why use hydrogen? Hydrogen is the lightest, the simplest, and one of the most abundant elements in nature. However, hydrogen gas does not exist in nature, therefore it is an energy carrier rather than an energy source. The gravimetric amount of energy produced during hydrogen combustion is high and clean (water is the only product), with a lower heating value (LHV) 120.21 MJ/kg, a lot higher than natural gas (47.14 MJ/kg), crude oil (42.69 MJ/kg) and wet basis coal (22.73 MJ/kg), respectively (ornl.org). Hydrogen can be obtained from clean energy sources such as solar energy, wind energy, biological routes, etc., that will avoid or minimize net CO_2 emissions (Figure 1.1). To use hydrogen as energy carrier there is a need to change the current energy system production coupled with the use of fuel cells to efficiently

transform energy into electricity and heat. However, the technology of producing hydrogen via renewable energy (Figure 1.1) is not yet mature. Currently, the majority of hydrogen production comes from hydrocarbons reforming (or steam reforming) of resources such as methane (Uemiya et al., 1990), methanol (Palo et al., 2007), or even ammonia (Choudhary et al., 2001).

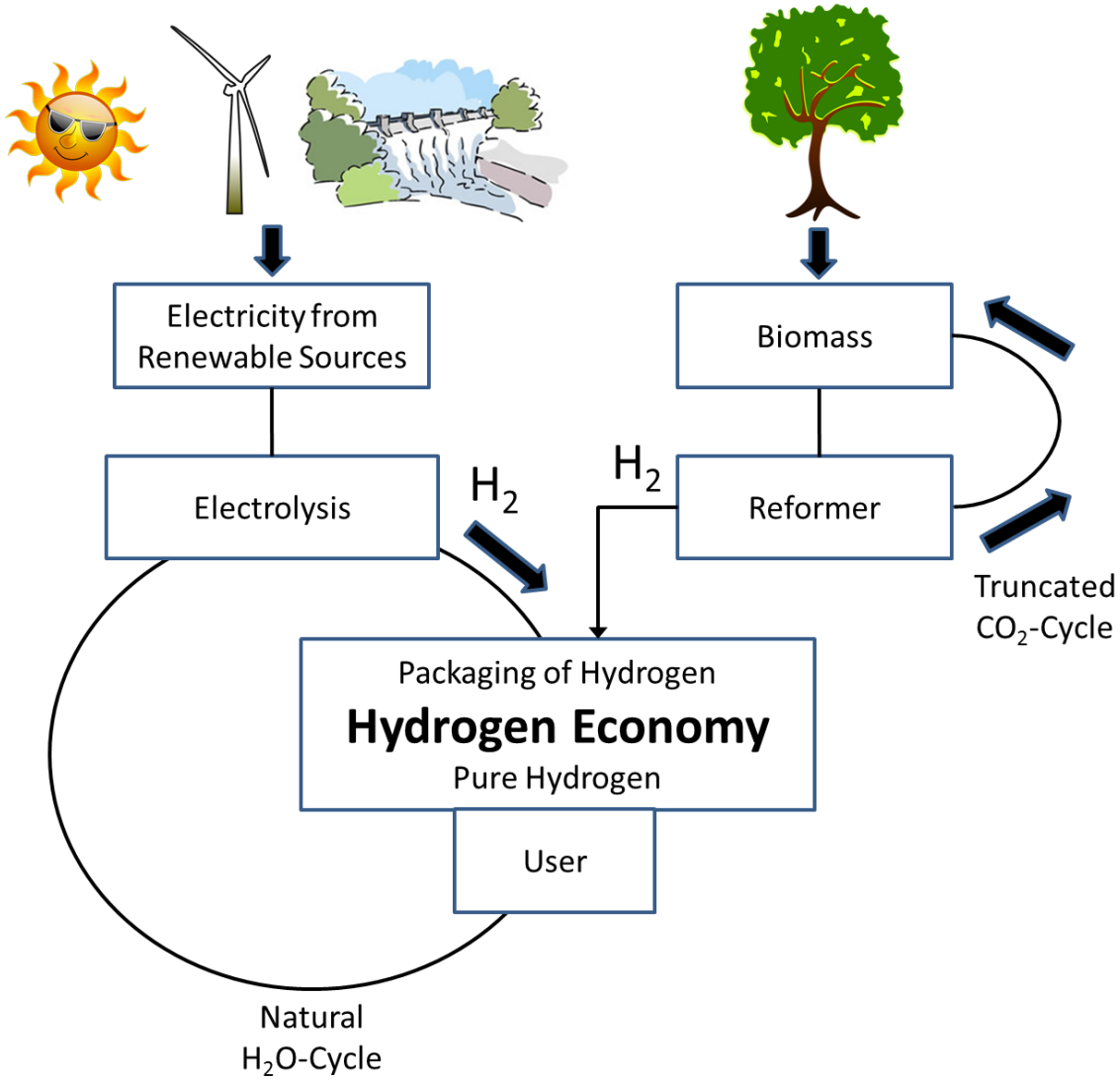

Figure 1.1 Schematic for hydrogen economy (re-draw from oilcrash.com).

There are three primary techniques used to produce hydrogen from hydrocarbon fuels (Holladay et al., 2009): steam reforming (SR), partial oxidation (POX), and autothermal reforming (ATR). Steam reforming is widely used in hydrogen production in industry with an efficiency of about

70-85% (Holladay et al., 2009). The reforming process produces a gas stream composed primarily of H_2, CO and CO_2 with traces of H_2S. To further purify hydrogen from the stream, one or more water gas shift (WGS) stages are applied to reform CO into CO_2 and additional H_2, followed by pressure swing adsorption (PSA) to separate hydrogen from mixed gas, mainly CO_2. The CO_2 may alternately be removed by solvent absorption (Rochelle, 2009). Hydrogen purity after PSA process range from 98.0~99.999% depending on the inlet pressure, purge gas pressure, hydrogen and impurities concentration. Preferential oxidation (PrOx) reaction or methanation may alternately be applied to reduce CO to less than 10 ppm required for fuel cells. The combination of SR, WGS and PSA is used for producing hydrogen for ammonia production. However, PSA is energy intensive. Among alternate technologies for hydrogen separation and purification, membrane separation in particular is drawing attention due to its attractive possibility of *in-situ* production of ultra-high purity hydrogen, continuous operation, process miniaturization, and energy saving (Fausto, et. al, 2009). By applying hydrogen separation membrane directly in a steam reformer (Figure 1.2, Ayturk et al., 2009), for example, or in a water gas shift reactor enables continuous withdrawal of hydrogen from the reactor and sequestration CO_2 rich gas at the other stream, in addition to overcoming thermodynamic limitations.

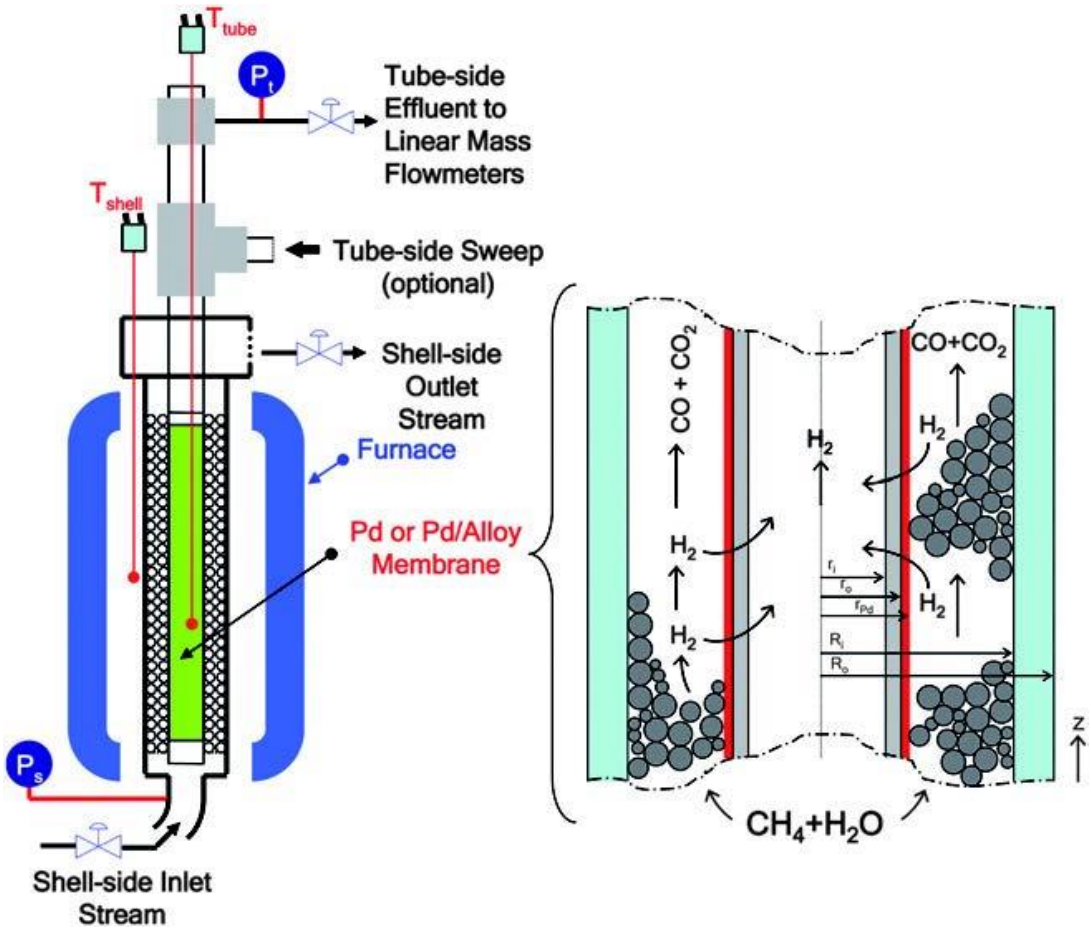

Figure 1.2 Schematic for the catalytic membrane reactor for methane steam reforming (Ayturk et al., 2009).

Literature investigation also suggests that by applying membrane separation reactor in Integrated Gasification Combined Cycles (IGCC) power plants for CO_2 sequestration, as shown in Figure 1.3, provids higher efficiency than commercial CO_2 capture using solvent absorption (Sina, et. al, 2009).

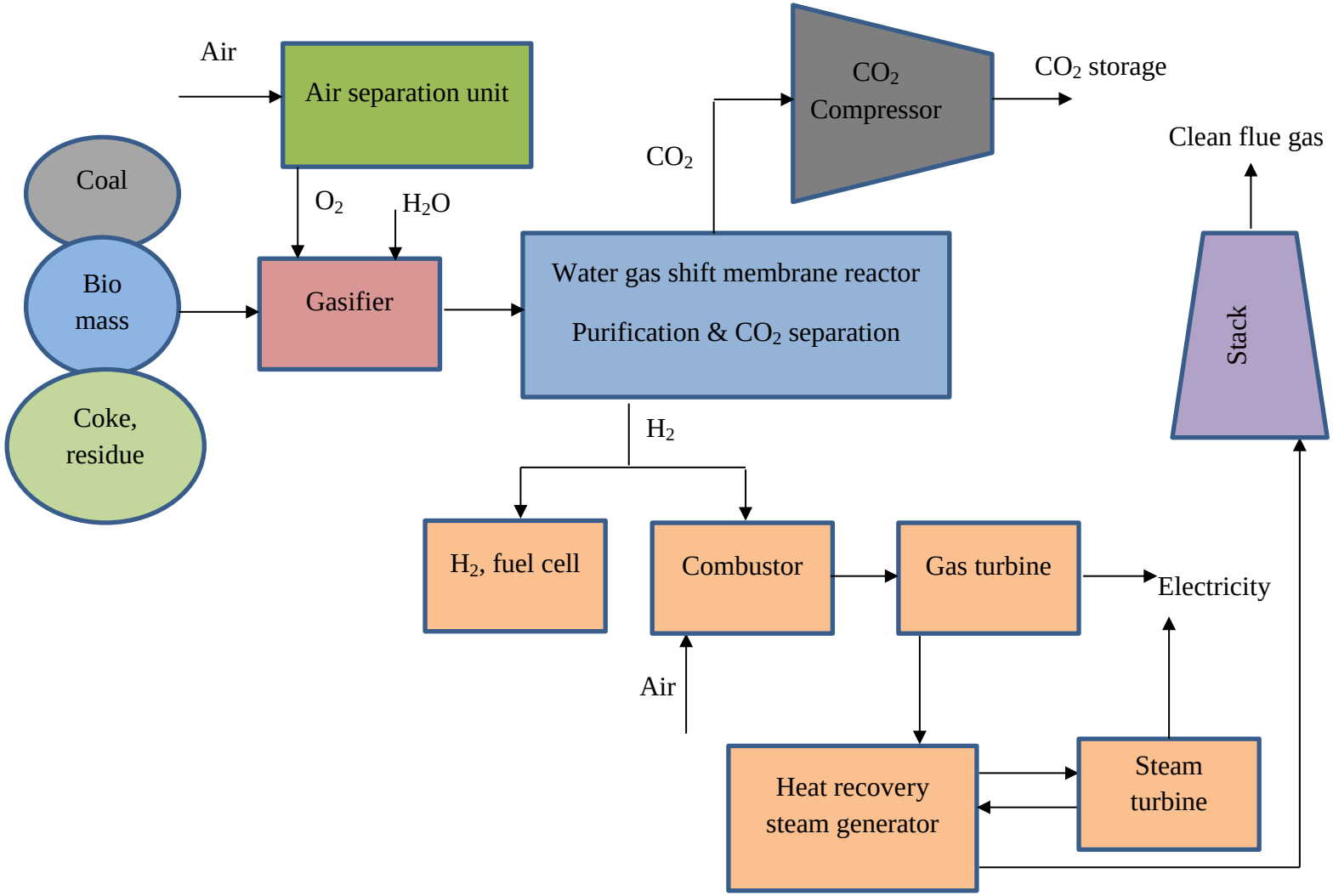

Figure 1.3 Schematic of IGCC power plant with membrane water gas shift reactor for CO_2 capture (modified from Muhammad and Lee, 2013)

1.2 Rationale for this Work

Palladium (Pd) and Pd-based alloy membranes are the most commonly used membrane materials for hydrogen separation and purification. Pd provides several advantages as hydrogen separation membrane. It has a very high hydrogen permeability and a very high hydrogen selectivity. Further, it demonstrates relatively high stability at the high operating temperature when provided with proper diffusion barrier between the thin Pd membrane and porous substrate (Ma et al., 2009). However, to commercialize Pd hydrogen separation membrane reactors and limitations such as high capital costs for large-scale applications and irreversible poisoning by sulphur compounds need to be overcome (Basile et al., 2011). Therefore, the search for replacing Pd with alternative lower cost material and high hydrogen permeability and stability is an ongoing task. For dense metallic membranes, hydrogen is first dissociatively adsorbed on the metal surface. It is then dissolved, and diffuses into metal lattice, followed by associative desorpion from low pressure side of the membrane. Hence, to develop a high hydrogen permeability membrane using a non-precious metallic material with high hydrogen solubility and diffusivity is a promising start.

Lots of attempts have been made in search of replacing Pd with refractory metals such as Nb, Ta, V, etc., to form amorphous alloy (Phair and Donelson, 2006). It is known that amorphous alloys do not show the α–β phase transition during hydrogen absorption, so that there is no hydrogen embrittlement and they are easy to scale up using cold-rolling method (Hara et al., 2000). Non-Pd based membranes seem to have comparable hydrogen permeance to Pd at lower temperatures. However, for practical application the big challenge remains its thermal stability and hydrogen embrittlement at the higher operating temperatures. Often a thin layer of Pd has to be deposited on amorphous alloy membrane surface to prompt its slow surface hydrogen dissociation kinetics

resulting from an oxidation layer formation. At higher temperatures such Pd layer, however, tends to form intermetallic compounds with the amorphous membrane material and lose their activity.

Supported liquid metal membranes (SLiMM) as shown in Figure 1.4 for hydrogen purification are, thus, proposed here for the first time for several reasons: 1) most of the low melting point metals such as Sn, In, Ga, etc. have a significantly lower price than Pd; 2) liquid metal membranes are highly selective if the wetting of support is good to provide a dense membrane; 3) they are ease to fabricate; 4) many of the liquid metals show high hydrogen diffusivity; and 5) there is no phase change or hydrogen embrittlement in a liquid metal. Of course, there are several drawbacks as well, such as the solubility of H_2 in some liquid metals is moderate, with the exception of alkaline metals. Liquid metal are highly reactive thus the search of proper support is also a great challenge. Unlike solid metal membrane, supported liquid metal membrane may not be able to withstand at high hydrogen pressure drop depending on the liquid metal surface tension and substrate pore size.

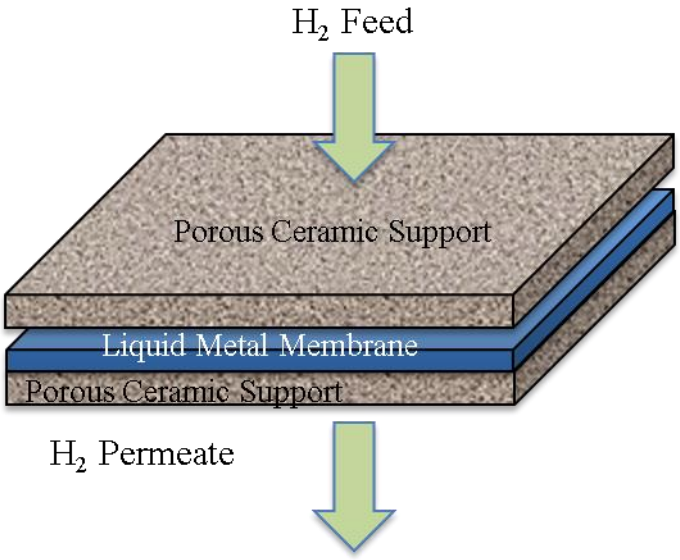

Figure 1.4 Concept of sandwiched liquid metal membrane (SLiMM).

The fabrication of a dense and stable liquid metal membrane is predicated on the following stringent requirements for an appropriate porous support/diffusion-barrier layer: 1) it should possess high chemical inertness, as the molten metals are very reactive at high temperature, and are likely to infiltrate the support. This means that naked porous metal supports are not suitable, readily forming alloys and intermetallic compounds with the molten metals at the higher operating temperatures. Many ceramics, on the other hand, were found to possess adequate chemical inertness; 2) the support must possess adequate wettability for the liquid metal. While most porous metal supports possess this characteristic, many ceramics are overly inert and are not easily wetted by liquid metals. In fact, chemical inertness and lack of wettability of the many ceramics go hand-in-hand, since wettability implies some interfacial bonding (physical or chemical) between the support and the liquid metal; 3) the support must possess adequate strength to allow compressive sealing, especially at the higher temperatures. While most metal supports meet this criterion, most ceramics are too fragile; and finally 4) the support should possess appropriate pore size and porosity to allow pressure drop across it without a significant diffusion resistance. In fact, a symmetric support with a skin layer with small pore size deposited on a coarser support may be ideal.

Gallium was chosen as the initial liquid metal membrane candidate in this study because of the its low melting point, low volatility, and role as catalyst in a number of heterogeneous catalytic reactions involving the formation/breakage of H-containing bonds, and evidence for the adsorption of hydrogen forming GaH, which could be reversibly released at 450 ^{o}C (Pan et al., 2011; Collins et al., 2002). It is very stable under ambient environment compared to some of the other low melting point metals, e.g. alkaline metals, which makes it easy to handle and process. The diffusivity of hydrogen in liquid Ga is 7 times higher than that in Pd at 250 ^{o}C (Mazayev and

Prokofiev, 1994). Further, the very low melting point coupled with low volatility and high stability could match the hydrogen reforming temperatures of 500 ºC and above.

Unfortunately, there is no literature on liquid metal hydrogen separation membranes, which implied little guidance so that there was a lot of trial and error involve in membrane fabrication, configuration, permeation testing, and membrane stability. Further, due to the lack of a fundamental theory of hydrogen solution and diffusion in liquid metals, this work focused on developing such a model to gain a better understanding of thermophysical properties, and thermodynamic and kinetic parameters of atomic hydrogen adsorption, solution, and diffusion in liquid metals. In short, we were able to demonstrate that the concept of SLiMM is feasible, and that theory of solution and diffusion in liquid developed here agrees with experimental permeance of the liquid gallium membrane.

1.3 Objectives of this Work

The objectives of this study were proposed as follows: 1. to demonstrate the feasibility of fabricating a stable SLiMM based on systematic support material screening; 2. to investigate the characteristics of hydrogen solution and diffusion in liquid metal and to prove of the concept of SLiMM; 3. to develop theoretical models and gain fundamental understanding of the thermodynamic and kinetic properties of liquid metals, and the dissociative adsorption, dissolution, and atomic diffusion of hydrogen in liquid metals; and finally and 4. to study the effect of gas composition on the surface tension of liquid metals to gain a better understanding of the wetting between liquid metals and ceramic supports under different gaseous atmospheres. Details of the process made toward these objectives are provided in this thesis.

In Chapter II, a detailed introduction is provided and current state of development of hydrogen separation membranes including Pd, Pd alloy, and amorphous alloys is reviewed. The advantages

and the limitations of these materials explicate the need and the direction for developing SLiMM for future industrial applications. The mechanism of hydrogen permeation through dense metals is also discussed, providing the basis for SLiMM as a good candidate for replacing Pd membrane.

Chapter III summarizes from the literature the physical and chemical properties of gallium of relevance to the design and the development of a stable SLiMM. To understand gallium interaction with hydrogen, the characteristics of GaH investigated via computer modeling and some limited experiments is discussed and gathered from the literature. It is known that hydrogen interstitially diffuses in metals. Thus the diffusivity is highly related to metal crystal structure. Both solid and liquid gallium structure are thus discussed in detail to lay the ground work for thermodynamic and kinetic modeling in Chapters IV and V.

In Chapter IV, we combine Pauling Bond Valence- with Modified Morse Potential (PBV-MMP) to propose a new semi-theoretical molecular model to predict relevant properties of liquid metals such as surface tension, viscosity, and self-diffusivity. Thus, Pauling's relationship between bond-valence (BV) and bond-length (BL) is incorporated within a modified Morse-Potential (MMP) description of the potential energy of interaction between two metal atoms in terms of the bond-valence. The PBV-MMP approach for bulk metals is in the spirit of Unity Bond Index-Quadratic Exponential Potential (UBI-QEP) of Shustorovich (1998). This new PBV-MMP approach allows us to obtain predictions of a number of properties of interest based on only needing the M-M bond energy for a specified valence along with liquid metal density. The resulting theory reliably predicts various liquid properties that agree with experimental results available in the literature for the case of liquid gallium, and also for some other liquid metals such as Cu, Al, and Na.

Chapter V extends the PBV-MMP approach, which is a refinement of the Unity-Bond Index-Quadratic-Exponential Potential (UBI-QEP) method originally developed for the predicting the energetics of *surface* reaction and diffusion steps for *solid* metals, to apply it for predicting solution and diffusion of atomic impurities such as hydrogen in *bulk liquid* metal. The PBV-MMP model is used for estimating the thermodynamic and kinetic parameters that describe atomic hydrogen adsorption, solution, and diffusion in liquid metals. The theoretical predictions agree well with solubility parameters determined from our experiments and the diffusion parameters reported in the literature.

In Chapter VI, a thermodynamic assessment to estimate the interaction of support material with liquid gallium along with coupon experiments are described to systematically screen suitable porous substrate materials for SLiMM. The goal was to find the proper porous supports for liquid Ga membrane in terms of wettability and stability. The results suggest that some common metal oxide and nitride ceramics materials are not suitable. On the other hand, carbide materials are the best candidates for supporting liquid metals as they provide adequate wetting and great stability at high temperatures.

Chapter VII demonstrates the design and skill in constructing seamless SiC supports for SLiMM permeation test and describes several approaches in testing and confirming hydrogen permeation through liquid gallium membrane without leakage for up to 360 hours. The measured hydrogen permeance of liquid gallium, $72.5\,m^3/m^2h\cdot atm^{0.5}$ at 500 ºC is about 35 times higher than that of Pd foil of similar thickness, $2\,m^3/m^2h\cdot atm^{0.5}$(Ayturk et al., 2009), while price is an order of magnitude lower (metal-pages.com). Permeability at 500 ºC 19850 $m^3\mu m/m^2h\cdot atm^{0.5}$ is only lower than Nb and higher than all the amorphous alloys described in Phair and Donelson (2006) review article as shown in Figure 1.5. This provides clear evidence that liquid gallium has

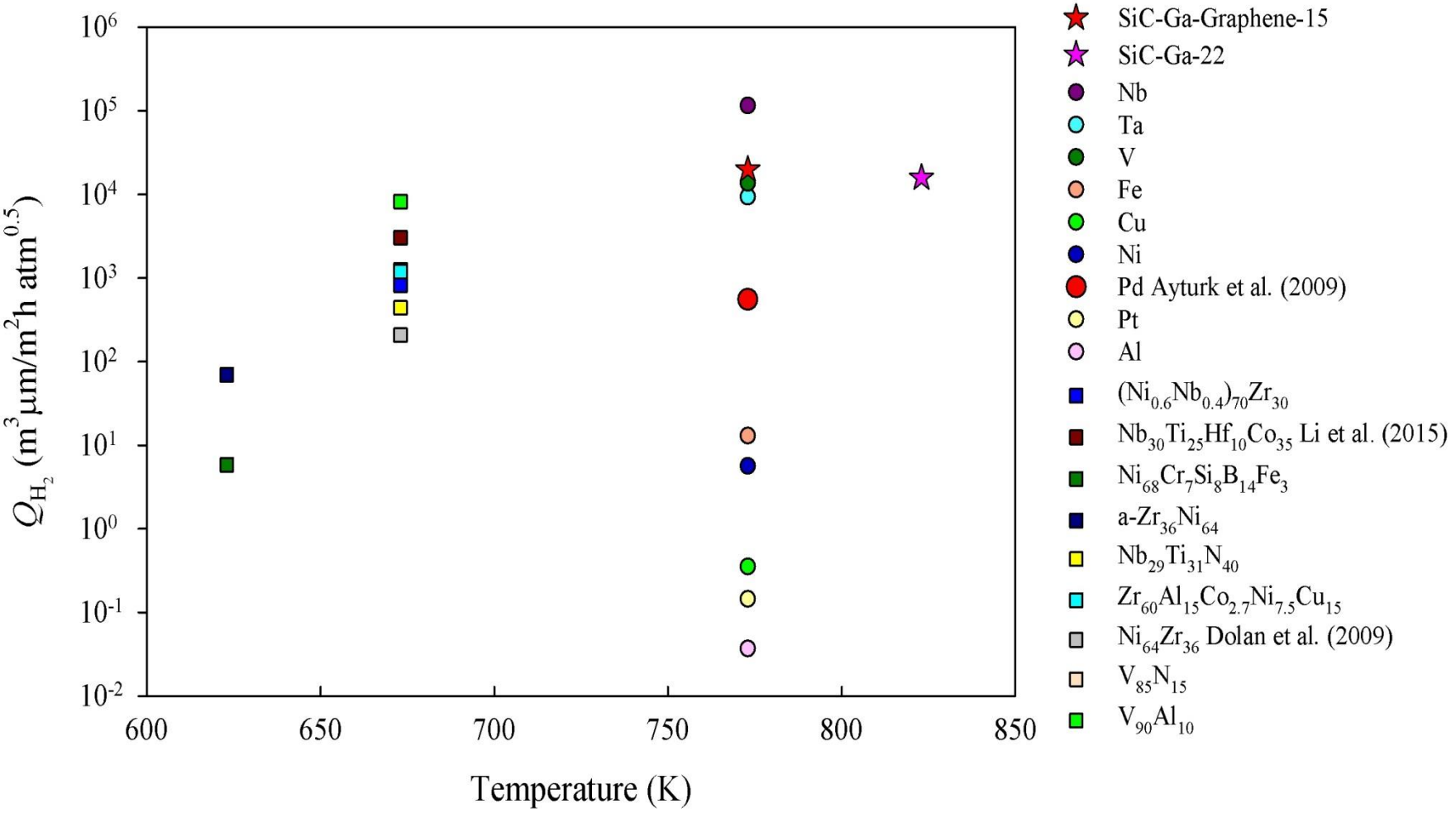

Figure 1.5 Hydrogen permeability of dense liquid gallium membrane, metals and amorphous metals between 623~823 K (Pd from Ayturk et al., 2009; $Nb_{30}Ti_{25}Hf_{10}Co_{35}$ from Li et al., 2015; $Ni_{64}Zr_{36}$ from Dolan et al., 2009; all others from Phair and Donelson, 2006).

considerable potential as a hydrogen separation membrane, although, much further study is needed before any application.

In Chapter VIII, a thermodynamic theory is developed to explain the change in the liquid-gas surface tension, solid-liquid surface tension and the contact angle of liquid metal/ceramic systems as a function of gas composition. Operating parameters used in testing hydrogen permeation such as temperature, pressure and gas environment affect surface energy and liquid membrane wettability, and can hence, change the membrane stability. The model was used to investigate the effect of oxygen partial pressure on liquid metal/ceramic systems in detail in this chapter, due to the lack of experimental investigations on hydrogen liquid metal systems in the literature. From these results we conclude that a sandwich configuration (Figure 1.4) for membrane fabrication is the key to avoid a free liquid metal whose surface energy and wettability can change with temperature, pressure and gas composition.

In summary, this thesis is concerned with advancing the hydrogen separation membrane technology by developing completely novel hydrogen membranes based on liquid metals to exploit their very high diffusivity. The developed PBV-MMP theoretical model gives insight into the relevant thermodynamic, kinetic and chemical properties of liquid metals, as well as theory atomic of impurities such as H in liquid metals. This work expands the knowledge and the potential application of liquid metal into hydrogen separation, hydrogen storage and possibly leading to a new way of constructing hydrogen separators and catalytic membrane reactor in the future.

1.4 References

Ayturk, M. E., Kazantzis, N. and Ma, Y. H., Modeling and performance assessment of Pd and Pd/Au-Based catalytic membrane reactors for hydrogen production, *Energy and Environmental Science*, 2, (2009), 430-438.

Basile, A., Iulianelli, A., Longo, T., Liguori, S. and De Falco, M., Pd-based selective membrane state-of-the-art. In Membrane reactors for hydrogen production processes, *Springer London*, p. 21-55, (2011).

Bockris, J.O'M., Hydrogen economy in the future, *International Journal of Hydrogen Energy*, 24, (1999), 1-15.

Choudhary, T. V., Sivadinarayana, C. and Goodman, D. W., Catalytic ammonia decomposition: COx-free hydrogen production for fuel cell applications, *Catalysis Letters*, 72, 3-4, (2001), 197-201.

Collins, S. E., Baltan´as, M. A., Garcia Fierro, J. L. and Bonivardi, A. L., Gallium-hydrogen bond formation on gallium and gallium-palladium silica-supported, *Catalysts Journal of Catalysis* , 211, (2002), 252-264.

Dolan, M., Dave, N., Morpeth, L., Donelson, R., Liang, D., Kellam, M. and Song, S., Ni-based amorphous alloy membranes for hydrogen separation at 400 ºC, *Journal of Membrane Science*, 326, 2, (2009), 549-555.

EPA, United State Environmental Protection Agency, Inventory of U.S. Greenhouse Gas Emissions and Sinks: 1990-2010, (2012).

Friedlingstein, P., Houghton, R. A., Marland, G., Hackler, J., Boden, T. A., Conway, T. J., Canadell, J. G., Raupach, M. R., Ciais, P. and Le Quere, C., Update on CO_2 emissions, *Nature Geoscience*, 3, 12, (2010), 811-812.

Gallucci, F., Basile, A., Iulianelli, A. and Kuipers, H. J., A review on patents for hydrogen production using membrane reactors, *Recent Patents on Chemical Engineering*, 2, 3, (2009), 207-222.

Hara, S., Sakaki, K., Itoh, N., Kimura, H. M., Asami, K. and Inoue, A., An amorphous alloy membrane without noble metals for gaseous hydrogen separation, *Journal of Membrane Science*, 164, (2000), 289-294.

Holladay, J. D., Hu, J., King, D. L. and Wang, Y., An overview of hydrogen production technologies, *Catalysis Today*, 139, 4, (2009), 244-260.

http://cta.ornl.gov/bedb/index.shtml

http://www.metal-pages.com/metalprices/gallium/

http://www.oilcrash.com/articles/h2_eco.htm

Li, X., Liu, D., Liang, X., Chen, R., Rettenmayr, M., Su, Y., Guo, J. and Fu, H., Substantial enhancement of hydrogen permeability and embrittlement resistance of $Nb_{30}Ti_{25}Hf_{10}Co_{35}$ eutectic alloy membranes by directional solidification, *Journal of Membrane Science*, 496, (2015), 165-173.

Ma, Y. H., Kazantzis, N. K., Mardilovich, I. P., Guazzone, F., Augustine, A. S. and Koc, R., Composite Pd and Pd Alloy porous stainless steel membranes for hydrogen production and process intensification, DOE Hydrogen Program, *FY 2009 Annual Progress Report*, (2009).

Mazayev, S. N. and Prokofiev, Y. G., Hydrogen inventory in gallium, *Journal of Nuclear Materials*, 212-215, B, (1994), 1497-1498.

Muhammad, Z. and Lee J. H., Carbon capture from stationary power generation sources: A review of the current status of the technologies, *Korean Journal of Chemical Engineering* 30, 8, (2013), 1497-1526.

Olivier, J. G. J., Janssens-Maenhout, G., Muntean, M. Peters, J. H. A. W., Trends in global CO_2 emissions - 2015 report, *JRC report 98184 / PBL report 1803*, (2015).

Palo, D. R., Dagle, R. A. and Holladay, J. D., Methanol steam reforming for hydrogen production, *Chemical Reviews*, 107, 10, (2007), 3992-4021.

Pan, Y. X., Mei, D., Liu, C. J. and Ge, Q., Hydrogen adsorption on Ga_2O_3 surface: a combined experimental and computational sudy, *Journal of Physical Chemistry C*, 115, (2011), 10140-10146.

Phair, J. W. and Donelson, R., Developments and design of novel (non-palladium-based) metal membranes for hydrogen separation, *Industrial and Engineering Chemistry Research*, 45, (2006), 5657-5674.

Rezvani, S., Huang, Y., McIlveen-Wright, D., Hewitt, N. and Mondol, J. D., Comparative assessment of coal fired IGCC systems with CO_2 capture using physical absorption, membrane reactors and chemical looping, *Fuel*, 88, 12, (2009), 2463-2472.

Rochelle, G. T., Amine scrubbing for CO_2 capture, *Science*, 325, 5948, (2009), 1652-1654.

Shustorovich, E. M. and Sellers, H., The UBI-QEP method: a practical theoretical approach to understanding chemistry on transition metal surfaces, Surface Science Reports, 31, 1, (1998), 1-119.

Uemiya, S., Sato, N., Ando, H., Matsuda, T. and Kikuchi, E., Steam reforming of methane in a hydrogen-permeable membrane reactor, *Applied Catalysis*, 67, 1, (1990), 223-230.

Chapter II

Hydrogen Separation Membranes

2.1 Abstract

Hydrogen has been touted as an energy carrier in the so-called "hydrogen economy," (Marbán, and Valdés-Solís, 2007) which envisions its widespread generation, distribution, and storage. It is currently produced from natural gas in large-scale plants via steam reforming and water gas shift reaction steps to produce a reformate (H_2 + CO_2), (Rostrup-Nielsen and Rostrup-Nielsen, 2002) followed by an energy-intensive pressure swing adsorption process for H_2 separation and purification. Thin (~ 20 μm) but dense palladium membranes, coated on porous sintered metal supports, are being developed as a more efficient alternate process to produce high purity H_2 from reformate (Rostrup-Nielsen and Rostrup-Nielsen, 2002; Armor, 1998). Membrane-related processes can provide an attractive alternative to PSA and cryogenic distillation since they consume less energy with the possibility of continuous operation. The *in-situ* hydrogen separation in the reforming reactor can further shift the reaction and increase hydrogen conversion (Adhikari and Fernando, 2006).

This chapter summarizes the literature on membrane development, mechanism of hydrogen permeation, material limitations, and hydrogen solubility/diffusivity of Pd, Pd alloy and non-Pd membranes. First the fabrication of Pd, and Pd alloy membranes and its advantages, and limitations are described. The Pd membranes are deposited as thin film on porous metal supports. Therefore a diffusion barrier is needed to impede intermetallic diffusion at the high operating temperatures. The function and the method of preparing such diffusion barrier layer are discussed. Also, to make a sufficiently thin and stable Pd membrane it is often combined with

surface pore modifications along with diffusion barrier on porous metal support in one or two steps. The mechanism of hydrogen permeation in metals systems is also introduced in this chapter. Hydrogen dissolution in metal usually follows Sieverts' law. The high hydrogen solubility of Pd makes it unique. However at temperature below 350 ºC, the α-β phase transition of pure Pd associated with hydrogen embrittlement is a key drawback (Basile et al., 2011), leading to the membrane embrittlement.

There is no literature on hydrogen permeation in liquid metal membrane. Therefore, to develop a hydrogen separation supported liquid metal membrane and to select a candidate, we start by gathering hydrogen solubility and diffusivity data available in the literature for various liquid metals.

2.2 Introduction

Since Graham first discovered the ability of hydrogen to permeate palladium tubes, the characteristics of Pd and Pd-based alloy membranes for hydrogen have been studied intensively (Graham, 1866; Mitacek and Aston, 1963; Frieske and Wicke, 1973; Clewley et al., 1973; Moon, 1956). Even though the outstanding hydrogen permeability of Pd is unique and highly desirable, it's high price, hydrogen embrittlement and sulfur poisoning (Morreale et al., 2004) are significant obstacles for its industrial applications. The search of replacements is thus continuing. One of the alternate approaches is to use amorphous non-precious metal materials comprised Nb, Ta, V, and Zr (Phair and Donelson, 2006). Some of the amorphous materials are quite promising in terms of hydrogen permeability. However, the life time of amorphous hydrogen membranes at high temperature and its slow dissociative adsorption kinetics (Hara et al., 2000) remain as issues. Amorphous alloys tend to become crystallized at higher temperatures and their permeation correspondingly drops (Dolan, 2010). Our novel liquid membrane would not have most of these

problems. Since it does involve a crystalline structure, therefore there would be no hydrogen embrittlement and they are cheaper than Pd. Even though the literature reports of hydrogen solubility and diffusivity of liquid metals are scarce, from the available information we know that they have high hydrogen diffusivity. Most of them have higher diffusivity than solid metals (Sacris and Parlee, 1970; Freudenberg and Glaser, 1985). This makes them good potential candidates as hydrogen separation membranes.

2.3 Permeation Mechanism and Sieverts' Law

The mechanism of hydrogen permeation through a solid metal, especially Pd membrane, is well investigated (Ayturk et al., 2009) and a similar mechanism is known to be operative in other metals. As depicted in Figure 2.1, thus, hydrogen permeation in Pd involves the following sequential steps (Deveau et al., 2013) : ① the H_2 molecules on the feed side dissociatively adsorb on the metal surface as H atoms, ② which next infiltrate the bulk lattice as interstitial H atoms, ③ which then diffuse across the membrane, and ④ on reaching the permeate side egress from the bulk metal to its surface, and finally ⑤ the adsorbed H atoms on permeate-side metal surface recombine and desorb as H_2 molecules.

The solubility of hydrogen in metals in the limit of dilute solutions is well-known to be described by Sieverts' law (Sieverts, 1929),

$$x_{\mathrm{H\cdot M}} \approx K_S \sqrt{p_{\mathrm{H_2}} / p^{\mathrm{o}}} \quad ; \quad K_S = \exp\left(\frac{\Delta S_S^{\mathrm{o}}}{R} - \frac{\Delta H_S^{\mathrm{o}}}{RT} \right) \tag{2.1}$$

where $x_{\mathrm{H\cdot M}}$ is the H/M mole fraction of interstitial H in metal, K_S is the Sieverts' equilibrium constant, given in terms of ΔS_S^{o} and ΔH_S^{o}, the standard entropy and enthalpy change of hydrogen solution in the metal, respectively, R is the gas constant, T is the temperature, $p_{\mathrm{H_2}}$ is the

hydrogen partial pressure, and p^{o} is the standard pressure (1 atm.). For hydrogen in Pd, for instance, $\Delta H_S^{o} = -12.1$ kJ/mol i.e. this is mildly exothermic, and $\Delta S_S^{o} = -63$ J/mol K (Deveau et al., 2013).

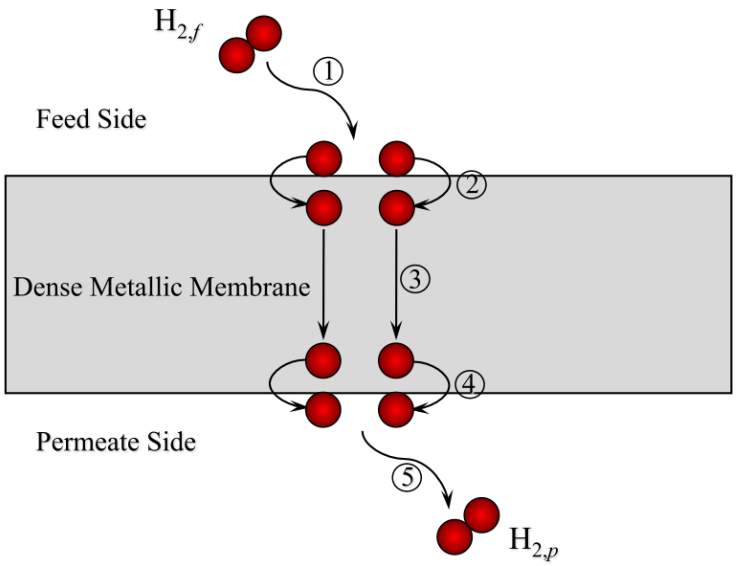

Figure 2.1 A schematic of the H_2 permeation process through a dense liquid metal membrane involving sequential steps of: ① surface dissociative adsorption, ② subsurface penetration, ③ bulk metal diffusion, ④ egression to surface, and ⑤ reassociation of H atoms on the surface to form molecular H_2 (Deveau et al., 2013).

Further, from Hess's law

$$\Delta H_S^{o} = \frac{1}{2}\Delta H_1^{o} + \Delta H_2^{o};\ \Delta S_S^{o} = \frac{1}{2}\Delta S_1^{o} + \Delta S_2^{o} \tag{2.2}$$

in terms of standard enthalpy change and entropy change of step 1 and 2. This further leads to

$$K_S = \sqrt{K_1}K_2 \tag{2.3}$$

which are the equilibrium constant of step 1 and 2, respectively.

At lower temperatures (300 ºC or less), H_2 permeation flux N_{H_2} is limited by surface adsorption/desorption rates, namely, steps ① and ⑤ (Deveau et al., 2013) as depicted in Figure 2.1. At higher temperatures that are more typical, however, the diffusion of the interstitial H atoms within the bulk metal is the rate-determining step. Then, combining Fick's law for interstitial H atom diffusion with Sieverts' law for H solution provides the H_2 flux through the metal membrane

$$N_{H_2} \approx P_{H_2}\left(p_{H_2,f}^{0.5} - p_{H_2,p}^{0.5}\right) \tag{2.4}$$

where the hydrogen *permeance* of the membrane

$$P_{H_2} \equiv \left(\frac{1}{2V_M\sqrt{p^o}}\right)\frac{K_S D_H}{\delta} \tag{2.5}$$

where D_H is the interstitial diffusion coefficient of H atoms, V_M is the molar volume of metal M (e.g., $V_M = 8.85$ cm^3 per g atom Pd), and δ is the dense membrane film thickness. The factor 2 in the denominator accounts for interstitial diffusion of two H atoms per H_2 molecule. An alternate transport characteristic commonly used is membrane *permeability*, i.e.,

$$Q_{H_2} = P_{H_2}\delta \tag{2.6}$$

which has the virtue of involving only material properties, not membrane thickness. Hydrogen permeability of Pd foil is $Q_{H_2} = 6322.7\exp(\frac{-15630}{RT})$ m$^3\mu$m/m^{2}h atm$^{0.5}$ as provided by Ayturk et al., (2009).

These alternate permeation parameters, P_{H_2} and Q_{H_2}, have an Arrhenius temperature dependence (Deveau et al., 2013) with an effective activation energy *E*, just as does the atomic H diffusion coefficient with an effective activation energy E_D

$$D_{\mathrm{H}} = D_{\mathrm{H},0} \exp\left(-\frac{E_D}{RT}\right) \tag{2.7}$$

where $D_{\mathrm{H},0}$ is the pre-exponential factor. The effective activation energy for P_{H_2} and Q_{H_2}, thus, $E = E_D + \Delta H_S^{\circ}$. For Pd, for instance, $E_D = 27$ kJ/mol, so that $E = 27 + (-12.1) = 14.9$ kJ/mol (Deveau et al., 2013).

Through Pd hydrogen permeation experiments it has been discovered that a more general expression is $N_{\mathrm{H}_2} \approx P_{\mathrm{H}_2}\left(p_{\mathrm{H}_2,f}^{n} - p_{\mathrm{H}_2,p}^{n}\right)$ with the n value not always being 0.5 which depends on the Pd membrane thickness, support layer thickness (external mass transfer), temperature, and hydrogen pressure at feed and permeate side (Caravella, et al., 2010; Gabitto and Tsouris, 2008). Generally n value is between 0.5~1. When membrane is ultra-thin, or tested at low temperature (under 200 ºC) the n value tends to be greater than 0.5 and closer to 1. The hydrogen bulk diffusion through Pd membrane is no longer the rate-determining step (McCool and Lin, 2001). Instead, surface adsorption/desorption kinetics is also a slow step. Another reason for having higher n value is the leakage through the membrane. Hydrogen may simultaneously diffuse though cracks via Knudsen diffusion and via viscous flow depending on the size of pinholes, rather than just penetrating through Pd membrane. As the ideal selectivity $\alpha \equiv N_{\mathrm{H}_2}/N_{\mathrm{He}}$ becomes lower than 400, the Knudsen diffusion and viscous flow of hydrogen through defects leads to n value higher than 0.75 at 500 ºC (Guazzone et al, 2006).

2.4 Pd and Pd Composite Membranes

A limitation of using pure Pd membrane for hydrogen permeation is the formation of Pd-H α+β phase under 295.3 ºC and hydrogen pressure below 19.87 atm (Gillespie and Galstaun, 1936; Knapton, 1977) critical temperature and pressure. The pressure concentration isotherms show in

Figure 2.2 the hydrogen solubility (H/Pd), i.e., the ratio of H atoms absorbed per Pd atom, as a function of hydrogen pressure and temperature. Below the critical point, the α phase coexists with β phase, where β phase has a considerably expanded lattice compared to α phase and significantly more hydrogen in the solution. After several cycles of hydrogen adsorption/desorption, the strain caused by hydrogen "stored" in metal lattice can induce volume expansion, resulting in hydrogen embrittlement and cracking of the Pd membrane (Goods and Guthrie, 1992).

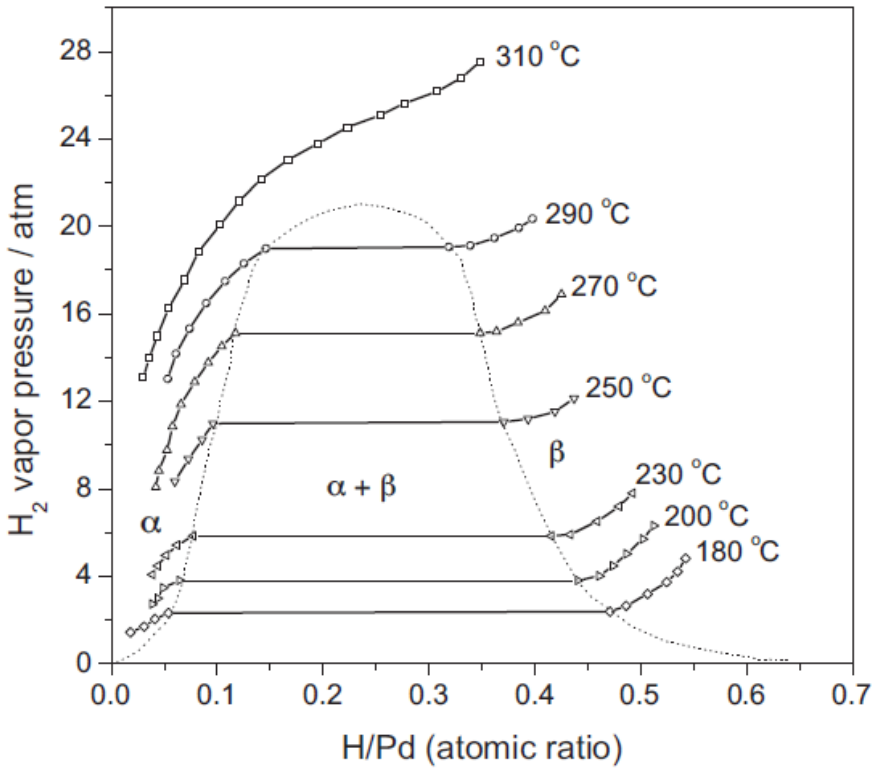

Figure 2.2 Pressure concentration isotherms of Pd-H (Yun and Oyama, 2011).

For hydrogen storage purpose, this would be a desirable phenomenon since the embrittlement could help accelerating the adsorption/desorption kinetics. However for hydrogen separation membrane, this leads to cracks and decreases the selectivity since other gases can diffuse through these cracks. Many studies have been conducted hence to investigate the optimum composition

and species to alloy with Pd for several reasons: 1) to increase hydrogen permeability; 2) to eliminate phase transition leading to embrittlement; and 3) to prevent the membrane from being poisoning. Such modification of Pd membrane via alloying makes it more viable in the application in steam reforming in terms of having wider temperature operation range, extended life time, and reduced cost (Shu et al., 1991).

To avoid embrittlement caused by phase transition, the easiest approach is to operate Pd membrane above its critical point, or alloy Pd with other metals that avoid phase change, for example, Pd-Ag (Hunter, 1956). When 20 % or more of silver is added to Pd, the resulting alloy has no embrittlement even at room temperature. It was further discovered that the optimum composition of Ag in Pd is 77 % Pd 23 %Ag (wt %), which provides a permeability in fact higher than pure Pd due to the change in diffusivity and solubility (McKinley, 1966; Knapton, 1977). Using Pd-Ag foils as hydrogen purifier was first tested in 1962 and commercialized in 1964 by Johnson Matthey. However, they could only be used in small to medium scale plants with less than 0.1 ppm of impurities allowed from the feed (Connor, 1962). The impurities such as sulfur, mercury, and arsenic could cause irreversible poisoning of the membrane, while chemisorption of hydrocarbons, and oxygen-containing compounds causes reversible poisoning. Either way, hydrogen permeability is lowered. Without poisoning, Pd-Ag membrane is stable under wide range of operating temperatures (150-400 ºC) and pressures (100-400 kPa) over a year long life time test (Tosti et al., 2006).

In order to successfully utilize Pd membrane in catalytic membrane reactors or in reformate stream to refine products, besides having a high permeability, high selectivity, low cost, long life time and resistance from poisoning by impurities (CO, H_2S, etc.) are essential criterion, often accomplished as described above by modifying Pd membrane by alloying (Armor, 1998). Both

Pd-Cu and Pd-Au alloys have been tested intensively for resisting hydrogen-sulfide poisoning, and partially oxidized Pd-Al alloy for resisting CO poisoning (Gabitto and Tsouris, 2009; Flanagan et al., 2000).

It was discovered that 60 % Pd 40 % Cu (wt %) has the highest hydrogen permeability with no α-β phase transition so that no hydrogen embrilittlement occurs even when operating at lower temperatures (McKinley, 1969). Further studies showed that the crystal structure of 60 % Pd 40 % Cu at temperature below 550 ºC is bcc-fcc mixed structure, which becomes fcc above at 550 ºC. Generally, Pd-Cu with bcc structure has a higher permeability, and the fcc structure has a lower permeability but a higher resistance to H_2S poisoning, possibly due to its surface structure and surface chemistry (Morreale et al., 2004; Howard et al., 2004). Therefore, to attain highest permeability along with the resistance to H_2S, it is preferable to have a thin layer of fcc structure Pd-Cu on the membrane surface (Pomerantz and Ma, 2009). Though a part of hydrogen permeability drop is reversible after H_2S poisoning, however, a part of the permeability is permanently lost because of the surface sulfide formation. The permeability of Pd-18% Cu (wt %) poisoned by 54.2 ppm H_2S/H_2 at 450 °C was recovered 60 % by switching to H_2, while the permeability of Pd-8%Cu (wt %) poisoned by 42.7 ppm H_2S/H_2 at 450 ºC was recovered 85 % .

Pd-Au has also been investigated for improving sulfur resistance of membrane. It was discovered that 95% Pd 5 % Au (wt %) has the highest hydrogen permeability along with good H_2S resistance (McKinley, 1967). Later research showed that the highest permeability of fcc PdAu was at 10 % Au (wt %) and at temperatures between 120–300 ºC (Flanagan and Wang, 2011). For the H_2S poisoning study, it was discovered that the permeability of Pd-8%Au (wt%) poisoned by 54.8 ppm H_2S/H_2 mixture at 400 ºC was recovered totally by switching back to H_2 at 500 ºC (Chen and Ma, 2010). The hydrogen permeance decline upon H_2S exposure resulted

from the surface site blocking that is reversible at higher temperature due to exothermic nature of dissociative adsorption of H_2S on Pd/Au metal.

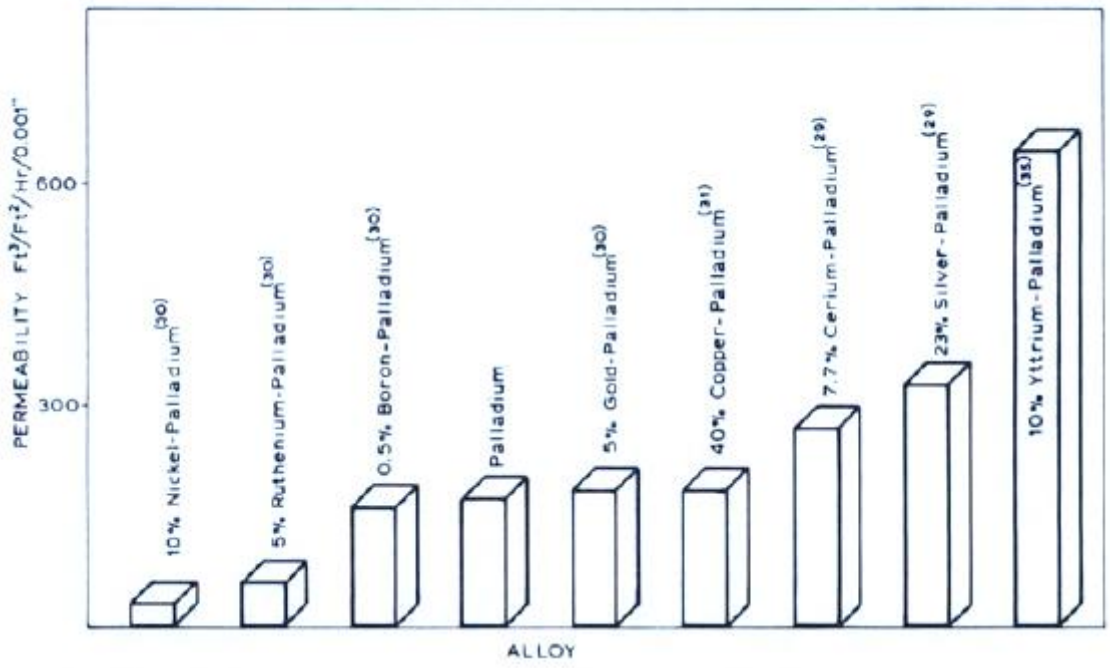

Figure 2.3 Maximum hydrogen permeability of Pd and Pd binary alloy system at 350 ºC, 300 psi (Grashoff et al., 1983).

The alloying of Pd with rare earth metals, La, Ce, Y, Pr, Gd, Tm, etc. was first investigated in 1968 (Doyle and Harris, 1988). It was discovered that La is insoluble in Pd; Pr, Ce, Y, Gd and Tm are soluble up to 2, 12, 12, 11, and 16%, respectively. The expansion of Pd lattice spacing is increased with increasing rare earth metal solute content at room temperature, where the expansion of Pd-Y, Pd-Ce lattice is much greater than that in Pd-Ag. The optimum addition to Pd in terms of permeability was reported to be 7.7wt% for Ce and 10wt% for Y, both having a higher permeability than pure Pd at the same operation condition (Farr and Harris, 1973; Fort et al., 1975). The enhanced permeability in rare earth Pd alloy is due to greater hydrogen solubility compared to $Pd_{75}Ag_{25}$ alloy (Hughes and Harris, 1979). However, the degradation of Pd-Ce, Pd-Y due to Ce and Y reacting with any oxygen present in hydrogen to form cerium oxide, yttrium

oxide was also discovered (Knapton, 1977). A comparison of hydrogen permeability at 350 ºC, 300 psi among various Pd alloy is shown in Figure 2.3.

2.5 Supported Pd Membrane Fabrication

Palladium foil membranes are impractical because of large thickness, which increases cost while reducing hydrogen permeability. The critical goal for supported Pd membrane fabrication is to have dense (high selectivity) as well as a thin membrane (high permeability). Depending on the porous substrate used for supporting the membrane, the method for preparing could be quite different. The most common methods include chemical vapor deposition (CVD), electroless plating, electroplating, cold rolling, and sputtering (Yun and Oyama, 2011).

1. Chemical Vapor Deposition

Chemical vapor deposition (CVD) is a method for obtaining thin films on a substrate, or even inside the pores, via the thermal decomposition of one or more volatile precursors on the surface of the substrate. This method can be used for depositing both on ceramic and on metal porous support, with the advantage of carefully controlling Pd membrane thickness (Xomeritakis and Lin, 1998). Thus, CVD deposited Pd membrane is usually very thin (2~5 μm). Therefore, the permeance through CVD made membrane is not necessarily via solution-diffusion transport mechanism but via surface adsorption coupled with diffusion mechanism (Kikuchi, 2000). However, with rather thin membrane the key disadvantage is lower selectivity toward H_2 due to the possibility of pin-holes. Itoh et al. (2005) applied $(CH_3COO)_2Pd$ as precursor and deposited Pd on 1.5 μm pore size α-alumina, resulted in 2-4 μm Pd thickness with permeance around 44-89 $cm^3/cm^2 min\ atm$ (26.4-53.4 $m^3/m^2 h\ atm$), and a 5000 N_2/H_2 selectivity at 300 ºC. Besides pure Pd, other metals are also able to be hence co-deposited to prepare Pd alloy membrane. Jun and Lee (2000) used $Pd(C_3H_5)(C_5H_5)$, $Ni(C_3H_5)(C_5H_5)$, $Nb(C_3H_5)(C_5H_5)_2$ precursors to prepare

$PdNi_{0.3}$, $PdNb_{0.3}$ on γ-alumina and Ni stainless steel support. The permeance was 16.59 $m^3/m^2h\,atm$ and 21.18 $m^3/m^2h\,atm$, while the selectivity was 317 and 120 at 450 ºC for $PdNi_{0.3}$, $PdNb_{0.3}$, respectively.

2. Cold Rolling

Cold rolling involves melting (usually arc-melting) the raw materials with chosen composition at temperature where at least one of the metals reaches melting point, ingot casting, homogenization, hot and cold forging or pressing, followed by repeated sequences of alternate cold rolling and annealing to reduce down to the required thickness (Sagel et al., 1998). The subsequence cooling rate determines the material structure. If it is fast enough, the material would be of an amorphous structure (Wilde et al., 2005). The advantages of cold rolling are similar to CVD, i.e., multi-compositions can be prepared in one step with controlled thickness. It is also easier to mass produce membrane using cold-rolling method. However, unlike CVD the cold-rolling prepared membranes are usually thick. Tosti et al. (2000; 2006) prepared 50 μm thick Pd and Pd-Ag membranes using cold-rolling. The permeability of Pd-Ag was about 1.0×10^{-8} mol/ms $Pa^{0.5}$ at 350~400 ºC (582~629 $m^3\mu m/m^2h\,atm^{0.5}$). Different from membranes directly plated on the porous tubes, cold rolled membrane needs to be placed or welded upon another porous substrate to withstand the pressure drop during operation. Therefore, the main issue is sealing, and the cracking caused by the difference in thermal expansion among different materials.

3. Electroless Plating

The electroless plating deposition (ELP) is a form of chemical deposition method from aqueous metallic salt electrolyte solution using a reduction agent to perform autocatalytic reduction reaction on the target surface. Electroless plating technique is attractive due to several reasons. It

can be used to plate on any support with proper prior nucleation treatments and no electricity is needed as in electroplating. It can be applied on large plating area with only simple equipment setup and provides uniform deposition on complex shapes (Mardilovich et al., 1998). There are a few drawbacks, however, including difficult to control plating thickness, and costly losses from Pd salt solution. Over the years, ELP has become the most common technique for preparing supported Pd and Pd-alloy membranes.

The electroless plating solution typically requires: 1) a source of metal ion; 2) a reducing agent; 3) a suitable complexing agent; 4) stabilizers/inhibitors; and 5) thermal energy (Mallory and Hajdu, 1990). The most common chemicals used in Pd plating bath as Pd ion source include $PdCl_2$, $Pd(NH_3)_4Cl_2$, $Pd(NH_3)(NO_3)_2$, $Pd(NH_3)_4Br_2$. Reducing agents include NH_2-NH_2, $NaBH_4$, $NaH_2PO_2{\cdot}H_2O$, and complexing agents include EDTA (Ethylenediaminetetraacetic acid), EDA (Ethylenediamine), and NH_3 (Mardilovich et al., 1998). Chemicals used for Pd deposition have reached general consensus in past decades of research, with a little variation depending on the substrate. Prior to electroless deposition substrate needs to be activated by plating Pd seeds on the target surface. The activation involves repeatedly immersing support in $SnCl_2$, H_2O, $PdCl_2$ and dilute HCl for 3~6 times (Mardilovich et al., 1998). The activated substrate is then immersed in Pd plating solution and reduction solution bath in a controlled temperature water bath. The plating temperature, plating time, ratio of reductant/Pd solution, Pd^{2+} concentration, pH value, and activation process are some of the key elements in determining the plating rate and Pd grain size (Yeung et al., 1999).

Table 2.1 summarizes the permeance of different Pd, Pd-alloy membrane synthesized using various method. It is noticed that membranes using electroless plating method have a wider variation of permeance, but higher selectivity compared to the CVD method. Hydrogen

permeability depends on many factors; however, with the right approach it is possible to obtain both high selectivity and high hydrogen permeability using electroless plating.

Table 2.1 Permeation data of various fabricated Pd-based membranes reported in literature.

Membrane	T(ºC)	ΔP(atm)	δ(μm)	Permeance ($m^3/m^2h \cdot atm^{0.5}$)	Selectivity	Method	Reference
Pd/PSS	450	1	–	10.86	–	ELP	Yeung et al, 1999
Pd/Vycor	550	2.5	–	1.86	10000	ELP	Yeung et al, 1999
Pd	350	20.41	25	14.19	∞	–	Knapton, 1977
Pd/PSS	350	1	20	9.66	5000	ELP	Mardilovich et al, 1998
Pd/Ag	350~400	1~3.9	50	0.26	–	Cold rolling	Tosti et al, 2006
$PdNi_{0.3}$/-Al_2O_3	450	0.68	0.5-3	31.60	317	CVD	Jun et al, 2000
Pd/-Al_2O_3	450	0.68	0.5-3	38.10	780	CVD	Jun et al , 2000
PdCu/-Al_2O_3	450	3.5	11	57.15	1150	ELP	Roa et al, 2003
Pd/PdAg Inconel	450	5	11.6	26.85	13376	ELP	Augustine et al, 2011
Pd/-Al_2O_3	300	1	1	176	>200	CVD	Xomeritakis et al, 1998

4. Electroplating

To perform electroplating, it is necessary to have a conductive porous substrate. Therefore, ceramic porous substrates cannot be utilized in this technique. To deposit two metals simultaneously in the same bath is also difficult due to complexity of the chemical complexing. Besides theses drawbacks, electroplating process is easy to scale up and apply to mass manufacturing and it is easy to control membrane thickness by controlling electroplating time, bath pH, temperature and current density.

To deposit Pd membrane, the support has to be placed at the cathode side and immersed in Pd solution (electrolyte solution) so that electric current flows from cathode to anode and provides electrons to Pd^{2+} in the solution to plate at the cathode. Raub (1982) hence prepared Pd membranes using $PdCl_2$, $Pd(NH_3)_4Cl_2$, $Pd(NO_3)_2$ and adjusted pH value to below 7 and over 10 using HCl, H_2SO_4. During the electroplating process, however hydrogen produced from electrolyte electrolysis may absorb onto Pd film, with internal stress being proportional to hydrogen concentration in Pd layer, creating porosity, hence the uniformity of Pd membrane may suffer. The internal stress caused by hydrogen stored in Pd film may eventually lead to hydrogen embrittlement. Hydrogen in Pd membrane can be removed using cyclic voltammetry in NaOH at potential from 20 to 1V, anodic polarization at 10.75 V for 2 hours in NaOH, vacuum extraction at 150 ºC for 2 hours and vapor phase desorption at 215 ºC for 5 minutes (Wei and Brewer, 1996). Nam et al. (1999) vacuum electro-deposited $Pd_{78}Ni_{22}$ on Ni powder modified porous stainless steel (PSS) in CuCN solution, and found the highest hydrogen permeance to be 158.41 $m^3/m^2 h\, atm^{0.5}$, and a H_2/N_2 selectivity of 4700 at 550 ºC. No long term test was performed so that the stability of this membrane is unknown.

2.6 Diffusion Barrier and Substrate Pore Size Modification for Pd Membrane

The composition and structure of the porous substrate is one of the key factors in determining the stability of the deposited dense metal membrane. Thus, high operating temperatures may lead to metal inter-diffusion between the membrane and a porous metallic support, changing membrane composition and eventually leading to decline in hydrogen permeance. A diffusion barrier built between the support and the deposited membrane is thus used to reduce or stop the intermetallic diffusion. There are several approaches for fabricating diffusion barriers, 1) *in-situ* oxidation of

the porous metal support at an appropriate temperature (Ma et al., 2004); 2) deposition of an oxide (or ceramic material) layer upon the metal support (Nam et al., 2001; 2005; Zahedia et al., 2009; Wang et al., 2004); 3) deposition of a thin layer of Pd/Ag or Pd/Cu alloy (Ayturk et al., 2006); and 4) a combination of the above mentioned methods (Yepes, 2006). A schematic of these diffusion barriers and substrate pore size modification is shown in Figure 2.4.

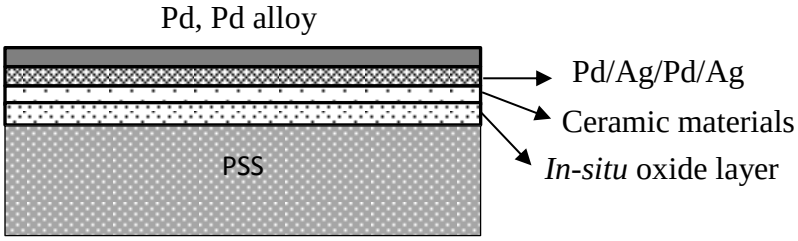

Figure 2.4 Schematic of diffusion barrier and substrate pore size modification.

Ma et al. (2004) performed *in-situ* oxide PSS at a temperature higher than 600 ºC before Pd alloy annealing and showed that the thin oxide layer was able to stop intermetallic diffusion between Pd and support at 500 ºC. Extra layer of ceramic material was also introduced as diffusion barrier because of the higher stability at high temperatures, and the small particles could smooth out PSS surface morphology, reducing effective pore size. Such modification via sol-gel silica, sputtering TiN, electrodeposition of WO_3, vacuum deposited ZrO_2 (Nam et al., 2001; 2005; Zahedia et al., 2009; Wang et al., 2004) were reported to provide good resistance to intermetallic diffusion. The thickness of ceramic layer must be carefully monitored, however, since the difference in thermal coefficient between Pd, ceramic, and metal support might cause membrane cracking at higher temperatures. Samingprai et al. (2010) electroplated Cr on *in-situ* oxidized PSS in air at 700 ºC to prepare Cr_2O_3 as diffusion barrier. The high Tamman temperature of Cr_2O_3 was the key to protect Pd membrane at 500 ºC. Yepes (2006) combined all of the techniques by first *in-situ* oxidized PSS at 800 ºC for 12 hours, followed by washcoated γ-Al_2O_3 and Pd/Ag electroless

plating. A membrane permeance of 13.15 $m^3/m^2 h\, atm^{0.5}$, and a H_2/N_2 selectivity of 5000 (1 bar) at 500 ºC was obtained.

To test the success of diffusion a barrier, the Pd membrane needs to undergo the longevity test. Ayturk et al., (2006) fabricated porous Pd/Ag/Pd/Ag/Pd layer (also called bi-metal multi-layer) combined with *in-situ* oxide PSS as diffusion layer, which proved to be very effective in stopping intermetallic diffusion. Thus, Pd permeation was stable for over 500 hours at temperatures exceeding 500 ºC. Lee et al. (2015) prepared 6 μm thickness membrane using 5 μm, 100 nm ZrO_2 pore modified porous stainless steel as substrate followed by successive DC magnetron sputtered multiple layers of Pd/Ag and Ag up-filling heat treatment. Membrane was stable at 723K for 2000 hours with permeance 34.17 $m^3/m^2 h\, atm^{0.5}$ and a H_2/N_2 selectivity of 1950. Ma et al. (2009) further extended Pd/Ag, Pd/Cu membrane stability up to 4500 hours at temperature between 400~450 ºC with infinite H_2/He selectivity and a permeance of 28.2 $m^3/m^2 h\, atm^{0.5}$. In summary, it is difficult but possible to carefully engineer supported Pd membrane with excellent permeance, selectivity and stability. Cost and poisoning, however, remain the key stumbling blocks.

2.7 Non-Pd Membranes

Though Pd is a very promising material for hydrogen separation, however, as mention above, it is expensive which limits its industrial applications. Many attempts have been consequently made in search of replacing Pd with other refractory metals including Nb, Ta, V, etc. (Phair and Donelson, 2006) because of lower cost, high hydrogen permeability, and high mechanical strength. In order to further improve hydrogen permeation characteristics, most of the non-Pd based alloy membranes tested are amorphous alloys. It is known that amorphous alloys do not show the α–β phase transition during hydrogen absorption, thus, avoiding hydrogen

embrittlement, and are easy to scale up using cold-rolling method (Hara et al., 2000). Vanadium is one of the most investigated metals. However, pure vanadium suffers from hydrogen embrittlement and oxidation and, thus, has to be alloyed with other metals. Thus, an alloy of V-10~15 at% Ni was made by arc-melting V and Ni is the desired ratio, followed by cold rolling to 1.2 mm thickness. The membrane showed improvement in resisting embrittlement at 200 ºC. Hydrogen permeance of V- 15 at% Ni was 5 times higher than that of Pd at 200 ºC. However, hydrogen permeance decreased by 5% in 2 weeks at 300 ºC and by 30% in 1 week at 200 ºC (Nishimura et al., 1991; 2002). No tests were done at higher temperatures. Other binary and ternary systems such as $V_xNi_{(1-x)}$, $V_xAl_{(1-x)}$, $V_{85}Ni_xAl_{(15-x)}$, $Nb_{95}M_5$ (M=Zr, Mo, Ru, Pd), $Nb_xTi_{(60-x)}Ni_{40}$ have also been investigated as shown in Figure 2.5 (Phair and Donelson, 2006).

Nickel based amorphous alloy systems here attracted a lot of attention, such as Ni-Nb, and Ni-Zr, with the addtion of other elements such as Hf, Ta, Co, Cu, Ti, Mo, W, etc., to improve hydrogen permeability, resist hydrogen embrittlement, and increase thermal stability (Paglieri et al., 2011). Permeability of $(Ni_{0.6}Nb_{0.4})_{70}Zr_{30}$ (54 μm) and $(Ni_{0.6}Nb_{0.3}Ta_{0.1})_{70}Zr_{30}$ (65 μm) membranes were found to be 1.4 and 1.2×10^{-8} mol/ms $Pa^{0.5}$ (880 and 754 $m^3\mu m/m^2 h\, atm^{0.5}$) at 450 ºC, respectively, i.e., very close to the permeability of a Pd/Ag membrane at the same condition. However, membrane permeability drop to 1.0×10^{-10} mol/ms $Pa^{0.5}$(629 $m^3\mu m/m^2 h\, atm^{0.5}$) after 40~50 hours of testing. Less Zr addition ($(Ni_{0.6}Nb_{0.3}Ta_{0.1})_{90}Zr_{10}$) slowed the hydrogen permeability decay at 450 ºC during 80 hours of testing, but also lowered the hydrogen permeability. Similar results were obtained with $(Ni_{0.6}Nb_{0.4})$70Zr30 (50-70 μm) alloys having hydrogen permeability 7×10^{-9} mol/ms $Pa^{0.5}$ (407 $m^3\mu m/m^2 h\, atm^{0.5}$) at 350 ºC (Kim et al., 2012). However, the life time of amorphous hydrogen membranes at higher temperatures

remains an issue, since at higher temperatures amorphous alloys tend to become crystallized and their permeation drops.

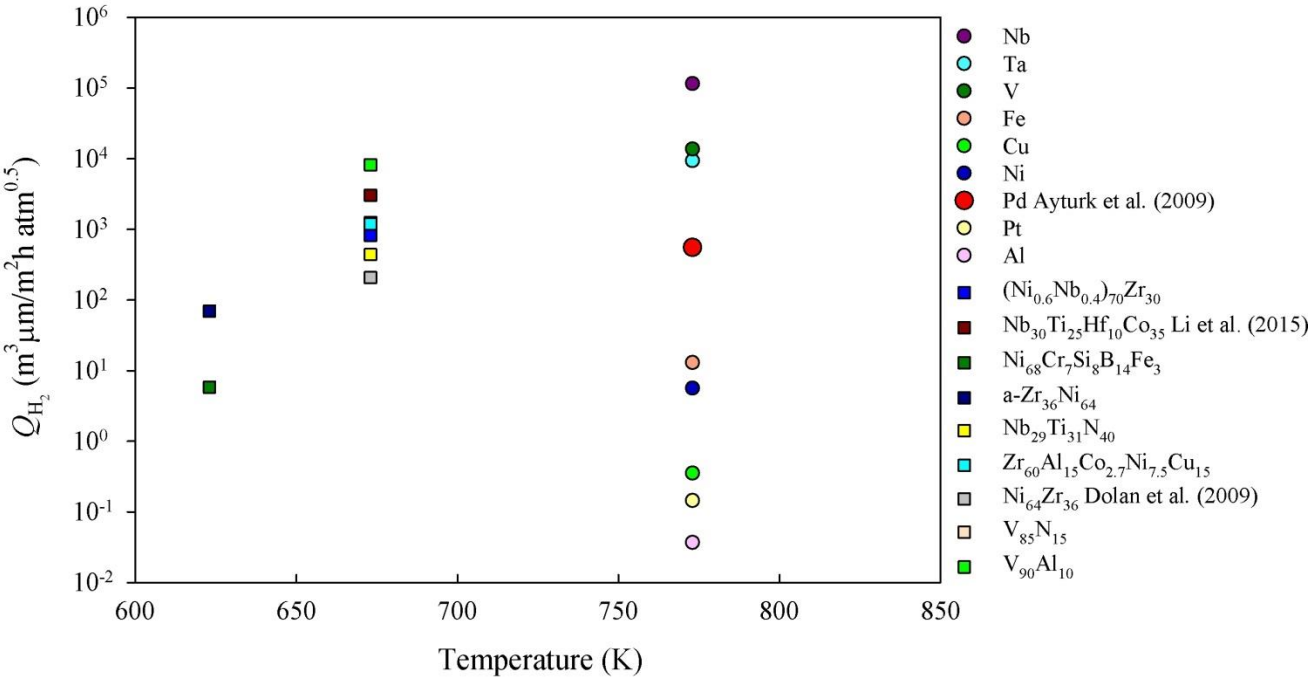

Figure 2.5 Hydrogen permeability of dense liquid gallium membrane, metals and amorphous metals between 623~823 K (Pd from Ayturk et al., 2009; $Nb_{30}Ti_{25}Hf_{10}Co_{35}$ from Li et al., 2015; $Ni_{64}Zr_{36}$ from Dolan et al., 2009; all others from Phair and Donelson, 2006).

Increasing the content of Nb may increase the stability at higher temperatures, as the rate of degradation is related to the Zr:Nb ratio. The most stable combination is $Ni_{90}Nb_{10}Zr_{30}$ with hydrogen permeability decay from 2.4 to 1.9×10^{-9} mol/ms $Pa^{0.5}$ (151 to 120 $m^3 \mu m/m^2 h\ atm^{0.5}$) at 400 ºC in 110 hours of testing (Dolan et al., 2009). Li et al. (2015) developed cold rolled membrane $Nb_{40}Ti_{20}Hf_{10}Ni_{30}$ that proved to have high hydrogen permeability with no hydrogen embrittlement for 72 hours at 673K. However, it is to be further noted that elements like Nb, Ta, or Zr used in the non-Pd membrane always have an adherent oxide film on the surface which is not readily reduced under normal operating temperatures (Sarker et al., 2016). Consequently,

thin Pd layers are often coated on the surface of Ni, Nb, Zr based alloy membrane to prevent surface oxidation and to increase dissociative hydrogen adsorption kinetics (Kim et al., 2012).

In summary, non-Pd based membranes seem to have comparable hydrogen permeability to Pd at lower temperatures. However, for practical application in hydrogen separation or in a reactor, the key challenge remains its thermal stability and hydrogen embrittlement at higher temperatures. The amorphous alloys have higher defects sites, providing for higher hydrogen absorption capacity than a crystalline alloy and, hence, a higher hydrogen solubility. The disadvantage of amorphous alloys is their tendency to crystallize at high temperature, which limits the amorphous alloys to only operate at lower temperatures. Further, thin layer of Pd has to be often deposited on non-Pd membrane surface to promote the slow surface hydrogen dissociative kinetics resulting from oxidation layer formation. However, at higher temperatures such layer tends to form intermetallic compound with the amorphous alloy membrane and loses its activity. In short, no good alternative metal membranes yet exist for hydrogen purification.

2.8 Liquid Metal Membranes

It is apparent from the above discussion that Pd is the most advanced and only practical hydrogen membrane in development at the moment. However, its cost, susceptibility to poisons and stability to higher temperature of operation needed for integration with reformers remain concerns. On the other hand, the alternate materials investigated so far have promising permeability but low stability and are limited to operating at lower temperatures. In this study, we propose for the first time, use of liquid metal for hydrogen separation membranes due to their higher diffusion coefficient, coupled with a lack of crystallographic change that solid membranes are susceptible to. Additionally, the presence of free volume or “holes” in a liquid promotes solubility as well as diffusivity. Although there are no permeability data for liquid metals

available in the literature, some solubility and diffusivity data in liquid metals are available as described below. There is, in fact, good support in the literature that such a hydrogen transport mechanism of Figure 2.1 is functional in liquid metals as well. Among others, the solution and diffusion of hydrogen and its isotopes in liquid metals (e.g., Li and its alloys) has been investigated in connection with their use as liquid breeder and coolant materials in nuclear fusion reactor (Schumacher and Weiss, 1990; Fruehan and Anyalebechi, 2008).

2.8.1 Hydrogen Solubility in Metals

As described in section 2.3, hydrogen diffusion through metal membrane generally includes 5 separate steps shown in Figure 2.1, and the flux at higher temperatures is generally described by Sieverts' law in Eq. (2.4). From this, hydrogen flux could conceivably be enhanced by: 1) increasing the dissociative adsorption equilibrium constant K_1; 2) enhancing the solubility of surface H-atoms into bulk K_2; 3) enhancing the H-atom diffusion coefficient D_{H}; 4) increasing the density of surface dissociative sites (surface geometry and surface roughness); 5) increasing the operating temperature; and 6) decreasing membrane thickness δ. Pressure, temperature, membrane thickness and surface geometry can be controlled by experimental technique. The rest of the terms are related to the inherent properties of membrane material. A material having both high diffusivity and high solubility would have high a hydrogen flux.

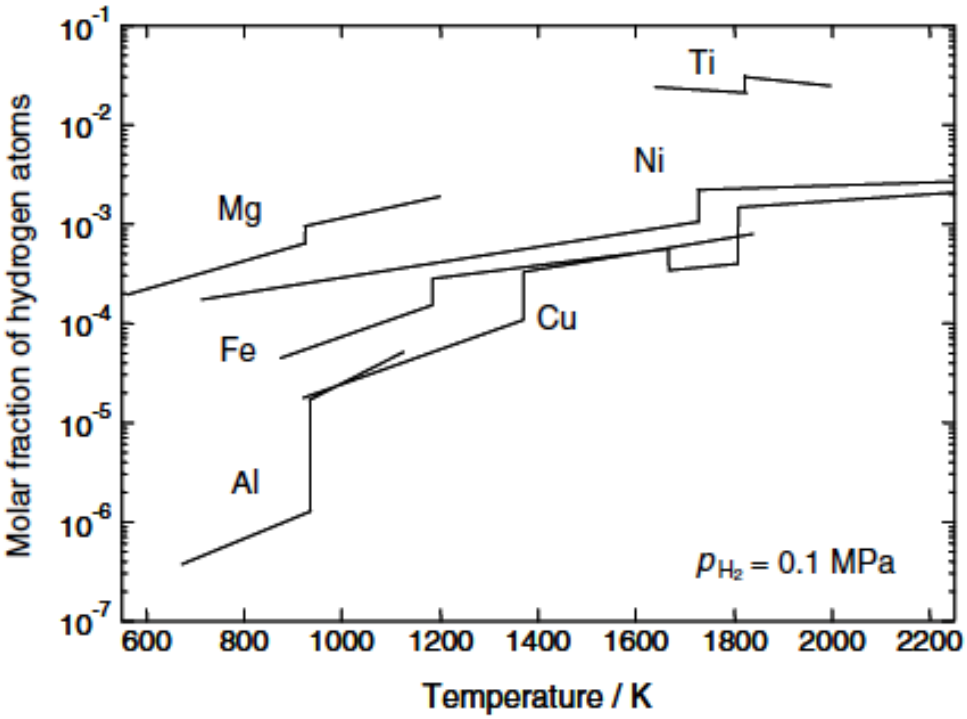

Figure 2.6 Hydrogen solubility of solid and liquid metal at 1 atm (Nakajima, 2007).

Hydrogen solubility of various metals in solid and liquid state is shown in Figure 2.6. It appears that hydrogen solubility of certain metals such as Al, Cu, Mg, Ni and Fe are higher in molten form than in solid form. Taking Al as an example, hydrogen solubility of Al increases as temperature increases, and jumps one order of magnitude higher at melting point (660.3 ºC) as Al is transformed from the solid to the liquid state. The reasons for this quantum change in solubility upon melting are not well-studied, but could be because of increased free volume or density in the liquid state.

Similar hydrogen solubility behavior can also be observed in Mg-H and its alloys as shown in Figure 2.7 (Fruehan and Anyalebechi, 2008). At the Mg melting point (650 ºC), the hydrogen solubility jumps from 30 to 45 cm^3/100g, and the slope of solubility in liquid state is also sharper than that in the solid state. The alloying of Mg with other metals changes the solubility. For example, the solubility of hydrogen in Mg increases from 52 to 60 cm^3/100g with 2 wt% Sr

addition at 700 ºC, but drops to 45 cm^3/100g with 5.3 wt% Al addition. Hydrogen solubility of liquid Li, K, Na and NaK is shown in Figure 2.8. Li has the highest solubility among the alkaline metals, and Na has the lowest solubility.

Several expressions for hydrogen solubility in liquid metals collected from the literature are listed in Table 2.2.

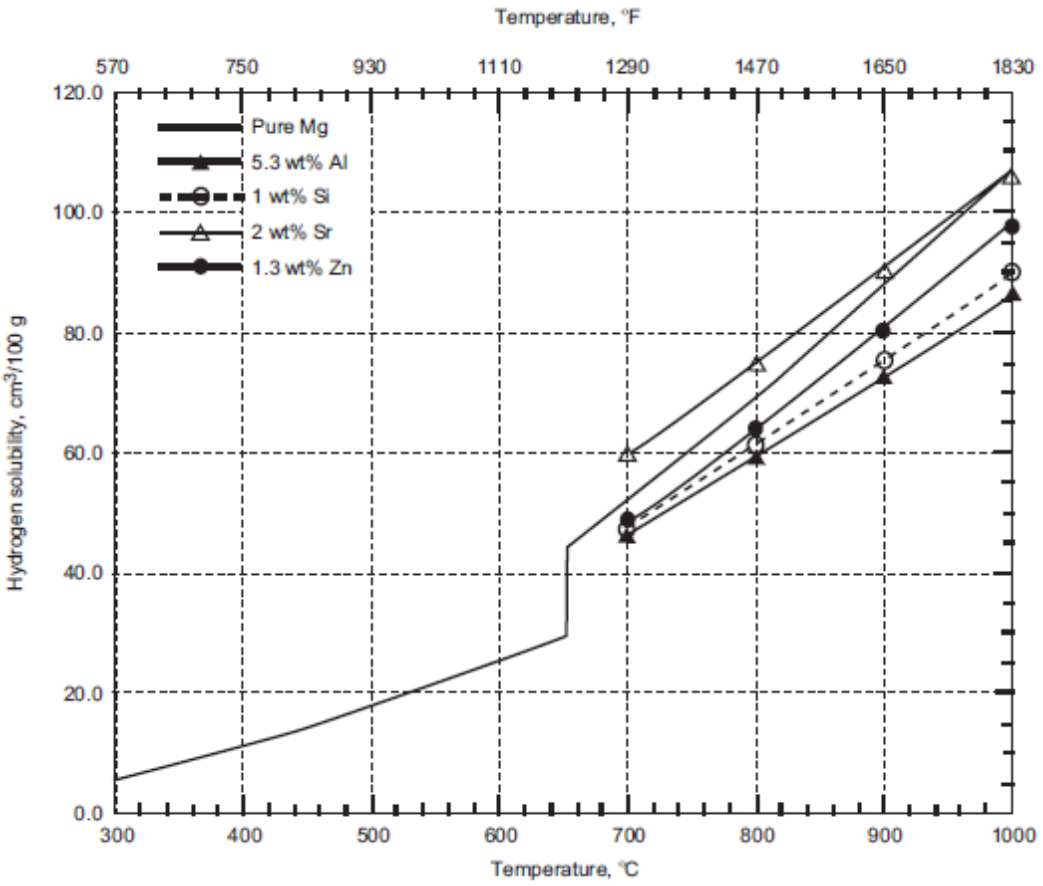

Figure 2.7 Solubility of hydrogen in Mg and Mg alloys at 1 atm hydrogen partial pressure (Fruehan and Anyalebechi, 2008).

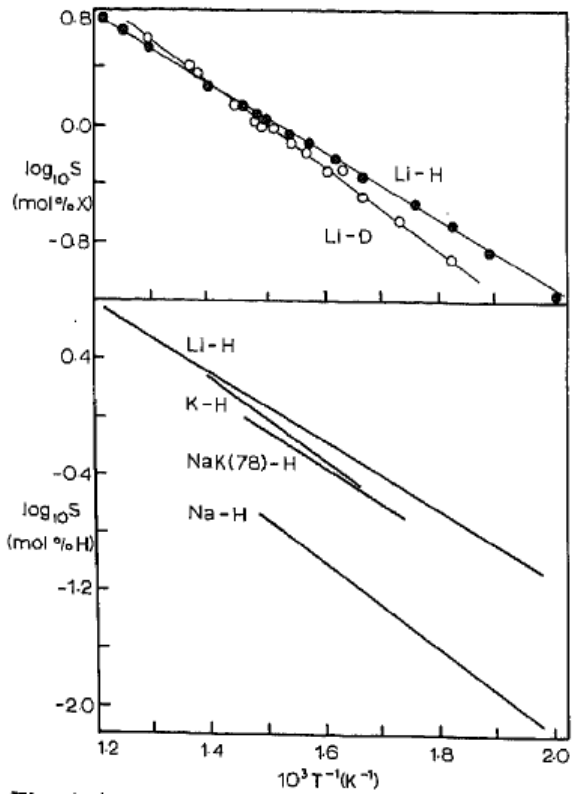

Figure 2.8 Solubility of hydrogen in liquid Li, K, Na, NaK(78wt%) (Hubberstey, 1976).

Table 2.2 Hydrogen solubility (cm^3 H_2@STP/100 g) of various metals at STP, 1atm.

Elements	Liquid Metal (cm^3/100g)	Solid Metal (cm^3/100g)	Temperature (ºC)	Reference
Al	$\log S = 2.7292 - \frac{2692}{T}$ $\log S = 2.713 - \frac{2674.8}{T}$		660~1000	Fruehan and Anyalebechi, 2008 Jiang and Li, 2011
Al		$\log S = 1.8032 - \frac{2965.8}{T}$	300~660	Fruehan and Anyalebechi, 2008
Cu	$\log S = 2.4649 - \frac{2327.59}{T}$ $\log S = 2.437 - \frac{2315.5}{T}$ $\log S = 2.442 - \frac{2325.2}{T}$		1084~1330 1084~1440	Fruehan and Anyalebechi, 2008 Sacris and Parlee, 1970 Jiang and Li, 2011

Table 2.2 Continued-hydrogen solubility (cm^3 H_2@STP/100 g) of various metals at STP, 1atm.

Cu		$\log S = 1.6829 - \frac{2057.76}{T}$	600~1084	Fruehan and Anyalebechi, 2008
Mg	$\log S = 3.042 - \frac{1290.5}{T}$ $\log S = 2.848 - \frac{1100.1}{T}$		650~1000	Fruehan and Anyalebechi, 2008 Jiang and Li, 2011
Mg		$\log S = 2.6254 - \frac{1062.5}{T}$	300~650	Fruehan and Anyalebechi, 2008
Na	$\log S = 6.25 - \frac{2800}{T}$ $\log S = 8.507 - \frac{3019}{T}$		260~350 230~400	McClure et al., 1966 Hubberstey, 1976
Li	$\log S = 8.732 - \frac{2308}{T}$ $\log S = 7.178 - \frac{2261.8}{T}$		220~550	Hubberstey, 1976 Jiang and Li, 2011
K	$\log S = 8.763 - \frac{2994}{T}$		330~440	Hubberstey, 1976
Ni	$\log S = 2.167 - \frac{929.6}{T}$ $\log S = 2.266 - \frac{1126.1}{T}$		1480~1600	Sacris and Parlee, 1970 Jiang and Li, 2011
Ag	$\log S = 2.154 - \frac{3512}{T}$		980~1210	Sacris and Parlee, 1970
Fe	$\log S = 2.381 - \frac{1741.1}{T}$			Jiang and Li, 2011
Sn	$\log S = 3{,}693 - \frac{6482.8}{T}$			Sacris and Parlee, 1970

The reports of measurement of hydrogen solubility in molten metals are scarce due to several reasons. First, metals typically melt at very high temperature and they are very active and are easily contaminated by oxygen, impurities, and further react with vessels. Additionally, metals

often uptake quite small amounts of hydrogen which makes it very difficult to get accurate data. The existing experimental data are often scattered.

A theoretical model has been proposed to estimate the solubility of hydrogen in molten metals. Jiang and Li (2011) model the hydrogen solubility based on electron interaction between hydrogen and the atoms of the liquid metal, using nearly free electron theory. Model results were compared with experimental data as shown in Figure 2.9.

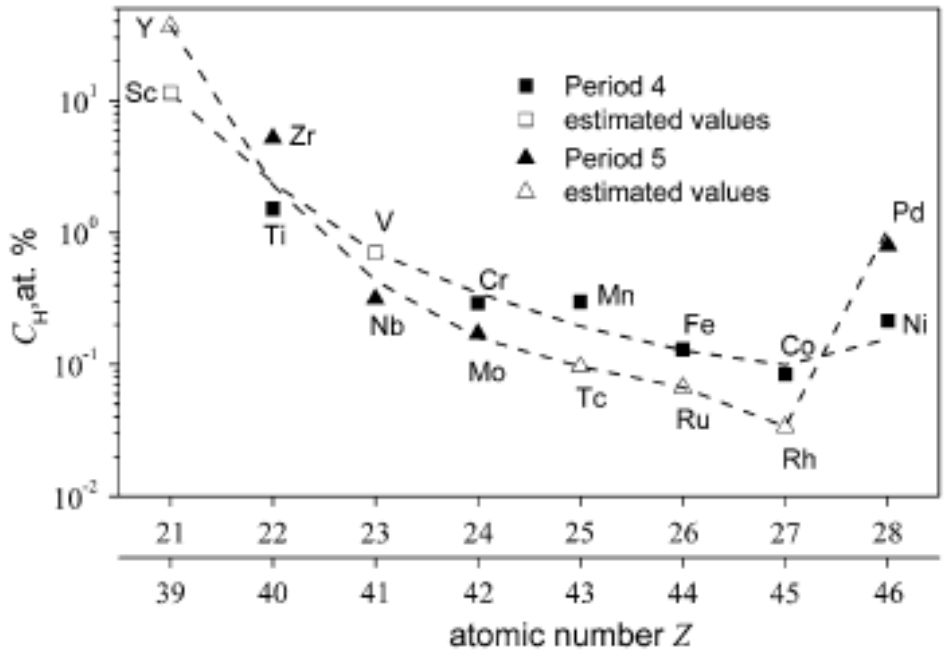

Figure 2.9 Hydrogen solubility of transition metals at its melting point at 1 atm (Jiang and Li, 2011).

It was discovered that the solubility of hydrogen in Groups IA, II A, IIIA, IB, and IIB is much lower than that in transition metals. However, the model only estimated the hydrogen solubility at the melting point, and was not able to compare the calculated value with experimental values outside transition metals to verify its broader applicability.

In conclusion, metals appear to have a higher hydrogen solubility in their liquid state than in their solid state, and hydrogen solubility generally increases with increasing temperature, i.e. it is an endothermic process in general, with exceptions being Pd and Ti which is exothermic as observed from Figure 2.6. The reason for hydrogen solubility jumping from solid to liquid state remains unknown. Considering the application of hydrogen separation in reactors with operating temperature around 500-600 ºC, this is too low for employing metals such Al, Cu, Ag and Ni even if they have high hydrogen diffusivity due to their high melting points.

2.8.2 Hydrogen Diffusivity in Metals

Hydrogen diffusivity measurements in liquid metals are scarce and were mostly performed in the 60s and 70s. Since such tests are easily contaminated by oxygen and, water, it is especially difficult to measure the diffusivity if the hydrogen solubility in liquid metal is low. The diffusivity result may also change depending on different experimental approaches (Yang et al., 2014). The various techniques include capillary and manometric measurements (Fisher, 1999), steady or unsteady state gas-liquid metal diffusion cell (Solar and Guthrie, 1971), and glow plasma discharge (Mazayev and Prokofiev, 1994). In short, information on hydrogen diffusion behavior in various liquid metals is very limited. The hydrogen diffusion coefficients in liquid metals collected from literature are summarized shown in Figure 2.10 and in Table 2.3 in terms of pre-exponential factor $D_{\mathrm{H},0}$ and the activation energy E_D:

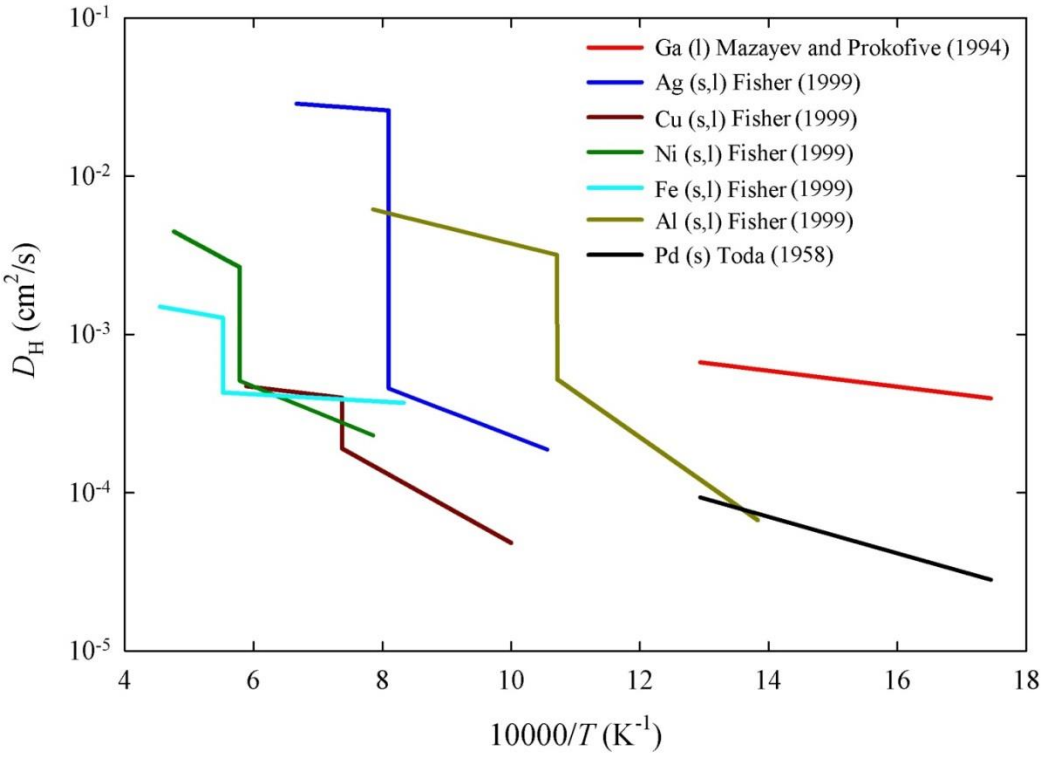

Figure 2.10 Hydrogen diffusion coefficient in some liquid and solid metals as a function of inverse absolute temperature (Mazayev and Prokofive, 1994; Fisher, 1999; Toda, 1958).

Table 2.3 Hydrogen diffusivity of various metals $D_H = D_{H,0}\exp(-E_D/RT)\,cm^2/s$.

Elements	Liquid $D_{H,0}$ cm^2/s	E_D kJ/mol	Temperature (°C)	Reference
Li	13 ± 1	104.5 ± 8.36	625~900	Alire, 1976
K	$D_H = (3.26\pm0.14)\times10^{-4}$		550	Freudenberg and Glaser, 1985
Ni	7.47×10^{-3}	35.74 ± 4.66	1478~1600	Sacris and Parlee, 1970; Fisher, 1999
Cu	1.09×10^{-2}	8.98 ± 1.46	1103~1433	Sacris and Parlee, 1970; Fisher, 1999
Ag	4.54×10^{-2}	5.68 ± 0.87	985~1208	Sacris and Parlee, 1970; Fisher, 1999

Table 2.3 Continued-hydrogen diffusivity of various metals.

Al	3.8×10^{-2}	19.23	780~1001	Fisher, 1999
Fe	2.57×10^{-3} 4.37×10^{-3}	17.14 ± 9.2 17.28 ± 4.23	1550~1720	Solar and Guthrie, 1971 Depuydt and Parlee, 1972; Fisher, 1999
Ga	3×10^{-3}	9.61	17~273	Mazayev and Prokofiev, 1994
Pd	5.18×10^{-3} $(2.83\pm0.15)\times10^{-3}$ 2.9×10^{-3}	23.62 21.60 ± 1.29 21.99	170~290 469~946 260~640	Genjiro, 1958 Katsuta et. al, 1979 Toda, 1958
Elements	Solid (cm^2/s)		Temperature (ºC)	Reference
Ni	2.3×10^{-3}	37.77		Birnbaum and Wert, 1972
Cu	1.1×10^{-2}	38.87		Birnbaum and Wert, 1972
Ag	2.82×10^{-3}	31.35		Birnbaum and Wert, 1972
Fe	$(\alpha)\ 6.4\times10^{-4}$ $(\gamma)\ 6.6\times10^{-3}$	8.03 44.73		Birnbaum and Wert, 1972

Comparing Pd and liquid gallium, the hydrogen diffusivity of liquid gallium diffusivity is about 7 times higher than Pd ($D_{H,Pd}=9.33\times10^{-5}\ cm^2/s$, $D_{H,Ga}=6.68\times10^{-4}\ cm^2/s$) at 500 ºC. Even though the hydrogen solubility of liquid gallium is unknown, however, the high diffusivity makes it an attractive potential candidate. Its other attractive features are low melting point, low volatility and low toxicity. For these reasons, it was chosen in this study.

Sacris and Parlee (1970) discovered that there is interrelation between diffusion coefficient and solubility in liquid metals as shown in Figure 2.11. It is further seen that for a given metal, the solubility increases with temperature, i.e., the enthalpy of solution is endothermic, as does the diffusion coefficient, except for the case of Sn, for which their experimental results were deemed unreliable.

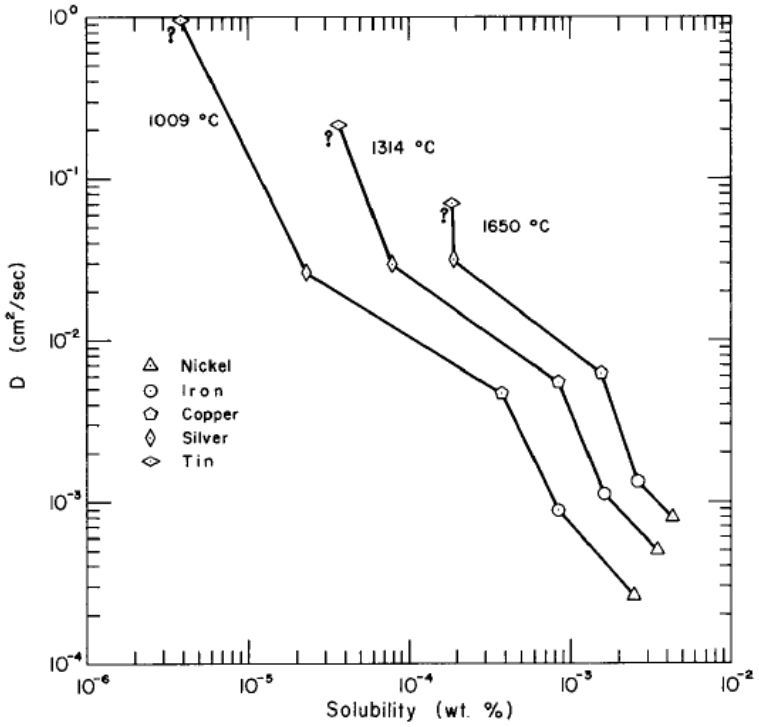

Figure 2.11 Correlation between diffusion coefficient and hydrogen gas solubility in Ni. Fe, Cu, Ag, and Sn (Sacris and Parlee, 1970).

In conclusion, Pd membranes are the most advanced and are approaching practical application. However, search for alternative membranes continues in an effort to lower their cost and susceptibility to poisons. This chapter reviewed the state of the art of hydrogen metal membranes and provides the rationale for our proposal to investigate liquid metal membranes.

2.9 References

Adhikari, S. and Fernando, S., Hydrogen membrane separation techniques, *Industrial and Engineering Chemistry Research*, 45, 3, (2006), 875-881.

Alire, R. M., Transport of hydrogen in liquid lithium, *Journal of Chemical Physics*, 65, 3, (1976), 1134-1137.

Armor, J. N., Applications of catalytic inorganic membrane reactors to refinery products, *Journal of Membrane Science*, 147, (1998), 217-233.

Augustine, A. S., Ma, Y. H. and Kazantzis, N. K., High pressure palladium membrane reactor for the high temperature water–gas shift reaction, *International Journal of Hydrogen Energy*, 36, 9, (2011), 5350-5360.

Ayturk, M. E., Kazantzis, N. and Ma, Y. H., Modeling and performance assessment of Pd and Pd/Au-Based catalytic membrane reactors for hydrogen production, *Energy and Environmental Science*, 2, (2009), 430-438.

Basile, A., Iulianelli, A., Longo, T., Liguori, S. and De Falco, M., Pd-based selective membrane state-of-the-art, 21-55, *Springer London*, (2011).

Birnbaum, H. K. and Wert, C. A., Diffusion of hydrogen in metals, *Berichte der Bunsengesellschaft für physikalische Chemie*, 76, 8, (1972), 806-816.

Buxbaum, R. E. and Kinney, A. B., Hydrogen transport through tubular membranes of palladium - coated tantalum and niobium, *Industrial and Engineering Chemistry Research*, 35, (1996), 530-537.

Caravella, A., Scura, F., Barbieri, G. and Drioli, E., Sieverts' law empirical exponent for Pd-based membranes: critical analysis in pure H_2 permeation, *Journal of Physical Chemistry B*, 114, (2010), 6033-6047.

Chen, C. H. and Ma, Y. H., The effect of H_2S on the performance of Pd and Pd/Au composite membrane, *Journal of Membrane Science*, 362, (2010), 535-544.

Clewley, J. D., Curran T., Flanagan, T. B. and Oates, W. A., Thermodynamic properties of hydrogen and deuterium dissolved in palladium at low concentrations over a wide temperature range, *Journal of the Chemical Society Faraday Transactions*, 1, 69, (1973), 449-458.

Connor, H., Palladium alloy diffusion cells, *Platinum Metals Review*, 6, 41, (1962), 130-135.

Depuydt, P. J. and Parlee, N. A. D., The diffusion of hydrogen in liquid iron alloys. *Metallurgical Transactions*, 3, 2, (1972), 529-536.

Deveau, N. D., Ma, Y. H. and Datta, R., Beyond Sieverts' law: A comprehensive microkinetic model of hydrogen permeation in dense metal membranes, *Journal of Membrane Science*, 437, (2013), 298-311.

Dolan, M. D., Non-Pd BCC alloy membranes for industrial hydrogen separation, *Journal of Membrane Science*, 362, 1, (2010), 12-28.

Doyle, M. L. and Harris, I. R., Palladium - rare earth alloys their order - disorder transformations and behavior with hydrogen, *Platinum Metals Review*, 32, 3, (1988), 130-140.

Farr, J. P. G. and Harris, I. R., U.S. Patent 3713270, (1973).

Fisher, D. J., Hydrogen diffusion in metals: A 30-year retrospective, *Scitec Publications Ltd, Switzerland*, (1999).

Flanagan, T. B. and Wang, D., Hydrogen permeation through fcc Pd-Au alloy membranes, *Journal of Physical Chemistry C*, 115, (2011), 11618-11623.

Flanagan, T. B., Wang, D. and Shanahan, K. L., Inhibition by gaseous impurities of hydrogen absorption by Pd and by internally oxidized PdAl alloys, *Physical Chemistry Chemical Physics*, 2, (2000), 4976-4982.

Fort, D., Farr, J. P. G. and Harris, I. R., A comparison of palladium-silver and palladium-yttrium alloys as hydrogen separation membranes, *Journal of the Less Common Metals*, 39, 2, (1975), 293-308.

Freudenberg, U. and Glaser, W., Hydrogen Diffusion in Molten Potassium at 550 ºC, *Journal of Physics F: Metal Physics*, 15, (1985), 253-255.

Frieske, H. and E. Wicke, Magnetic susceptibility and equilibrium diagram of PdH_n, *Berichte der Bunsengesellschaft für Physikalische Chemie*, 77, (1973), 48-52.

Fruehan, R. J. and Anyalebechi, P. N., Gases in metals, *ASM Handbook*, 15, (2008), 64-73.

Gabitto, J. F. and Tsouris, C., Hydrogen transport in composite inorganic membranes, *Journal of Membrane Science*, 312, (2008), 132-142.

Gabitto, J. F. and Tsouris, C., Sulfur poisoning of metal membranes for hydrogen separation, *International Review of Chemical Engineering*, 1, 5, (2009), 394-411.

Genjiro, T., Rate of permeation and diffusion coefficient of hydrogen through palladium, *Journal of The Research Institute for Catalysis Hokkaido University*, 6, 1, (1958), 13-19.

Gillespie, L. J. and Galstaun, L. S., The palladium-hydrogen equilibrium and new palladium hydrides, *Journal of American Chemical Society*, 58, 12, (1936), 2565-2573.

Goods, S. H. and Guthrie, S. E., Mechanical properties of palladium and palladium hydride, *Scripta Metallurgica*, 26, 4, (1992), 561-566.

Graham, T., On the absorption and dialytic separation of gases by colloid septa, *Philosophical Transactions of the Royal Society of London*, 156, 399, (1866), 399-439.

Grashoff, G. J., Pilkington, C. E. and Corti, C. W., The purification of hydrogen a review of the technology emphasizing the current status of palladium membrane diffusion, *Platinum Metals Review*, 27, 4, (1983), 157-169.

Guazzone, F., Engwall, E. E. and Ma, Y. H., Effects of surface activity, defects and mass transfer on hydrogen permeance and n-value in composite palladium - porous stainless steel membranes, *Catalysis Today*, 118, (2006), 24-31.

Hara, S., Sakaki, K., Itoh, N., Kimura, H. M., Asami, K. and Inoue, A., An amorphous alloy membrane without noble metals for gaseous hydrogen separation, *Journal of Membrane Science*, 164, (2000), 289-294.

Howard, B. H., Killmeyer, R. P., Rothenberger, K. S. and Cugini, A. V., Hydrogen permeance of palladium - copper alloy membranes over a wide range of temperatures and pressures, *Journal of Membrane Science*, 24, 1, (2004), 207-218.

Hubberstey, P., Adams, P. F., Pulham, R. J., Down, M. G. and Thunder, A. E., Hydrogen in liquid alkali metals, *Journal of the Less Common Metals*, 49, (1976), 253-269.

Hughes, D. T. and Harris, I. R., Hydrogen diffusion membranes based on some palladium - rare earth solid solution alloys, *Zeitschrift für Physikalische Chemie*, 117, 117, (1979), 185-193.

Hunter, J. B., U.S. Patent 2773561, (1956).

Itoh, N., Akiha, T. and Sato, T., Preparation of thin palladium composite membrane tube by a CVD technique and its hydrogen permselectivity, *Catalysis Today*, 104, (2005), 231-237.

Jiang, G. and Li, Y., A model for calculating hydrogen solubility in liquid transition metals, *Metallurgical and Materials Transactions A*, 42A, (2011), 1038-1043.

Katsuta, H., Farraro, R. J. and McLellan, R. B., The dffusivity of hydrogen in palladium, *Acta Metallurgica*, 27, 7, (1979), 1111-1114.

Kikuchi, E., Membrane reactor application to hydrogen production, *Catalysis Today*, 56, (2000), 97-101.

Kim, S. M., Chandra, D., Pal, N. K., Dolan, M. D., Chien, W. M., Talekar, A., Lamb, J., Paglien, S. N. and Flanagan, T. B., Hydrogen permeability and crystallization kinetics in amorphous Ni - Nb - Zr alloys, *International Journal of Hydrogen Energy*, 37, 4, (2012), 3904-3913.

Knapton, A. G., Palladium alloys for hydrogen diffusion membranes - A review of high permeability materials, *Platinum Metals Review*, 21, 2, (1977), 44-50.

Lee, J. H., Han, J. Y., Kim, K. M., Ryi, S. K. and Kim, D. W., Development of homogeneous Pd -Ag alloy membrane formed on porous stainless steel by multi-layered films and Ag-upfilling heat treatment, *Journal of Membrane Science*, 492, (2015), 242-248.

Li, X., Liu, D., Chen, R., Yan, E., Liang, X., Rettenmayr, M., Su, Y., Guo, J. and Fu, H., Changes in microstructure, ductility and hydrogen permeability of Nb - (Ti, Hf) Ni alloy membranes by the substitution of Ti by Hf, *Journal of Membrane Science*, 484, (2015), 47-56.

Ma, Y. H., Akis, B. C., Ayturk, M. E., Guazzone, F., Engwall, E. E. and Mardilovich, I. P., Characterization of intermetallic diffusion barrier and alloy formation for Pd/Cu and Pd/Ag porous stainless steel composite membranes, *Industrial and Engineering Chemistry Research*, 43, 12, (2004), 2936-2945.

Ma, Y. H., Kazantzis, N. K., Mardilovich, I. P., Guazzone, F., Augustine, A. S. and Koc, R., Composite Pd and Pd Alloy porous stainless steel membranes for hydrogen production and process intensification, DOE Hydrogen Program, FY 2009 Annual Progress Report, (2009).

Mallory, G. O. and Hajdu, J. B., Electroless plating: fundamentals and applications, *Noyes Publications Mnlliam Andrew Publishing*, (1990).

Marbán, G. and Valdés-Solís, T., Towards the hydrogen economy ?, *International Journal of Hydrogen Energy*, 32, (2007),1625-1637.

Mardilovich, P. P., She, Y., Ma, Y. H. and Rei, M. H., Defect - free palladium membranes on porous stainless - steel support, *AIChE Journal*, 44, 2, (1998), 310-322.

Mazayev, S. N. and Prokofiev, Yu. G., Hydrogen inventory in gallium, *Journal of Nuclear Materials*, 212-215, (1994), 1497-1498.

McCool, B. A. and Lin, Y. S., Nanostructured thin palladium - silver membranes: effects of grain size on gas permeation properties, *Journal of Materials Science*, 36, (2001), 3221-3227.

McKinley, D. L., Metal alloy for hydrogen separation and purification, U.S. Patent 3350845, (1967).

McKinley, D. L., Method for hydrogen separation and purification, U.S. Patent 3247648, (1966).

McKinley, D. L., Method for hydrogen separation and purification, U.S. Patent 3439474, (1969).

Mitacek, P., Jr. and Aston, J. G., The thermodynamic properties of pure palladium and its alloys with hydrogen between 30 and 300 K, *Journal of the American Chemical Society*, 85, 2, (1963), 137-141.

Moon, B. E., Pressure - composition temperature relations in the palladium-hydrogen system, *Journal of Physical Chemistry*, 60, 4, (1956), 502-504.

Morreale, B. D., Ciocc , M. V., Howard, B. H., Killmeyer, R. P., Cugini, A. V. and Enick, R. M., Effect of hydrogen-sulfide on the hydrogen permeance of palladium - copper alloys at elevated temperatures, *Journal of Membrane Science*, 241, (2004), 219-224.

Nakajima, H., Fabrication, properties and application of porous metals with directional pores, *Progress in Materials Science*, 52, 7, (2007), 1091-1173.

Nam, S. E. and Lee, K. H., Hydrogen separation by Pd alloy composite membranes: introduction of diffusion barrier, *Journal of Membrane Science*, 192, (2001), 177-185.

Nam, S. E. and Lee, K. H., Preparation and characterization of palladium alloy composite membranes with a diffusion barrier for hydrogen separation, *Industrial and Engineering Chemistry Research*, 44, (2005), 100-105.

Nam, S. E., Lee, S. H. and Lee, K. H., Preparation of a palladium alloy composite membrane supported in a porous stainless steel by vacuum electrodeposition, *Journal of Membrane Science*, 153, (1999), 163-173.

Nishimura, C., Komaki, M. and Amano, M., Hydrogen permeation character of vanadium - nickel alloys, *Materials Transactions, JIM*, 32, 5, (1991), 501-507.

Nishimura, C., Komaki, M., Hwang, S. and Amano, M., V - Ni alloy membranes for hydrogen purification, *Journal of Alloys and Compounds*, 330-332, (2002), 902-906.

Paglieri, S. N., Pal, N. K., Dolan, M. D., Kim, S. M., Chien, W. M., Lamb, J., Chandra, D., Hubbard, K. M. and Moored, D. P., Hydrogen permeability, thermal stability and hydrogen embrittlement of Ni - Nb - Zr and Ni - Nb - Ta - Zr amorphous alloy membranes, *Journal of Membrane Science*, 378, (2011), 42-50.

Phair, J. W. and Donelson, R., Developments and design of novel (non-palladium-based) metal membranes for hydrogen separation, *Industrial and Engineering Chemistry Research*, 45, (2006), 5657-5674.

Pomerantz, N. and Ma Y. H., Effect of H_2S on the performance and long - term stability of Pd/Cu membranes, *Industrial and Engineering Chemistry Research*, 48, (2009), 4030-4039.

Raub, C. J., Electroplating of palladium for electrical contacts, *Platinum Metals Review*, 26, 4, (1982), 158-166.

Roa, F., Way, J. D., McCormick, R. L. and Paglieri, S. N., Preparation and characterization of Pd-Cu composite membranes for hydrogen separation, *Chemical Engineering Journal*, 93, (2003) 11-22.

Rostrup-Nielsen, J. R. and Rostrup-Nielsen, T., Large-scale hydrogen production. *Cattech*, 6, 4, (2002), 150-159.

Sacris, E. M. and Parlee, N. A. D., The diffusion of hydrogen in liquid Ni, Cu, Ag, and Sn, *Metallurgical Transactions B*, 1, (1970), 3377-3382.

Sagel, A., Sieber, H., Fecht, H. J. and Perepezko, J. H., Synthesis of an amorphous Zr-Al-Ni-Cu alloy with large supercooled liquid region by cold-rolling of elemental foils, *Acta Materialia*, 46, 12, (1998), 4233-4241.

Samingprai, S.,Tantayanon, S. and Ma, Y. H., Chromium oxide intermetallic diffusion barrier for palladium membrane supported on porous steel, *Journal of Membrane Science*, 347 (2010), 8-16.

Sarker, S., Chandra, D., Hirscher, M., Dolan, M., Isheim, D., Wermer, J., Viano, D., Baricco, M., Udovic, T.J., Grant, D. and Palumbo, O., Developments in the Ni - Nb - Zr amorphous alloy membranes, *Applied Physics A*, 122, 3, (2016), 1-9.

Schumacher, R. and Weiss, A., Hydrogen solubility in the liquid alloys lithium-indium, lithium-lead, and lithium - tin, *Berichte der Bunsengesellschaft für Physikalische Chemie*, 94, (1990), 684-691.

Shu, J., Grandjean, B. P. A., Van Neste, A. and Kaliaguine, S., Catalytic palladium - based membrane reactors: A review, *Canadian Journal of Chemical Engineering*, 69, 5, (1991), 1036-1060.

Sieverts, A., Absorption of gases by metals, *Zeitschrift Fur Metallkunde*, 21, (1929), 37-46.

Solar, M. Y. and Guthrie, R. I. L., Hydrogen transport in stagnant molten iron, *Metallurgical and Materials Transactions A*, (1971), 457-464.

Toda, G. Rate of permeation and diffusion coefficient of hydrogen through palladium, *Journal of Research Institute Catalysis Hokkaido University*, 6, (1958), 13-19.

Tosti, S., Bettinali, L. and Violante, V., Rolled thin Pd and Pd-Ag membranes for hydrogen separation and production, *International Journal of Hydrogen Energy*, 25, (2000), 319-325.

Tosti, S., Basile, A., Bettinali, L., Borgognoni, F., Chiaravalloti, F. and Gallucci, F., Long - term tests of Pd-Ag thin wall permeator tube, *Journal of Membrane Science*, 284, (2006) 393-397.

Wang, D., Tong, J., Xu, H. and Matsumur, Y., Preparation of palladium membrane over porous stainless steel tube modified with zirconium oxide, *Catalysis Today*, 93-95, (2004), 689-693.

Wei, I. Y. and Brewer, J., Desorption of hydrogen from palladium plating, *AMP Journal of Technology*, 5, (1996), 49-53.

Wilde, G., Dinda G. P. and Rosner, H., Synthesis of bulk nanocrystalline materials by repeated cold rolling, *Advanced Engineering Materials*, 7, 1-2, (2005), 11-15.

Xomeritakis, G. and Lin, Y. S., CVD synthesis and has permeation properties of thin palladiurn/alurnina, *AIChE Journal*, 44, 1, (1998), 174-183.

Yang, Q. Q., Yuan, L. I. U. and Li, Y. X., Hydrogen diffusion coefficient in liquid metals evaluated by solid - gas eutectic unidirectional solidification, *Transactions of Nonferrous Metals Society of China*, 24, 12, (2014), 4030-4037.

Yepes, D., Cornaglia, L. M., Irusta, S. and Lombardo, E. A., Different oxides used as diffusion barriers in composite hydrogen permeable membranes, *Journal of Membrane Science*, 274,1, (2006), 92-101.

Yeung, K. L., Christiansen, S. C. and Varma, A., Palladium composite membranes by electroless plating technique: relationships between plating kinetics, film microstructure and membrane performance, *Journal of Membrane Science*, 159, (1999), 107-122.

Yun, S. and Oyama, S. T., Correlations in palladium membranes for hydrogen separation: a review, *Journal of Membrane Science*, 375, (2011), 28-45.

Zahedia, M., Afra, B., Dehghani-Mobarake, M. and Bahmani, M., Preparation of a Pd membrane on a WO_3 modified porous stainless steel for hydrogen separation, *Journal of Membrane Science*, 333, (2009), 45-49.

Chapter III

Gallium Properties of Relevance

3.1 Abstract

This chapter summarizes physical and chemical properties of gallium of relevance to the design and development of a stable sandwiched liquid metal membrane (SLiMM) for H_2 purification. In fact, almost all the metals interact with hydrogen. Different characteristics of hydrogen in metal (Me-H) such as solubility, diffusivity, effect-of temperature, pressure and phase transition, etc., lead to various applications, such as hydrogen separation, hydrogen storage, battery electrode, etc. All of the metals and alloys currently being investigated for hydrogen storage and hydrogen separation membrane, however, are solid crystalline or amorphous structures. Properties and the applications of these metals are well discussed and recorded in the literature. Using liquid metal as hydrogen separation membrane as proposed here is a novel concept and represents an approach that has never been investigated. The reaction mechanism between hydrogen and a liquid metal are scarcely investigated or understood. Limited information on hydrogen diffusivity and solubility in liquid alkaline and since transition metals can be found in the literature. However, there is only one record of hydrogen diffusivity and there is no study in the literature on hydrogen solubility in liquid gallium. Further, physical properties such as surface tension, wettability and volatility would determine the nature and viability of the supported liquid metal membrane. Thus, to develop a liquid gallium membrane we have to start at the very beginning by understanding gallium physical, chemical properties, and reaction mechanism with hydrogen.

3.2 Introduction

Gallium (Ga), atomic number 31, was discovered by P.E. Lecoq de Boisbaudan at 1875 (Moskalyk, 2003). Gallium is a silvery, glass-like, soft metal that is liquid near room temperature (melting point 29.77 °C) and has the second largest liquid range of all elements (29.77 °C~2200 °C).

Figure 3.1 Image of solid gallium (wiki/Gallium).

Gallium has supercooling property. It can remain in liquid form as low as 70 °C below its melting point (Carlson et al., 1974), therefore seeding is sometimes necessary to initiate solidification. Gallium is more abundant than antimony, silver, bismuth, molybdenum, and tungsten. There is no direct gallium ore, the manufacture of Ga today mainly comes as a side product of aluminum mineral. Gallium is not produced in the United States. More than 95% of gallium is consumed in the United States is in the form of gallium arsenide (GaAs) and gallium nitride (GaN) used in semiconductor application. The second largest application for gallium is in the manufacture of optoelectronic devices such as laser diodes and light-emitting diodes (USGS Mineral Resources, 2012).

Metallic gallium is not considered toxic. Gallium is insoluble in water and therefore it cannot be readily absorbed through skin, although gallium ions interact in cells in a manner similar to Fe (III). If liquid gallium were to spill on a floor, the suggested practice is to freeze it with ice. After

gallium solidifies, it is easy to mechanically remove from the floor without any residue since liquid gallium does not wet most of the surfaces (Cadwallader, 2003). Liquid gallium has a tendency to react with oxygen and moisture at room temperature. At a controlled 1.8×10^{-4} torrs oxygen pressure, 5 Å thick layer of gallium oxide was forms. The thickness and roughness of gallium oxide did not change when subsequently heated to 573 K, 1.6×10^{-3} torrs (Regan et al., 1997). However, if it is oxide under air the oxide layer thickness could reach to 30 Å at 103 °C in 170 hours (Plech et al., 1998). The structure of this oxide layer is poorly crystallized or it could be an amorphous solid. Gallium oxide first forms as isolated oxide clusters on the liquid surface and gradually aggregates into a thin porous film (Wang et al., 1994).

Liquid gallium reacts with almost all the metals and forms intermetallic compounds at elevated temperatures (Lyon and Verne Katz, 1950). The information an metal solubility in liquid gallium is summarized in Table 3.1 and 3.2. At 500~973 K elements Fe, Ni, Cr and Ti (porous stainless steel, porous Inconel, porous Ni, porous Ti) commonly used as porous support are forming intermetallic compounds with liquid gallium.

Table 3.1 Metal solubility in liquid gallium and gallium intermetallic compounds (Yatsenko, 2008).

Metal	IMC	Interval T, K	lg*C*=A−B/*T*		*C*, at.%	
			A	−B, 10^3	673 K	773 K
In gallium						
Copper	$CuGa_2$	500–700	3.52	1.61	15.0	28
Calcium	$CaGa_4$	500–700	3.25	2.30	0.62	1.7
Scandium	$ScGa_3$	623–973	3.99	3.65	$3.5\cdot10^{-2}$	0.20
Titanium	$TiGa_3$	600–800	2.60	3.12	$9.5\cdot10^{-3}$	$3.9\cdot10^{-2}$
Germanium	Ge	400–600	3.60	1.78	8.9	19.8
Vanadium	VGa_4	600–800	3.20	4.0	$2.0\cdot10^{-3}$	$1.0\cdot10^{-2}$
Chromium	$CrGa_4$	600–800	2.70	3.10	$1.2\cdot10^{-2}$	$4.9\cdot10^{-2}$
Manganese	$MnGa_6$	500–700	5.40	3.90	0.40	2.3
Iron	$FeGa_3$	500–700	4.00	3.85	$1.9\cdot10^{-2}$	0.11
Cobalt	$CoGa_3$	500–700	3.50	3.10	$7.8\cdot10^{-2}$	0.31
Nickel	$NiGa_3$	500–700	2.52	1.85	0.59	1.35
Zirconium	$ZrGa_3$	500–800	3.05	4.22	$6.0\cdot10^{-4}$	$3.9\cdot10^{-3}$
Hafnium	$HfGa_3$	500–800	6.56	7.25	$6.1\cdot10^{-5}$	$1.5\cdot10^{-3}$

Table 3.2 Elements of fifth period solubility in liquid gallium and gallium intermetallic compounds (Yatsenko, 1970).

Solubility of Elements of the Fifth Period in Liquid Gallium

Element	Constants of the equation log C = A − B/T		Thermodynamic parameters			Solubility, at.%		Solid phase
	A	$B \cdot 10^{-3}$	ΔH_m, kcal/g-atom	$\Delta\overline{H}$, kcal/g-atom	$\Delta\overline{S}$, kcal/g-atom·deg	673° K	773° K	
Sr	0.87	2.64	2.08	9.90	1.90	$0.89 \cdot 10^{-1}$	0.28	$SrGa_4$
Y	1.00	2.37	2.70	8.10	2.60	0.291	0.845	YGa_2
Zr	1.05	4.22	3.0	16.30	2.60	$6.3 \cdot 10^{-4}$	$4.0 \cdot 10^{-3}$	$ZrGa_3$
Nb	4.79	9.2	—	38.5	2.61	$2.0 \cdot 10^{-7}$	$1.0 \cdot 10^{-5}$	$NbGa_3$
Mo	−0.14	2.80	6.70	6.00	−3.29	$5.0 \cdot 10^{-3}$	$1.9 \cdot 10^{-2}$	$MoGa_2$
Ru	3.08	5.85	6.20	20.5	11.80	$7.6 \cdot 10^{-4}$	$4.56 \cdot 10^{-3}$	$RuGa_2$
Rh	1.04	2.25	5.10	5.1	2.30	0.50	1.27	$RhGa_6$
Pd	0.30	0.82	1.00	1.00	−0.90	10.00	18.00	$PdGa_5$
Ag	—	—	—	—	—	38.50	57.00	Ag_3Ga_3
Cd	0.75	0.98	1.46	3.02	0.96	100.00	100.00	Cd
In	—	—	—	—	—	100	100	In
Sn	—	—	—	—	—	100	100	Sn
Sb	3.40	5.31	6.0 ± 2.0	18.00	9.50	$3.1 \cdot 10^{-3}$	$3.2 \cdot 10^{-2}$	GaSb
Te	11.5	12.40	10	46.50	42.00	$3.2 \cdot 10^{-4}$	$4.0 \cdot 10^{-2}$	Ga_2Te

Liquid gallium has complete miscibility in the liquid state with lead (Mathon et al., 1996), thallium, mercury (Manasijević et al., 2003) and silicon (Keck and Broder, 1953). Only a few metals are temporarily resistant to gallium, such as tungsten, which is stable with gallium up to 800 °C. The resistance of reaction with tantalum is good up to 450 °C, limited between 450~600 °C, and poor at higher temperatures. The resistance of reaction with niobium and molybdenum is good up to 400 °C limited between 400~450 °C, and poor at higher temperature (Lyon and Verne Katz, 1950). For the rest of the metals, the formation of intermetallic compounds is inevitable. Gallium also reacts with some of the ceramic materials at high temperature such as silica, magnesia, but the amount of literature work in this area is very limited. Even though liquid gallium is extremely reactive and corrosive with other metals at high temperature, however, it is quite stable at room temperature with polymers such as polyethylene, polypropylene, polystyrene, and polymethyl methacrylate resins (Cadwallader, 2003). These properties are of great significance in finding appropriates porous substrate and scaling materials for SLiMM.

3.3 Solid Gallium Bulk Crystal Structure

The solid crystal structure for Ga is shown in Figure 3.2 (Züger and Dürig, 1992; Rühm et al., 2003; Lyapin et al., 2008). The stable phase at normal conditions, α-Ga, is based-centered orthorhombic (Figure 3.2 a).

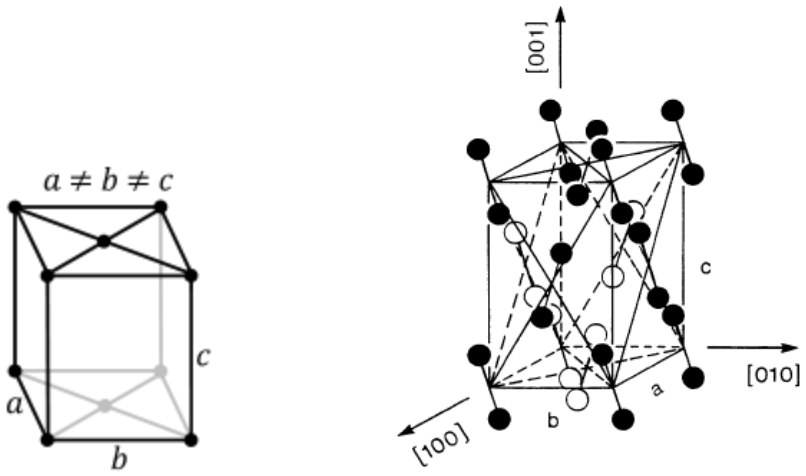

Figure 3.2 (a) Base-centered rthorhombic unit cell. The dimer bonds are indicated in the figure on the right as rods connecting pairs of Ga atoms (Züger and Dürig, 1992; Rühm et al., 2003).

There are eight atoms in the conventional unit cell (Figure 3.2 b) and the most striking feature of α-Ga crystal structure is the co-existence of metallic and covalent (dimer, Ga_2) bonds that determine many of gallium's unusual physical properties. The immediate (dimer) neighbors are at a distance of 2.44 Å, the other six being two each that are 0.27, 0.30, and 0.39 Å further apart. The detailed crystal structure of Ga is: Space group: *Cmca*; structure: base-centered orthorhombic; cell parameters: sides, a = 451.97 pm, b = 766.33 pm, c = 452.6 pm, angles, α = 90.0°, β = 90.0°, and γ = 90.0°. The nearest-neighbor atom pairs are located within (100) planes and are centered at the lattice sites of the unit cell. The pairs are alternatingly tilted by ~16.9 º with respect to the [001] axis.

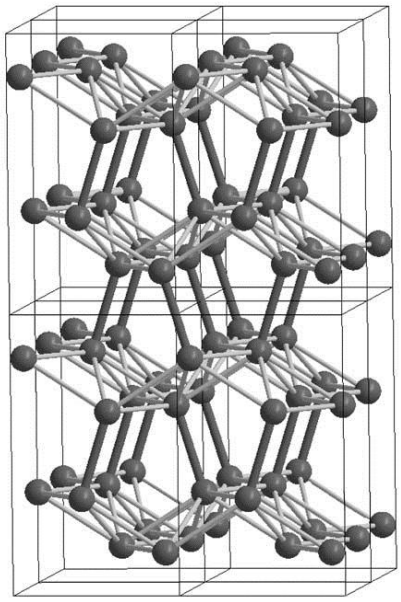

Figure 3.2 (b) Eight unit cells of Ga are shown (thin lines indicate their boundaries). Thick dark lines represent covalent Ga quasi-molecules linking puckered sheets (Lyapin et al., 2008).

As mentioned above, each Ga atom has 7 nearest neighbors (Gong et al., 1991; Donohue, 1974): one at 2.44 Å, two at 2.71 Å, two at 2.74 Å, and two at 2.81 Å. The six atoms lie in a strongly buckled plane that is about 1.49 Å thick. From this point of view, the α-Ga structure can be regarded as consisting of strongly buckled parallel planes connected by short bonds between the first neighbor atoms which lie in different planes (Figure 3.3).

Thus, the α-Ga structure may be described as consisting of a stacking of somewhat distorted and puckered hexagonal closed packed layers, with bonds between the layers being the strongest, i.e., approximately, single bond valence, and bonds within the layers rather weak, i.e., somewhat less than half bond valence. A view perpendicular to one of the layers is shown in Figure 3.3 (a), and the view showing the bonding between the layers is shown in Figure 3.3 (b).

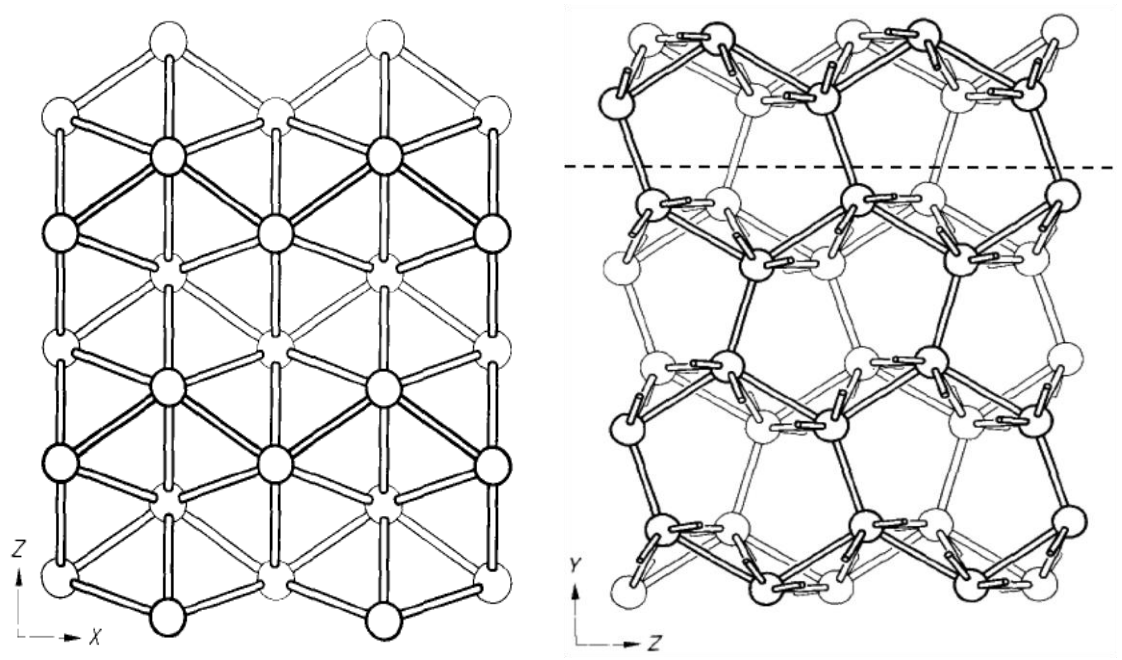

(a) (b)

Figure 3.3 (a) A portion of 4 unit cells of Ga projected on (010). The bonds between the layers, i.e., down from the lower atoms and up from the upper atoms, are not shown. (b) Four unit cells of Ga structure projected on (100) (Sharma and Donohue, 1962).

It turns out that the Ga surface structure is well-studied now. There is a detailed STM study of the α-Ga surfaces by Züger and Dürig (1992), and further analyzed by Bernasconi et al. (1995b). Other relevant studies, including DFT, include Moré et al. (2003), Søndergaard et al. (2003) Lizzit et al. (2009), and Voloshina et al. (2009). The DFT structure is shown in Figure 3.4 (Voloshina et al., 2009). However, liquid gallium structure is not well studied. In our "quasi-crystalline lattice" model discussed later on in chapter IV we will implicitly assume that the bonding and structure in a liquid metal is similar to that in a crystalline solid metal.

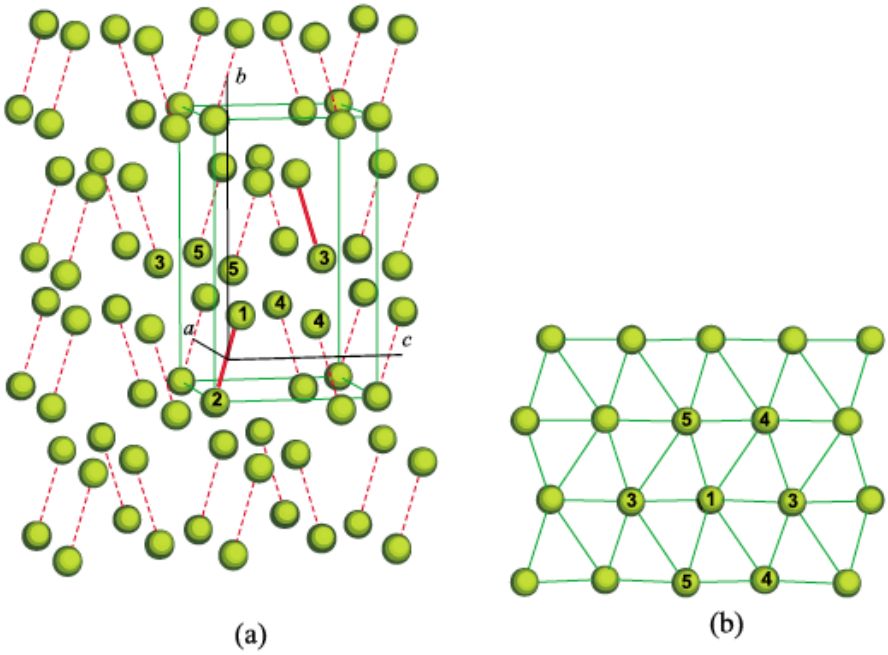

Figure 3.4 (a) Crystallographic structure of α-Ga with 7 nearest neighbors are marked with numbers (b) plan containing atoms 1, 3, 4, 5 (Voloshina et al. 2009).

3.4 Liquid Gallium Structure

In a dilute gas system molecules are widely spread and move freely before colliding to each other (Rowlinson and Evans, 1975). In solid system the atom distances are fixed and arranged in specific crystalline structure such as body center cubic, face center cubic and simple structure. In liquid system, the packing and the structural arrangement in the vicinity of atoms is similar to solids. Liquid atoms flow without easily dispersion, and are moving in all directions similar to a gas system (Jagannadham and Sanjeev, 2011). However, in liquids each molecule is interacting with its neighbors and there are no mean-free paths, binary collisions (Rowlinson and Evans, 1975), etc.

Before introducing liquid gallium structure, we have to first understand the approach of defining liquid structures. Liquid gallium, like other liquid metals is known to have an ordered, close-

packed structure that extends for four or more layers below the surface but is disordered in directions parallel to the surface (Phillips and Nesbitt, 2012). Generally due to the lack of fix crystalline structure, liquids have long range disorder but have short range order. Therefore, structure factor $S(Q)$ and radial distribution function $g(r)$ are used to describe atom distance, structure and coordination number of a liquid system (McGreevy, 1991). Radial distribution function (RDF) or pair correlation function is the probability of finding a neighbor atom separated at distance r averaged over time and configurations of the remaining atoms in the liquid (Hines et al., 1985). The coordination number n_M is defined as the average number of nearest neighbors within various distances and can be computed from the maxima peak area of RDF from Eq. (3.1). The average coordination number of a liquid metal at its melting point is approximate 10.56 obtained from experimental data with over 20 liquid metals (Tao, 2005).

$$n_M(r) = 4\pi r^2 \rho g(r) \tag{3.1}$$

where ρ is the average number density, r is the distance between atom, $g(r)$ is the radial distribution function.

To observe liquid gallium radial distribution function changes with temperature, it is most common to perform neutron and x-ray diffraction experiments (Bellissent-Funel, 1989; Bizid, 1978; Vahvaselkä, 1980). These experiments do not measure $g(r)$ directly but its Fourier inversion, structure factor $S(Q)$ (Soper, 1986), where Q is the momentum transfer in the diffraction experiment as defined by

$$Q = 4\pi \sin\theta / \lambda \tag{3.2}$$

where $\sin\theta$ is the scattering angle and λ is the radiation wavelength.

Figure 3.5 demonstrates the radial distribution function of liquid gallium at 293, 838 and 1303 K at different truncations of the structure factor measured by neutron scattering. Liquid gallium at 293 K is under supercooled condition (Bizid, 1978).

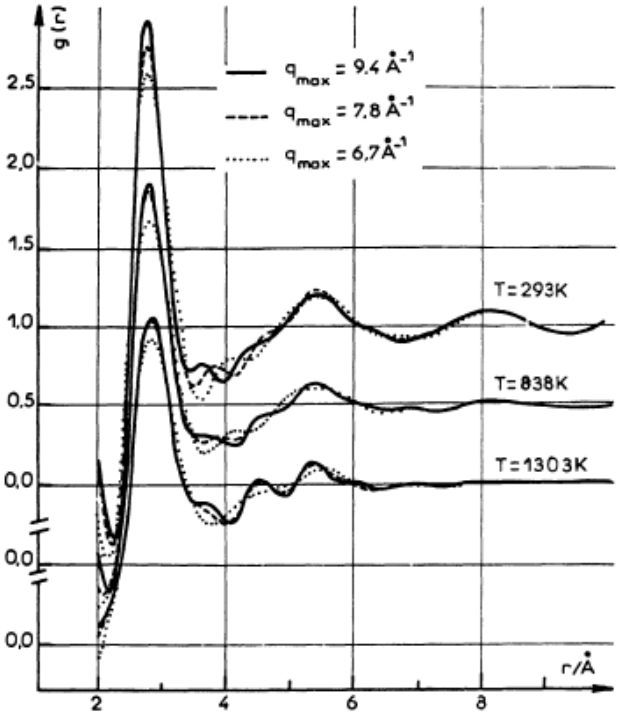

Figure 3.5 The radial distribution function of liquid gallium at 293, 838 and 1303 K at different cut-offs of the structure factor (Bizid, 1978).

From Figure 3.5 the calculated first peak, second and third radial positions of 293, 838, and 1303 K are 2.81($g(r_1) = 2.96$), 2.82 ($g(r_1) = 2.42$) and 2.85 Å ($g(r_1) = 2.08$); 5.50 ($g(r_2) = 1.20$), 5.31 ($g(r_2) = 1.12$) and 4.55 Å ($g(r_2) = 1.02$); 8.24 ($g(r_3) = 1.09$), 8.15 ($g(r_3) = 1.03$) and 5.35 Å ($g(r_3) = 1.13$), respectively. This means at 293 K in supercool liquid gallium there is a 2.96 times higher chance to find two molecules at 2.81 Å distance and there is 1.2 times higher chances to find two molecules at 5.50 Å distance (Andrew, 2001). As temperature increases, the distance between two molecules are more likely to be further apart from 2.81 Å at 293 K to 2.85 Å at

1303 K. However at longer range as temperature increases, the distance between two molecules are more likely to be closer from 5.50 Å at 293 K to 4.55 Å at 1303 K. Calculated coordination numbers at 293, 838, and 1303 K are 10.2, 9.2 and 8.4, respectively.

Figure 3.6 demonstrates the radial distribution function of liquid gallium at 283 (10 °C), 308 (35 °C), 523 (250 °C), 723 (450 °C) and 973 K (700 °C) measured by X-ray scattering (Vahvaselkä, 1987). Liquid gallium under 283 K is at supercooled condition. The calculated first peak positions are 2.84 Å, 2.84 Å, 2.82 Å, 2.81 Å, and 2.76 Å, respectively. The calculated coordination numbers are 10.8, 10.7, 10.5, 10.0 and 9.6. From this close up it is noted that at 10 °C the shape of the first peak of radial distribution function is sharper and narrower compared to 700 °C. This means at higher temperature two molecules are separated at shorter distance than 10 °C in average (2.84 Å at 10 °C compared to 2.76 Å at 700 °C). However, there are higher possibilities of finding two molecules at distance distributed between 2.6~3.2 Å at 700 °C than at 10 °C.

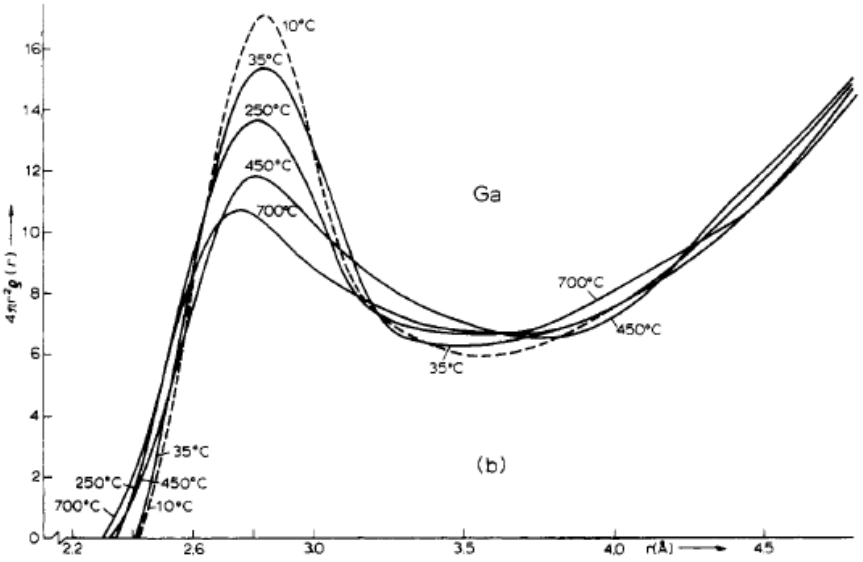

Figure 3.6 Radial distribution function of liquid gallium at 283 (10 °C), 308 (35 °C), 523 (250 °C), 723 (450 °C) and 973 K (700 °C) measured by X-ray scattering (Vahvaselkä, 1987).

Besides experimental determination the radial distribution function can also be obtained from first-principles molecular-dynamics (MD) simulations. Molecular-dynamics calculates the total energy and the forces of atoms by utilizing the density functional theory to determine the electronic ground state (Holender et al., 1995). It is typically applied in calculating liquid metal structures, electronic density (Kresse and Hafner, 1993), viscosity and diffusion coefficient (Cherne Iii and Deymier, 2001; Yu and Kaviany, 2014).

Figure 3.7 shows the calculated radial distribution function at 702 and 982 K using molecular-dynamic simulation (Holender et al., 1995) compared with experimental result from Bellissent-Funel et al. (1989). The first peak positions of 702, 982 K are 2.74 Å, 2.7 Å and the corresponding coordination number are 8.7 and 9.1. Later González and González (2008) also applied MD in liquid gallium structure simulation and gave first peak position of 3.81, 3.72, and 3.45 Å at 373, 523, and 959 K, with coordination number of 11.8, 11.2, and 8.5 atoms.

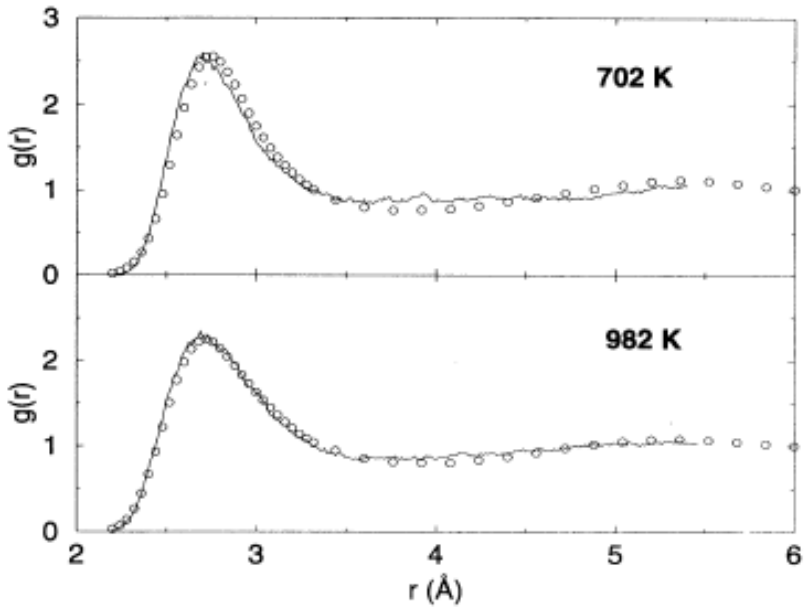

Figure 3.7 Solid line is the radial distribution function of liquid gallium at 702 and 982 K (Holender et al., 1995) and circles represent experimental results (Bellissent-Funel et al., 1989).

It is difficult to conclude the exact Ga-Ga molecule distance and the coordination number based on previous findings. On the other hand, these results shed a light on the liquid structure, which is short range ordered similar to solid structure with bond distances between 2.81~2.84 Å near melting point (30ºC). At high temperatures, bond distance of first peak position tend to decrease with increasing temperature from X-ray and MD study, but increases from neutron scattering result. Even though bond distance increases at first peak position with neutron study, both second and the third peak position decrease with increasing temperature (5.31 at 838 K and 4.55 Å at 1303 K; 8.15 at 838 K and 5.35 Å 1303 K). All of the study suggests that coordination number decreases with increasing temperature. Bond distances and coordination numbers are crucial parameters in determining thermodynamic and physical properties as discussed in chapters IV and V.

3.5 Liquid Gallium Density

Gallium has an unusually low melting temperature of 29.77 ºC and the density in the liquid state is in fact higher than in the solid crystalline state, the corresponding change in specific volume being about 3.2 %. Thus, for Ga the liquid density is a bit higher (6.095 g/cm^3 at the m.p. and 5.91 g/cm^3 for solid). The liquid density as a function of temperature in the range of 303-1,500 K is given by (Assael et al., 2012) as shown in Figure 3.8.

$$\rho_{\mathrm{M}} = \rho_{\mathrm{M},ref} - \alpha(T - T_{ref}) \ \ \mathrm{kg/m^3} \tag{3.3}$$

where $\rho_{\mathrm{M},ref}$ = 6077 kg/m^3, α = 0.611 kg/m^{3}K, and T_{ref} = 302.914 K. For instance at 773 K, the density of liquid Ga is 5.79 g/cm^3.

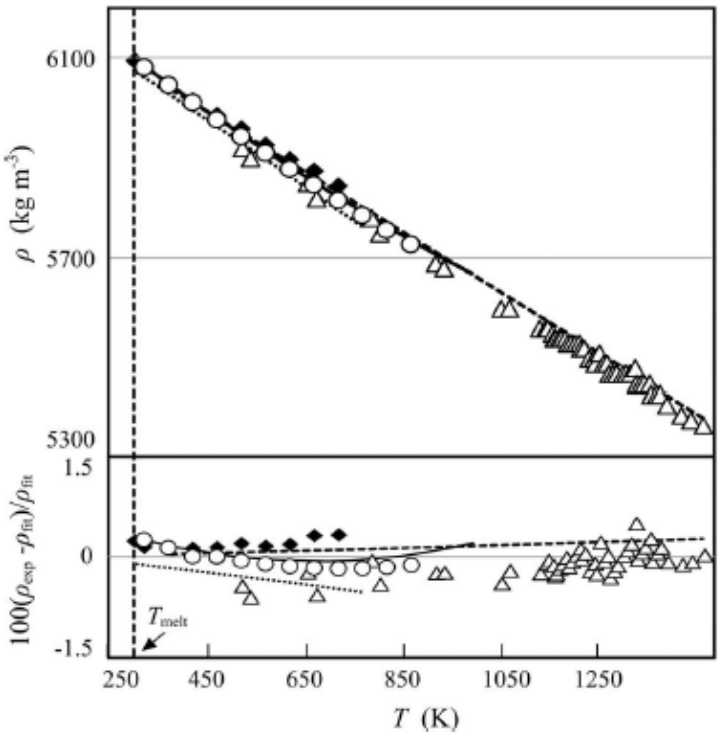

Figure 3.8 Liquid gallium temperature vs density (Assael et al., 2012).

3.6 Liquid Gallium Surface Tension

Surface tension of liquid metal is strongly affected by its surrounding elements, especially oxygen. As mentioned earlier, liquid gallium tends to form a thin oxide layer on the surface, so that to accurately measure surface tension is extremely difficult. Besides ultra-high vacuum, inert gas purging such as He (Passerone et al., 1990), Ar or the mixture of inert gas with reduction gas H_2 (Saravanan et al., 2002) are common techniques to reduce and control oxygen partial pressure. To obtain liquid/solid surface tension it is necessary to use a sessile drop method with a controlled amount of liquid drop on solid ceramic surface (Nikolopoulos et al., 1992; Nogi et al., 1989). However, liquid metals tend to react with one or more element in the solid ceramic surface. Thus, several surface-free methods such as oscillating drop, pendent drop method (Mills

and Su, 2006) have been developed and are usually utilized for determining liquid-gas surface tension measurement to avoid direct contact.

Liquid gallium surface tension under vacuum and hydrogen are shown in Figure 3.9. The surface tension reported by Ayyad and Freyland (2002), Eq. (3.4), are relatively similar to values of Mills and Su (2006), Eq. (3.5). Values from Alchagirov and Mozgovoi (2005), Eq. (3.6) are lower in comparison. Surface tension of liquid gallium under hydrogen environment is a lot lower than under vacuum. König and Keck (1983), Eq. (3.7), introduced palladium purified hydrogen into surface tension measurement in the hope of eliminating oxygen contamination from gas environment.

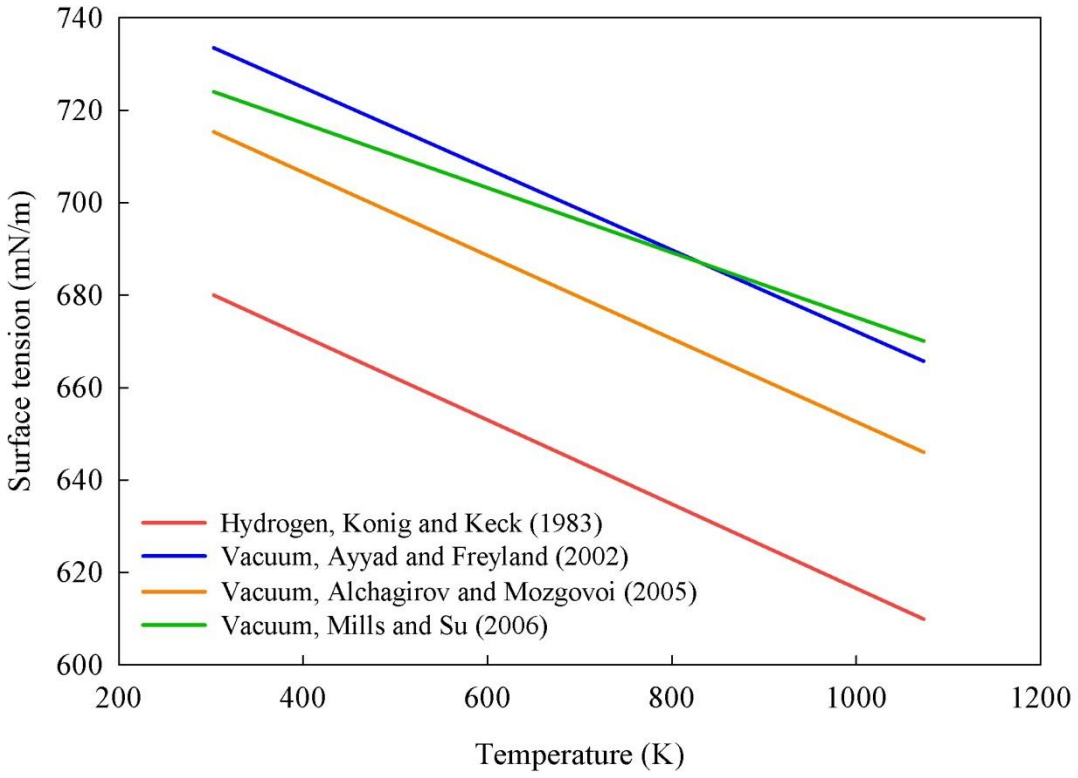

Figure 3.9 Surface tension of liquid gallium vs temperature under vacuum and hydrogen gas. (König and Keck, 1983; Ayyad and Freyland, 2002; Alchagirov and Mozgovoi, 2005; Mills and Su, 2006).

However, judging by the low surface tension compared to vacuum it is likely that hydrogen was reacting with gallium. Saravanan et al. (2002) also discovered that when introducing 4% H_2 in N2, the surface tension of liquid aluminum drops accordingly due to hydrogen adsorption

$$\sigma = 733.5 - 0.088(T - 303) \text{ mN/m in vacuum} \quad (3.4)$$

$$\sigma = 724 - 0.07(T - 303) \text{ mN/m in vacuum} \quad (3.5)$$

$$\sigma = 715.3 - 0.09(T - 303) \text{ mN/m in vacuum} \quad (3.6)$$

$$\sigma = 680 - 0.091(T - 303) \text{ mN/m in hydrogen} \quad (3.7)$$

3.7 Gallium Vapor Pressure

The vapor pressure of liquid gallium is very low. Therefore, a liquid gallium film is stable over a range of temperature and thus suitable for supported liquid membrane synthesis compared to e.g., liquid alkaline metals. Vapor pressure experimental data gathered from literature is shown in Figure 3.11. Plotted liquid gallium vapor pressure below 1180 K is out of measurement range. However, extrapolated liquid gallium vapor pressure is essentially the same as solid gallium vapor pressure at its melting point (Alcock et al., 1984). Vapor pressure of Ga, In, Ag, Sn, Cu and Au at higher temperatures are compared in Figure 3.10 (Geiger et al., 1987).

Vapor pressure relation with temperature between 906~2403 °C from Cochran and Forcester, (1962)

$$\log p_v = 7.34 - 14900/T - 0.515 \log T \text{ atm} \quad (3.8)$$

The experimental value of vapor pressure 2109-2600 K (in bars) of gallium is given by Geiger et al., (1987)

$$\log p_v = 5.517 - 13798/T \text{ bar} \quad (3.9)$$

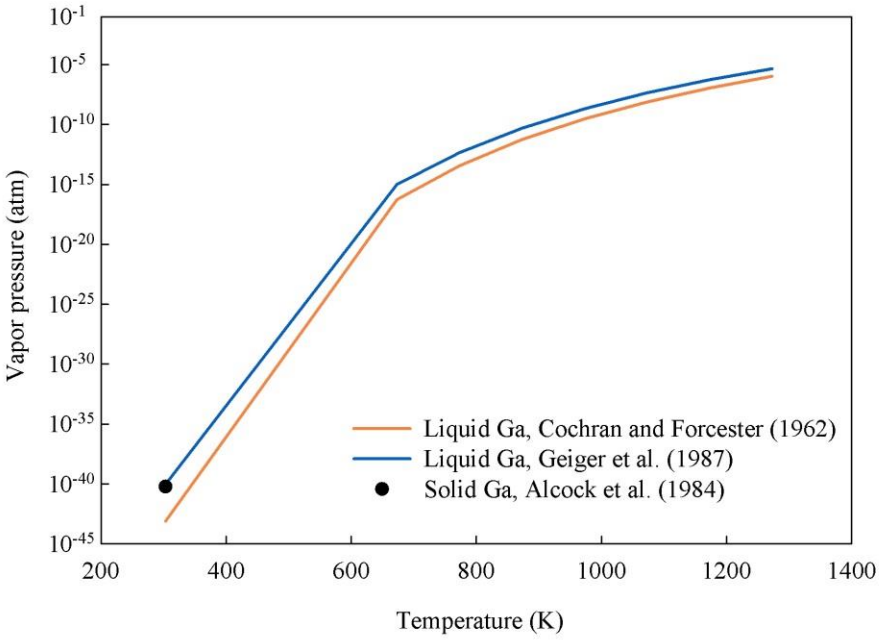

Figure 3.10 Liquid and solid gallium vapor pressure (Cochran and Forcester, 1962; Geiger et al., 1987; Alcock et al., 1984).

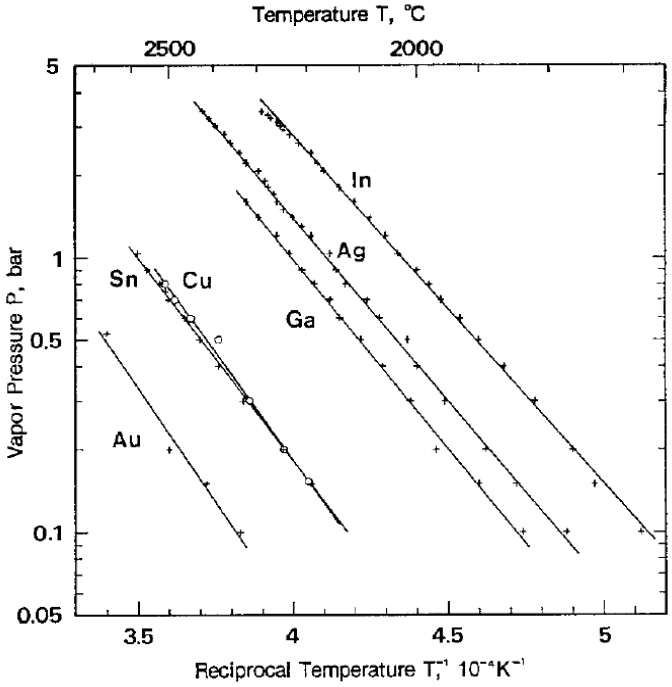

Figure 3.11 Vapor pressure of Ga, In, Ag, Sn, Cu and Au at high temperatures (Geiger et al., 1987).

Vapor pressure of both liquid and solid gallium is provided by Alcock et al., (1984)

$$\text{Liquid: } \log p_v = 6.754 - 13984/T - 0.3413 \log T \text{ atm} \tag{3.10}$$

$$\text{Solid: } \log p_v = 6.657 - 14208/T \text{ atm} \tag{3.11}$$

3.8 Chemistry of Gallium with Hydrogen

Xiao et al. (1993) first trapped Ga_2, H_2 and Ar matrix onto solid rhodium-coated copper surface at 12 K and gallium dimer Ga_2 reacted spontaneously with H_2 to yield a dibridged $Ga(l\text{-}H)_2Ga$ species. Ga_2, H_2 trapped matrix was heated between 890~1100 °C and vapor was examined with FT-IR, as shown in Figure 3.12.

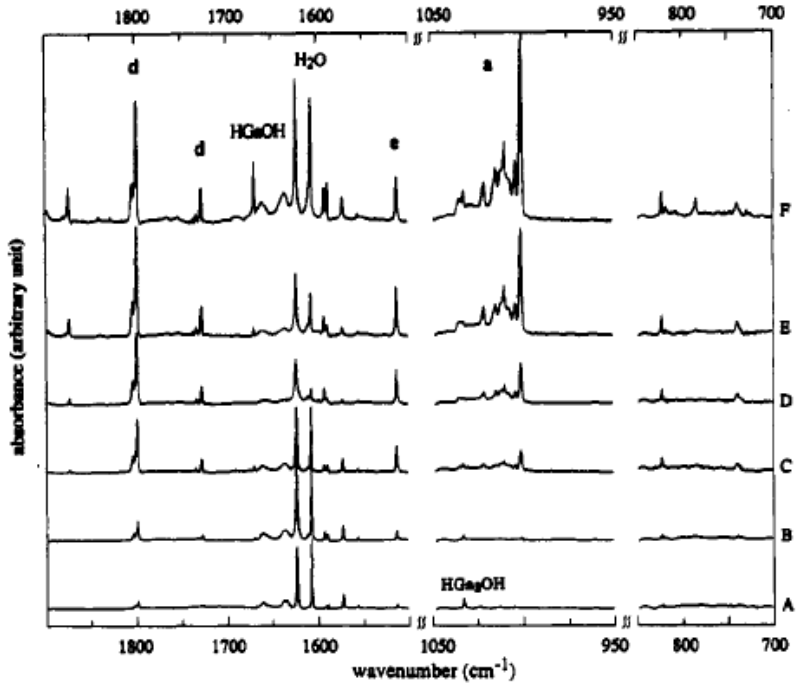

Figure 3.12 IR spectra for different gallium concentrations (controlled by temperature) with H_2 pressure at 2.0×10^{-6} torr (A) 890 °C, (B) 947 °C, (C) 980 °C, (D) 1030 °C, (E) 1060 °C, (F) 1100 °C, a = $Ga_2(b\text{-}H)_2$, b = $Ga_3(t\text{-}H)_2$, c = $Ga_2(t\text{-}H)_2$, d = GaH_2, and e = GaH, where b-H and t-H represent bridging and terminal hydrogen, Xiao et al. (1993).

It is found that excited atomic gallium reacts with H_2 to yield both GaH and GaH_2, the dimer of gallium (Ga_2) reacts with H_2 to form $Ga_2(b\text{-}H)_2$ with two bridging hydrogens, which can be converted to $Ga_2(t\text{-}H)_2$. The trimer of gallium, Ga_3, has also been found to react with H_2. As the concentration of gallium increases, the intensity of GaH_2 (d) and GaH (e) rise steadily, the reaction between gallium and hydrogen seems to be weak at 980 °C. Similar tests were done using CH_4, and the only compound founded in the reaction was $HGaCH_3$.

Besides gallium vapor, there is some evidence in the literature that $Ga^{\delta+}$ might activate hydrogen at lower temperatures. Collins et al. (2002) performed a series of tests using IR Spectroscopy to identify gallium-hydrogen, gallium-palladium-hydrogen (both coated on SiO_2 support and oxidized in air for 2 hours at 400 °C bonding at various temperatures.

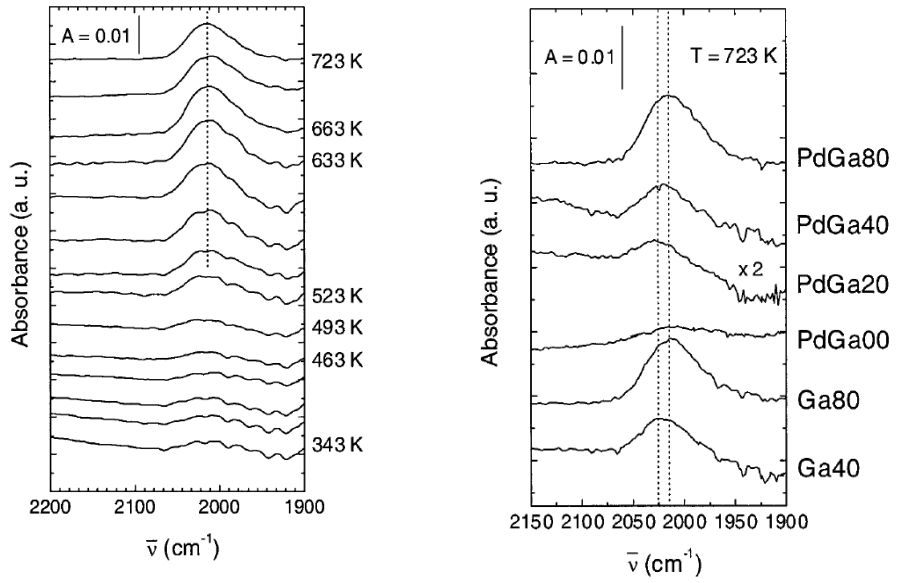

Figure 3.13 (a) Evolution of the $Ga^{\delta+}$–H stretching band (2020 cm^{-1}) over PdGa80 under flowing H_2 (100 cm^3/min), from 343 to 723 K, heating rate 5 K/min (b) Infrared spectra at 723 K for various Pd-Ga combinations, hydrogen flow 100 cm^3/min, (Collins et al., 2002).

Figure 3.13 (a) discuss the evolution of Ga-H stretching band over PdGa80 (Pd-Ga/SiO_2, atom ratio of Ga/Pd = 10/80) under flowing H_2 at various temperatures. The band signal is reliably

against background above approximately 500 K. The intensity between Ga-H starts to increase above 523 K (250 °C) and grows up until 660 K, which suggests that the Ga in Pd-Ga alloy forms hydrogen bond at temperatures as low as 250 °C.

Figure 3.13 (b) shows Ga-H stretching band over $PdGa_x$ compositions (x = atom ratios, for example atom ratio of $PdGa40/SiO_2$ is Ga/Pd = 4) and Ga_x (gallium weight of Ga40 is the same as gallium in PdGa40) under flowing H_2 at 723 K (450 ºC). The band intensity of Ga80 is very similar to PdGa80. The intensity of PdGa00 is almost none which also confirms 2020 cm^{-1} peak is not related to Pd. The band intensity is proportional to Ga weight loading suggests that Pd did not contribute to the formation of Ga-H.

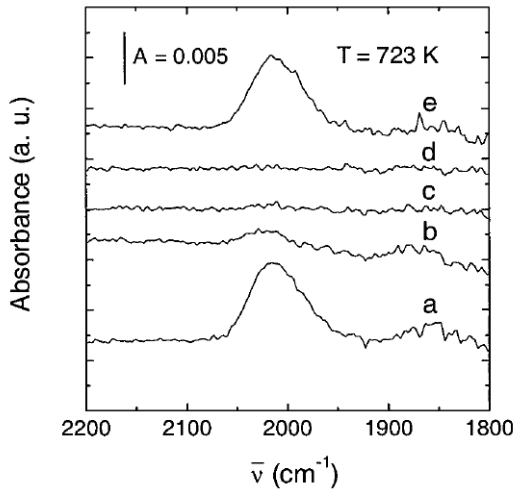

Figure 3.14 Infrared spectra of $Ga^{\delta+}$–H on the PdGa80 (a) under flowing hydrogen (100 cm^3/min), then evacuating at 10^{-6} torr for (b) 5, (c) 10, and (d) 15 min and (e) restoring the hydrogen, (Collins et al., 2002).

Figure 3.14 is the Ga-H infrared spectra of PdGa80 before and after removing hydrogen under vacuum. It is noticed that hydrogen could be removed from PdGa80 at 450 ºC under vacuum within 5 minutes, and re-adsorbs hydrogen once the vacuum stops. The same result was obtained

from Ga/SiO_2 sample at 653 K. These results provide confirmation of interaction between Ga and H_2, which is, of course, essential for Ga to serve as a H_2 membrane.

Köhn et al. (2003) combined FTIR experiment and quantum chemical calculations to examine the mechanism of Ga reacting with H_2. The authors discovered that Ga_2 dimer is more reactive than Ga because of its access to greater range of excited electronic states at lower energies. Ga atom tends to react with H_2 and form radicals GaH·, H·, and then forms GaH_2 (exothermic reaction, –2 ~ –13 kJ/mol). The activation barrier (50~60 kJ/mol) of Ga atoms with hydrogen is higher than for Ga_2. Ga_2 tend to form $Ga(\mu\text{-}H)_2Ga$ and it is also an exothermic reaction (–93 ~ –96 kJ/mol).

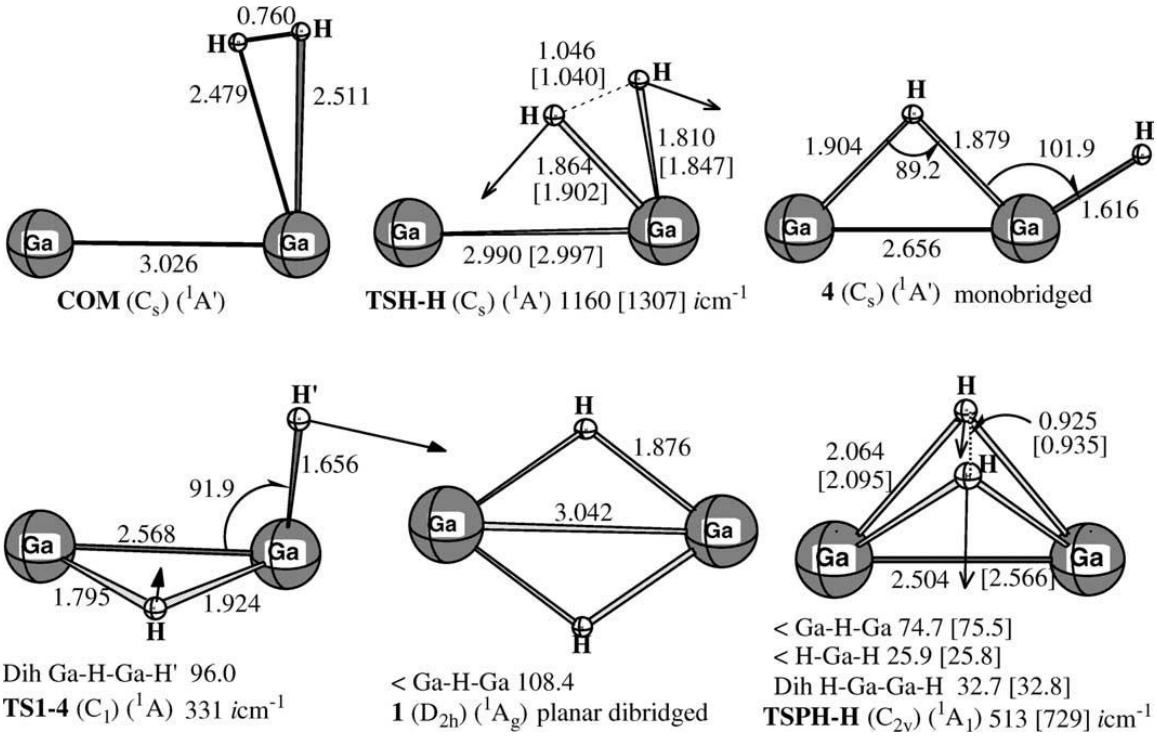

Figure 3.15 Singlet structures transition state for the reaction of Ga_2 with H_2 calculated with B3LYP and CASSCF methods, bond lengths in Å, bond angles in degrees (Moc, 2004).

Moc (2004) later assumed that as Ga_2 dimer starts from the ground-state triplet PES (potential energy surface), a spin crossing will move the Ga_2 into singlet PES and reacts with H_2 in the path

as shown in Figure 3.15. The activation barrier of ground state into transition state is 11.29 kJ/mol. The overall Ga_2 ($3\Pi_u$) + $H_2 \rightarrow Ga(\mu\text{- }H)_2Ga$ is found to be exothermic by –100.32 ~ –108.68 kJ/mol.

Besides GaH and Ga_2G_2 hydride, low concentration of Ga_3H_2 was also discovered during cryogenic reaction in FTIR experiments by Margrave et al. (2002) and Xiao et al. (1993). Moc (2009) later extended the computer modeling into Ga_3 trimer and H_2 to determine the possible reaction path. H_2 dissociation on Ga_3 trimer occurs on the lowest energy doublet PES via the transition state with 64 kJ/mol activation barrier above the ground-state and leads directly to the Ga_3H_2 product isomer. This is also an exothermic reaction –62.7 kJ/mol. The higher diffusion barrier of trimer with hydrogen than dimer is the reason that Ga_3H_2 is seen less than Ga_2H_2. Over all of these reactions, the activation barrier of Ga trimer is the highest, second is Ga atom and Ga dimer with hydrogen gas has the lowest value. Therefore, the tendency is to form Ga_2H_2.

All of the literature works on gallium and hydrogen are based on gas phase reaction or solid phase catalytic reaction. There is no information available in the literature on hydrogen and liquid gallium reaction. Nevertheless, the above description provide a good indication that hydrogen and liquid gallium may have similar interaction properties and mechanism.

3.9 References

Alchagirov, B. B. and Mozgovoi, A. G., The surface tension of molten gallium at high temperatures, *High Temperature*, 43, 5, (2005), 791-792.

Alcock, C. B., Itkin, V. P. and Horrigan, M. K., Vapour pressure equations for the metallic elements: 298–2500K, *Canadian Metallurgical Quarterly*, 23, 3, (1984), 309-313.

Andrew, R. L., Molecular Modelling: Principles and Applications, *Pearson Education*, 311-312, (2001).

Assael, M. J., Armyra, I. J., Brillo, J., Stankus, S. V., Wu, J. and Wakeham, W. A., Reference data for the density and viscosity of liquid cadmium, cobalt, gallium, indium, mercury, silicon, thallium, and zinc, *Journal of Physical and Chemical Reference Data*, 41, 3, (2012), 033101.

Ayyad, A. H. and Freyland, W., Wetting transition in liquid Ga-Bi alloys: light scattering study of surface energy and entropy, *Surface Science*, 506, (2002), 1-11.

Bellissent-Funel, M. C., Chieux, P., Levesque, D. and Weis, J. J., Structure factor and effective two-body potential for liquid gallium, *Physical Review A*, 39, 12, (1989), 6310-6318.

Bernasconi, M., Chiarotti, G. L. and Tosatti, E., Ab initio calculations of structural and electronic properties of gallium solid-state phases, *Physical Review B*, 52, 14, (1995a), 9988-9998.

Bernasconi, M., Chiarotti, G. L. and Tosatti, E., Theory of the structural and electronic properties of α-Ga(001) and (010) surfaces, *Physical Review B*, 52, 14, (1995b), 9999-10016.

Bizid, A., Defrain, A., Bellissent, R. and Tourand, G., Neutron diffraction investigation and structural model for liquid gallium from room temperature up to 1303 K, *Journal de Physique*, 39, 5, (1978), 554-560.

Cadwallader, L. C., Gallium safety in the laboratory, *Idaho National Laboratory*, (2003).

Carlson, D. G., Feder, J. and Segmuller, A., Measurement of the liquid structure factor of supercooled gallium and mercury, *Physical Review A*, 9, 1, (1974), 400-403.

Cherne Iii, F. J. and Deymier, P. A., Calculation of the transport properties of liquid aluminum with equilibrium and non-equilibrium molecular dynamics, *Scripta Materialia*, 45, 8, (2001), 985-991.

Cochran, C. N. and Foster, L. M., Vapor pressure of gallium, stability of gallium suboxide vapor, and equilibria of some reactions producing gallium suboxide vapor, *Journal of the Electrochemical Society*, 109, 2, (1962), 144-148.

Collins, S. E., Baltan´as, M. A., Garcia Fierro, J. L. and Bonivardi, A. L., Gallium-hydrogen bond formation on gallium and gallium-palladium silica-supported, *Catalysts Journal of Catalysis*, 211, (2002), 252-264.

Donohue, J., Structures of the Elements, *John Wiley*, New York, (1974).

Geiger, F., Busse, C. A. and Loehrke, R. I., The vapor pressure of indium, silver, gallium, copper, tin, and gold between 0.1 and 3.0 bar, *International Journal of Thermophysics*, 8, 4, (1987), 425-436.

Gong, X. G., Chiarotti, G. L., Parrinello, M. and Tosatti, E., α-gallium: A metallic molecular crystal, *Physical Review B*, 43, 17, (1991), 14277-14280.

González, L. E. and González, D. J., Structure and dynamics of bulk liquid Ga and the liquid-vapor interface: An ab initio study, *Physical Review B*, 77, 6, (2008), 064202.

https://en.wikipedia.org/wiki/Gallium

Himmel, H. J., Manceron, L., Downs, A. J. and Pullumbi, P., Formation and characterization of the gallium and indium subhydride molecules Ga_2H_2 and In_2H_2: A matrix isolation study, *Journal of the American Chemical Society*, 124, 16, (2002), 4448-4457.

Hines, A. L., Walls, H. A. and Jethani, K. R., Determination of the coordination number of liquid metals near the melting point, *Metallurgical Transactions A*, 16, 1, (1985), 267-274.

Holender, J. M., Gillan, M. J., Payne, M. C. and Simpson, A. D., Static, dynamic, and electronic properties of liquid gallium studied by first-principles simulation, *Physical Review B*, 52, 2, 1995, 967-975.

Jagannadham, V. and Sanjeev, R., Is the liquid a condensed gas or collapsed solid ? A statistical thermodynamic and cell theory approach: A simple introductory and lucid one-hour class-room lecture for physical chemistry senior under-hraduate and graduate level students, *American Journal of Chemistry*, 1, 2, (2011), 26-28.

Keck, P. H. and Broder, J., The solubility of silicon and germanium in gallium and indium, *Physical Review*, 90, 4, (1953), 521-522.

Köhn, A., Himmel, H. J. and Gaertner, B., Why does a Ga_2 dimer react spontaneously with H_2, but a Ga atom does not ? - A detailed quantum chemical investigation of the differences in reactivity between Ga atoms and Ga_2 dimers, in combination with experimental results, *Chemistry-A European Journal*, 9, 16, (2003), 3909-3919.

König, U. and Keck, W., Measurement of the surface tension of gallium and indium in a hydrogen atmosphere by the sessile drop method, *Journal of the Less Common Metals*, 90, 2, (1983), 299-303.

Kresse, G. and Hafner, J., Ab initio molecular dynamics for liquid metals, *Physical Review B*, 47, 1, (1993), 558-561.

Lizzit, S., Baraldi, A., Grütter, Ch, Bilgram, J. H. and Hofmann, Ph., The surface phase transition and low-temperature phase of α-Ga (010) studied by SPA-LEED, *Surface Science*, 603, 21, (2009), 3222-3226.

Lyapin, A. G., Gromnitskaya, E. L., Yagafarov, O. F., Stal'gorova, O. V. and Brazhkin, V. V., Elastic properties of crystalline and liquid gallium at high pressures, *Journal of Experimental and Theoretical Physics*, 107, 5, (2008), 818-827.

Lyon, R. N. and Verne Katz, D., Liquid metals handbook, *United States Office of Naval Research Committee on the Basic Properties of Liquid Metals Washington U.S. Government Printing*, 68-69, (1950), 100-101.

Manasijević, D., Živković, D., Katayama, I. and Živković, Ž. D., Calculation of activities in some gallium-based systems with a miscibility gap, *Journal of the Serbian Chemical Society*, 68, 8-9, (2003), 665-675.

Mathon, M., Miane, J. M., Gaune, P., Gambino, M. and Bros, J. P., Gallium + lead system: molar heat capacity and miscibility gap, *Journal of Alloys and Compounds*, 237, 1, (1996), 155-164.

McGreevy, R. L., Understanding liquid structures, *Journal of Physics: Condensed Matter*, 3, 42, (1991), F9-F22.

Mills, K. C. and Su, Y. C., Review of surface tension data for metallic elements and alloys: Part 1- Pure metals, *International Materials Reviews*, 51, 6, (2006), 329-351.

Moc, J., Interaction of Ga_3 cluster with molecular hydrogen: combined DFT and CCSD (T) theoretical study, *The European Physical Journal D*, 53, 3, (2009), 309-317.

Moc, J., Reaction of gallium dimer with H_2: a theoretical study of the process mechanism, *Chemical Physics Letters*, 395, 1, (2004), 38-43.

Moré, S., Soares, E. A., Van Hove, M. A., Lizzit, S., Baraldi, A., Grütter, Ch., Bilgram, J. H. and Hofmann, Ph., α-Ga (010) surface reconstruction: A LEED structural analysis of the (1×1) room temperature and $(2\sqrt{2}\times\sqrt{2})$ R 45° low-temperature structures, *Physical Review B*, 68, 7, (2003), 075414.

Moskalyk, R. R., Gallium: the backbone of the electronics industry, *Minerals Engineering*, 16, 10, (2003), 921-929.

Nikolopoulos, P., Los, S. A. P., Angelopoulos, G. N., Naoumidis, A. and Grübmeier, H., Wettability and interfacial energies in SiC-liquid metal systems, *Journal of Materials Science*, 27, 1, (1992), 139-145.

Nogi, K., Oishi, K. and Ogino, K., Wettability of solid oxides by liquid pure metals, *Materials transactions, JIM*, 30, 2, (1989), 137-145.

Passerone, A., Ricci, E. and Sangiorgi, R., Influence of oxygen contamination on the surface tension of liquid tin, *Journal of Materials Science*, 25, 10, (1990), 4266-4272.

Phillips, L. F. and Nesbitt, D. J., The surface of liquid gallium, *Chemical Physics Letters*, 536, (2012), 61-64.

Plech, A., Klemradt, U., Metzger, H. and Peisl, J., *In situ* x-ray reflectivity study of the oxidation kinetics of liquid gallium and the liquid alloy $Ga_{0.93}Hg_{0.07}$, *Journal of Physics: Condensed Matter*, 10, 5, (1998), 971-982.

Regan, M. J., Tostmann, H., Pershan, P. S., Magnussen, O. M., DiMasi, E., Ocko, B. and Deutsch, M. M., X-ray study of the oxidation of liquid-gallium surfaces, *Physical Review B*, 55, 16, 15, (1997), 10786-10790.

Rowlinson, J. S. and Evans, M., The motion of simple molecules in liquids, *Annual Reports on the Progress of Chemistry, Section A: Physical and Inorganic Chemistry*, 72, (1975), 5-30.

Rühm, A., Reichert, H., Donner, W., Dosch, H., Grütter, C. and Bilgram, J., Bulk and surface premelting phenomena in α-gallium, *Physical Review B*, 68, 22, (2003). 224110.

Saravanan, R. A., Molina, J. M., Narciso, J., Garcia-Cordovilla, C. and Louis, E., Surface tension of pure aluminum in argon/hydrogen and nitrogen/hydrogen atmospheres at high temperatures, *Journal of Materials Science Letters*, 21, 4, (2002), 309-311.

Sharma, B. D. and Donohue, J., A refinement of the crystal structure of gallium, *Zeitschrift für Kristallographie-Crystalline Materials*, 117, 1-6, (1962), 293-300.

Søndergaard, Ch., Schultz, Ch., Agergaard, S., Li, H., Li, Z., Hoffmann, S. V., Grütter, Ch., Bilgram, J. H. and Hofmann, Ph., Electronic structure of α-Ga, *Physical Review B*, 67, 20, (2003), 205105.

Soper, A. K., On the determination of the pair correlation function from liquid structure factor measurements, *Chemical Physics*, 107, 1, (1986), 61-74.

Tao, D. P., Prediction of the coordination numbers of liquid metals, *Metallurgical and materials transactions A*, 36, 12, (2005), 3495-3497.

USGS Mineral Resources http://minerals.usgs.gov/minerals/pubs/commodity/gallium/, (2012).

Vahvaselkä, K. S., Temperature dependence of the liquid structure of Ga, *Physica Scripta*, 22, 6, (1980), 647-652.

Voloshina, E., Rosciszewski, K. and Paulus, B., First-principles study of the connection between structure and electronic properties of gallium, *Physical Review B*, 79, 4, (2009), 045113.

Wang, Y. L., Doong, Y. Y., Chen, T. S. and Haung, J. S., Oxidation of liquid gallium surface: Nonequilibrium growth kinetics in 2+1 dimensions, *Journal of Vacuum Science and Technology A*, 12, (1994), 2081-2086.

Xiao, Z. L., Hauge, R. H. and Margrave, J. L., Cryogenic reactions of gallium with molecular hydrogen and methane, *Inorganic Chemistry*, 32, (1993), 642-646.

Yatsenko, S. P, Sabirzyanov, N. A. and Yatsenko, A. S., Dissolution rates and solubility of some metals in liquid gallium and aluminum, *13th International Conference on Liquid and Amorphous Metals, Journal of Physics: Conference Series*, 98, (2008), 1-7.

Yatsenko, S. P. Anikin, Yu. A. Khimicheskaya, F. and Materialov, M., Solubility of metals of the fifth period in liquid gallium, *Materials Science*, 6, 3, (1970), 57-62.

Yu, S. and Kaviany, M., Electrical, thermal, and species transport properties of liquid eutectic Ga-In and Ga-In-Sn from first principles, *The Journal of Chemical Physics*, 140, 6, (2014), 064303.

Züger, O. and Dürig, U., Atomic structure of the α-Ga (001) surface investigated by scanning tunneling microscopy: Direct evidence for the existence of Ga 2 molecules in solid gallium, *Physical Review B*, 46, 11, (1992), 7319-7323.

Chapter IV

Combined Pauling Bond Valence-Modified Morse Potential (PBV-MMP) Model for Metals: Thermophysical Properties of Liquid Gallium

4.1 Abstract

The modeling of the basic properties liquid metals such as surface tension, viscosity, and self-diffusivity, is important for many applications and also for developing robust semi-empirical theories of matter. Here, we develop a new quasi-crystalline approach for estimating the thermodynamic and kinetic properties of liquid metals.

We use a combined Pauling Bond Valence-Modified Morse Potential (PBV-MMP) approach, in which the Pauling's classical relationship between bond-valence (BV) and bond-length (BL) is incorporated within a modified Morse-Potential (MMP) description of the potential energy of interaction between two metal atoms in the bulk in terms of the bond-valence, with the further assumption that these interactions are limited to the nearest neighbors with a coordination number n_{M} . This results in a semi-theoretical approach that only needs a thermodynamic parameter, namely, the M-M bond energy for a specified valence, readily obtained from metal cohesive energy, the energy needed to rip a sample apart into a gas of widely separated atoms, to provide a predictions of a number of properties of interest for liquid metals.

For the kinetic and diffusion steps, we utilize Eyring's transition-state theory framework that requires estimates of entropy and enthalpy of activation. For estimating the entropy changes for both thermodynamics and kinetic parameters, we use the "free volume" model of Eyring. The

resulting theory reliably predicts the various properties that agree with experimental results for the case of liquid gallium, and other liquid matels such as Cu, Al, and Na.

The PBV-MMP approach for *bulk metals* is in the spirit of the so-called Unity Bond Index-Quadratic Exponential Potential (UBI-QEP) of Shustorovich, which has been highly successful in predicting thermodynamics and kinetics of *metal surface* catalyzed reactions. There are, however, important differences between the PBV-MMP and the UBI-QEP approaches. Thus, the UBI-QEP model involves a "quadratic-exponential" potential energy model, a modified form of Morse potential, in terms of a "bond-index" that sums to unity. The PBV-MMP model, on the other hand invokes a modified Morse potential in terms of the well-accepted Pauling "bond valence" that sums over all its bonds to atomic valence, another well-accepted rule widely used in the modern bond valence theory to elucidate inorganic solid structures. Further, the UBI-QEP model is silent on the bond-valence (BV) bond-length (BL) relationship, being concerned mainly with the extrema, i.e., maximum and minimum on the energy landscape. On the other hand, the PBV-MMP model is able to predict the individual bond lengths and the bond valences along with bond energies, based on the Pauling BV-BL correlation.

4.2 Introduction

While *ab intio* methods can now provide detailed information on bond lengths (BL) and bond energies (BE) of crystals, and consequently the material properties resulting from these, the cluster size in these calculations is limited because of the significant computational effort involved with increasing size. For example, to model bulk surface properties, clusters used have to be as large as 560 atoms (Kleis et al., 2011). First-principles studies so far are limited to specific systems, and offer limited generalizations. On the other hand, semi-theoretical or phenomenological approaches such as the model developed here, involving heuristics or

empirical observations, e.g., the Evans-Polanyi or the Sabatier relations in catalysis (Boudart and Djéga-Mariadassou, 1984), incidentally confirmed in detailed DFT studies of metal catalysis (Nørskov et al., 2009), can facilitate learning and offer intuitive insights and important practical guidelines, in addition to providing important predictions with limited computational effort.

One of such model is the Pauling's bond valence (BV) method (Pauling, 1947; 1949; 1960; Morse, 1929), based on a set of rules or heuristic principles, that has proved highly useful in recent years in structure elucidation of ionic solids (Brown, 2009; Brown and Poeppelmeier, 2014). In its modern version, known simply as the "bond valence" (BV) method (Brown, 2009; Brown and Poeppelmeier, 2014; Brown, 2000), it is focused on the crystal structure of inorganic ionic solids, not on their energetics, or on crystal structure of metals or alloys. This chapter is concerned with the application and extension of the BV approach to structural as well as energetic considerations of metals, the latter by invoking a modified Morse potential (MMP) for two-center bond energy, and is hence called the PBV-MMP approach. Here, we illustrate its utility in estimating many useful properties of liquid metals, specifically for liquid gallium. Clearly, many extensions of the PBV-MMP theory presented here are possible, including to solid metals.

The BV method is based on a set heuristic principles, articulated by Pauling (Pauling, 1947; 1960, pp. 543; Brown, 2009; Morse, 1929), as governing the structure of ionic crystals, the more directly relevant of which to our development here are described below:

1. The bond length r_{ij} of the anion (*i*)-cation (*j*) in a solid crystal can be estimated by adding the radii of the two terminal ions, while the coordination number of the cation can be determined from the ratio of these two radii.

2. For each anion *i*, the sum of its electrostatic bond valences (BV) v_{ij} in bonds with cations *j* equals the charge number z_i of the anion. Further, Pauling assumed that the electrostatic bond valences for all bonds are equivalent, and given by $v_{ij} = z_j / n_j$, where z_j is the charge number of the cation and n_j is the coordination number of the cation. This rule, the so-called *electrostatic valence principle* or *valence sum rule*, is essentially a statement of *local charge balance*, or alternately that in each bond between a cation and an anion, the bond valence contributions by the two ions are equal. The estimation of average bond valence based on the coordination number further implies that interactions considered are limited to the *nearest neighbors*.
3. The final heuristic of great relevance here is the empirical correlation proposed by Pauling for metals (Pauling, 1947), and later adopted for ionic solids (Brown, 1994), namely, $r_{ij} \equiv r_{ij}^{\mathrm{I}} - b \ln v_{ij}$, where r_{ij} is the bond length for a bond of valence v_{ij}, r_{ij}^{I} being a model parameter which may be used viewed as the bond length for a (hypothetical) bond of unit valence, i.e., for $v_{ij} = 1$. The other parameter in this equation, $b \approx 0.26 - 0.6$ Å, with a common proposed value of $b = 0.37$ Å (Pauling and Kamb, 1986).

Some comments are needed on the terminology related to the various bond descriptors used in the literature. Thus, the terms "bond valence," "bond number," and "bond strength," signify basically the same descriptor v_{ij}, being the number of electrons each terminal atom contributes to a bond, i.e., the number of electron pairs that form the bond, which in crystal structures is not an integral but often a fractional number. On the other hand, "bond order," ϕ (Pauling, 1947), has a slightly different connotation for fractional bonds that are stabilized by resonance. For instance, the bond valence for C-C in benzene is $v = 1.5$ but the bond-order $\phi \approx 1.66$ as calculated from the

molecular orbital theory (Pauling, 1960). For integral bonds, however, $\phi = v$. Further, it is to be noted that the Pauling bond length correlation implies that for fractional bonds, $v_{ij} \leq 1,\ r_{ij} \geq r_{ij}^{\mathrm{I}}$, while for $v_{ij} \geq 1,\ r_{ij} \leq r_{ij}^{\mathrm{I}}$.

The above-described heuristic principles and correlations along with others proposed by Pauling (1947), also form the underpinnings of the modern bond valence (BV) model (Brown, 2009; 2013), supplemented with others derived from Graph theory, e.g., Kirchhoff laws. There is also available a large data set for the model parameters r_{ij}^{I} and b (Brese and O'Keeffe, 1991; iucr.org), allowing estimations of bond valences v_{ij} from experimentally observed bond lengths for a given crystal structure. This, in turn, has allowed experimentally determined structures of ionic solids to be validated against rules such as the valence sum rule. The modern bond valence theory has thus proved to be very successful in elucidating the chemical structure of inorganic solids (Brown, 2009; Brown and Poeppelmeier, 2014; Brown, 2000) as well as ion-diffusion paths (Adams and Swenson, 2000). However, it is unfortunately silent on the equally important question of describing bond energy Q_{ij}. Johnston and Parr (1963) had earlier proposed a simple empirical correlation between bond energy Q_{ij} and bond order, namely, $Q_{ij} = D_{ij}^{\mathrm{I}}\phi^{p}$, where p is nearly unity (e.g., Johnston and Parr (1963) provide $p = 0.81-1.09$), and the model parameter D_{ij}^{I} is the bond energy for unit bond order, i.e., when the bond order $\phi = 1$. This relation, coupled with Pauling BV-BL correlation, has, in fact, been successfully used in the bond energy-bond order (BEBO) methodology for gas-phase (Johnston, 1966) as well as for metal surface reactions (Weinberg, 1973; Miyazaki, 1980). The accuracy of the concept of bond-order conservation (BOC) inherent in the BEBO methodology was confirmed by Blowers and Masel (1998).

Clearly, however, the power-law BEBO correlation has its limitations (Shustorovich, 1986). For instance, it describes a monotonic *i-j* attractive interaction with no equilbrium distance, energy and no repulsive inreaction. Shustorovich (1986), consequently, replaced it by a modified two-center Morse potential termed quadratic-exponential potential (QEP), that includes both attractive and repulsive terms, in terms of a "bond index," that sums to unity, hence called unity bond index (UBI). Thus, Shustorovich's method is called the UBI-QEP method (Shustorovich and Sellers, 1998), as a generalization of his earlier bond-order conservation-Morse potential (BOC-MP) (Shustorovich, 1986). The UBI-QEP has proven to be highly successful in predicting step energies of metal surface-catalyzed reactions. The second key limitation of the modern bond valence method is that it has not so far been applied to metal crystal structures.

We address the first limitation by using a modified Morse potential for two-center potential energy in terms of bond valence after Benziger (1991; 1994), and we follow Pauling (1947) in addressing the second who argued for the use of the above listed heuristics being equally applicable to metals. Thus, Pauling (1947) contended that the metallic bond is closely related to the covalent (shared electron pair) bond, so that each atom in a metal may be considered as forming covalent bonds with the neighboring atoms, the number of covalent bonds resonating among the available interatomic positions about an atom, that vary from nearly 1 to nearly 6. In spirit, thus, our method is similar to the Shustorovich UBI-QEP approach (Shustorovich, 1986; Shustorovich and Sellers, 1998). The UBI-QEP method is based on many of the Pauling rules mentioned above, but diverges mainly on two counts: 1) it employs a "bond-index" rather than bond order to characterize the bond valence, which sums to unity over all bonds, and 2) it utilizes a modified Morse potential (Morse, 1929) for bond energy. However, it does not concern itself with stipulation of bond lengths or bond valences. Further, the Shustorovich approach has been

applied only to surface catalysis, not to properties of bulk metals. Our model described below is, thus, an amalgam of the Pauling and the Shustorovich approaches.

4.3 Model Development

4.3.1 Key Postulates

PBV-MMP model involves the following heuristics and assumptions (Morse, 1929; Pauling, 1947; 1960 pp. 543; Pauling and Kamb, 1986; Shustorovich, 1986; Benziger, 1991):

1. Interactions of a given atom *i* in a crystal structure are limited to its nearest n_i neighbors of atoms *j*, where n_i is the ligancy, or coordination number of *i*. The *average* coordination number of atom *i* is denoted as $\bar{n}_i$. For many cubic metal crystals, the average coordination number $\bar{n}_{\mathrm{M}} \approx 12$ (Pauling and Kamb, 1986) and assume to be the same for liquid metal.
2. The *atomic valence* V_i of the atom *i* is equal to the sum of individual *bond valences* v_{ij} of the atom *i* with surrounding *j* atoms plus any dangling or free bonds (or electrons) v_{iF},

$$V_i = \sum_{j=1}^{n_i} v_{ij} + v_{iF} \quad ; \quad V_j = \sum_{i=1}^{n_j} v_{ji} + v_{jF} \tag{4.1}$$

and similarly for atoms *j*.

This is the principle of bond valence conservation (BVC), or charge balance. Here, the valence V_i of an atom *i* is the conventional Lewis-Pauling valence, i.e., the average number of electrons an atom *i* uses for bonding, including the effect of any resonance. In simple compounds, it determines the stoichiometry. In our analysis, we allow for any unsaturated or dangling bonds v_{iF}, as at the metal surface, although it is assumed here that in the bulk metal $v_{iF} = 0$, except for very small metal clusters with a small number of

atoms. This is a key point of difference, besides the form of the MP, from the UBI-QEP method, in which the "bond-indices" x_{ij}, not defined unambiguously, sum to unity for every atom. Benziger (1991), on the other hand, took bond index to imply a normalized bond valence, i.e., $x_{ij} \equiv v_{ij}/V_i$, which is also the interpretation here.

3. Each of the terminal atoms contributes an equal numbers of electrons to their shared bond. Thus, the bond valence is also equal to the number of electron *pairs* that form a bond. It is further assumed that all bond valences v_{ij} are equal to the average bond valence $\bar{v}_{ij}$ as below, which means that the ligancy of the two atoms *i* and *j*, is in ratio of their valences. Thus if $v_{ij} \approx \bar{v}_{ij}$ then $\frac{n_i}{n_j} = \frac{V_i}{V_j}$ (Pauling and Kamb, 1986). The Pauling BV-BL relation may alternately be written in terms of "normalized bond valence" $x_{ij} \equiv v_{ij}/V_i$ (Benziger, 1991; 1994).
4. The Pauling BV-BL correlation between bond length r_{ij} (distance between the nuclei of two bonded atoms) and bond valence v_{ij} (vu) is assumed valid, which is typically written in the form $v_{ij} = \exp\left(-\frac{r_{ij} - r_{ij}^{\mathrm{I}}}{b}\right)$ where r_{ij}^{I} is bond parameter (Pauling and Kamb, 1986; Brese and O'keeffe, 1991) empirically determined and tabulated that denotes the hypothetical bond length for the case of unit bond valence, i.e., when the bond valence $v_{ij} = 1$, while the other empirical parameter b = 0.37Å, the common, albeit by no means universal value. The average bond length $\bar{r}_{ij}$ corresponds to the average valence $\bar{v}_{ij}$ of all bonds of an atom *i*.

We can also express the total atomic valence V_i in terms of a hypothetical internuclear distance r_{ij}^{o} *defined* by the following Pauling relation, i.e.,

$$V_i \equiv \exp\left(-\frac{r_{ij}^{o} - r_{ij}^{I}}{b}\right) \tag{4.2}$$

Combining these relations, thus, the normalized bond valence-bond length (NBV-BL) Pauling correlation may be written in the form

$$x_{ij} \equiv \frac{v_{ij}}{V_i} = \exp\left(-\frac{r_{ij} - r_{ij}^{o}}{b}\right) \tag{4.3}$$

where the characteristic BL r_{ij}^{o} is given by Eq. (4.3) for an assumed BV of V_i, i.e., it can be calculated given the parameters r_{ij}^{I} and b (Pauling and Kamb, 1986; Brown, 2009).

5. The total bond energy of an atom i is a sum of its bond energies of two-center i–j interactions, limited here to nearest neighbors,

$$Q_i = \sum_{j=1}^{n_i} Q_{ij} \tag{4.4}$$

6. Each two-center i–j interaction in the crystal, the bond energy of the i–j bond Q_{ij} is described by a modified Morse potential, as an extension of the power-law relation (Johnston and Parr, 1963), and by writing it in terms of bond valence rather than bond order, i.e., $Q_{ij} = D_{ij}^{I} v_{ij}^{p} = (D_{ij}^{I} V_i^{p}) x_{ij}^{p}$, where p is nearly unity, and the model parameter D_{ij}^{I} is the bond energy for a unit BV ($v_{ij} = 1$), or when the dimensionless bond valence $x_{ij} = 1/V_i$. Then, combining this with the Pauling correlation (Albe et al., 2002), the potential energy of interaction

$$-E_{ij} = Q_{ij} = D_{ij}^{I} v_{ij}^{p} = D_{ij}^{I} e^{-\left(\frac{r_{ij} - r_{ij}^{I}}{b/p}\right)} \tag{4.5}$$

where $a \equiv b/p \approx b$.

This relation has been used with good outcome in a number of studies based on the so-called bond-energy bond-order (BEBO) method (Johnston and Parr, 1963; Johnston, 1966; Weinberg, 1973). However, as mentioned above, this correlation includes only an attractive term. In addition, we need a repulsive term for a suitable potential function. Thus, taking cue from Benziger (1991), we propose the following modified form of Morse potential (MP) for the potential energy of interaction E_{ij} of a metal atom M_i to another M_j, written in terms of the normalized bond valence

$$-E_{ij} = Q_{ij} = D_{ij}^{o}(2x_{ij} - x_{ij}^{2}) \tag{4.6}$$

where the characteristic bond dissociation energy D_{ij}^{o} is *defined* in terms of a reference bond energy D_{ij}^{v} (usual form in metals) corresponding to a *reference* bond of valence v_{ij}^{v}

$$D_{ij}^{o} \equiv \left\{ \frac{D_{ij}^{v}}{x_{ij}^{v}(2 - x_{ij}^{v})} \right\} \tag{4.7}$$

where for the *reference* bond, the bond valence, $v_{ij} = v_{ij}^{v}$, or the normalized bond valence $x_{ij}^{v} = v_{ij}^{v}/V_i$, and the internuclear distance $r_{ij} = r_{ij}^{v}$, when $Q_{ij} = D_{ij}^{v}$, the two-center binding energy, obtained, e.g., from spectroscopic experiments (e.g., Himmel and Garetner, 2004). This is distinct from Shustorovich's quadratic exponential potential (QEP), in which the unity "bond-index" *x* remains unspecified in its relationship to bond valence. Using $x_{ij} \equiv v_{ij}/V_i$ the alternate form of MP in terms of bond valence

$$-E_{ij} = Q_{ij} = D_{ij}^{o}\left\{ 2\left(\frac{v_{ij}}{V_i}\right) - \left(\frac{v_{ij}}{V_i}\right)^{2} \right\} \tag{4.8}$$

This is similar to the modification to the Morse potential suggested by Benziger (1991). However, additionally we have related the bond energy Morse parameter D_{ij}^{o} to a reference bond energy and valence, in turn related through the Pauling BV-BL relation to a reference internuclear radius r_{ij}^{v}.

As an example, if we were to take the reference valence $v_{ij}^{v}=1$, i.e., unit valence as in Pauling relation, when $r_{ij}^{v}=r_{ij}^{I}$, $D_{ij}^{v}=D_{ij}^{I}$. Thus, the normalized bond valence $x_{ij}^{v}=1/V_i$, so that an alternate form of the MMP is obtained by using the Pauling relation for v_{ij}

$$-E_{ij}=Q_{ij}=D_{ij}^{I}\left(\frac{V_i^2}{2V_i-1}\right)\left\{\frac{2}{V_i}e^{-\left(\frac{r_{ij}-r_{ij}^{I}}{b}\right)}-\frac{1}{V_i^2}e^{-2\left(\frac{r_{ij}-r_{ij}^{I}}{b}\right)}\right\} \tag{4.9}$$

which would be the analog of the Johnston relation, Eq. (4.5). The modified Morse potential model adopted here, thus, is well behaved, and provides results similar to those from Pauling/Johnston relation, Eq. (4.5). It is further assumed that the Morse model parameters remain the same for both isolated *i–j* bond, and each additive contribution in multiple bonds in a condensed phase, solid or liquid.

Finally, the conventional MP form is obtained by combining Eq. (4.3) and (4.6)

$$-E_{ij}=D_{ij}^{o}\left\{2e^{-\left(\frac{r_{ij}-r_{ij}^{o}}{b}\right)}-e^{-2\left(\frac{r_{ij}-r_{ij}^{o}}{b}\right)}\right\} \tag{4.10}$$

where the MP bond dissociation energy D_{ij}^{o} (that if bond valence were indeed = V_i) is given by Eq. (4.7), and the characteristic internuclear distance r_{ij}^{o} is given by Eq. (4.2).

The advantage of the proposed MMP form, thus, rather than those proposed by Shustorovich (1986) or Benziger (1991), albeit a bit more complex, is that it incorporates the Pauling BV-BL

relation, so that the MP parameters in this, D_{ij}^{I}, r_{ij}^{I}, and *b*, are the same here as in the Pauling relation, many of which are available in the literature (e.g., Pauling, 1960, pp. 403; Pauling and Kamb, 1986; Brown 2009). The UBI-QEP method of Shustorovich (1986) also does not explicitly treat the bonding capacity V_i of the atoms, and he further assumes that the bond indices, not explicitly defined or related to bond valence, simply sum to unity. Van Santen (1990) has pointed out that conservation of bond index to unity is equivalent to normalization of the weighing functions within the valence bond theory. Also the MP parameters in his model are not provided or used by Shustorovich (1986), as his method deals only with stationary points, minima and maxima, of the potential energy surface. For this, only the thermodynamic data (bond energies) are needed.

4.3.2 Metal Bond Energy Using PBV-MMP Model Approach

The total energy of dissociation of *all* bonds in the metal cluster, or cohesive energy, i.e., the energy needed to rip a metal sample of *n* atoms apart into a gas of widely separated *n* atoms, i.e., for the process $\mathrm{M}_n(s) \leftrightarrows n\mathrm{M}(g)$ for which

$$\begin{aligned} Q_t &= \sum_i^{n_\mathrm{M}} \sum_j^{n_\mathrm{M}} Q_{\mathrm{M}_i \cdot \mathrm{M}_j} = \frac{1}{2} n \sum_j^{n_\mathrm{M}} Q_{\mathrm{M}_i \cdot \mathrm{M}_j} = \frac{1}{2} n Q_{\mathrm{M} \cdot \mathrm{M}_{n_\mathrm{M}}} \\ &= n\Delta H_{coh}^{\mathrm{o}} = nH_{f,\mathrm{M}(g)}^{\mathrm{o}} - H_{f,\mathrm{M}_n(s)}^{\mathrm{o}} \end{aligned} \tag{4.11}$$

where $Q_{\mathrm{M} \cdot \mathrm{M}_{n_\mathrm{M}}}$ is the total binding energy between a metal atom and its n_M nearest neighbors.

In this formula the factor of ½ is due to the fact that each pair of interactions between two given atoms *i* and *j* should be counted only once. The sum over neighboring atoms *j* is limited by the range of the cutoff for $Q_{\mathrm{M}_i \cdot \mathrm{M}_j}$, which is generally one to four neighbor shells in the perfect crystal. In other words

$$\Delta H^{o}_{coh} = \frac{1}{2} Q_{\mathrm{M{\cdot}M}_{n_\mathrm{M}}} \tag{4.12}$$

Let us obtain some basic PBV-MMP model results for these based on the above listed assumptions for the case of unit bond valence as reference. Combining Eq. (4.2) and (4.4), the total binding energy between a given metal atom M_i and its n_M nearest neighbors

$$Q_{\mathrm{M{\cdot}M}_{n_\mathrm{M}}} = D^{o}_{\mathrm{M{\cdot}M}} \sum_{j=1}^{n_\mathrm{M}} (2x_{ij} - x_{ij}^2) = 2\Delta H^{o}_{coh} \tag{4.13}$$

where for the case of unit valence, recall $D^{o}_{\mathrm{M{\cdot}M}} = D^{1}_{\mathrm{M{\cdot}M}} V_\mathrm{M}^2 / (2V_\mathrm{M} - 1)$. Here V_M is the metal valence, and n_M = its ligancy, or coordination number. In this, and in much of what follows, within the bulk metal it is assumed that there are *no dangling bonds*, i.e., $v_{\mathrm{M}F} = 0$. Given a solid structure and experimental bond lengths r_{ij}, which are well-known for many pure metals, this may be used to relate $D^{o}_{\mathrm{M{\cdot}M}}$ to the enthalpy of cohesion ΔH^{o}_{coh} or atomization ΔH^{o}_{atom}, i.e., the heat of sublimation ΔH^{o}_{sub} for a solid or the heat of vaporization ΔH^{o}_{v} for a liquid metal, respectively.

In case the experimental bond lengths r_{ij} are not available, we may make the additional assumption that the fractional bond-valence of a metal atom (Pauling and Kamb, 1986), based on the assumption of equal bond lengths with all nearest neighbors, are all approximately the same,

$$x_{ij} \approx \bar{x}_{ij} = \frac{1}{n_\mathrm{M}} \tag{4.14}$$

For example, Ni has metal valence V_M = 6, and its ligancy n_M = 12 (cubic closest packing, the A1 structure) for bulk metal, so that $v_{ij} = \bar{v}_{ij} = V_\mathrm{M} / n_\mathrm{M}$ = ½ for all its bonds, and $x_{ij} = \bar{x}_{ij} = v_{ij} / V_M$ = 1/12. This assumption is clearly not true, but is adequate for many purposes.

Combining the last two equations, thus,

$$Q_{\mathrm{M}\cdot\mathrm{M}_{n_\mathrm{M}}} \approx D^{\mathrm{o}}_{\mathrm{M}\cdot\mathrm{M}}\left(2-\frac{1}{n_\mathrm{M}}\right)=2\Delta H^{\mathrm{o}}_{coh} \tag{4.15}$$

The alternative to using the proposed modified Morse (quadratic) potential is to simply use the power-law potential of Pauling and Johnston $Q_{\mathrm{M}\cdot\mathrm{M}_{n_\mathrm{M}}} = D^{\mathrm{I}}_{\mathrm{M}\cdot\mathrm{M}} V_\mathrm{M}^{p} n_\mathrm{M}^{1-p} = 2\Delta H^{\mathrm{o}}_{coh}$. This is thus an approximate relation for cohesive energy or heat of atomization of a condensed phase, solid or liquid. It is of the form of the Shustorovich model (1986) developed for a metal surface catalysis. Note that when Eq. (4.14), (4.15) and (4.7) are combined, it results $D^{v}_{\mathrm{M}\cdot\mathrm{M}} = (2/n_\mathrm{M})\Delta H^{\mathrm{o}}_{v}$ (Conway and Bockris 1957).

Thus, the characteristic binding energy for unit bond valence $D^{\mathrm{o}}_{\mathrm{M}\cdot\mathrm{M}}$ may be estimated from Eq. (4.15) given experimental heats of sublimation of vaporization, which are well-known for all metals (Kittel, 1986), as are the crystal structures, namely, r_{ij} and n_M (Donohue, 1974), and other relevant model parameters (Pauling and Kamb, 1986). Consequently, we can readily estimate the MP energy parameter $D^{\mathrm{o}}_{\mathrm{M}\cdot\mathrm{M}}$ for any metal of interest. Once this information is available, many properties based on binding energy can be calculated, as illustrated below for the example of Ga, along with a few other metals .

Alternatively, if DFT estimates of bond energies and bond lengths are available, as they now are for finite but large nanoclusters, although not necessarily for bulk metals, these can be used to test the efficacy of the model, as done below, or predict energetic parameters.

4.4 Gallium PBV-MMP Model Parameters

As discussed in chapter III solid Ga has an unique structure that contains 8 atoms in one unit cell and each Ga has 7 nearest neighbors (Gong et al., 1991; Donohue, 1974) one at 2.44 Å, two at

2.71 Å, two at 2.74 Å, and two at 2.81 Å. The density of liquid gallium versus temperature is $\rho_{\mathrm{M}} = 6077 - 0.611(T - 302.914\,\mathrm{K})\ \mathrm{kg/m}^3$ provided by (Assael et al., 2012).

4.4.1 Metal Bond Energy Using PBV-MMP Approach

Let us use Eq. (4.15) to investigate the energetics for Ga. Using the NIST data for Ga, $\Delta H^{\mathrm{o}}_{coh} = \Delta H^{\mathrm{o}}_{sub} = 271.96$ kJ/mol (cohesive energy/atom = 2.82 eV/atom), $\Delta H^{\mathrm{o}}_{fusion} = 5.58$ kJ/mol, and $\Delta H^{\mathrm{o}}_{v} = 266.38$ kJ/mol and $n_{\mathrm{M}} = 7$ (Gong et al., 1991). However, an oft-quoted value in the literature is $\Delta H^{\mathrm{o}}_{v} = 256$ kJ/mol (e.g., Wikpedia). From this we can calculate the bond dissociation energy of gallium dimer in the *gas phase* of $D^{v}_{\mathrm{Ga\text{-}Ga}}(g) = 112$ kJ/mol for $H^{\mathrm{o}}_{f,\mathrm{Ga}}(g) = 271.96$ kJ/mol. This provides one estimate of the reference bond energy.

Further, using the approximate expression for equal bond lengths and valences, Eq. (4.15) provides for Ga $D^{\mathrm{I}}_{\mathrm{M\text{-}M}}(s) = 141.8$ kJ/mol for solid phase Ga and $D^{\mathrm{I}}_{\mathrm{M\text{-}M}}(l) = 138.8$ kJ/mol for liquid phase Ga. This assumes that n_{M} remains unchanged upon melting. Alternatively, one may assume that $D^{\mathrm{I}}_{\mathrm{M\text{-}M}}$ remains unchanged. Then the coordination number may be assumed to change from $n_{\mathrm{M}} = 7$ in the solid phase to $n_{\mathrm{M}} = 6.6$ in the liquid phase upon melting. Alternatively, we may use the complete expression, Eq. (4.13), based on the known bond lengths and the corresponding bond valences calculated as above. This provides for Ga $D^{\mathrm{I}}_{\mathrm{M\text{-}M}}(s) = 143.6$ kJ/mol for solid phase Ga and $D^{\mathrm{I}}_{\mathrm{M\text{-}M}}(l) = 140.3$ kJ/mol for liquid Ga. These values compare with the experimental BDE of the gas-phase dimer molecule $D^{v}_{\mathrm{M\text{-}M}} = 145$ kJ/mol (or 1.50 eV/atom) (Froben and Schulze, 1983; Himmel and Gaertner, 2004; Song and Cao, 2005). Thus, it appears that for Ga, $D^{v}_{\mathrm{M\text{-}M}} = D^{\mathrm{I}}_{\mathrm{M\text{-}M}}$, i.e., the dimer molecule is likely to have a bond of unit valence along with unbound electrons. Consequently, we will adopt this independently determined value of $D^{v}_{\mathrm{M\text{-}M}} = D^{\mathrm{I}}_{\mathrm{M\text{-}M}} = 145$ kJ/mol (or 1.50 eV/atom) based on a characterization of the dimer molecule via

Raman and UV/Vis spectroscopy and fitting the data to Morse potential (Himmel and Gaertner, 2004). It is, in fact, remarkable that the unit valence bond dissociation energy of the dimer molecule in the solid phase calculated via the metal cohesive energy is so similar to that of the gas-phase dimer molecule. This provides some reassurance that the Morse potential energetic parameters obtained for gas-phase species are also applicable to the condensed phase, as assumed in this approach (Girifalco and Weizer, 1959).

A comparison of the Pauling-Johnston power-law relation, Eq. (4.6) and the corresponding modified Morse potential correlation proposed here, Eq. (4.11), both for the same set of above parameters as above for Ga is shown in Figure 4.1. It is clear that with a fitted power-law exponent p = 0.9 (in the neighborhood of unity), the two correlations provide bond energies that are very close to each other in the range of bond lengths of interest.

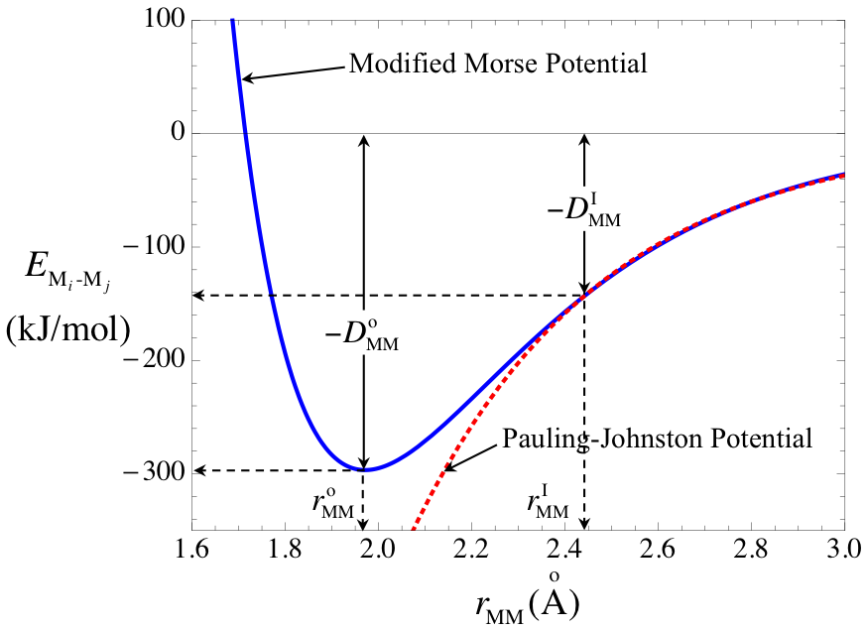

Figure 4.1 A comparison the Pauling-Johnston power-law relation, Eq. (4.5) and the modified Morse correlation proposed here, Eq. (4.4), for the above parameters for Ga, i.e., $D^{I}_{M\cdot M}(s) = 143.6$ kJ/mol, V_M = 3.55, $b = 0.37$ Å and $r^{I}_{ij} = 2.44$ Å , and a fitted p = 0.9.

4.4.2 Comparison of Modified Morse Potential with DFT Results for Small Ga Crystals ($n \leq 26$)

Metal clusters with a small number of metal atoms behave differently from bulk metal (Roduner, 2006), in that the structure and bond valences and lengths can be different from those in the bulk crystal, along with the possibility of dangling bonds, especially for a rather small number n of atoms in the cluster. Gallium clusters have, in fact, been investigated via DFT for sizes up to n = 26 atoms (Song and Cao, 2005; Drebov et al., 2011; Tonner and Gaston, 2014), and these studies are used to confirm the applicability of the above potential model.

We apply Eq. (4.15) to calculate the cohesive energy of a cluster with n atoms, i.e., the total cluster energy per atom, based on the assumption, as above for bulk metal, that above a critical size of cluster, $x_{ij} \approx \bar{x}_{ij} = 1/n_{\mathrm{M}}$. Above this threshold this implies that there are no dangling bonds. Below this size, the cluster is more molecule-like rather than as a bulk metal, with the possibility of unbound electrons or dangling bonds.

A key descriptor in our model, Eq. (4.15), is the coordination number, i.e., the number of bonds per metal atom, $n_{\mathrm{M}} = n_{\mathrm{B}}/n$, where n_{B} is the number of bonds in a cluster of n metal atoms. Recall that for bulk Ga, $n_{\mathrm{M}} = 7$. However, this number is approached only for quite large number of atoms, perhaps $n \geq 200$, as indicated by the cluster melting point versus size (Pyfer et al., 2014). For smaller number of atoms, this ratio is quite small and rises only very gradually with n. This is evident e.g., in examples of minimal energy cluster structures obtained via DFT as shown in Figure 4.2 (Song and Cao, 2005).

Song and Cao (2005) further noted that there is a pattern to these clusters. Thus, above a critical n in the range investigated (n = 2 – 26), the lowest energy strictures of Ga_n can be obtained by simply capping an atom on the structure of the smaller Ga_{n-1} minimal energy structure, with an additional 3 to 4 bonds. Thus, we find that the number of bonds in a cluster (Song and Cao,

2005) of size $n > 5$ may be roughly estimated by the simple empirical formula: $n_B \approx 6 + 4(n-5)$, so that the number of bonds per atom for size $n > 5$ may be approximated by $n_M \approx \{6 + 4(n-5)\}/n$.

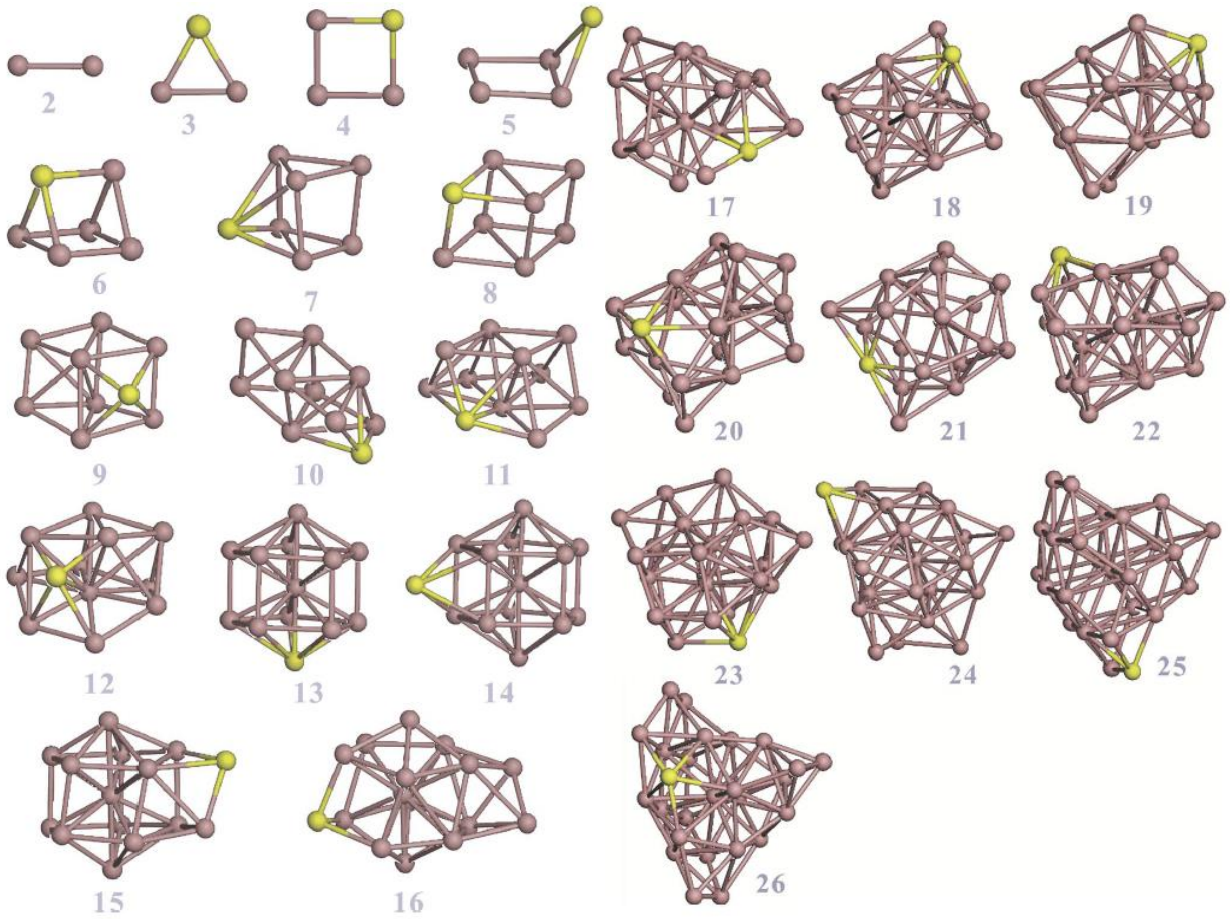

Figure 4.2 Lowest energy cluster structures for Ga for different size (Song and Cao, 2005).

Using this in Eq. (4.15) along with their DFT estimate of $D^{I}_{M\cdot M}$=1.59 eV/atom (153 kJ/mol) for the Ga_2 dimer (Song and Cao, 2005), assuming unit valence for the dimer, and an atomic valence of 3, appropriate for molecular rather than bulk metal (4.55) gallium, as clusters lie somewhere in between molecules and bulk metals, thus, we can estimate the cohesive energy, as shown in Figure 4.2. It is seen that for size $n > 5$ it agrees well, without any fitted parameters, with the DFT calculations of Song and Cao (2005). Further, for much larger clusters ($n_M = 7$), our model

predicts ΔH_{coh}^{o} = 256 kJ/mol for a valence V_M = 3, in reasonable agreement with experimental value of 272 kJ/mol. On the other hand, for V_M = 3.55, the prediction is ΔH_{coh}^{o} = 294 kJ/mol. Thus, the DFT estimate of $D_{M\cdot M}^{I}$=1.59 eV/atom (153 kJ/mol) is perhaps a bit on the high side. However, for the experimental value $D_{M\cdot M}^{I}$=1.5 eV/atom (144.7 kJ/mol) (Froben and Schulze, 1983; Himmel and Gaertner, 2004; Song and Cao, 2005), the predicted ΔH_{coh}^{o} = 278 kJ/mol.

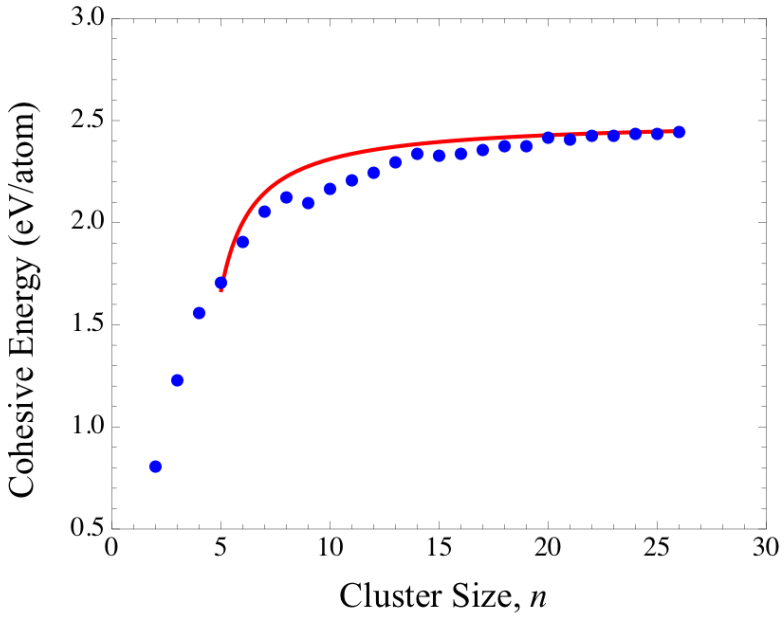

Figure 4.3 A comparison of prediction of modified Morse potential versus DFT for cohesive energy versus cluster size for Ga (Song and Cao, 2005).

Of course, for smaller crystals (n < 5) that are rather molecular in nature, it is no longer adequate to assume that there are no dangling bonds, and so the bond valence conservation to V_M included in Eq. (4.15) is no longer applicable. Without an estimate of the bond valence available for these smaller clusters, not provided by Song and Cao (2005), thus the applicability of the modified Morse potential suggested here cannot be ascertained.

This comparison of the predictions (Figure 4.3) of Eq. (4.15) with DFT estimates for the lowest energy cluster structures (Figure 4.3), provides further confidence in the robustness of the

proposed modified Morse potential model for bulk metal, along with support for the fact that the assumptions listed above in arriving at the above simplified formula, including valence conservation and average valence, appear to be adequate even for very small clusters.

4.5 Vapor Pressure

For estimating the entropy changes for both thermodynamics and kinetic (viscosity and self-diffusion) parameters, e.g., in Eyring's transition-state theory framework, we will use the "free volume" model of Eyring, within with an atom is free to move about, thus determining its entropy (Frank, 1945a; 1945b; Frank and Evans, 1945; Cohen and Turnbull, 1959). Therefore, let us first consider how one might estimate the free volume for a condensed phase.

Within this framework, the liquid phase is treated as if its molecules (or atoms in a liquid metal) were free to move around within its cage of "free" volume v_f in an average potential field because of its neighbors. Then, the partition function of a molecule in a liquid (Eyring and Hirschfelder, 1937; Glasstone et al., 1941, p. 478)

$$F_l = \left(\frac{v_f}{\lambda_t^3}\right) b_l \exp\left(-\frac{E_0}{RT}\right) \tag{4.16}$$

where the first term on the RHS is the translational contribution of a single molecule moving in its free volume v_f. Further, b_l is the combined vibrational and rotational contribution, and E_0 is the difference in energy per mole between molecules in the liquid and those in the gas at 0 ºK. In the above, the thermal wave-length is given by (see also the corresponding entropy for an ideal monatomic gas as given by the Sackur-Tetrode equation in Atkins and de Paula, 2002, p 650)

$$\lambda_t = \frac{h}{\sqrt{2\pi m k_B T}} \tag{4.17}$$

4.5.1 Atomic Free Volume in a Condensed Phase

The molecular or atomic free volume $v_f \equiv v_l - v_0$ where v_0 is the molecular volume at absolute zero (when there is no translation). The "accessible volume," or "free volume," of a crystal is that accessible to a mobile atom, the accessible volume fraction being the ratio of the accessible volume to the total volume of the crystal (Brown, 2009). Let us relate the free volume v_f of a molecule or atom in a liquid to the volume of liquid per molecule or atom, i.e., $v_f = \beta v_l$, where $v_l = \tilde{V}_l / N_{Av}$, and $\tilde{V}_l$ is volume of a mole of the liquid. Consider a *simple cubic* packing, for which number of atoms in a unit cell $N_M = 1$ for example, with one atom (pink) oscillating about its origin and its $n_M = 6$ nearest neighbors assumed fixed at their lattice positions along the 3 axes, one of which is shown in Figure 4.4, where d is incompressible diameter of the atom. However if consider liquid as fcc structure and its $n_M = 12$ nearest neighbors.

To simplify the model we assume liquid as simple structure which gives $l = v_l^{1/3}$. The distance that the central (pink) atom/molecule is free to move along the shown axis $2l - 2d = 2v_l^{1/3} - 2d$. Thus, the free volume per molecule or atom

$$v_f \equiv v_l - v_0 = (2v_l^{1/3} - 2d)^3 = 2^3(v_l^{1/3} - d)^3 \tag{4.18}$$

where v_0 is the van der Waals volume of the molecule, the molar free volume $v_f = \tilde{V}_f / N_{Av}$.

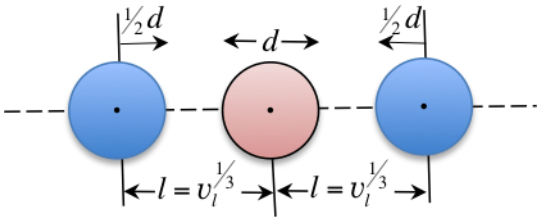

Figure 4.4 Estimation of free volume for an atom from its volume inhabited and exclusion diameter d (Glasstone et al., 1941, p. 478).

More accurately (Frank, 1945b), a fluctuation factor f should be included, i.e., $v_f = \tilde{V}_f / N_{Av} f$, which accounts for encroachment of other atoms/molecules in each others free volume. The inhabited volume of an atom may be estimated accurately from its density

$$v_l = \frac{v_{cell}}{N_{\mathrm{M}}} = \frac{AW_{\mathrm{M}}}{N_{Av}\rho_{\mathrm{M}}} \tag{4.19}$$

where N_{M} is the total number of atoms in a unit cell. Thus, N_{M}= 1 + 3 = 4 atoms/cell of fcc crystal, N_{M} = 2 in bcc crystal, and N_{M} = 1 in a simple cubic crystal. The maximum free volume available to an atom $v_{void} = v_l(1-\varepsilon_{PF})$ where ε_{PF} is the volumetric packing fraction. For bcc, ε_{PF} = 0.68, for fcc, ε_{PF} = 0.74, and for simple cubic, ε_{PF} = 0.52.

For estimating free volume, we must further subtract the volume of the mobile atom from the void volume using Eq. (4.18). In the case of a pure metal (self diffusion) the solute atom is the same size as the host atom, so that the free volume

$$v_f \approx \kappa\left\{\left(\frac{AW_{\mathrm{M}}}{N_{Av}\rho_{\mathrm{M}}}\right) - 2\left(\frac{\pi d_{\mathrm{M}}^3}{6}\right)\right\} \tag{4.20}$$

which needs only density and atomic diameter to compute the free volume, in addition to the factor κ, which accounts for further restriction of the percolation volume because of steric and electronic reasons. Thus, the actual accessible volume for percolation by an atom would be even lower, perhaps half as much or lower, than the term within brackets on the right of the above expressions because this includes nooks and crannies that an atom cannot access, i.e., because of steric reasons. In addition, the accessible volume is likely further limited by electronic reasons, or by the sum of bond valence changes as an atom moves within the matrix, binding with the neighboring atoms, especially for solutes with ionic character (Adams and Swenson, 2000). These authors estimated that $v_f \approx 8\%$ of the crystal volume for ion conduction. As a rough order

of magnitude estimate, thus, we may take κ = 1/3 – 1/10. Further, they (Adams and Swenson, 2000) found that the activation energy and the ion conductivity were both linear functions of $v_f^{1/3}$, as discussed further later on in connection with the free-volume theory of Eyring.

In other words, in molar units

$$\tilde{V}_f = \beta \tilde{V}_l \tag{4.21}$$

and

$$\beta = \kappa \left\{ 1 - \frac{N_{Av}}{\tilde{V}_l} \left(\frac{\pi d_{\mathrm{M}}^3}{3} \right) \right\} \tag{4.22}$$

Testing many different solids (Frank, 1945a) and liquids (Frank, 1945b), Frank estimated that the free volume is ~0.5% of the condensed phase (solid or liquid) volume, i.e., $\beta = \tilde{V}_f / \tilde{V}_l \approx 0.5\%$.

4.5.2 Vapor Pressure of a Liquid

As an example of the use of these relations, consider a liquid in contact with its vapor. Then, the change in entropy for vaporization proposed by Frank (1945a)

$$\Delta S = S_g - S_l = R \ln \left(\frac{\tilde{V}_g}{\omega \tilde{V}_{f,l}} \right) \tag{4.23}$$

where ω is a correction factor, here assumed 1. For an *equilibrium* $\Delta G_v = 0 = \Delta H_v - T \Delta S_v$ and $\tilde{V}_g = RT / p_v$, so that the vapor pressure of the liquid

$$p_v = \frac{RT}{\beta \tilde{V}_l} \exp \left(- \frac{\Delta H_v}{RT} \right) \tag{4.24}$$

where for β we use the molar form, Eq. (4.21).

As an example, the Ga vapor pressure may be evaluated via Eq. (4.24), where for Ga, $\Delta H_v = 256$ kJ/mol. Further, in Eq. (4.21) both β and $\tilde{V}_l$ are functions of temperature through density and

the coefficient of thermal expansion, and are left as such. To be able to calculate β from Eq. (4.21), we need to first get κ and v_f. Eq. (4.24) is combined with Eq. (4.20)

$$p_v = \frac{RT}{\kappa\left\{\left(\frac{AW_{\mathrm{M}}}{\rho_{\mathrm{M}}}\right) - 2N_{Av}\left(\frac{\pi d_{\mathrm{M}}^3}{6}\right)\right\}} \exp\left(-\frac{\Delta H_v}{RT}\right) \tag{4.25}$$

Compare experimental vapor pressure data with calculated value from Eq. (4.25) provides an excellent source to avoid arbitrarily assuming κ value. Theoretical predictions and experimental results (Geiger et al., 1987) for vapor pressure are compared in Figure 4.5 for Ga.

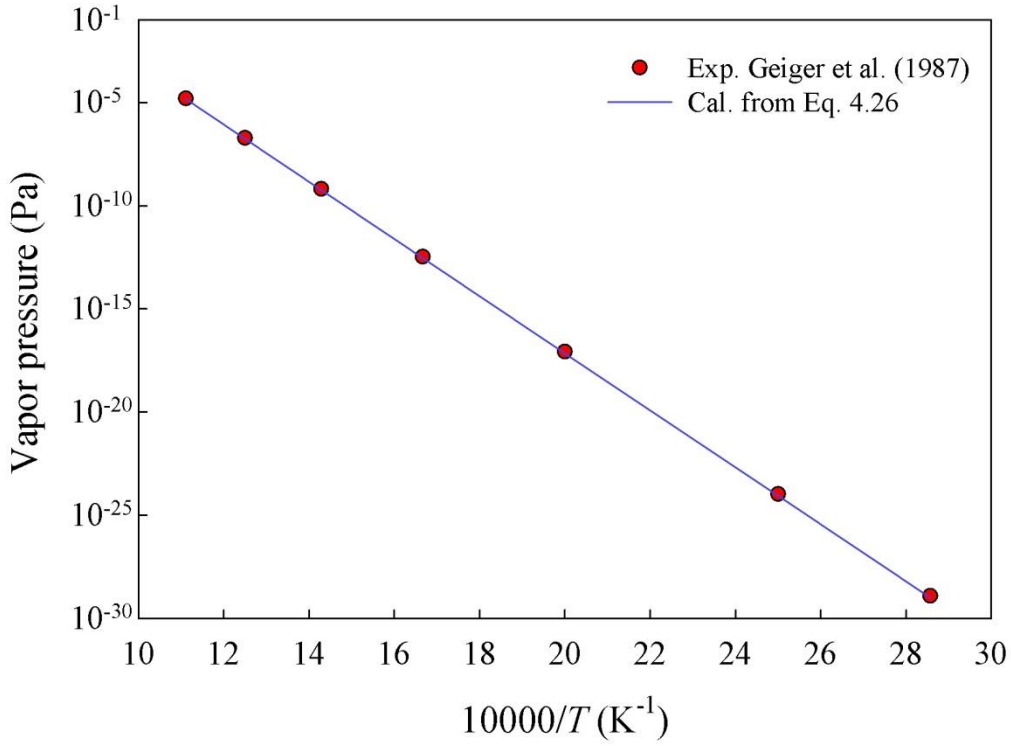

Figure 4.5 Prediction of Ga vapor pressure versus experimental data, κ = 1/9 (Geiger et al., 1987).

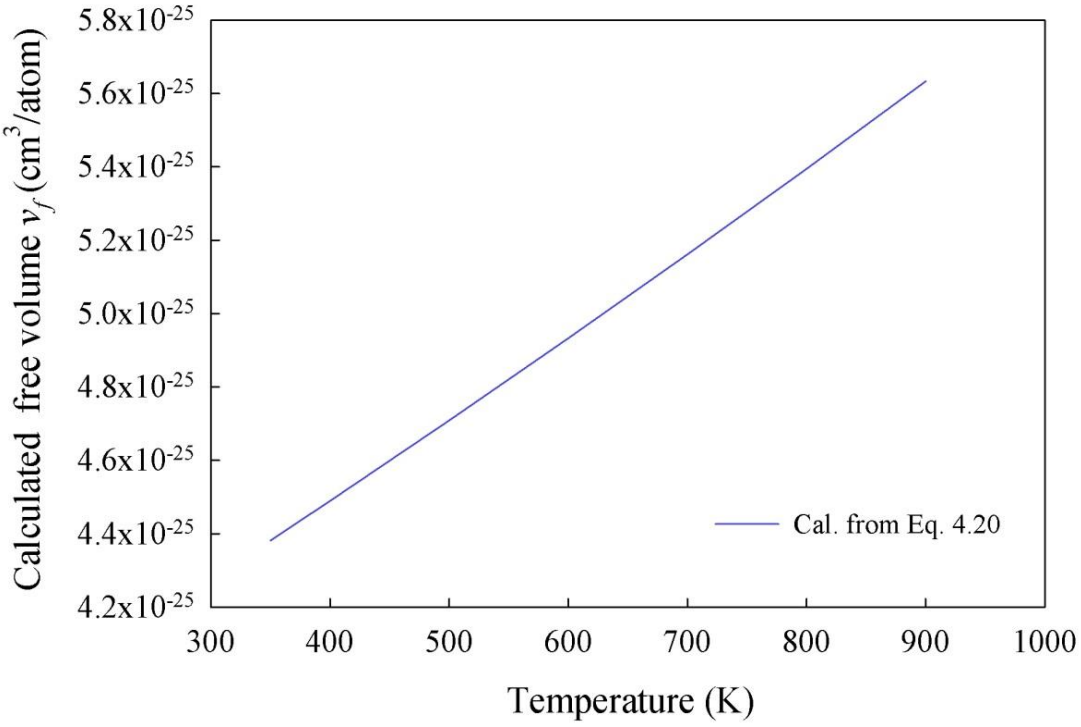

Figure 4.6 Calculated free volume of liquid Ga from Eq. (4.20) versus temperature.

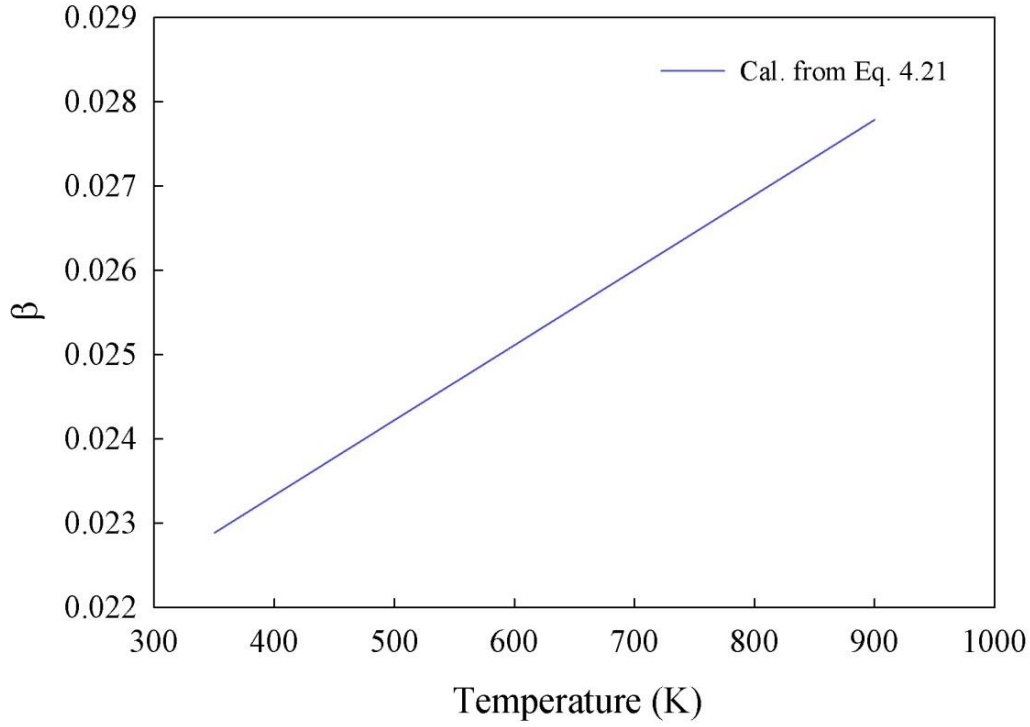

Figure 4.7 Parameter β for Ga calculated from Eq. (4.21) versus temperature.

The calculated vapor pressure using κ = 1/9 fits experimental well as shown in Figure 4.5, however, this method does not apply to all the liquid metals. Liquid metals covered with a thin oxide layer on metal surface or other impurity source may interfer with the experimental results if not carefully remove before the experiments. Using fitted κ value now we can calculate v_f with Eq. (4.20) and β with Eq. (4.21) as shown in Figure 4.6 and 4.7. Thus, it is seen as predicted that it increases linearly with temperature.

4.6 Viscosity & Self-Diffusion Coefficient in Liquid Metals

Liquid metals are monoatomic and thus their properties are simpler to comprehend and model. Various approaches used for modeling diffusion in liquid metals are (Protopapas et al., 1973): 1) those based on some atomic level model of the structure of the liquid state as well as that of the diffusion mechanism; 2) those based on the thermodynamic corresponding states principle (Prakash et al., 2004), rather than on a physical model; and 3) those based on the molecular dynamics (MD) approach. Here we are concerned with only the first approach. Further, a lot of the literature is concerned with self-diffusion of a metal (tagged atoms) or with the diffusion of another metal as the solute

The structure/mechanism based models of diffusion in liquid metals include (Protopapas et al., 1973): 1) the jump-diffusion model of Eyring and coworkers, which imagines a jump of a solute atom or molecule over an activation energy barrier from one equilibrium position to a neighboring vacant lattice site (hole) in the liquid. There are very similar models for the viscosity coefficient as well; 2) the significant structure theory of Eyring and coworkers, 3) the Stokes-Einstein approach provides a relation between diffusion- and viscosity-coefficient. This is based on assuming that the solute is translating through a continuum fluid described by hydrodynamic equations; 4) hard sphere model of the liquid (Itami and Sugimura, 1995) based on Enskog

theory, in which the solute undergoes a series of hard core binary collisions with its neighbors, and that the successive binary collisions are uncorrelated with each other; 5) the theory of Parlee and coworkers (Protopapas et al., 1973), which extends the theory of Enskog by using correction factors from MD calculations; 6) other examples of such an approach include the fluctuation theory of Swalin (Swalin, 1968); 7) the vibrational atom motion theory of Nachtrieb (Nachtrieb, 1967); 8) the free volume theory of Cohen and Turnbull (Cohen and Turnbull, 1959). A further critical discussion of the different modeling approaches is provided by Nachtrieb (1967).

4.6.1 The Hole Theory of Eyring for Liquid Transport

The activated-state model of Eyring for a liquid is based on a quasi-crystalline model of the liquid phase, with molecule-sized holes playing a part akin to vacancies in solid diffusion. Both viscosity and diffusion coefficient can be treated in an interrelated manner in this way (Glasstone et al., 1941, Ch IX). The model is based on certain aspects of the liquid state. Just as gas is considered as molecules moving about in an empty space, a liquid may be considered as composed of holes moving about in a lattice. Thus the hole theory for liquid diffusion postulates the existence of molecule size vacancies in the liquid and that liquid diffusion occurs via a mechanism similar to the vacancy mechanism for solid diffusion. Of course, these vacancies must first be created in a solid for vacancy diffusion.

The viscosity η and diffusion coefficient D are interrelated through the Stokes-Einstein relation based on hydrodynamics, i.e.,

$$D = \left(\frac{k_B T}{3\pi d_A} \right) \frac{1}{\eta} \tag{4.26}$$

where d_A is solute molecule diameter. Therefore, we follow Glasstone et al. (1941, Ch IX) in first considering treatment of the theory of liquid metal viscosity before taking on diffusion.

Consider layers of molecules in a pure liquid a distance δ_1 apart as shown in Figure 4.8 (Bird, et al. 2007, p29), and suppose that one slides past the other in the *x*-direction under the influence of a shear stress τ_{yx}. As per the Eyring theory, an atom in the top layer jumps to an adjacent vacancy.

The motion of one layer over the other is assumed to involve passage of a molecule from one equilibrium position to another in the same layer. For this, a suitable hole, or lattice vacancy, must be available, which requires expenditure of energy to push back the other molecules. The resulting jump of a molecule from one equilibrium position to the next may hence be regarded as the passage of the system over an energy barrier, $\Delta\vec{G}_{\eta}^{,o}$, assume in Figure 4.8.

The jump frequency from an equilibrium position to the hole, assuming the jump direction is aligned with the *x*-axis (note that in the corresponding relation for diffusion, the jump directions are not all aligned with the *x*-axis)

$$\vec{\nu}_x = \nu_0 \exp\left(-\frac{\Delta\vec{G}_{\eta}^{\ddagger,o}}{RT}\right) \;\; ; \;\; \overleftarrow{\nu}_x = \nu_0 \exp\left(-\frac{\Delta\overleftarrow{G}_{\eta}^{\ddagger,o}}{RT}\right) \tag{4.27}$$

In the above, the Gibbs free energy change for activation in the forward and reverse directions from linear free energy relation (LFER), assuming a symmetrical energy barrier is expressed as $\Delta\vec{G}_{\eta}^{\ddagger,o} = \Delta G_{\eta}^{\ddagger,o} - \frac{1}{2}\left(n_{\xi}\tilde{V}_l \frac{\lambda_x}{\delta_1}\tau_{yx}\right)$ and $\Delta\overleftarrow{G}_{\eta}^{\ddagger,o} = \Delta G_{\eta}^{\ddagger,o} + \frac{1}{2}\left(n_{\xi}\tilde{V}_l \frac{\lambda_x}{\delta_1}\tau_{yx}\right)$ where $\tilde{V}_l$ is the volume of a mole of liquid, and $\Delta G_{\eta}^{\ddagger,o}$ is the barrier height at *equilibrium*, i.e., when there is no shear stress.

When a shear stress is applied, the total work of moving the molecule is force per molecule times distance moved, $f \times \lambda$, where the force per molecule, $f = n_{\xi}(\delta_2\delta_3)\tau_{yx}$, where δ_2 is mean distance between two adjacent molecules in the direction perpendicular to the direction of

motion, while δ_3 is that in the direction of motion (Figure 4.8). Thus, $\delta_2\delta_3$ is the effective area per molecule on which shear stress is applied, which may be approximated as $\delta_2\delta_3 \approx \tilde{V}_l/(N_{Av}\delta_1)$. In the above, n_ξ is the number of nearest neighbor molecules against which the traversing molecule shears. As an example, for the case shown in Figure 4.9 $n_\xi = 6$ (Eyring and Ree, 1961) is also consistent with the essentially hexagonal structure in the moving layer. Thus, the total area on which shear applies is $n_\xi(\delta_2\delta_3)$.

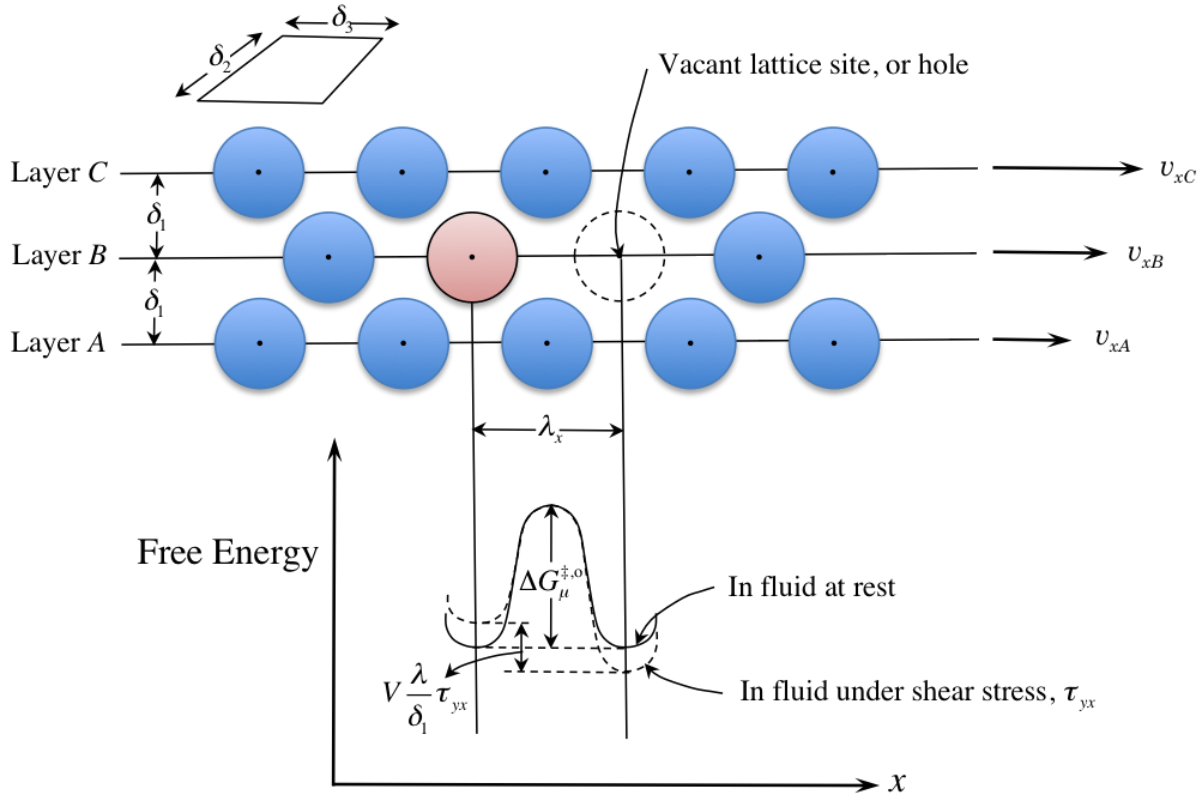

Figure 4.8 Molecular jumps involved in the motion of one liquid layer past another (Bird, et al. 2007, p29). The molecular volume, $v_l = \delta_1 \times \delta_2 \times \delta_3 = \tilde{V}_l / N_{Av}$.

The *net* velocity in the x-direction in layer B, thus, is the distance traveled in the x-direction per jump (λ_x) times the net frequency of forward jumps, $(\vec{v}_x - \overleftarrow{v}_x) = \lambda_x(\vec{\nu}_x - \overleftarrow{\nu}_x)$ which is also the velocity difference between the velocities of layers A and B, i.e., $v_{xA} - v_{xB} = \lambda_x(\vec{\nu}_x - \overleftarrow{\nu}_x)$.

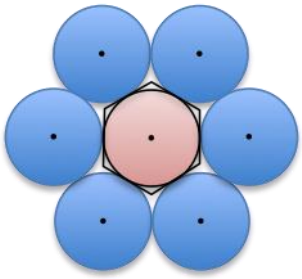

Figure 4.9 Cross-section of a hexagonal-packed condensed phase *normal* to the direction of flow.

Here, the number of nearest neighbor molecules against which the traversing molecule shears, $n_\xi = 6$ (redrawn from Eyring and Ree, 1961).

The velocity gradient, or shear rate, thus

$$\frac{dv_x}{dy} \approx \frac{\Delta v_x}{\delta_1} = \frac{\lambda_x(\vec{\nu}_x - \overleftarrow{\nu}_x)}{\delta_1} = \frac{\lambda_x \nu_0}{\delta_1}\left\{\exp\left(-\frac{\Delta\vec{G}_\mu^{\ddagger,o}}{RT}\right) - \exp\left(-\frac{\Delta\overleftarrow{G}_\mu^{\ddagger,o}}{RT}\right)\right\} \tag{4.28}$$

Using the above LFER in this and define $\nu \equiv \nu_0 \exp\left(-\frac{\Delta G_\mu^{',o}}{RT}\right)$

$$\frac{dv_x}{dy} = \frac{\lambda_x}{\delta_1} 2\nu \sinh\left\{\frac{1}{2}\left(n_\xi \frac{\tilde{V}_l}{RT}\frac{\lambda_x}{\delta_1}\tau_{yx}\right)\right\} \tag{4.29}$$

where ν is jump frequency (TOF) from one equilibrium position to a neighboring equilibrium position in the absence of any stress. Thus is a nonlinear relation between velocity gradient and shear stress, i.e., Non-Newtonian flow (Glasstone et al., 1941, p. 513). Typically the argument of the sinh function $x \to 0$, so that $\sinh x \to x$. Then the above is simplified to

$$\frac{dv_x}{dy} = \left\{\left(\frac{\lambda_x}{\delta_1}\right)^2 \nu n_\xi \frac{\tilde{V}_l}{RT}\right\}\tau_{yx} \tag{4.30}$$

Comparing this to Newton's law of viscosity $\tau_{yx} = \eta \frac{dv_x}{dy}$ and further assuming that $\lambda_x = s\delta_1$, where $s = 0.5$ for solid, $s = 1.12$ (Bird, et al. 2007) for gas system the viscosity coefficients thus

$$\eta = \left\{ \frac{h}{s^2 n_\xi} \frac{N_{Av}}{\tilde{V}_l} \exp\left(-\frac{\Delta S_\eta^{\ddagger,o}}{R} \right) \right\} \exp\left(\frac{\Delta H_\eta^{\ddagger,o}}{RT} \right) \tag{4.31}$$

which may be written in the Arrhenius form, with $\Delta H_\eta^{\ddagger,o} = E_\eta$, i.e. $\eta = B \exp\left(\frac{E_\eta}{RT} \right)$.

We could further use the interrelation between free volume and entropy or partition function to obtain alternate forms of the pre-exponentinal factor above. Recall Eq. (4.16) for the partition function of a molecule in liquid. The chief difference between a molecule in the initial state and one in the activated state for flow is that the latter has one degree of translational freedom less than the former (Glasstone et al., 1941, p. 485, 189). Thus, if the product of F_{rot} and F_{vib} is almost the same in the two states, as it generally would be since the corresponding degrees of freedom are not affected.

$$\exp\left(\frac{\Delta S_\eta^{\ddagger,o}}{R} \right) = \frac{F}{F_l} = \frac{\lambda_t}{v_f^{1/3}} = \frac{h}{\sqrt{2\pi m_M k_B T}} \frac{1}{v_f^{1/3}} \tag{4.32}$$

Note that this provides $\Delta S_\eta^{\ddagger,o} < 0$, which implies that in the liquid the transition state is in fact more ordered than the initial state. Further using the relation, $v_f = \beta v_l = \beta \tilde{V}_l / N_{Av}$ in Eq. (4.32), the pre-exponential factor may be written as

$$B = \beta^{1/3} \left\{ \frac{\sqrt{2\pi m_M k_B T}}{s^2 n_\xi} \left(\frac{N_{Av}}{\tilde{V}_l} \right)^{2/3} \right\} \tag{4.33}$$

4.6.2 Prediction of the Activation Energy for Viscosity

The activation energy, or enthalpy, is predicted as follows within the framework of the PBV-MMP model. It is envisioned that as an atom jumps from an initial position to a neighboring vacancy, assumed to exist in a liquid metal (although in a solid, these need to be created and involve an expenditure of energy), its coordination number changes (Figure 4.10) from an initial coordination number n_M with other metal atoms to $n_M^{\ddagger}$, corresponding to the saddle point, as shown schematically in Figure 4.10, the remaining atoms becoming too distant, and then back to n_M corresponding to the final sate after the jump. Of course, during its journey on the minimum energy path, the bond lengths and bond valences of the mobile atom change continuously, subject to, of course, the bond valence conservation to the atomic valence V_M that remains unchanged. However, we are not concerned with tracing the entire minimum energy path, only with the highest (saddle) point on the minimum energy path, presumably at the mid-point geometrically, as shown in Figure 4.10, between the initial and the final positions.

This approach is along the lines of Wynblatt (1968), who computed the barrier height for self-diffusion in a solid metal by moving one of the nearest neighbors of the vacancy along a straight line trajectory from its initial to its final position and calculating its energy at intervals along this trajectory. Interactions of the moving atom with all other atoms in the array, modeled via the Morse potential, were considered. All atoms, except the moving atom, were held fixed at their lattice positions so that the resulting change in energy arose exclusively from the changes in bond lengths of the moving atom. He found that the position of the moving atom corresponding to maximum energy along the trajectory, invariably turned out to be half-way between its initial and final position, as might have been expected from symmetry considerations (Figure 4.10).

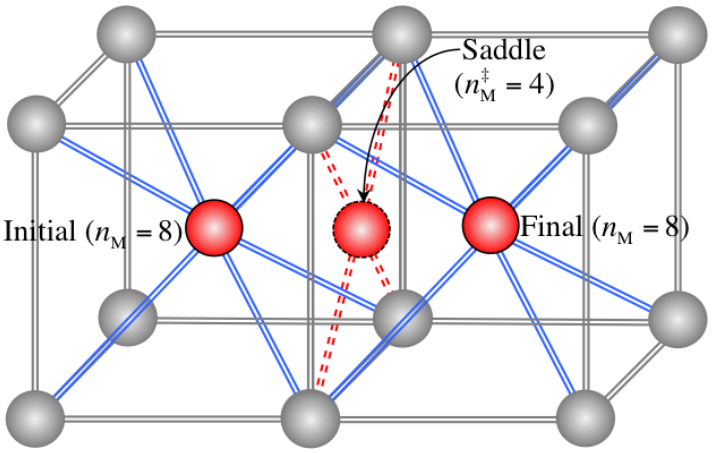

Figure 4.10 Schematic of an atom (red) jump in a body cubic metal and the corresponding change in the effective coordination number n_M from initial state to the saddle point.

Thus, as the atom moves toward this saddle point, many of the original bonds are elongated by of the order of atom radius and consequently, their valence and energy become inconsequential beyond a cut-off bond length because of the exponential nature of the Pauling relation, so that they may be considered broken, i.e., with essentially zero energy. Similarly, even though it begins to form bonds with the new nearest neighbors at the new site, these also are distant enough to be inconsequential. Thus, the only bonds of consequence are the smaller number of nearest neighbors (Figure 4.10) with stronger bond strengths and bond valences, so that the valence conservation is still conserved.

In the example of bcc structure shown in Figure 4.10, $n_M = 8$ and the "effective" coordination at the saddle point $n_M^{\ddagger} = 4$. Thus, the total energy for the jump first monotonically increases ($n_M \to n_M^{\ddagger}$) and then monotonically decreases ($n_M^{\ddagger} \to n_M$), assumed limited to the nearest neighbors. (This cannot be explained in terms of the average BV/average BL model of the Eq. (4.14) type, which predicts that the binding energy declines monotonically with an increase in the coordination number, n_M). However, although clearly there is a difference among the bond

valences and lengths, we will assume the average bond valence $\bar{v}_{ij}$ and bond length model $\bar{r}_{ij}$ as assumed above, because at the saddle point majority of the atoms are distant enough to have effective zero bond energy. It is, thus, worth pointing out again that during the traverse over the reaction coordinate, even though the actual number of bonds is larger than the initial coordination number n_{M}, the vast majorities are negligibly weak and the effective coordination number of consequential bonds is smaller.

We have assumed that at the saddle point, the mobile atom is bonded to fewer atoms, but since atomic valence to be conserved remains unchanged at V_{M}, i.e., there are no dangling bonds ($v_{\mathrm{M}F}=0$), then it means that these bonds at the saddle point have higher bond valence and, therefore, shorter bond lengths, as seen schementically in Figure 4.10. However, our PBV-MMP model incorporates these considerations. We start with the difference of potential energy between an atom at the saddle point and that in the initial position, i.e., $E_\eta=\Delta U=U_{f,\mathrm{M}^\ddagger}-U_{f,\mathrm{M}}=Q_{\mathrm{M}\cdot\mathrm{M}n_{\mathrm{M}}}/2-Q_{\mathrm{M}\cdot\mathrm{M}n^\ddagger_{\mathrm{M}}}/2$, and use in it the approximate PBV-MMP model based on the assumption that the bond-valence of a metal atom (Pauling and Kamb, 1986), assuming equal bond lengths with all nearest neighbors, are all approximately the same and given by $\bar{v}_{ij}=V_{\mathrm{M}}/n_{\mathrm{M}}$, and further that in the bulk metal there are no dangling or free bonds, $v_{\mathrm{M}F}=0$, including at the saddle point. The potential energy corresponds to the average energy per atom, i.e., the total binding energy of bonds per atom divided by 2. Further, recall that the total binding energy of the initial and final position is given in Eq. (4.15), while at the saddle point, the corresponding binding energy, is

$$Q_{\mathrm{M}\cdot\mathrm{M}_{n_{\mathrm{M}}}}=D^{\mathrm{o}}_{\mathrm{M}\cdot\mathrm{M}}\left(2-\frac{1}{n^\ddagger_M}\right) \tag{4.34}$$

Finally, the activation barrier for viscosity is estimated using this method, i.e., $E_\eta = \Delta U = U_{f,\mathrm{M}^\ddagger} - U_{f,\mathrm{M}} = Q_{\mathrm{M}\cdot\mathrm{Mn}_\mathrm{M}}/2 - Q_{\mathrm{M}\cdot\mathrm{Mn}^\ddagger_\mathrm{M}}/2 = (Q_{\mathrm{M}\cdot\mathrm{M}_n}/2)(1 - Q_{\mathrm{M}\cdot\mathrm{M}_n}/Q_{\mathrm{M}\cdot\mathrm{M}_n})$ along with $Q_{\mathrm{M}\cdot\mathrm{M}_n} = 2\Delta H_v^\mathrm{o}$ (for liquid) resulting in

$$E_\eta = \frac{\Delta H_v^\mathrm{o}}{(2n_\mathrm{M} - 1)}\left(\frac{n_\mathrm{M}}{n_\mathrm{M}^\ddagger} - 1\right) \tag{4.35}$$

Since we have assumed that the bond lengths $\bar{r}_{ij}$ and valences $\bar{v}_{ij}$ change with the coordination number n_M that changes at the saddle point to $n_\mathrm{M}^\ddagger$, where $n_\mathrm{M}^\ddagger = (1 - f_\mathrm{M}^\ddagger)n_\mathrm{M}$.

As indicated in Eq. (4.35) activation energy of viscosity sould be in linearly relation with heat of vaporization, since both n_M and $n_\mathrm{M}^\ddagger$ are constants. Figure 4.11 illustrates experimental and calculated activation of viscosity using Eq. (4.35) from PVB-MP model and the model predits well for all the analyized fcc, simple, hpc and bcc all the structures. This suggests that PBV-MMP model can accurately describe the binding energy of bulk liquid metal as well as the activation energy for viscosity.

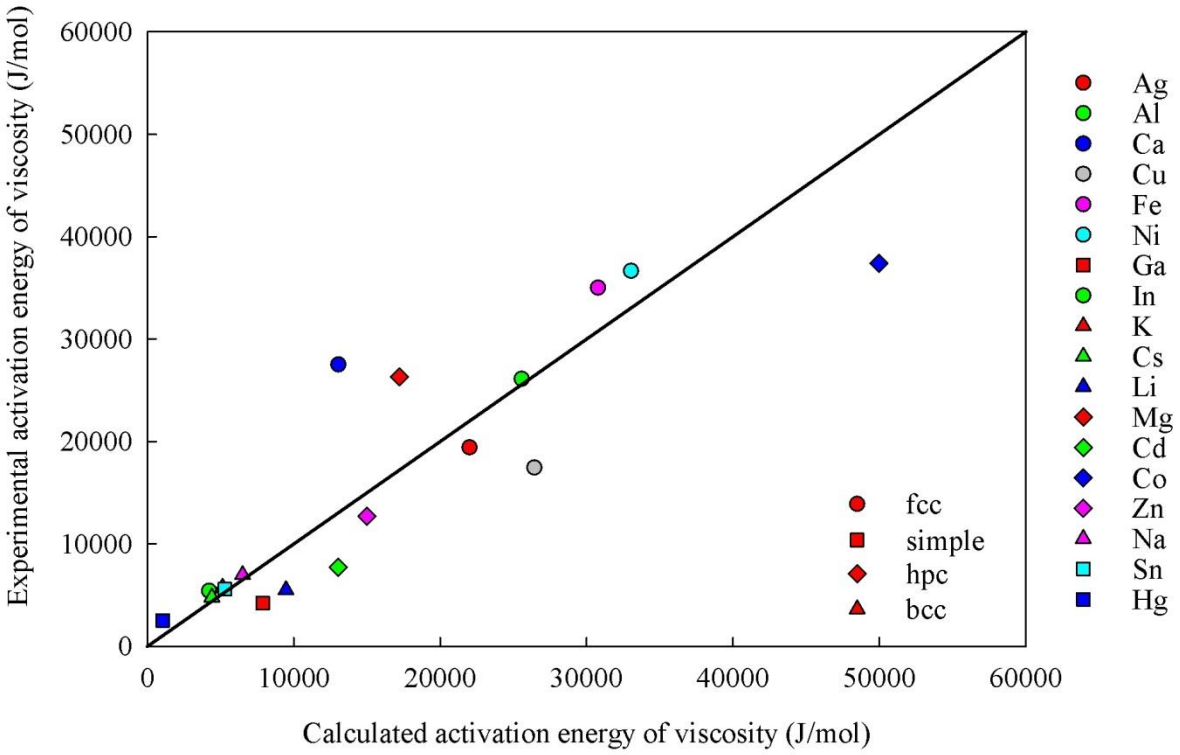

Figure 4.11 Experimental and calculated activation of viscosity using Eq. (4.35) (Chhabra and Sheth, 1990).

Table 4.1 lists the parameters used for activation energy of viscosity calculation for the various metals. To simplfy the calculation it was assumed that the coordination numbers of a metal are the same as in liquid or as a solid. However, in reality we know the coordination numbers in liquid is slightly less than solid for fcc, and a little higher than solid in bcc. This assumption could hence be further improved. Nearest coordination numbers for saddle point assumed are 4 for fcc and bcc, 3 for hpc, and for simple structure $n_{\mathrm{M}}^{\ddagger} = 5$ is assumed.

Table 4.1 Parameters used for activation energy of viscosity (Chhabra and Sheth, 1990; Iida and Guthrie, 2009).

	B (cP) Exp.	E_η (J/mol) Exp.	ΔH_v^o (kJ/mol)	structure	n_M	$n_M^\ddagger$	E_η (J/mol) cal. from Eq. 4.37
Ag	0.5847	19410	253	fcc	12	4	22000
Al	0.1245	26120	294	fcc	12	4	25565.22
Ca	0.0579	27520	150	fcc	12	4	13043.48
Cu	0.7448	17450	304	fcc	12	4	26434.78
Fe	0.4847	35010	354	fcc	12	4	30782.61
Ni	0.3818	36660	380	fcc	12	4	33043.48
Ga	0.4164	4229	256	simple	7	5	7876.92
In	0.4242	5417	231.8	simple	6	5	4214.55
K	0.685	5748	76.9	bcc	8	4	5126.67
Cs	0.1014	4794	65.9	bcc	8	4	4393.33
Li	0.1388	5518	142	bcc	8	4	9466.67
Mg	0.0404	26320	132	hcp	12	3	17217.39
Cd	0.5939	7730	100	hcp	12	3	13043.48
Co	0.3272	37420	383	hcp	12	3	49956.52
Zn	0.413	12690	115	hcp	12	3	15000
Na	0.0804	6979	97.42	bcc	8	4	6494.67
Sn	0.4774	5587	291	simple	6	5	5290.91

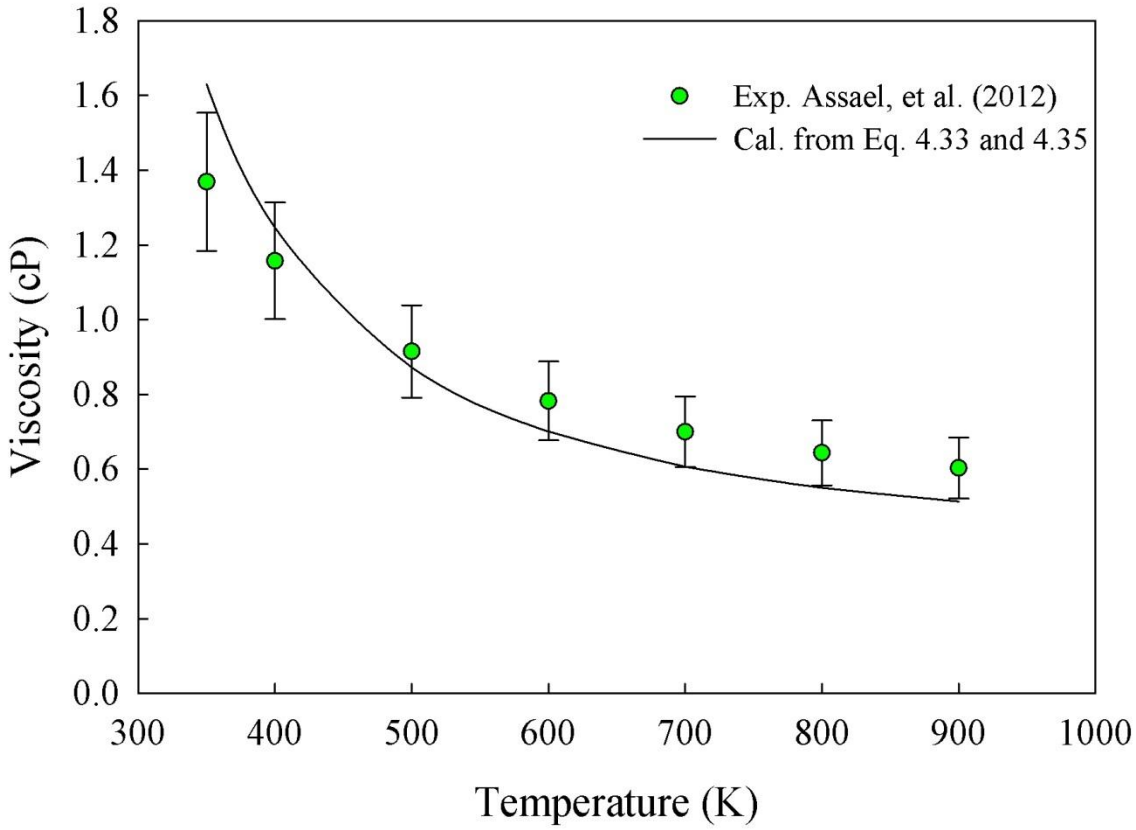

Figure 4.12 Experimental (Assael et al., 2012) and calculated viscosity of liquid Ga using Eq. (4.33) and (4.35), with parameters $\lambda_x = 0.6\delta_1$, ($s = 0.6$), $n_\xi = 6$, $\kappa = 1/9$ and covalent radius 122 pm.

The pre-exponential factor was calculated using Eq. (4.33) and activation of viscosity using Eq. (4.35). Comparisons of the model developed here with this correlation fitted to experiments for Ga is shown in Figure 4.12. As shown in the Figure Eq. (4.33) and Eq. (4.35) together satisfactorily predit viscosity as a function of temperature. Jumping distance $\lambda_x = 0.6\delta_1$ was used. This fitted value located in between solid and gas $0.5 \le s \le 1.12$ seems to be a reasonable assumption (Jagannadham and Sanjeev, 2011).

4.6.3 Eyring Hole Theory of Liquid Diffusion

Eyring treated liquid self-diffusion at the molecular level in a manner very similar to the treatment of viscosity above (Glasstone et al., 1941, p. 516). Let λ_x be the distance through which an atom of solute traverses in each jump, aligned along the *x*-axis (Figure 4.8). The flux in the *x*-direction $N_x = c(\vec{v}_x - \overleftarrow{v}_x) = c\lambda_x(\vec{\nu}_x - \overleftarrow{\nu}_x)$ where c is the concentration. Assuming that in the diffusion jumps in a solvent of viscosity μ and jump frequency is the same as above

$$N_x = c\lambda_x \nu_0 \left\{ \exp\left(-\frac{\Delta \vec{G}_\eta^{\ddagger,o}}{RT} \right) - \exp\left(-\frac{\Delta \overleftarrow{G}_\eta^{\ddagger,o}}{RT} \right) \right\} \tag{4.36}$$

In the above, further, the Gibbs free energy change for activation in the forward and reverse directions from LFER, assuming a symmetrical energy barrier are $\Delta \vec{G}_D^{\ddagger,o} = \Delta G_D^{\ddagger,o} + \frac{1}{2}\Delta G_D$ and $\Delta \overleftarrow{G}_D^{\ddagger,o} = \Delta G_D^{\ddagger,o} - \frac{1}{2}\Delta G_D$. At equilibrium, the barrier height $\Delta \vec{G}_D^{\ddagger,o} = \Delta G_D^{\ddagger,o}$, and $\Delta \overleftarrow{G}_D^{\ddagger,o} = \Delta G_D^{\ddagger,o}$, and the net flux $N = 0$. Here $\Delta G_D \approx \lambda_x \frac{d\mu}{dx}$, where μ is the chemical potential, so that the flux is

$$N_x = -c\lambda_x \underbrace{\nu_0 \exp\left(-\frac{\Delta G_\eta^{\ddagger,o}}{RT} \right)}_{\nu} \left\{ 2\sinh\left(\frac{1}{2}\frac{\lambda}{RT}\frac{d\mu}{dx} \right) \right\} \tag{4.37}$$

Since $\lambda \to 0$, so that $\Delta G_D \to 0$, and we may linearize the function, $\sinh x \to x$, so that

$$N_x = -c\frac{\lambda_x^2}{RT}\nu\left(\frac{d\mu}{dx}\right) = -c\frac{D}{RT}\left(\frac{d\mu}{dx}\right)_{T,p} = cu \tag{4.38}$$

which may be compared to the Einstein-Darken equation for the one-dimensional diffusive flux of a species through a stagnant medium at constant *T* and *p*. *u* is the diffusion velocity and $D = \lambda_x^2 \nu$, $\nu \equiv \nu_0 \exp\left(-\frac{\Delta G_\mu^{\ddagger,o}}{RT} \right)$. Combine these relations we derive self-diffusivity

$$D = \left\{ \lambda_x^2 \left(\frac{k_B T}{h} \right) \exp\left(\frac{\Delta S_\eta^{\ddagger,o}}{R} \right) \right\} \exp\left(-\frac{\Delta H_\eta^{\ddagger,o}}{RT} \right) \tag{4.39}$$

which may be rewritten in the form $D = D_0 \exp\left(-\frac{E_D}{RT} \right)$. Here the pre-exponential factor

$$D_0 = \underbrace{\lambda_x^2 \left(\frac{k_B T}{h} \right) \exp\left(\frac{\Delta S_\eta^{\ddagger,o}}{R} \right)}_{\Lambda_D} \tag{4.40}$$

Further, we may use Eq. (4.20) from above into diffusion coefficient pre-exponential term

$$D_0 = \lambda_x^2 \left\{ \frac{1}{\beta^{1/3} v_l^{1/3}} \right\} \sqrt{\frac{k_B T}{2\pi m_{\mathrm{M}}}} \tag{4.41}$$

where correctly indicates that $D_0 \propto 1/\sqrt{m_{\mathrm{M}}}$. The dependence on free volume is followed by ion diffusion in solids (Adams and Swenson, 2000).

Finally, we need to relate λ_x to liquid molecular size. For instance, Cahoon (2003) simply follows the case of solid diffusion and writes $\lambda_x^2 = f\gamma a^2$, where *f* is the correlation coefficient, γ is a geometric factor and a is the lattice constant. The correlation coefficient has a value between 0.684 and 1.0, and so may be taken simply as unity. Here we assume $\lambda_x = s\delta_1$ (the same as in viscosity section 4.6.1) where δ_1 is assume to be lattice constant a thus the approximated in the above relation by $a \approx v_l^{1/3}$. Combining $\lambda_x^2 = s^2 a^2$ with Eq. (4.41)

$$D_0 = s^2 \frac{v_l^{1/3}}{\beta^{1/3}} \sqrt{\frac{k_B T}{2\pi m_{\mathrm{M}}}} \tag{4.42}$$

Finally, comparing Eq. (4.38) and (4.28), along with $\nu_0 = k_B T / h = RT / (N_{Av} h)$

$$\frac{D\eta}{k_B T} = \frac{1}{n_\xi} \left(\frac{N_{Av}}{\tilde{V}_l} \right)^{1/3} \tag{4.43}$$

where n_ξ is representing the nearest neighbors of solvent molecules in a basal plane (Figure 4.9), typically around 6 (Ree et al., 1958). This provides a relation between self-diffusion coefficient and the viscosity of the solvent it is diffusing in. Eq. (4.43) is also similar to Stokes-Einstein relation (Eq. 4.26) as mentioned above, although the latter is derived from continuum hydrodynamics, in which the solute molecule is assumed large and the solvent is continuous.

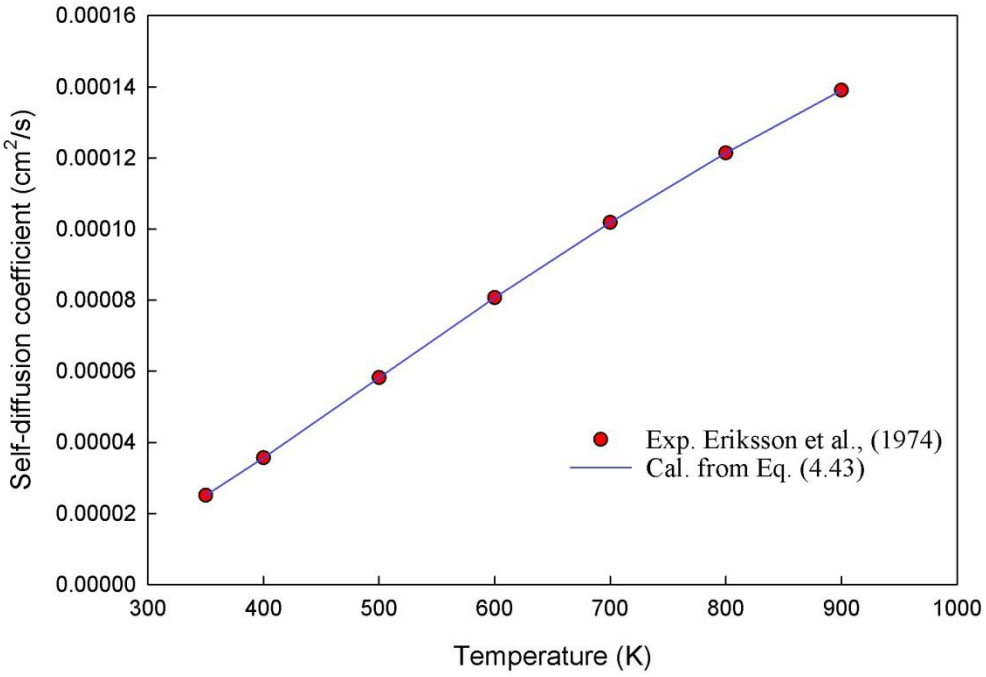

Figure 4.13 Fitted self-diffusion coefficient of Ga using Stokes-Einstein relation Eq. (4.43), $n_\xi = 4$ (Eriksson et al. 1974).

The fitted liquid Ga self-diffusion using experimental viscosity along with Stokes-Einstein relation is presented in Figure 4.13. The fitted value of $n_\xi = 4$ under liquid Ga is a little bit lower than the typical value 6. Hsu and Eyring (1972) calculated the of n_ξ value for liquid alkaline metal systems (bcc structures) and here we further compared metals with simple and fcc structure in their solid states.

The fitted n_ξ value for liquid Al, Cu, Sn, Ni and In versus colvent radius is shown in Figure 4.14. It is seen that atom with smaller colvent radius might be surrounded by fewer nearest neighbors. Fitted n_ξ value ranges between 4~7.8 and most of the numbers are around 6 when colvent radius is above 140 pm. Below 140 pm n_ξ value scattered between 4~7.8 regardless to its structure. For estimation purposes, then it is fair to start with $n_\xi = 6$.

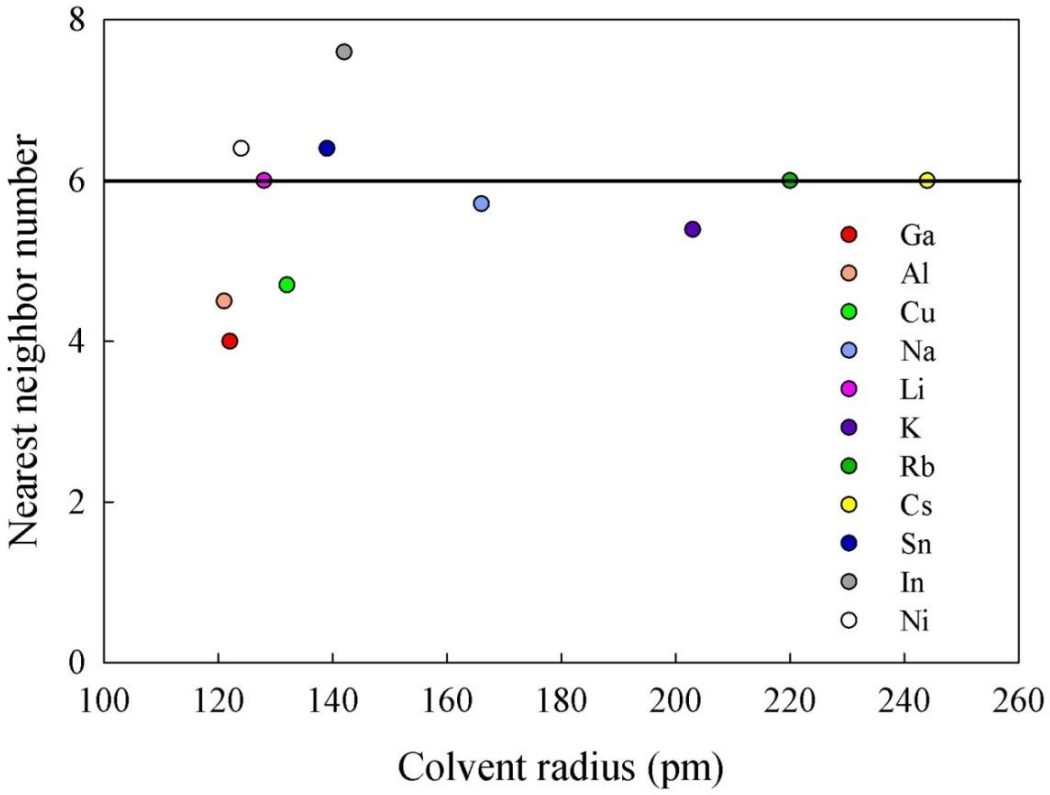

Figure 4.14 Comparison between colvent radius and n_ξ value calculated from Eq (4.43) (Li, K, Cs, Rb and Na data obtained from Hsu and Eyring, 1972).

With available self-diffusion coefficient and viscosity data from experiments n_ξ can also be estimated from Eq. 4.46 or Stokes-Einstein relation. Further, these activation energies for *self-diffusion* in liquid metals are linearly related to the metal melting point T_m, i.e. (Poirier, 1988)

$$E_D = 3.2RT_m \tag{4.44}$$

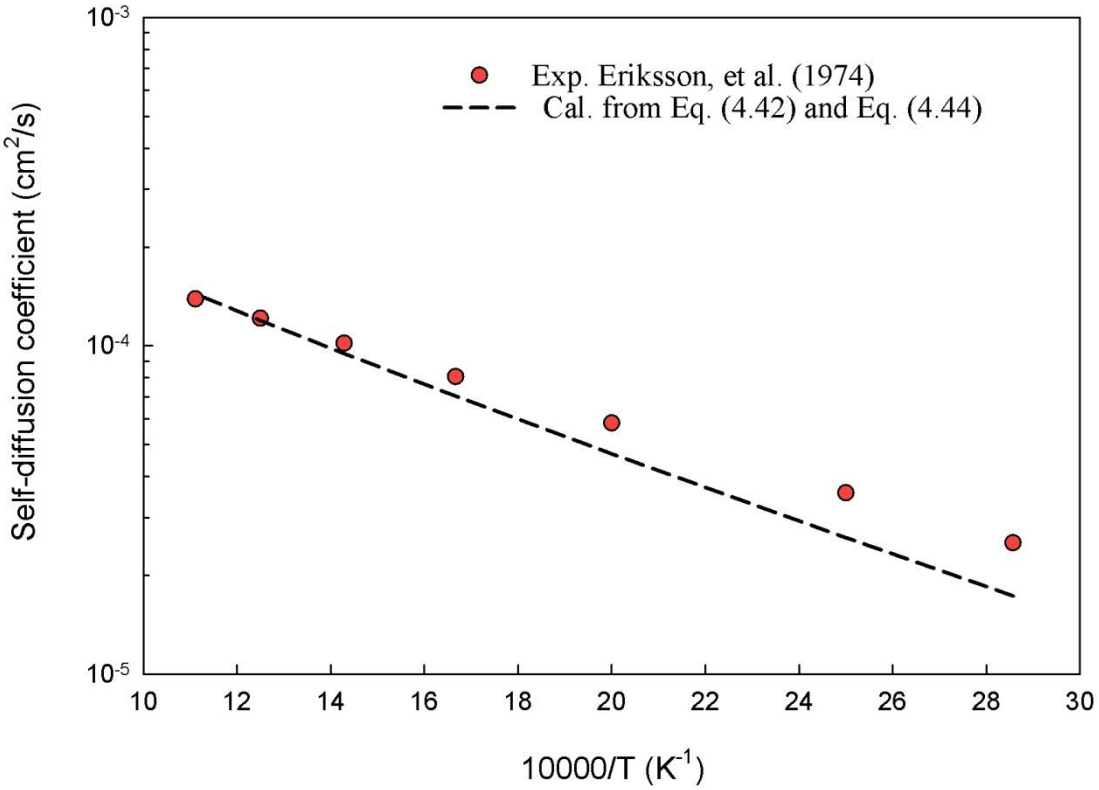

Figure 4.15 Experimental and calculated self diffusion of liquid Ga from Eq. (4.42) and Eq. (4.44), $n_{\xi} = 6$, $\lambda_x = 0.6\delta_1$ (Eriksson et al., 1974).

As further indicated in Figure 4.15 and 4.16 the fitted self-diffusion coefficient results are well predicted from Eq. 4.42 and Eq. 4.44 with proper assumption. Even with the poorest agreement the predicted self-diffusion coefficient still shows within a factor of 2 in our study. In fact, by adjusting jumping distance between $0.6 \le s \le 0.65$ would give both viscosity and self-diffusion coefficient a satisficatory predictions. The parameters that we need for this calculation such as liquid density, molecular weights, melting point and heat of vaporization are common properties that are obtained easily.

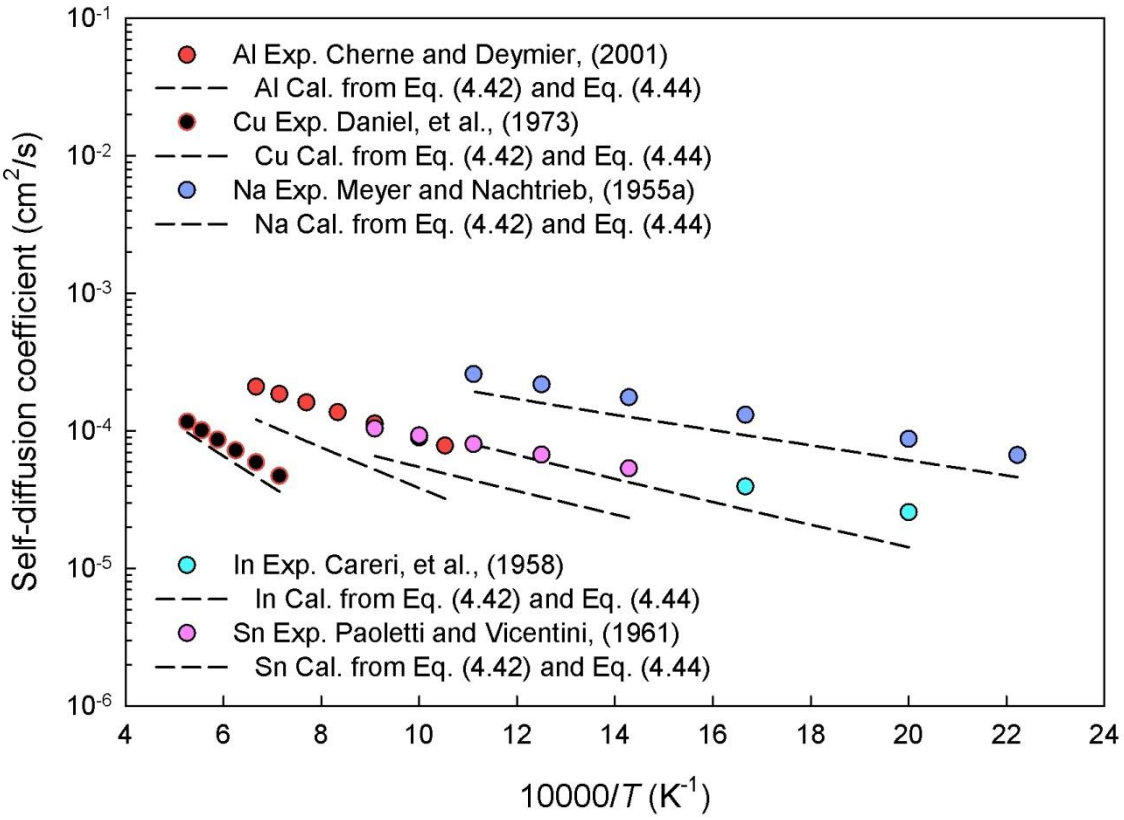

Figure 4.16 Experimental and calculated self diffusion of liquid Al, Cu, Na, Sn, and In Eq. (4.42) and Eq. (4.44), $n_\xi = 6$, $\lambda_x = 0.6\delta_1$ (Cherne and Deymier, 2001; Butrymowicz et al., 1973; Meyer and Nachtrieb, 1955a; Paoletti and Vicentini, 1961; Careri et al., 1958).

4.7 Liquid Metal Surface Tension

We will develop a model for predicting the surface tension of a pure liquid metal based on Skapski's approach (Skapski, 1948a; 1948b; 1956), but will use the PBV-MMP result for the bond energy of M-M bonds. Let us, therefore, first review Skapski's nearest neighbour interaction-broken-bond model of surface tension.

4.7.1 Skapski's Model for Surface Tension

Imagine that the surface of a *pure* liquid is enlarged by an area $\tilde{A}_{\Sigma}$ occupied by N_{Av} number (or 1 mol) of atoms in a monatomic layer. The work done against the surface tension then is (Skapski, 1948a; 1948b; 1956) $\sigma\tilde{A}_{\Sigma} = \Delta U - T\Delta S$ which is the integrated form of the fundamental equation of thermodynamics. In differential form for a pure component, this relation is $\sigma d\tilde{A}_{\Sigma} = dU - TdS$ (Yen and Datta, 2014). In the above, ΔU is the change in the total energy and ΔS is the change in the entropy of N_{Av} atoms located within the bulk metal to move to the surface, i.e., $\Delta U = U_{f,\mathrm{M}\Sigma} - U_{f,\mathrm{M}} = Q_{\mathrm{M}\cdot\mathrm{M}_{n_{\mathrm{M}}}}/2 - Q_{\mathrm{M}\cdot\mathrm{M}_{n_{\mathrm{M}\Sigma}}}/2$ where Q is the binding energy as before. The temperature coefficient of the surface tension at α phase

$$-\sigma_{\alpha} = -\frac{d\sigma_{\alpha}}{dT} = \frac{\Delta S}{\tilde{A}_{\Sigma_{\alpha}}} + \left(\frac{\sigma_{\alpha}}{\tilde{A}_{\Sigma_{\alpha}}}\right)\frac{d\tilde{A}_{\Sigma_{\alpha}}}{dT} \tag{4.45}$$

Within the framework of the liquid as a "quasi-crystalline lattice," we assume that the surface atoms have $f_{\Sigma}n_{\mathrm{M}}$ broken bonds, where n_{M} is the coordinance in the bulk metal, i.e., the number of nearest atoms surrounding an atom in the bulk (Pauling and Kamb, 1986). Then, ΔU may be taken as difference of potential energy between atoms at the surface and those in the bulk

$$\begin{aligned}\Delta U = U_{f,\mathrm{M}_{\Sigma}} - U_{f,\mathrm{M}} &= \frac{Q_{\mathrm{M}\cdot\mathrm{M}_{n_{\mathrm{M}}}}}{2} - \frac{Q_{\mathrm{M}\cdot\mathrm{M}_{n_{\mathrm{M}\Sigma}}}}{2} \\ &\approx n_{\mathrm{M}}\left(\frac{N_{Av}\varepsilon^{v}_{\mathrm{M}\cdot\mathrm{M}}}{2}\right) - n_{\mathrm{M}_{\Sigma}}\left(\frac{N_{Av}\varepsilon^{v}_{\mathrm{M}\cdot\mathrm{M}}}{2}\right) = f_{\Sigma}n_{\mathrm{M}}\left(\frac{N_{Av}\varepsilon^{v}_{\mathrm{M}\cdot\mathrm{M}}}{2}\right)\end{aligned} \tag{4.46}$$

where the terms on the right in the first equality represent the energy of interaction between the chosen atom and its next nearest neighbors, i.e., the work necessary to separate the atom to infinite distance, i.e., binding energy. In the above it is assumed that all bonds are the same. In other words, ΔU is the difference in potential energy related to removing one atom from the bulk

(where it is surrounded by n_{M} next-neighbors) to the surface (where it is surrounded by, n_{M_Σ} next-neighbors). Here n_{M_Σ} is the number of nearest atoms on the surface $n_{M_\Sigma} = (1 - f_\Sigma) n_M$, where f_Σ is the fraction of bonds in the bulk broken to form the liquid metal surface.

Further, $\varepsilon^v_{\mathrm{M\cdot M}}$ is the pair-wise binding energy per bond between M-M, i.e., $\varepsilon^v_{\mathrm{M\cdot M}} = D^v_{\mathrm{M\cdot M}} / N_{Av}$. It is assumed to be constant and the same in the bulk as well as on the surface. This is related to the heat of evaporation of the metal or binding energy $\Delta H^o_v = N_{Av} n_M \dfrac{\varepsilon^v_{\mathrm{M\cdot M}}}{2}$. Combining with Eq. (4.45) thus simply $\Delta U = f_\Sigma \Delta H^{\mathrm{o}}_v$ so that it is the

$$\sigma_\alpha = \frac{f_{\Sigma_\alpha}}{\tilde{A}_{\Sigma_\alpha}} \left(\Delta H^{\mathrm{o}}_v\right) - T \frac{\Delta S}{\tilde{A}_{\Sigma_\alpha}} \tag{4.47}$$

Here $\tilde{A}_{\Sigma_\alpha} = N_{Av} a_{\mathrm{M}\Sigma_\alpha}$ is the molar effective monoatomic layer area, while $a_{\mathrm{M}\Sigma}$ is the effective interfacial area occupied by an atom of M. This is approximated as $a_{\mathrm{M}\Sigma} \approx f (\tilde{V}_{\mathrm{M}} / N_{Av})^{2/3}$ (m^2/mol) (Skapski, 1948a) in terms of metal molar volume $\tilde{V}_{\mathrm{M}} = AW_{\mathrm{M}} / \rho_{\mathrm{M}}$ (m^3/mol). Here *f* is a geometric factor, of the order of unity, for a given crystal plane, accounting for the configuration or the packing of the liquid, discussed in more detail later on. Thus $\tilde{A}_\Sigma = f N_{Av}^{1/3} \tilde{V}_{\mathrm{M}}^{2/3}$ m^2/mol.

Using this in Eq. (4.47)

$$\sigma_\alpha = \underbrace{\frac{f_\Sigma}{f N_{Av}^{1/3}}}_{C} \left(\frac{\Delta H^{\mathrm{o}}_v}{\tilde{V}_{\mathrm{M}}^{2/3}}\right) \left\{1 - \left(\frac{T}{\Delta H^{\mathrm{o}}_v}\right) \frac{\Delta S}{f_\Sigma}\right\} = C \left\{1 - \left(\frac{T}{\Delta H^{\mathrm{o}}_v}\right) \frac{\Delta S}{f_\Sigma}\right\} \left(\frac{\Delta H^{\mathrm{o}}_v}{\tilde{V}_{\mathrm{M}}^{2/3}}\right) \tag{4.48}$$

where $C = f_\Sigma / (f N_{Av}^{1/3})$ is the structural Skapski constant as a function of the liquid metal quasi-crystalline structure. If the liquid metal structure is similar for all metals, *C* would be a constant.

Skapski, (1948a; 1948b; 1956) and Kaptay (2008) have provided a good discussion of these parameters.

$$f = \left(\frac{3}{4} PF_b\right)^{2/3} \frac{\pi^{1/3}}{PF_\Sigma} \tag{4.49}$$

where PF_b and PF_Σ are the packing fractions of the bulk and surface.

The arrangement in the surface layer of a liquid must correspond to that in the most densely populated plane of the respective configuration, because only such an arrangement assures the minimum of the free surface (and, of course, of free energy). Thus, *f* is inversely proportional to the density of population in this surface arrangement and its value is (Skapski, 1948a; 1948b): for close-packed liquids (coordination number, n_M = 12) f = 1.091, for body-centered cubic liquids (coordination number, n_M = 8) f = 1.12, for liquid mercury (coordination number, n_M = 6) f =1.04.

On the other hand, Kaptay (2008) argues that the structure of liquid metals must correspond to the most densely packed crystal plane, namely, the {111} plane of the bulk fcc crystal. The corresponding PF_Σ = 0.906. For a bulk fcc crystal further, PF_b = 0.740, leading to f = 1.09 from the above expression. However, this is obviously an overestimate, as the volume packing of liquid metals is surely below that of the solid fcc crystal. For an everage simple liquid metal, Kaptay (2008) estimates PF_b = 0.65±0.02. Then, for PF_Σ = 0.906 as above, from the above equation, f = 1.00±0.02. Values for the parameter f_Σ are given from Benziger (1991) for *solid* surfaces of different structures, typically being 1/4, 1/3, and 1/2. In a liquid, it might make sense that the surface takes the orientation where the numbers of bonds broken are minimal, as discussed below.

4.7.2. The PBV-MMP Approach for Surface Tension

Our basic hypothesis, as in Spaski's approach, is that the surface is formed by cleaving some of the bonds among the metal atoms. We further follow Spaski's approach in metal-metal atom interactions being limited to nearest neighbor interactions, but use the PBV-MMP method to estimate the bond energy, which, involves the use of a modified Morse potential and the concept of bond valence conservation to atomic valence. Further, instead of considering a generic liquid metal structure, we focus on the Ga surface structure, which is relatively well-studied, so that there is little reason to make arbitrary assumptions regarding its structure and the fraction of bonds broken to form the surface.

The (solid) Ga surface may formed by cleaving some of the bonds among the metal atoms in Ga crystal. There are, in fact, two alternate ways to form the (010) surface, as shown in Figure 4.17. Splitting the metallic bilayer creates surface A, while cutting through the dimers creates surface B. Surface A is thus created by breaking of 4 metallic bonds per surface atom, i.e., $f_{\Sigma} = 4/7$, while surface B results from breaking of one covalent bond, i.e., $f_{\Sigma} = 1/7$. The resulting surface energetics would of course be vastly different. Using XRD, Walko et al. (1998) determined that the surface is, in fact, formed by cutting through the covalent bonds, i.e., surface B in Figure 4.20 (Moré et al, 2003). Further, the metallic bonds on the surface relax significantly from those in the bulk, as determined via STM by Züger and Dürig (1992). It may be expected that the energetics would be different from those that simply account for the energetics of the dimer bond, which is stronger than the average bond, since it has a lower bond length and a higher valance. In fact, it may be recalled that its valence $v_{\mathrm{M-M}} = 1.0$, and its binding energy is $Q_{\mathrm{M}_i \cdot \mathrm{M}_j} = D^{\mathrm{I}}_{\mathrm{M \cdot M}} = 143.6$ kJ/mol. Due to surface reorganization we may expect the surface energy to be less than this.

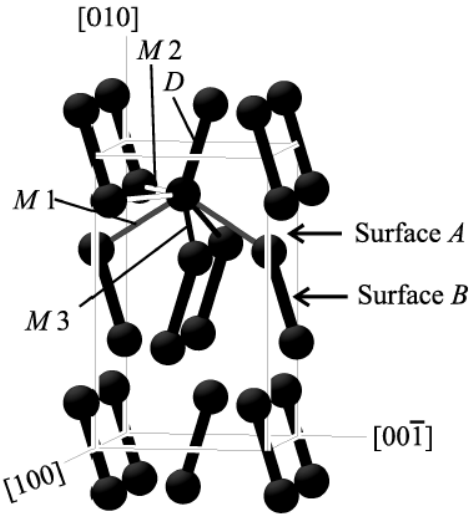

Figure 4.17 Two possible cleaved surfaces (Walko et al., 1998).

Further, there is the question of whether the atoms on the surface have any dangling bonds. For example, if we assume there aren't any, i.e., $v_{MF} = 0$ in Eq. (4.1), then the average bond valence at the surface with the surface coordination of 6 atoms, $\bar{v}_{\text{M-M}} = V_{\text{M}} / n_{\text{M}_\Sigma} = 3.55/6 = 0.592$. The corresponding average bond length from Pauling correlation $r_{ij} = r_{ij}^1 - b \ln v_{ij} = 2.44 - 0.37 \ln 0.592 =$ 2.634 Å. The corresponding average bond energy from Morse potential then $\overline{D}_{\text{M}_i \cdot \text{M}_j} = 90.7$ kJ/mol. Therefore, total binding energy of an atom at the surface is 544 kJ/mol, exactly the same as in bulk. This is clearly incorrect, since it would mean that there is no change in the energy! Thus, it appears that surface valence to be conserved needs to include any unbound electrons (dangling bonds, $v_{MF} \neq 0$ in Eq. 4.1).

For a liquid metal surface the crystal is not frozen, and the surface is likely to restructure itself to minimize the surface energy. Thus, Benziger (1991) proposed that adsorbate bonding may be assumed to occur on a *n*-fold coordination site with no disruption of the M–M bonding as long as

the sum of the metal-adsorbate bond-orders does not exceed the excess metal valance, i.e., $\sum_{j=1}^{m} \phi_{\mathrm{M},j} \le v_{\mathrm{M,ex}}$.

We follow Spaski's approach, and start with the difference of potential energy between atoms at the surface and those in the bulk, i.e., $\Delta U = U_{f,\mathrm{M}\Sigma} - U_{f,\mathrm{M}} = Q_{\mathrm{M{\cdot}M}_{n_\mathrm{M}}}/2 - Q_{\mathrm{M{\cdot}M}_{n_{\mathrm{M}\Sigma}}}/2 = (Q_{\mathrm{M{\cdot}M}_{n_\mathrm{M}}}/2)(1 - Q_{\mathrm{M{\cdot}M}_{n_{\mathrm{M}\Sigma}}}/Q_{\mathrm{M{\cdot}M}_{n_\mathrm{M}}}) = \Delta H_v^{\mathrm{o}}(1 - Q_{\mathrm{M{\cdot}M}_{n_{\mathrm{M}\Sigma}}}/Q_{\mathrm{M{\cdot}M}_{n_\mathrm{M}}})$, but use the PBV-MMP formulae for the total binding energy of an atom, i.e., Eq. 4.13 on the surface

$$Q_{\mathrm{M{\cdot}M}_{n_{\mathrm{M}_\Sigma}}} = D^{\mathrm{o}}_{\mathrm{M{\cdot}M}} \left\{ 2\sum_{j=1}^{n_{\mathrm{M}_\Sigma}} x_{ij,\Sigma} - \sum_{j=1}^{n_{\mathrm{M}_\Sigma}} x_{ij\Sigma}^2 \right\} \tag{4.50}$$

where $x_{ij,\Sigma} = v_{ij,\Sigma}/V_\mathrm{M}$ is the normalized bond valence at the surface.

For the case of Ga, the structure is unusual, in that one of the bonds (covalent-like) is much stronger than the others. As discussed above it is this bond that is cleaved between the bulk atoms and the surface atoms in Ga. In a more typical metal crystal, the bond lengths are more equal. Nonetheless, the surface structure, unlike in a solid surface, is not frozen in a liquid, and the surface restructures itself to minimize the energy difference from the bulk. Consequently, we will assume that in a liquid metal the bond lengths are the same, as are the bond valences. Then we can follow the following procedure.

The relation for the bulk binding energy remains the same as above, as in the bulk there are no free bonds. On the surface, however, since there are free bonds, $\sum_{j=1}^{n_{\mathrm{M}_\Sigma}} x_{ij,\Sigma} = (1 - f_\Sigma)$. Further, in $x_{ij,\Sigma} = v_{ij,\Sigma}/V_\mathrm{M}$, the bond valence $v_{ij\Sigma} \approx \bar{v}_{ij\Sigma} = (1 - f_\Sigma)V_\mathrm{M}/n_{\mathrm{M}_\Sigma} = (1 - f_\Sigma)V_\mathrm{M}/\{n_{\mathrm{M}_\Sigma}(1 - f_\Sigma)\} = V_\mathrm{M}/n_\mathrm{M}$,

i.e., the bond valence and strength at surface remains the same as in bulk, in this case (as implicit in Skapski's approach), so that the term $\sum_{j=1}^{n_{\mathrm{M}_\Sigma}} x_{ij\Sigma}^2 = n_{\mathrm{M}_\Sigma}/n_{\mathrm{M}}^2 = (1-f_\Sigma)/n_{\mathrm{M}}$. Consequently,

$$Q_{\mathrm{M\cdot M}_{n_{\mathrm{M}\Sigma}}} = D^{\mathrm{o}}_{\mathrm{M\cdot M}}(1-f_\Sigma)\left(2-\frac{1}{n_{\mathrm{M}}}\right) \tag{4.51}$$

Using this in $\Delta U = f_\Sigma \Delta H_v^{\mathrm{o}}$ and then $\Delta U = \Delta H_v^{\mathrm{o}}(1-Q_{\mathrm{M\cdot M}_{n_{\mathrm{M}\Sigma}}}/Q_{\mathrm{M\cdot M}_{n_{\mathrm{M}}}})$.

Thus, we may conclude that the Skapski model with PBV-MMP predicted heat of vaporization provides a good fit of the surface tension of liquid metals in terms of coordination number of the metal crystal, metal valence, and the fraction of bonds broken to create the surface. Thus, the predictive relation results in

$$\sigma_\alpha = \frac{1}{fN_{Av}^{1/3}\tilde{V}_{\mathrm{M}}^{2/3}}\left\{ f_\Sigma\left(\frac{D^{\mathrm{o}}_{\mathrm{M\cdot M}}}{2}\right)\left(2-\frac{1}{n_{\mathrm{M}}}\right) - T\Delta S\right\} \tag{4.52}$$

where $D^{\mathrm{o}}_{\mathrm{M\cdot M}}$ corresponds to the liquid metal, and may be theoretically estimated, e.g., via DFT.

4.7.3 Estimation of Entropy Change

The entropy change was estimated by Skapski as follows. The calculation of ΔS for liquid metals and other monatomic liquids is relatively simple (Skapski, 1948a), as there is no contribution of rotation or vibration of an atom within a molecule. Only oscillation of an atom has to be considered. The entropy change due to oscillations is shown to be (Skapski, 1948a)

$$\Delta S_{Osc} = 3R\ln\left(\frac{n_{\mathrm{M}}}{n_{\mathrm{M}_\Sigma}}\right)^{1/2} = -\frac{3}{2}R\ln(1-f_\Sigma) \tag{4.53}$$

where n_{M} is the number of nearest atoms surrounding an atom in the bulk and $n_{\mathrm{M}\Sigma}$ is the corresponding number on the surface, and $n_{\mathrm{M}_\Sigma} = (1-f_\Sigma)n_{\mathrm{M}}$. The estimate hence ranges from

$\Delta S_{Osc} = +3.6$ J.K/mol to $\Delta S_{Osc} = +8.6$ J.K/mol. Eustathopoulos et al. (1998) provide an average estimate of $\Delta S_{Osc} = +5.3$ J.K/mol.

However, the total entropy change is apparently larger than this, as this implies a surface of sharp discontinuity, which is untrue (Skapski, 1948a). On the other hand, including the configurational entropy change

$$\Delta S_{Conf} = -\frac{N_{Av} k_B}{n_{\mathrm{M}} + 1} \left\{ (n_{\mathrm{M}} - n_{\mathrm{M}\Sigma}) \ln\left(\frac{n_{\mathrm{M}} - n_{\mathrm{M}_\Sigma}}{n_{\mathrm{M}} + 1} \right) + (n_{\mathrm{M}\Sigma} + 1) \ln\left(\frac{n_{\mathrm{M}_\Sigma} + 1}{n_{\mathrm{M}} + 1} \right) \right\} \tag{4.54}$$

provides an overestimate (Skapski, 1948a). Therefore, Skapski simply assumed that $\Delta S \approx \Delta S_{Osc} + (1/2)\Delta S_{Conf}$. Combining, thus, and using $n_{\mathrm{M}\Sigma} = (1 - f_\Sigma) n_{\mathrm{M}}$

$$\Delta S \approx -\frac{1}{2}\left(\frac{R}{n_{\mathrm{M}} + 1} \right) \left\{ (n_{\mathrm{M}} f_\Sigma) \ln\left(\frac{n_{\mathrm{M}} f_\Sigma}{n_{\mathrm{M}} + 1} \right) + \{(1 - f_\Sigma) n_{\mathrm{M}} + 1\} \ln\left(\frac{(1 - f_\Sigma) n_{\mathrm{M}} + 1}{n_{\mathrm{M}} + 1} \right) \right\} - \frac{3}{2} R \ln(1 - f_\Sigma) \tag{4.55}$$

For example, for fcc liquids $n_{\mathrm{M}} = 12$ and $f_\Sigma = 1/4$, $\Delta S_{Osc} = +3.6$ J.K/mol, $\Delta S_{Conf} = +4.5$ J.K/mol, and $\Delta S = +5.8$ J.K/mol. On the other hand, for bcc liquids ($n_{\mathrm{M}} = 8$ and $f_\Sigma = 1/4$), $\Delta S_{Osc} = +3.6$ J.K/mol, $\Delta S_{Conf} = +4.4$ J.K/mol, and $\Delta S = +5.8$ J.K/mol. Finally, for liquid mercury (coordination number, n_{M} = 6, and $f_\Sigma = 1/2$, $\Delta S_{Osc} = +8.6$ J.K/mol, $\Delta S_{Conf} = +5.7$ J.K/mol, and $\Delta S = +11.5$ J.K/mol. On the other hand, Kaptay (2008) estimated these quantities based on experimental data. Thus, he included an experimental estimate of $\Delta S_{Osc} = 5.8$ mol/J.K. To this he added the configurational entropy correction, which is connected with the transfer of an atom from the disordered bulk liquid to the ordered surface so that it is negative. Thus, Kaptay (2008) provides an estimate $\Delta S_{Conf} = -7$ J.K/mol, so that overall, $\Delta S = \Delta S_{Osc} + \Delta S_{Conf} = -1.2$ J.K/mol.

Using Eq. (4.52) and Eq. (4.55) the calculated and experimental liquid Ga, Al, Cu, Na, In, Sn, and Ni surface tension change over temperature is shown in Figure 4.18.

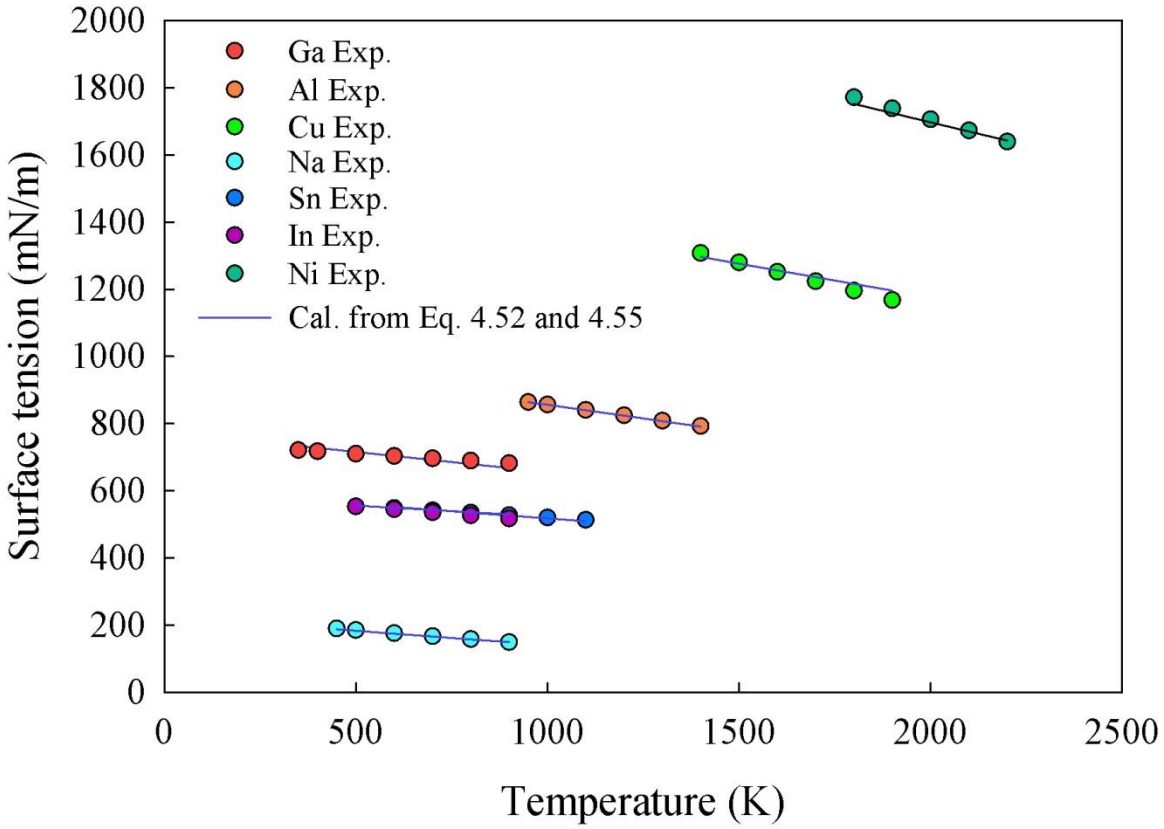

Figure 4.18 Calculated and experimental surface tension change over temperature of liquid Ga, Al, Cu, Na, Sn, In and Ni (Mills and Su, 2006).

In Eq. (4.52) and Eq. (4.55) there are only two parameters f_Σ and n_M that are unknown. Similar to previous calculations n_M was assumed to be the same as if they were in solid state. Fitted f_Σ value and calculated *f*, ΔS and n_{M_Σ} are shown in Table 4.2. It may be mentioned again that, unlike for a solid metal surface (Benziger, 1991), we may expect $f_\Sigma \approx 1/4$ or smaller for liquid metals in an effort by the liquid to reorganize and minimize the surface energy. As predicted all the f_Σ values are lower than 1/4 and mostly locate between 0.11~0.16. Fcc structures tend to have higher f_Σ between 0.14~0.17 whereas simple structures have lower f_Σ 0.11~0.14. Na (bcc) f_Σ is in between fcc and simple structure however with only 1 data it is difficult to jump

into the conclusion. And it is apparent that the entropy change of all the elements are similar with values between 3~4 J/molK.

Table 4.2 Parameter used in surface tension calculation.

	Structure	n_M	Geometric factor f	f_Σ	Cal. ΔS J/mol.K
Ga	simple	7	1	0.128	3.17
Sn	simple	6	1	0.112	2.80
In	simple	6	1	0.138	3.36
Al	fcc	12	1.01	0.138	3.45
Ni	fcc	12	1.01	0.170	4.13
Cu	fcc	12	1.01	0.164	4.00
Na	bcc	8	0.97	0.154	3.75

4.8 Conclusion

A Pauling Bond Valence-Modified Morse Potential (PBV-MMP) model, in which the Pauling's relationship between bond-valence (BV) and bond-length (BL) incorporated within a modified Morse-Potential (MP) was developed in this chapter. The model is similar to Shustorovich UBI-QEP approach for metal surface, however, we further replace the bond-index concept with bond length and bond valence to extend the theory into bulk metal. The calculation only requires simple physical properties such as density, atomic weight, colvent radius and thermodynamic parameter, e.g. liquid metal M-M bond energy calculated from heat of vaporization. These parameters are readily recorded in the literature.

Thus, we were able to calculate thermodynamic properties of *liquid* metal surface with PBV-MMP approach, and further extended it into calculate *bulk liquid metal* transport properties such

as activation energy of viscosity, viscosity, self-diffusivity. To predict self-diffusion and viscosity PBV-MMP was incorperated with Eyring's hole theory and Skapski's model was utilized to predict surface tension. Model was applied on liquid Ga (simple), Cu (fcc), Al (fcc) and Na (bcc) representing different origin solid structure. Several basic assumptions were made based on quasi-crystalline model that maynot fully describe the liquid metal characteristic (for example, the coorodination number), however, the result gave reasonable prediction compared to experimental data. Even with the poorest fitting in self-diffusion coefficicent prediction it is within a factor of 2 in our study. This model hence provides a steping stone for further development and guidance that could lead to estimating other liquid metal properties.

4.9 References

Adams, S. and Swenson, J., Migration pathways in Ag-based superionic glasses and crystals investigated by the bond valence method, *Physical Review B*, 63, 5, (2000), 054201.

Albe, K., Nordlund, K., Nord, J., and Kuronen, A., Modeling of compound semiconductors: Analytical bond-order potential for Ga, As, and GaAs, *Physical Review B*, 66, 3, (2002), 035205.

Assael, M. J., Kakosimos, K., Banish, R. M., Brillo, J., Egry, I., Brooks, R., Quested, P. N., Mills, K. C., Nagashima, A., Sato, Y. and Wakeham, W.A., Reference data for the density and viscosity of liquid aluminum and liquid iron, *Journal of Physical and Chemical Reference Data*, 35, 1, (2006), 285-300.

Assael, M. J., Kalyva, A. E., Antoniadis, K. D., Banish, R. M., Egry, I., Wu, J., Kaschnitz, E. and Wakeham, W. A., Reference data for the density and viscosity of liquid copper and liquid tin, *Journal of Physical and Chemical Reference Data*, 39, 3, 2010, 033105.

Assael, M. J., Armyra, I. J., Brillo, J., Stankus, S. V., Wu, J., and Wakeham, W. A., Reference data for the density and viscosity of liquid cadmium, cobalt, gallium, indium, mercury, silicon, thallium, and zinc, *Journal of Physical and Chemical Reference Data*, 41, 3, (2012), 033101.

Atkins, P. and De Paula, J., Physical Chemistry, 7th ed., W. *H. Freeman & Co., New York*, (2002).

Benziger, J. B., Thermochemical methods for reaction energetics on metal surfaces in Shustorovich, E. M., Ed., Metal-surface reaction energetics: theory and applications to heterogeneous catalysis, chemisorption, and surface diffusion, *VCH Publishers, New York*, (1991).

Benziger, J. B., Thermochemistry of metal catalyzed reactions, *Catalysis Today*, 21, 1, (1994), 211-228.

Bird, R. B., Stewart, W. E. and Lightfoot, E. N., Transport Phenomena, *John Wiley & Sons*, (2007).

Blowers, P., Masel, R. I., Conservation of bond order during radical substitution reactions: Implications for the BEBO model. *The Journal of Physical Chemistry A*, 102, 48, (1998), 9957-9964.

Boudart M, and Djéga-Mariadassou G., Kinetics of Heterogeneous Catalytic Reactions, *Princeton University Press, Princeton NJ*, (1984).

Brese, N. E. and O'Keeffe, M. Bond-valence parameters for solids, *Acta Crystallographica*, B47, (1991), 192-197.

Brown, I. D., Bond-Length-Bond-Valence Relationships in Inorganic Solids. In Burgi, H.-B., and Junitz, J. D., Eds., Structure Correlation, Volume 2, *VCH, Weinheim*, 405-429, (1994).

Brown, I. D., The chemical bond in inorganic chemistry: the bond valence model, IUCr Monographs in Crystallography 12, *Oxford Science Publications*, (2002).

Brown, I. D., Recent developments in the methods and applications of the bond valence model, *Chemical Reviews*, 109, 12, (2009), 6858-6919.

Brown, I. D., Bond Valence Theory, *Springer Berlin Heidelberg*, (2013).

Brown, I. D. and Poeppelmeier, K., R., Bond Valences, *Springer Berlin Heidelberg*, (2014).

Brown, I. D., The bond valence model as a tool for teaching inorganic chemistry: the ionic model revisited, *Journal of Chemical Education*, 77, 8, (2000), 1070-1075.

Butrymowicz, D. B., John, R. M., and Michael E. R., Diffusion in Copper and Copper alloys. Part I. Volume and surface self- diffusion in Copper, *Journal of Physical and Chemical Reference Data*, 2, 3, (1973), 643-656.

Cahoon, J. R., The entropy factor in liquid diffusion, *Metallurgical and Materials Transactions A*, 34, 3, (2003), 882-883.

Careri, G., Paoletti, A. and Vicentini, M., Further experiments on liquid indium and tin self-diffusion, *IL Nuovo Cimento*, 10, 6, (1958), 1088-1099.

Cherne Iii, F.J. and Deymier, P.A., Calculation of the transport properties of liquid aluminum with equilibrium and non-equilibrium molecular dynamics, *Scripta Materialia*, 45, 8, (2001), 985-991.

Chhabra, R. P. and Sheth, D. K., Viscosity of molten metals and its temperature dependence, *Zeitschrift fur Metallkunde*, 81, 4, (1990), 264-271.

Cohen, M. H., and Turnbull, D., Molecular transport in liquids and glasses, *The Journal of Chemical Physics*, 31, 5, (1959), 1164-1169.

Conway, B. E. and Bockris, J. M., Electrolytic hydrogen evolution kinetics and its relation to the electronic and adsorptive properties of the metal, *The Journal of Chemical Physics*, 26, 3, (1957), 532-541.

Donohue, J., Structures of the Elements, *John Wiley, New York*, (1974).

Drebov, N., Weigend, F., and Ahlrichs, R., Structures and properties of neutral gallium clusters: a theoretical investigation, *The Journal of chemical physics*, 135, 4, (2011), 044314.

Eriksson, P. E., Larsson, S. J., and Lodding, A., Tracer impurity diffusion in liquid metals: In in Gallium and Ga in Indium, *Zeitschrift für Naturforschung A*, 29, 6, (1974), 893-896.

Eustathopoulos, N., Drevet, B. and Ricci, E., Temperature coefficient of surface tension for pure liquid metals, *Journal of Crystal Growth*, 191, 1, (1998), 268-274.

Eyring, H. and Ree, T., Significant liquid structures, VI. The vacancy theory of liquids, *Proceedings of the National Academy of Sciences of the United States of America*, 47, 4, (1961), 526-537.

Eyring, H. and Hirschfelder, J., The theory of the liquid state, *Journal of Physical Chemistry*, 41, 2, (1937), 249-257.

Frank, H. S., Free volume and entropy in condensed systems I. General principles fluctuation entropy and free volume in some monatomic crystals, *The Journal of Chemical Physics*, 13, 11, (1945a), 478-492.

Frank, H. S., Free volume and entropy in condensed systems II. Entropy of vaporization in liquids and the pictorial theory of the liquid state, *The Journal of Chemical Physics*, 13, 11, (1945b), 493-507.

Frank, H. S. and Evans, M. W., Free volume and entropy in condensed systems III. Entropy in binary liquid mixtures; partial molal entropy in dilute solutions; structure and thermodynamics in aqueous electrolytes, *The Journal of Chemical Physics*, 13, 11, (1945), 507-532.

Froben, F. W., Schulze, W., and Kloss, U., Raman spectra of matrix-isolated group IIIA dimers: Ga_2, In_2, Tl_2, *Chemical Physics Letters*, 99, 5, (1983), 500-502.

Geiger, F., Busse, C. A., and Loehrke, R. I., The vapor pressure of indium, silver, gallium, copper, tin, and gold between 0.1 and 3.0 bar, *International Journal of Thermophysics*, 8, 4, (1987), 425-436.

Girifalco, L. A. and Weizer, V. G, Application of the Morse potential function to cubic metals, *Physical Review*, 114, 3, (1959), 687-690.

Glasstone, S., Eyring, H. and Laidler, K. J., The Theory of Rate Processes, *McGraw-Hill, New York*, (1941).

Gong, X. G., Chiarotti, G. L., Parrinello, M. and Tosatti, E. α-gallium: A metallic molecular crystal, *Physical Review B*, 43, 17, (1991), 14277.

Himmel, H. J., and Gaertner, B., Characterization of isolated Ga_2 molecules by resonance Raman spectroscopy and variations of Ga−Ga bonding, *Chemistry-A European Journal*, 10, 23, (2004), 5936-5941.

Hsu, C. C. and Eyring, H., Significant liquid-structure theory of viscosity and self-diffusion of the alkali metals, *Proceedings of the National Academy of Sciences*, 69, 6, (1972), 1342-1345.

http://www.iucr.org/resources/data/data-sets/bond-valence-parameters

Huijben, M. J., Van Hasselt, J. P., Van der Weg, K. and Van der Lugt, W., Density of liquid sodium-potassium and potassium-rubidium alloys, *Scripta Metallurgica*, 10, 6, (1976), 571-574.

Itami, T. and Sugimura, K., A hard-sphere model in analytic form for atomic transport properties of liquid metals, *Physics and Chemistry of Liquids*, 29, 1, (1995), 31-41.

Iida, T. and Guthrie, R., Performance of a modified Schytil model for the surface tension of liquid metallic elements at their melting point temperatures, *Metallurgical and Materials Transactions B*, 41, 2, (2010), 437-447.

Jagannadham, V. and Sanjeev, R., Is the liquid a condensed gas or collapsed solid? A statistical thermodynamic and cell theory approach: A simple introductory and lucid one-hour class-room lecture for physical chemistry senior under-graduate and graduate level students, *American Journal of Chemistry*, 1, 2, (2011), 26-28.

Johnston, H. S., Gas Phase Reaction Rate Theory, *Ronald Press, New York*, (1966).

Johnston, H. S. and Parr, C., Activation energies from bond energies. I. Hydrogen transfer reactions, *Journal of the American Chemical Society*, 85, 17, (1963), 2544-2551.

Kittel, C., Introduction to solid state physics, 5th ed., John Wiley, New York, (1986).

Kleis, J., Greeley, J., Romero, N. A., Morozov, V. A., Falsig, H., Larsen, A. H., Lu, J., Mortensen, J. J., Dułak, M., Thygesen, K. S. and Nørskov, J. K., Finite size effects in chemical bonding: from small clusters to solids, *Catalysis Letters*, 141, 8, (2011), 1067-1071.

Kaptay, G., A unified model for the cohesive enthalpy, critical temperature, surface tension and volume thermal expansion coefficient of liquid metals of bcc, fcc and hcp crystals, *Materials Science and Engineering: A*, 495, 1, (2008), 19-26.

Meyer, R. E. and Nachtrieb, N. H., Self-diffusion of liquid sodium, *The Journal of Chemical Physics*, 23, 10, (1955a), 1851-1854.

Meyer, R. E. and Nachtrieb, N. H., Self-diffusion in Sodium near the melting point, *The Journal of Chemical Physics*, 23, 2, (1955b), 405-406.

Mills, K. C., Recommended values of thermophysical properties for selected commercial alloys, *Woodhead Publishing*, (2002).

Mills, K. C. and Su, Y. C., Review of surface tension data for metallic elements and alloys: Part 1-Pure metals, *International Materials Reviews*, 51, 6, (2006), 329-351.

Miyazaki, E., Chemisorption of diatomic molecules (H_2, N_2, CO) on transition d-metals, *Journal of Catalysis*, 65, 1, (1980), 84-94.

Moré, S., Soares, E. A., Van Hove, M. A., Lizzit, S., Baraldi, A., Grütter, C., Bilgram, J. H. and Hofmann, P., α-Ga (010) surface reconstruction: A LEED structural analysis of the (1×1) room temperature and (2×2× 2) R 45° low-temperature structures, *Physical Review B*, 68, 7, (2003), 075414.

Morse, P. M., Diatomic molecules according to the wave mechanics II. Vibrational levels, *Physical Review*, 34, 1, (1929), 57-64.

Nachtrieb, N. H., Self-diffusion in liquid metals, *Advances in Physics*, 16, 62, (1967), 309-323.

Nørskov J. K., Bligaard, T., Rossmeisl, J. and Christensen, C. H. Towards the computational design of solid catalysts, *Nature Chemistry*, 1, 1, (2009), 37-46.

Pauling, L., Atomic radii and interatomic distances in metals, *Journal of the American Chemical Society*, 69, 3, (1947), 542-553.

Paoletti, A. and Vicentini, M., Diffusion in a liquid Indium- Tin alloy at the eutectic concentration, *Journal of Applied Physics*, 32, 1, (1961), 22-24.

Pauling, L., A resonating-valence-bond theory of metals and intermetallic compounds, *Proceedings of the Royal Society of London A: Mathematical, Physical and Engineering Sciences*, 196, 1046, (1949), 343-360.

Pauling, L., The Nature of the Chemical Bond, Ithaca, *NY: Cornell University Press*, (1960).

Pauling, L. and Kamb, B., A revised set of values of single-bond radii derived from the observed interatomic distances in metals by correction for bond number and resonance energy, *Proceedings of the National Academy of Sciences*, 83, 11, (1986), 3569-3571.

Prakash, S. G., Ravi, R. and Chhabra, R. P., Corresponding states theory and transport coefficients of liquid metals, *Chemical Physics*, 302, 1, (2004), 149-159.

Poirier, J. P., Transport properties of liquid metals and viscosity of the Earth's core, *Geophysical Journal International*, 92, 1, (1988), 99-105.

Protopapas, P., Andersen, H. C. and Parlee, N. A. D., Theory of transport in liquid metals. I. Calculation of self- diffusion coefficients, *The Journal of Chemical Physics*, 59, 1, (1973), 15-25.

Pyfer, K. L., Kafader, J. O., Yalamanchali, A. and Jarrold, M. F., Melting of size-selected gallium clusters with 60-183 atoms, *The Journal of Physical Chemistry A*, 118, 27, (2014), 4900-4906.

Shustorovich, E. M., Chemisorption phenomena: analytic modeling based on perturbation theory and bond-order conservation, *Surface Science Reports*, 6, 1, (1986), 1-63.

Shustorovich, E. M. and Sellers, H., The UBI-QEP method: a practical theoretical approach to understanding chemistry on transition metal surfaces, *Surface Science Reports*, 31, 1, (1998), 1-119.

Skapski, A. S., The temperature coefficient of the surface tension of liquid metals, *The Journal of Chemical Physics*, 16, 4, (1948a), 386-389.

Skapski, A. S., The surface tension of liquid metals, *The Journal of Chemical Physics*, 16, 4, (1948b), 389-393.

Skapski, A. S., A theory of surface tension of solids-I application to metals, *Acta Metallurgica*, 4, 6, (1956), 576-582.

Song, B. and Cao, P. L., Evolution of the geometrical and electronic structures of Gan (n= 2-26) clusters: a density-functional theory study, *The Journal of Chemical Physics*, 123, 14, (2005), 144312.

Swalin, R. A., On the fluctuation model of diffusion in liquid metals, *Zeitschrift für Naturforschung A*, 23, 6, (1968), 805-813.

Tonner, R. and Gaston, N., The dimeric nature of bonding in gallium: from small clusters to the α-gallium phase, *Physical Chemistry Chemical Physics*, 16, 44, (2014), 24244-24249.

Van Santen, R. A., On Shustorovich's bond-order conservation method as applied to chemisorption, *Recueil des Travaux Chimiques des Pays-Bas*, 109, 2, (1990), 59-63.

Walko, D. A., Robinson, I. K., Grütter, C. and Bilgram, J. H., Surface Structure of α-Ga (010), *Physical Review Letters*, 81, 3, (1998), 626-629.

Weinberg, W. H., The bond-energy bond-order (BEBO) model of chemisorption, *Journal of Vacuum Science and Technology*, 10, 1, (1973), 89-94.

Wynblatt, P., Calculation of the vacancy migration energy in cubic crystals, *Journal of Physics and Chemistry of Solids*, 29, (1968), 215-224.

Yen, P. S. and Datta, R., Butler-Sugimoto monomolecular bilayer interface model: The effect of oxygen on the surface tension of a liquid metal and its wetting of a ceramic, *Journal of Colloid and Interface Science*, 426, (2014), 314-323.

Züger, O. and Dürig, U., Atomic structure of the α-Ga (001) surface investigated by scanning tunneling microscopy: Direct evidence for the existence of Ga 2 molecules in solid gallium, *Physical Review B*, 46, 11, (1992), 7319-7323.

Chapter V

A Combined Pauling Bond Valence-Modified Morse Potential (PBV-MMP) Model for Metals. II. Dissociative Adsorption, Dissolution, and Atomic Diffusion of Hydrogen in Liquid Metals

5.1 Abstract

This chapter describes the theory behind supported liquid metal membrane (SLiMM) involving sequential steps of surface adsorption, dissolution, and diffusion across the liquid metal membrane, followed by the reverse sequence on the permeate side. Improved understanding of hydrogen solution and diffusion is also important in the application of liquid metals as coolants in fast neutron reactors, metal/alloy casting, or for hydrogen storage. However, theoretical modeling of these steps in liquid metals is significantly less advanced as compared to these in solid metals. In fact, curiously liquid metals have not so far been considered as potential hydrogen storage materials.

Consequently, here we develop a new quasi-crystalline approach for estimating the thermodynamic and kinetic parameters of atomic hydrogen adsorption, solution, and diffusion in liquid metals. It is based on the use of combined Pauling Bond Valence-Modified Morse Potential (PBV-MMP) approach for metals, a refinement of the Unity-Bond Index-Quadratic-Exponential Potential (UBI-QEP) approach originally developed for the predicting the energetics of *surface* reaction and diffusion steps and apply it for the first time to atomic impurities in bulk metal. For the kinetic and diffusion steps, we utilize Eyring's transition-state theory framework that requires estimates of entropy and enthalpy of activation. For estimating the entropy changes

for both thermodynamics and kinetic parameters, we adopt the simple "free volume" model of Eyring. The resulting theory reliably predicts the various parameters that agree with experimental results on solution and diffusion of hydrogen in a supported liquid gallium membrane. Below 350 ºC, the rate of adsorption controls the rate of permeation, while above it the permeation is controlled by diffusion.

5.2 Introduction

There is a great deal of interest in developing dense metal membranes for separating and purifying hydrogen to the high purity needed for fuel cells and other applications. Those based on Pd and its alloys are the most advanced, and are being considered at the pilot plant stage for hydrogen purification (Ayturk et al., 2009). However, Pd membranes are still too expensive, subject to poisoning, and wanting in durability. Consequently, other metals are being investigated for this application (Phair and Donelson, 2006), but their development is not as far along as Pd. We have developed an entirely novel class of supported liquid metal membranes (SLiMM) (Figure 7.1) that shows considerable promise. However, there are a number of technical problems that still need to be resolved for practical applications including choice of robust and inert supports, and membrane wetting and stability. Further, much work is needed to develop the fundamental understanding needed to advance the technology further. This chapter represents a start in that direction. Another reason for understanding solution and diffusion of hydrogen and its isotopes in liquid metals is because of their use in fast neutron reactors as coolants (Schumacher and Weiss, 1990). The solubility of hydrogen is also important in casting metals as appied in the aerospace, automotive, and structural components (Shivkumar et al., 1991) and potentially in hydrogen storage. There is also little in the way of robust modeling of solution and interstitial diffusion or solubility of hydrogen (Emi and Pehlke, 1970; Mainwood

and Stoneham, 1976; Nachtrieb, 1976) and other diatomic gases such as O_2 and N_2, in liquid metals.

The objective of this work is the development of a predictive quasi-crystalline model of surface dissociative adsorption, dissolution, and atomic diffusion in a liquid metal for the case of a dilute solution, when thermodynamic nonideality is not important. We will follow the overall theoretical framework developed in our recent work on Pd (Deveau et al., 2013). For the diffusion, we will follow the quasi-crystalline approach of Eyring and coworkers coupled with free volume theory for estimation of entropy change. For reaction thermodynamics and activation barriers, we utilize our semi-empirical approach (as described in chapter 4) based on a combined Pauling Bond Valence-Morse Potential (PBV-MMP), which is a refinement of the Unity-Bond Index-Quadratic-Exponential Potential (UBI-QEP) of Shustorovich (1986) developed for predicting energetics of metal surface catalysis.

The Pauling bond valence (PBV) method (Morse, 1929; Pauling, 1947; 1949; 1960) is based on a set of rules or heuristic principles, which have proved in recent years to be highly useful in structure elucidation of ionic solids (e.g., Brown, 2009; Brown and Poeppelmeier, 2014). However, the focus of this work has been on the crystal structure of inorganic ionic solids, not on their energetics, or on crystal structure of metals or alloys. Our methodology, on the other hand, is concerned with the application and extension of the PBV approach to structural as well as energetic considerations of metals, the latter by invoking a modified Morse potential (MMP) for two-center bond energy, and is hence called the PBV-MMP approach. While it is similar to the UBI-QEP method, there are some key differences. Thus, the UBI-QEP model involves a "quadratic-exponential" potential energy model, a modified form of Morse potential, in terms of a "bond-index" that sums to unity. However, the nature of the bond index and any relation to

bond valence is not explicated. The PBV-MMP model adopts a modified Morse potential in terms of the PBV that sums over all its bonds to atomic valence, another well-accepted rule widely used in the modern bond valence theory (Brown, 2009). Further, the UBI-QEP model is silent on the bond-valence (BV) bond-length (BL) relationship, being concerned mainly with the extrema, i.e., maximum and minimum on the energy landscape. On the other hand, the PBV-MMP model is able to predict the individual bond lengths and the bond valences along with bond energies, based on the PBV-BL correlation.

5.3 Sequence of Steps

The mechanism of hydrogen permeation through a dense metal membrane is shown in Figure 5.1 and as described in section 2.3. It involves the following steps (Deveau et al., 2013): s_1) the H_2 molecules on the feed side (denoted by the subscript "*f*") undergo dissociative adsorption on surface sites S forming adsorbed H atoms, $H \cdot S_f$, s_2) which then infiltrate bulk lattice, occupying the sub-surface interstitial sites M as $H \cdot M_f$, s_3) the interstitial H atoms then diffuse across the membrane via hopping, s_4) on reaching the permeate side (denoted by the subscript "*p*") of the Pd membrane, the interstitial H atoms $H \cdot M_p$ then egress from the bulk metal to its surface, and finally s_5) the adsorbed H atoms $H \cdot S_p$ associatively desorb as H_2 molecules on the permeate side.

$$
\begin{array}{lll}
\underline{s_\rho} & & \underline{\sigma_\rho} \\
s_1: & H_{2,f} + 2S_f \leftrightarrows 2H \cdot S_f & +1 \quad K_1 \\
s_2: & H \cdot S_f + X_f \leftrightarrows H \cdot X_f + S_f & +2 \quad K_2 \\
s_3: & H \cdot X_f + X_p \leftrightarrows H \cdot X_p + X_f & +2 \quad K_3 \\
s_4: & H \cdot X_p + S_p \leftrightarrows H \cdot S_p + X_p & +2 \quad K_4 \\
\underline{s_5:} & 2H \cdot S_p \leftrightarrows H_{2,p} + 2S_p & \underline{+1 \quad K_5} \\
OR: & H_{2,f} \leftrightarrows H_{2,p} &
\end{array}
\tag{5.1}
$$

The surface site, in general, may require binding to n_Σ metal atoms, i.e., $\mathrm{S} = n_\Sigma \mathrm{M}$, while the interstitial site, X may require binding to n metal atoms, i.e., $\mathrm{X} = n\mathrm{M}$.

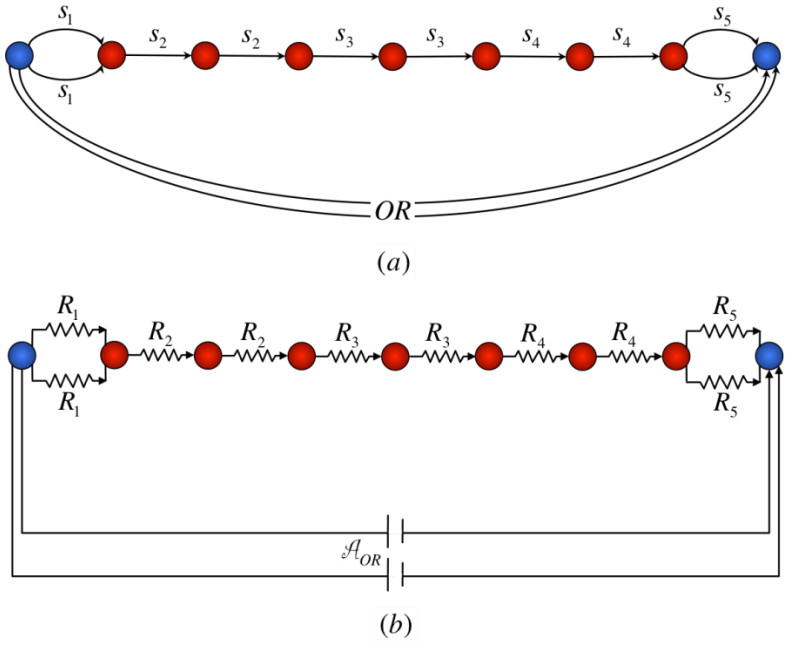

Figure 5.1 (a) RR Graph for the H_2 permeation mechanism through a metal membrane, and (b) its electrical analog (Deveau et al., 2013).

The RR graph and the corresponding electrical analog of this sequence of steps involved in the permeation of hydrogen in a dense metal membrane is shown in Figure 5.1, based on our Reaction Route (RR) Graph approach (Fishtik et al., 2004), which shows graphically how the various steps are interconnected in a reaction network depicting the overall reaction system and its pathways, and how these interconnections constrain the rates of the individual steps, and that of the OR.

There are, thus, four independent intermediates, namely, $\mathrm{H}\cdot\mathrm{S}_f$ and $\mathrm{H}\cdot\mathrm{X}_f$ on the feed side, and $\mathrm{H}\cdot\mathrm{X}_p$ and $\mathrm{H}\cdot\mathrm{S}_p$ on the permeate side, besides the surface site, S and the interstitial site, X, which are not independent by virtue of site, i.e., mass balance on both the feed side and the permeate side. The concentrations of these four independent intermediates are unknown, and

their determination is the key goal in kinetics analysis of the sequence, e.g., via the quasi-steady-state (QSS) approach.

At steady-state, there are the following correlations that apply

$$r_{OR} = r_1 = \frac{r_2}{2} = \frac{r_3}{2} = \frac{r_4}{2} = r_5 \tag{5.2}$$

as evident from Figure 5.1 along with the QSS species mass balance used in kinetic analysis, i.e., $\sum_{\rho=1}^{p} \nu_{\rho i} r_\rho = 0$, where $\nu_{\rho i}$ is the stoichiometric coefficient of species *i* in step s_r.

For the four unknown intermediates, these Kirchhoff's flux law (KFL) QSS relations, Q_i, are (Fishtik et al., 2004)

$$\left.\begin{aligned} Q_{\mathrm{H{\cdot}S}_f}: &\quad 0 = (+2)r_1 + (-1)r_2 \\ Q_{\mathrm{H{\cdot}X}_f}: &\quad 0 = (+1)r_2 + (-1)r_3 \\ Q_{\mathrm{H{\cdot}X}_p}: &\quad 0 = (+1)r_3 + (-1)r_4 \\ Q_{\mathrm{H{\cdot}S}_p}: &\quad 0 = (+1)r_4 + (-2)r_5 \end{aligned}\right\} \tag{5.3}$$

which are akin to KFL relations at the nodes (Figure 5.1). These species QSS relations provide the 4 relations that are needed to solve for the concentrations of the 4 unknown intermediate species. The combination of step 1 and 2 is hydrogen dissolution into liquid gallium and step 3 is the hydrogen diffusion in the liquid bulk. The equilibrium constant K_ρ of these individual steps are $K_\rho = \frac{\vec{k}_\rho}{\overleftarrow{k}_\rho}$ and the Arrhenius relations for the different rate parameters are

$$\begin{aligned} &\vec{k}_1 = \vec{\Lambda}_1 \exp\left(-\frac{\vec{E}_1}{RT}\right);\ \overleftarrow{k}_1 = \overleftarrow{\Lambda}_1 \exp\left(-\frac{\overleftarrow{E}_1}{RT}\right); \\ &\vec{k}_2 = \vec{\Lambda}_2 \exp\left(-\frac{\vec{E}_2}{RT}\right);\ \overleftarrow{k}_2 = \overleftarrow{\Lambda}_2 \exp\left(-\frac{\overleftarrow{E}_2}{RT}\right) \end{aligned} \tag{5.4}$$

where from the transition-state theory, the frequency factors

$$\vec{\Lambda}_\rho = \kappa \frac{k_B T}{h} \exp\left(\frac{\Delta \vec{S}_\rho^{\ddagger,o}}{R}\right) \; ; \; \overleftarrow{\Lambda}_\rho = \kappa \frac{k_B T}{h} \exp\left(\frac{\Delta \overleftarrow{S}_\rho^{\ddagger,o}}{R}\right) \tag{5.5}$$

while the entropy changes of activation and activation energies are related to step thermodynamics via the relations

$$\Delta S_\rho^o = \Delta \vec{S}_\rho^{\ddagger,o} - \Delta \overleftarrow{S}_\rho^{\ddagger,o} \; ; \; \Delta H_\rho^o = \vec{E}_\rho - \overleftarrow{E}_\rho \tag{5.6}$$

5.4 Hydrogen Dissociative Surface Adsorption

5.4.1 Heat of Dissociative Adsorption

To evaluate the enthalpy change of dissociative hydrogen adsorption $\mathrm{H_2 + 2S \leftrightarrows 2H \cdot S}$, $\Delta H_{ad} = \Delta H_1$, we consider the following Hess's cycle

$$\begin{array}{lllll} \underline{s_\rho} & & & \underline{\Delta H_\rho^o} & \underline{\sigma_\rho} \\ s_i: & \mathrm{H_2}(g) \leftrightarrows \mathrm{H}(g) + \mathrm{H}(g) & & +D_{\mathrm{H\text{-}H}}^o & +1 \\ s_{ii}: & \mathrm{H}(g) + n_\Sigma \mathrm{M} \leftrightarrows \mathrm{H \cdot M}_{n_\Sigma} & & -Q_{\mathrm{H \cdot M}_{n_\Sigma}} & +2 \\ \hline OR: & \mathrm{H_2} + n_\Sigma \mathrm{M} \leftrightarrows 2\mathrm{H \cdot M}_{n_\Sigma} & & \Delta H_1^o = D_{\mathrm{H\text{-}H}}^o - 2Q_{\mathrm{H \cdot M}_{n_\Sigma}} & \end{array} \tag{5.7}$$

where $D_{\mathrm{H\text{-}H}}^o$ is the binding energy of $\mathrm{H_2}$, while $Q_{\mathrm{H\text{-}M}_{n_\Sigma}}$ is the binding energy for the surface bound H atom, and the surface site, $\mathrm{S} = n_\Sigma \mathrm{M}$. Assuming that the binding is limited to the nearest neighbor metal atoms (Figure 5.2), or equivalently, the number of metal atoms defining the binding site, $n_\Sigma = 1$ for ontop (t), $n_\Sigma = 2$ for bridge (b), $n_\Sigma = 3$ for fcc (111) hollow (h), $n_\Sigma = 4$ for fcc (100) hollow, $n_\Sigma = 5$ for bcc (100) hollow. Since the fcc (111) and (100) surfaces are densely packed, the metal atoms from the second layer are not nearest neighbors and therefore are considered to be not coordinated with A. Unlike this, however, $n_\Sigma = 4$ for fcc (100), the coordination of $n_\Sigma = 5$ for bcc (100) can be realized because bcc (100) is not densely packed and the fifth metal atom from the second layer may also be a nearest neighbor (being at the same or

even shorter distance as the four metal atoms of the top layer) and available for coordination with adsorption atom A.

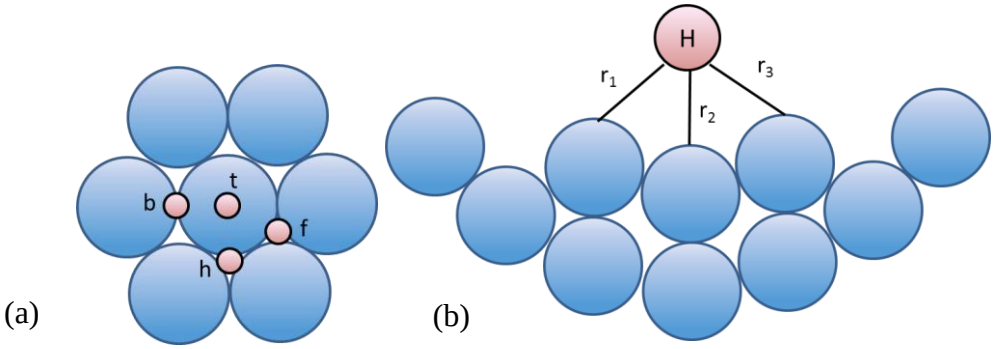

Figure 5.2 (a) Top view of adsorption sites on 111 metal surface: t, ontop; b, bridge; f, fcc hollow; h, hcp hollow (German et al., 2008); (b) side view of adsorbed atom in an fcc (111) 3-fold ($n_\Sigma = 3$) metal binding site. The corresponding bond orders are $x_{\mathrm{AM},i}(r_i)$ (i = 1, 2, 3), all assumed equal (Shustorovich and Sellers, 1998).

In other words, the heat of adsorption step

$$\Delta H_1^o = D_{\mathrm{H-H}}^o - 2Q_{\mathrm{H\cdot Mn_E}} \tag{5.8}$$

For determining the binding energy of an atom A on a metal surface, $Q_{\mathrm{A\text{-}M}_{n_\Sigma}}$, we follow Our PBV-MMP model, along the lines of the UBI-QEP method of Shustorovich (1986) developed for metal-surface catalysis, involving the heuristics and assumptions that are thoroughly described in chapter 4 (Morse, 1929; Pauling , 1947; 1960 pp. 543; Pauling and Kamb, 1986; Shustorovich, 1986; Benziger, 1991).

Assuming next that the n_Σ bonds are all *equivalent*, then $x_{\mathrm{A-M,i}} = 1/n_\Sigma$. The total bond energy of the adsorbed A for all the n_Σ bonds then, using the PBV-MMP reduces to

$$Q_{\mathrm{A\cdot M}_{n_\Sigma}} = D_{\mathrm{AM}}^{\mathrm{o}}\left(2 - \frac{1}{n_\Sigma}\right) \tag{5.9}$$

In short, the on-top site ($n_\Sigma = 1$, $Q_{\mathrm{A{\cdot}M}_{n_\Sigma}} = D^{\mathrm{o}}_{\mathrm{AM}}$) is energetically the least favorable, but energy differences among the various hollow sites ($n_\Sigma = 3, Q_{\mathrm{A{\cdot}M}_{n_\Sigma}} = 1.67 D^{\mathrm{o}}_{\mathrm{AM}}$; $n_\Sigma = 4$, $Q_{\mathrm{A{\cdot}M}_{n_\Sigma}} = 1.75 D^{\mathrm{o}}_{\mathrm{AM}}$; $n_\Sigma = 5, Q_{\mathrm{A{\cdot}M}_{n_\Sigma}} = 1.8 D^{\mathrm{o}}_{\mathrm{AM}}$) are relatively small. The bridge site ($n_\Sigma = 2$, $Q_{\mathrm{A{\cdot}M}_{n_\Sigma}} = 1.5 D^{\mathrm{o}}_{\mathrm{AM}}$) is the saddle point between two hollow site minima.

To be fully predictive, one would require the MP parameters, $D^{\mathrm{o}}_{\mathrm{AM}}$, *b*, and $r^{\mathrm{I}}_{\mathrm{AM}}$ (or $r^{\mathrm{o}}_{\mathrm{AM}}$) described in chapter 4. However, to make it free of the structural parameters *b*, and $r^{\mathrm{I}}_{\mathrm{AM}}$, the UBI-QEP method focuses only on the stationary points, minima and maxima, of the potential energy surface. For this, only the thermodynamic data, $D^{\mathrm{o}}_{\mathrm{AM}}$, is needed. Shustorovich and Sellers (1998) have provided these values for common ad atoms on transition metals. However, these are not available for liquid metals of interest to us. Further, by incorporating the Pauling relation between BL and BV, we have available estimates of *b* and $r^{\mathrm{I}}_{\mathrm{AM}}$ as well (e.g., Pauling and Kamb, 1986).

Note further that the energy minimum Q_{AM_n} is obtained above without detailed knowledge of bond lengths or angles, and this simplicity is a key advantage of the UBI-QEP method, although with our combination of the Pauling and the Morse relations, this is now accessible. Further, the maximum A–M bond energy (for on-top site) $D^{\mathrm{o}}_{\mathrm{AM}}$ is a characteristic of the metal and applies to any surface configuration of the metal. The accuracy of predictions is clearly dependent on the accuracy of available value of $D^{\mathrm{o}}_{\mathrm{AM}}$.

5.4.2 Gallium Hydrogen Adsorption Energy

While we need to carefully consider a model for the restructured liquid Ga surface and decide on a coordination number for a H atom on the surface, if the liquid Ga surface is assumed similar to that of solid as shown in Figure 5.2, then it is conceivable that the H atom is indeed coordinated

to $n_\Sigma = 3$ Ga atoms forming the triangles in the hexagonal puckered surface (as shown in section 3.3, Figure 3.4). Let's assume for now that this is the case.

We can estimate the H-Ga bond length as follows. Following Pauling (1960, p. 257), since H has unit valence, i.e., V_A = 1, we can assume that the unit valence internuclear distance between H and Ga is roughly $r^{o}_{H\cdot Ga} = (d_H + d_{Ga})/2$, where $d_H = 62\,\text{pm}$ is the covalent diameter of H (covalent radius of 0.31 Å from Cordero et al., (2008)) and $d_{Ga} = 244\,\text{pm}$ is that for Ga. Thus, $r^{o}_{H\cdot Ga} \approx 153$ pm. On the other hand, Campbell et al. (1993) provide $r^{o}_{H\cdot Ga} = 166$ pm based on IR spectra of GaH, which is adopted here in the Pauling correlation,

$$r_{ij} = r^{I}_{ij} - b_i \ln v_{ij} = r^{o}_{ij} - b_i \ln v_{ij} \tag{5.10}$$

Further, we can estimate the H-Ga adsorption energteics as follows. Thus, Krishtalik (1970) and Appleby (1983) reports $-\Delta H^{o}_{H,ad} = Q_{H\cdot Gan_\Sigma} = 40\,\text{kcal/g-atm H}$ on liquid Ga surface, i.e., 167.5 kJ/g-atom H. Using this in the relation $-\Delta H^{o}_{H,ad} = Q_{H\cdot Gan_\Sigma} = D^{o}_{H\cdot Ga}(2 - 1/n_\Sigma) = 167.5\,\text{kJ/g-atom H}$, and assuming the $n_\Sigma = 3$ the calculated MP binding energy for H on Ga is $D^{o}_{H\cdot Ga} = 100.5\,\text{kJ/g-atom H}$ on Ga. (On the other hand, based on IR spectra of GaH, Campbell et al. (1993) provide $D^{o}_{H\cdot Ga} = 2.29\times10^{-4}$ cm^{-1} that provides $D^{o}_{H\cdot Ga} = 57.5$ kJ/mol at 1400 ºC.)

Further, from above, with $D^{o}_{H\text{-}H} = 435.8$ kJ/mol H_2, the heat of adsorption of hydrogen on Ga is $\Delta H^{o}_1 = D^{o}_{H\text{-}H} - 2Q_{H\cdot Mn_\Sigma} = 435.8 - 2\times167.5 = 100.8\,\text{kJ/mol H}_2$. In other words, the H adsorption on Ga is significantly endothermic, as expected. In contrast, the heat of adsorption of H on Pd is exothermic, with $\Delta H^{o}_{H,ad} = -83.7$ kJ/mol H_2 (Deveau et al., 2013), that is incidentally also well-predicted by the UBI-QEP method $\Delta H^{o}_1 = 435.8 - 2\times259.1 = -82.52\,\text{kJ/mol H}_2$ (Pd-H on (111) surface $D^{o}_{AM} = 259.1\,\text{kJ/mol}$ provided by Benziger (1991)).

Figure 5.3 is a plot of the MPP Eq. (4.6), combined with the Pauling correlation, Eq. (4.3) in chapter 4, i.e., of

$$-E_{\mathrm{H\cdot Ga}} = D^{\mathrm{o}}_{\mathrm{H\cdot Ga}}\left\{2e^{-\left(\frac{r_{\mathrm{H\cdot Ga}}-r^{\mathrm{o}}_{\mathrm{H\cdot Ga}}}{b_{\mathrm{H}}}\right)} - e^{-2\left(\frac{r_{\mathrm{H\cdot Ga}}-r^{\mathrm{o}}_{\mathrm{H\cdot Ga}}}{b_{\mathrm{H}}}\right)}\right\} \tag{5.11}$$

with the paremeters estimated as above, i.e., $D^{\mathrm{o}}_{\mathrm{H\cdot Ga}} = 100.5\,\mathrm{kJ/g\text{-}atom}$, $r^{\mathrm{I}}_{\mathrm{H\cdot Ga}} = r^{\mathrm{o}}_{\mathrm{H\cdot Ga}} = 166$ pm, since $V_{\mathrm{H}} = 1.0$, and with a fitted parameter $b_{\mathrm{H}} = 0.75$. The parameter b determines the width of the energy well. For H, Shustorovich (1986) proposes $b = 0.8-1$ Å. It is possible that the common average value of the parameter $b = 0.37$ Å used in chapter 4 is not applicable to this system (Shustorovich, 1986). In fact, we find that $b_{\mathrm{H}} = 0.75$ Å provides a good fit of the modified Morse potential with the Born-Oppenheimer potential for H-Ga proposed by Campbell et al. (1993), as shown in the Figure 5.3, based on IR spectra for H-Ga.

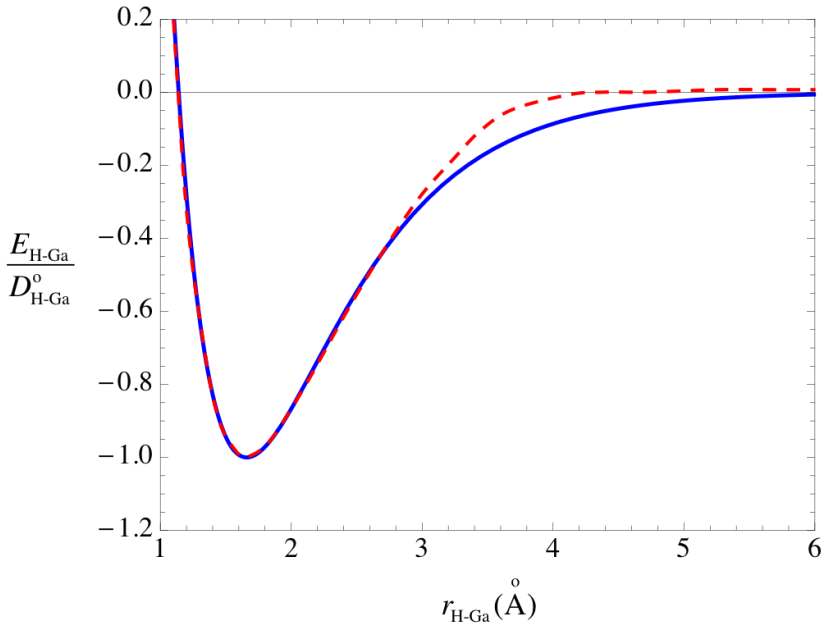

Figure 5.3 A comparison of the proposed modified Morse potential for H-Ga two-center interactio with the Born-Oppenheimer potential (Campbell et al., 1993). The MMP parameters used are $D^{\mathrm{o}}_{\mathrm{H\cdot Ga}} = 100.5\,\mathrm{kJ/g\text{-}atom\,H}$ on Ga, $r^{\mathrm{o}}_{\mathrm{H\cdot Ga}} = 166$ pm, and $b_{\mathrm{H}} = 0.75$.

Now that $b_{\mathrm{H}} = 0.75$ is has been determined for H, the Ga-H bond length is plotted in Figure 5.4 versus the coordination number *n* with Ga, using Eq. (5.10). Thus, for surface coordination in a hollow site, i.e., for $n_{\Sigma} = 3$, the internuclear distance between H and Ga atoms is roughly $r_{\mathrm{H\cdot Ga}}$ = 250 pm.

Finally, Figure 5.5 provides a plot of the potential energy of multi-center interaction between H atom and the Ga surface $-E_{\mathrm{H\cdot Ga}} = D^{\mathrm{o}}_{\mathrm{H\cdot Ga}} = 100.5(2 - 1/n_{\Sigma})$ versus the coordination number n_{Σ}, using Eq. (5.9).

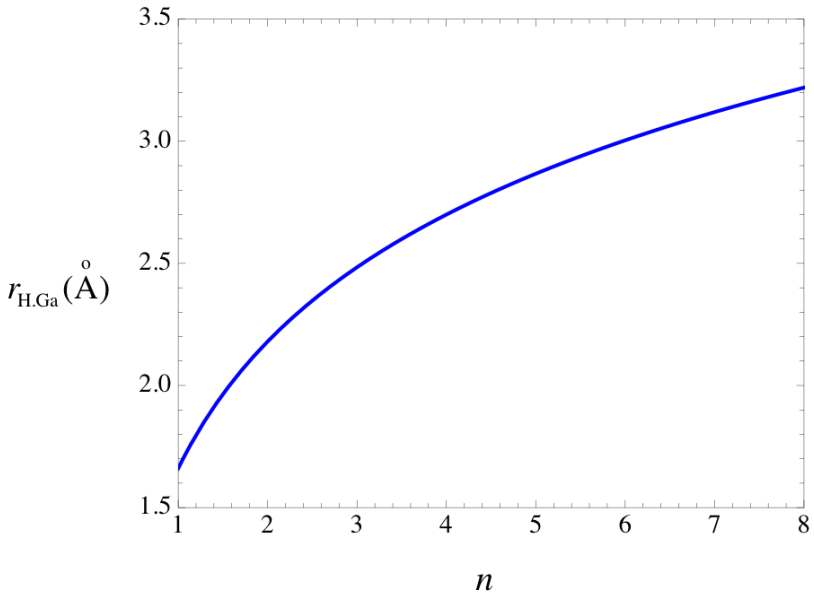

Figure 5.4 Estimated average internuclear distance between H and Ga atoms versus coordination number *n*, with parameters $r^{\mathrm{o}}_{\mathrm{H\cdot Ga}} = 166$ pm, and $b_{\mathrm{H}} = 0.75$, based on Eq. (5.10).

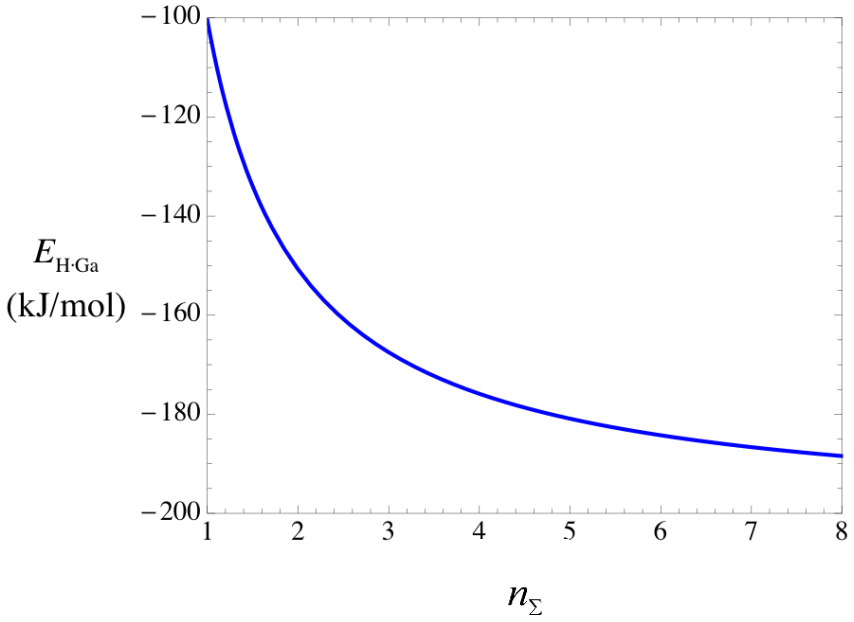

Figure 5.5. The total potential energy of interaction between H atom and the Ga atoms $-E_{\mathrm{H\cdot Ga}} = D^{\circ}_{\mathrm{H\cdot Ga}}$ versus the coordination number n_Σ, with parameters $D^{\circ}_{\mathrm{H\cdot Ga}} = 100.5$ kJ/g-atom H on Ga, $r^{\circ}_{\mathrm{H\cdot Ga}} = 166$ pm, and b_{H} = 0.75, based on Eq. (5.9).

5.4.3 Molecular Adsorption and Step-wise Dissociation

Even though the first step assumed in the above sequence of steps adopted in the mechanism of hydrogen dissolution and diffusion is the direct dissociative adsorption of hydrogen in the hollow sites on the metal surface, this can conceivably be broken down further into two (or more) elementary steps, as shown schematically in Figure 5.6 : 1) thus, the first step is the barrierless molecular adsorption of the diatomic molecule on an on-top site, comprising of two adjacent metal atoms; 2) this is followed by the surface dissociation reaction via a transition state into two H adsorbed atoms in the more stable configuration of a hollow site, i.e., each H atom bound to 3 surface atoms, as shown schematically in Figure 5.6. A schematic of the energy landscape of the molecular adsorption and surface dissociation of a diatomic molecule on a metal surface is also depicted in Figure 5.6.

In general, thus, a diatomic molecule AB (with the bond dissociation energy D^{o}_{AB}) can bind to a surface via *both* A and B contact atoms leading to di-AB-coordination, typically spanning a bridge site, as shown in Figure 5.7.

The total energy then is

$$E_{AB} = Q^{o}_{AM}(x^{2}_{A} - 2x_{A}) + Q^{o}_{BM}(x^{2}_{B} - 2x_{B}) + D^{o}_{AB}(x^{2}_{AB} - 2x_{AB}) \tag{5.12}$$

where Q^{o}_{AM} and Q^{o}_{BM} are the binding energies of the atomic species A and B at the surface and D^{o}_{AB} the dissociation energy of AB in the gas phase. This is subject to the UBI constraint

$$x_{A} + x_{B} + x_{AB} = 1 \tag{5.13}$$

The energy minimization is discussed by Shustorovich (1986), by Shustorovich and Sellers (1998), and by Maestri and Reuter (2011). The resulting formula for the binding energy of the AB molecule to the surface is provided therein. Here, we are interested mainly in the version of the formula applicable for homonuclear diatomic molecule (A_2 e.g., H_2), for which the binding energy takes the form

$$Q_{AA\cdot M_2} = \frac{9(Q^{o}_{AM})^{2}}{6Q^{o}_{AM} + D^{o}_{AA}} \tag{5.14}$$

For instance, for dicoordinated H_2 molecule adsorption on Ga surface, this yields $Q_{HH\cdot\cdot M_2} = 9(100.5)^{2}/(6(100.5) + 435.8) = 87.5$ kJ/mol H_2, which is also the exothermic heat of molecular H_2 adsorption (Figure 5.6).

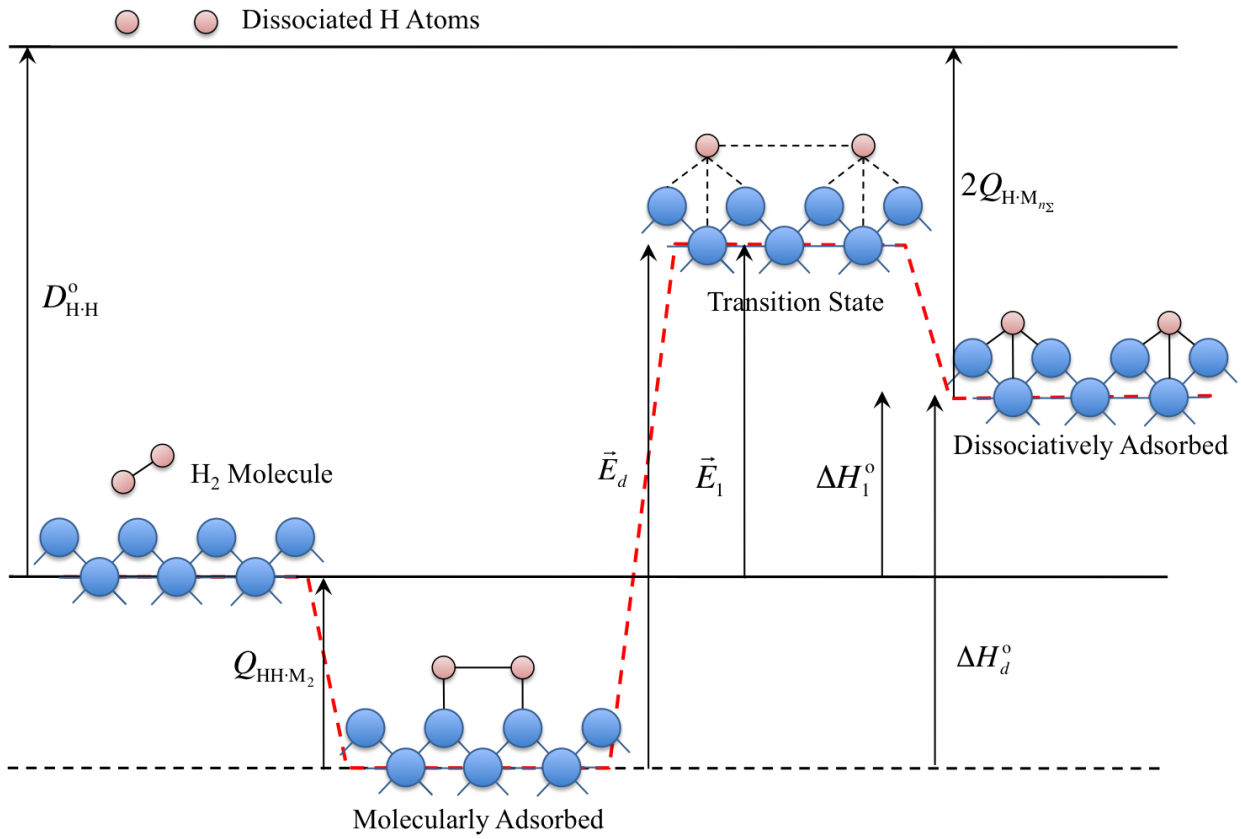

Figure 5.6 Schematic of a mechanism and the corresponding energy landscape of two-step dissociative adsorption of H_2 on a metal surface including the transition state for the surface dissociation reaction. The bonds among the various atoms (hydrogen and metal) are shown, with dashed lines representing bonds of the transition state complex.

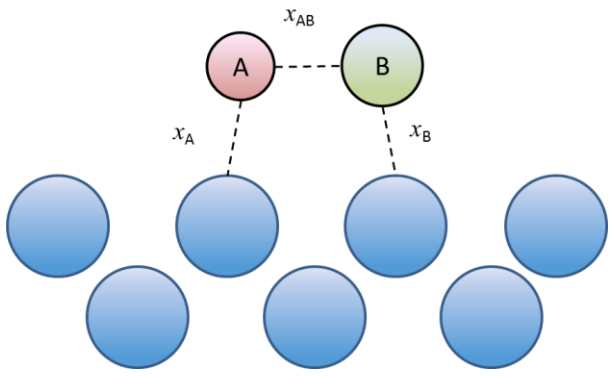

Figure 5.7. Adsorbed molecule A-B in a bridge metal binding site (Shustorovich and Sellers, 1998).

The total energy then is

$$E_{\mathrm{AB}} = Q^{\mathrm{o}}_{\mathrm{AM}}(x^2_{\mathrm{A}} - 2x_{\mathrm{A}}) + Q^{\mathrm{o}}_{\mathrm{BM}}(x^2_{\mathrm{B}} - 2x_{\mathrm{B}}) + D^{\mathrm{o}}_{\mathrm{AB}}(x^2_{\mathrm{AB}} - 2x_{\mathrm{AB}}) \tag{5.12}$$

where $Q^{\mathrm{o}}_{\mathrm{AM}}$ and $Q^{\mathrm{o}}_{\mathrm{BM}}$ are the binding energies of the atomic species A and B at the surface and $D^{\mathrm{o}}_{\mathrm{AB}}$ the dissociation energy of AB in the gas phase. This is subject to the UBI constraint

$$x_{\mathrm{A}} + x_{\mathrm{B}} + x_{\mathrm{AB}} = 1 \tag{5.13}$$

The energy minimization is discussed by Shustorovich (1986), by Shustorovich and Sellers (1998), and by Maestri and Reuter (2011). The resulting formula for the binding energy of the AB molecule to the surface is provided therein. Here, we are interested mainly in the version of the formula applicable for homonuclear diatomic molecule (A_2 e.g., H_2), for which the binding energy takes the form

$$Q_{\mathrm{AA{\cdot}M_2}} = \frac{9(Q^{\mathrm{o}}_{\mathrm{AM}})^2}{6Q^{\mathrm{o}}_{\mathrm{AM}} + D^{\mathrm{o}}_{\mathrm{AA}}} \tag{5.14}$$

For instance, for dicoordinated H_2 molecule adsorption on Ga surface, this yields $Q_{\mathrm{HH{\cdot\cdot}M_2}} = 9(100.5)^2/(6(100.5)+435.8) = 87.5\,\mathrm{kJ/mol\ H_2}$, which is also the exothermic heat of molecular H_2 adsorption (Figure 5.6).

For the next step, from a Hess cycle (Figure 5.6) composed of AB molecular desorption, AB gas-phase molecular dissociation, and A and B atomic chemisorption onto the hollow sites, the enthalpy change for the surface dissociation reaction $\mathrm{AB{\cdot}M_2} \leftrightarrows \mathrm{A{\cdot}M_{n_\Sigma}} + \mathrm{B{\cdot}M_{n_\Sigma}}$

$$\Delta H^{\mathrm{o}}_d = Q_{\mathrm{AB{\cdot}M_2}} + D^{\mathrm{o}}_{\mathrm{AB}} - Q_{\mathrm{A{\cdot}M_{n\Sigma}}} - Q_{\mathrm{B{\cdot}M_{n\Sigma}}} = \vec{E}_d - \overleftarrow{E}_d \tag{5.15}$$

For example, for adsorbed H_2 dissociation on Ga surface, $\Delta H^{\mathrm{o}}_d = Q_{\mathrm{AB{\cdot}M_2}} + D^{\mathrm{o}}_{\mathrm{H\text{-}H}} - 2Q_{\mathrm{H{\cdot}M_{n\Sigma}}}$ $= 87.5 + 435.8 - 2(167.5) = 188.3\,\mathrm{kJ/mol}$, i.e., it is a significantly endothermic reaction.

Next, for calculating the activation barrier for the dissociative chemisorption $\mathrm{H_2} + 2\mathrm{S} \leftrightarrows 2\mathrm{H}\cdot\mathrm{S}$, we write this as the sum of the following two steps (Figure 5.6)

$$\begin{array}{lllll} \underline{s_\rho} & & & \underline{\Delta H_\rho^{\mathrm{o}}} & \underline{\sigma_\rho} \\ s_i: & \mathrm{H_2}(g) + 2\mathrm{M} \leftrightarrows \mathrm{HH}\cdot\mathrm{M_2} & & -Q_{\mathrm{AB}\cdot\mathrm{M_2}} & +1 \\ s_r: & \mathrm{HH}\cdot\mathrm{M_2} + (n_\Sigma - 2)\mathrm{M} \leftrightarrows 2\mathrm{H}\cdot\mathrm{M}_{n_\Sigma} & & \Delta H_D^{\mathrm{o}} & +1 \\ \hline OR: & \mathrm{H_2}(g) + n_\Sigma\mathrm{M} \leftrightarrows 2\mathrm{H}\cdot\mathrm{M}_{n_\Sigma} & & \Delta H_1^{\mathrm{o}} = \Delta H_D^{\mathrm{o}} - Q_{\mathrm{AB}\cdot\mathrm{M_2}} & \end{array} \tag{5.16}$$

Consequently, $\Delta H_1^{\mathrm{o}} = \Delta H_d^{\mathrm{o}} - Q_{\mathrm{HH}\cdot\mathrm{M_2}} = 188.3 - 87.5 = 100.8\,\mathrm{kJ/mol}$ as calculated independently above, so that the above calculations are self-consistent.

We are also interested in the activation energy for dissociation of the hydrogen molecule on the surface, as shown in Figure 5.6. The interaction energy E_{AB} between the molecule AB and the surface is given by Eq. (5.12) above, subject to the UBI constraint, Eq. (5.13). The other energy curve in Figure 5.7 is the sum of the atom-surface energies of non-interacting ($x_{\mathrm{AB}} = 0$) adatoms, A and B, as a function of atom-surface distance, or bond order

$$E_{\mathrm{A+B}} = E_{\mathrm{A}} + E_{\mathrm{B}} = Q_{\mathrm{AM}}^{\mathrm{o}}(x_{\mathrm{A}}^2 - 2x_{\mathrm{A}}) + Q_{\mathrm{BM}}^{\mathrm{o}}(x_{\mathrm{B}}^2 - 2x_{\mathrm{B}}) \tag{5.17}$$

This is not subject to the UBI constraint, since the adatoms are independent of each other. The intersection of the two curves is the Lennard-Jones maximum energy barrier.

Then the Lennard-Jones activation barrier relative to the adsorbed reactant

$$\vec{E}_{d,\mathrm{LJ}} = \Delta H_d^{\mathrm{o}} + \frac{Q_{\mathrm{A}\cdot\mathrm{M}_{n_\Sigma}} Q_{\mathrm{B}\cdot\mathrm{M}_{n_\Sigma}}}{Q_{\mathrm{A}\cdot\mathrm{M}_{n_\Sigma}} + Q_{\mathrm{B}\cdot\mathrm{M}_{n_\Sigma}}} \tag{5.18}$$

where enthalpy change for the surface dissociation reaction is given above. For example, for $\mathrm{H_2}$ dissociation on Ga surface, $\vec{E}_{d,\mathrm{LJ}} = \Delta H_d^{\mathrm{o}} + Q_{\mathrm{A}\cdot\mathrm{Mn}_\Sigma}/2 = 188.3 + 167.5/2 = 272\,\mathrm{kJ/mol}$. If this were true, then we could estimate, e.g., (Figure 5.6) that $\vec{E}_1 = \vec{E}_{\mathrm{d}} - Q_{\mathrm{HH}\cdot\mathrm{M_2}} = 272 - 87.5 = 184.5\,\mathrm{kJ/mol}$. Further, $\overleftarrow{E}_1 = \vec{E}_1 - \Delta H_1^{\mathrm{o}} = 184.5 - 100.8 = 83.7\,\mathrm{kJ/mol}$.

However, this is possibly an overestimation of the activation barrier for the dissociation reaction as it assumes $x_{\mathrm{AB}} = 0$ at the transition state, when in fact it is finite. If we could estimate x_{AB} at the transitional state (TS), we could estimate the activation barrier. An interpolated (tantamount to choosing the x_{AB} at the TS) estimate for energy barrier of surface dissociation reaction is (Shustorovich and Sellers, 1998)

$$\vec{E}_d = \beta_d \left(\Delta H_d^{\mathrm{o}} + \frac{Q_{\mathrm{A{\cdot}M}_{n_\Sigma}} Q_{\mathrm{B{\cdot}M}_{n_\Sigma}}}{Q_{\mathrm{A{\cdot}M}_{n_\Sigma}} + Q_{\mathrm{B{\cdot}M}_{n_\Sigma}}} \right) \tag{5.19}$$

where the parameter $\beta_d \to 1$ for a late TS, while $\beta_d \to 0$ for an early TS (Maestri and Reuter, 2011). In the standard formulation of the UBI-QEP methid $\beta_d = 1/2$ is assumed (Shustorovich and Sellers, 1998). Thus, for adsorbed H_2 dissociation on the Ga surface, $\vec{E}_{\mathrm{d}} = (188.3 + 167.5^2/(2\times 167.5))/2 = 136\,\mathrm{kJ/mol}$ i.e., half of the LJ estimate. In this case, $\vec{E}_1 = \vec{E}_{\mathrm{d}} - Q_{\mathrm{HH{\cdot}M_2}} = 136 - 87.5 = 48.5\,\mathrm{kJ/mol}$ then $\overleftarrow{E}_1 = \vec{E}_1 - \Delta H_1^{\mathrm{o}} = 48.5 - 100.8 = -52.3\,\mathrm{kJ/mol}$ which is clearly incorrect.

On the other hand, Maestri and Reuter (2011), proposed while $\beta_d \approx 0.7$ based on comparison of the UBI-QEP predictions with a fitted parameter β_d versus DFT predictions for various surface dissociation reactions. Using this we get $\vec{E}_d = 190.5\,\mathrm{kJ/mol}$ and $\vec{E}_1 = 103\,\mathrm{kJ/mol}$.

Thus, if these are correct then from $\overleftarrow{E}_1 = \vec{E}_1 - \Delta H_1 = 103 - 100.8 = 2.2\,\mathrm{kJ/mol}$ which is certainly plausible. However, to avoid making arbitrary assumptions regarding the parameter β_d and because the dissociative adsorption step is significantly endothermic, we will simply assume that $\vec{E}_1 = \Delta H_1^{\mathrm{o}} = 100.8\,\mathrm{kJ/mol}$ and that the reverse step is barrierless, i.e., $\overleftarrow{E}_1 = 0$.

5.4.4 Entropy Change of Adsorption

Instead of using the transition-state theory for $\vec{\Lambda}_1$, i.e., Eq. (5.5), we use, as is common (Ward and Dao, 1999; Deveau et al., 2013), the collision theory, i.e.,

$$\vec{\Lambda}_1 = \frac{p^{\circ}}{c_{S,t}} \sqrt{\frac{1}{2\pi M_{H_2} RT}} \tag{5.20}$$

where $c_{S,t} = 1/\overline{V}_M$ is the total concentration of the surface metal atoms, $\overline{V}_M$ is the molar volume of metal M and p° is the standard pressure. Eq. (5.20) provides $\vec{\Lambda}_1 = 1.42 \times 10^7$ atm^{-1}s^{-1} of Pd at 623 K. For liquid gallium at 773 K the calculated frequency factor of forward step is $\vec{\Lambda}_1 = 1.7 \times 10^7$ atm^{-1}s^{-1}. The frequency factor for the reverse step 1 is obtained from this and a combination of Eq. (5.5) and the first part of Eq. (5.6), i.e., from

$$\overleftarrow{\Lambda}_1 = \vec{\Lambda}_1 \exp\left(-\frac{\Delta S_1^{\circ}}{R}\right) \tag{5.21}$$

where the standard entropy change for step 1 is calculated, as described below, by assuming that the adsorption causes a total loss of translational entropy. Hydrogen entropy of adsorption of Pd is $\Delta S_1 = -118.7$ J/mol K (Deveau et. al., 2013). This provides, e.g., at 623 K for Pd, $\overleftarrow{\Lambda}_1 = 2.25 \times 10^{13}$ s^{-1}, similar to what might have been predicted from the TST.

The entropy change of adsorption of a monatomic gas A, i.e., for $\mathrm{A(g)} + \mathrm{S} \leftrightarrows \mathrm{A \cdot S}$

$$\Delta S_{ad}^{\circ} \equiv S_{A\cdot S}^{\circ} - S_A^{\circ}(g) \tag{5.22}$$

where ΔS_{ad}° is the standard entropy of formation of a surface species $\mathrm{A \cdot S}$, and the second term on the right is the gas-phase entropy of A. For hydrogen adsorped on liquid gallium the monatomic gas A is hydrogen atom then $S_A^{\circ}(g) = S_H^{\circ}(g)$, $\Delta S_{ad}^{\circ} = \Delta S_1^{\circ}$. The gas-phase entropy

(translational) of an ideal monatomic gas is given by the Sackur-Tetrode equation (Atkins and de Paula, 2002, p. 650)

$$S_{\mathrm{A}}^{\mathrm{o}}(g) = R\ln\left(\frac{e^{5/2}}{\lambda_t^3} v_f\right);\ \lambda_t = \frac{h}{\sqrt{2\pi m_{\mathrm{A}} k_B T}} \tag{5.23}$$

where

$$v_f = \frac{k_B T}{p^{\mathrm{o}}} \tag{5.24}$$

is the free volume in which the atom is free to move, and λ_t is the thermal wave-length. If it is assumed that there is a *total* loss of translational entropy upon adsorption (Benziger, 1991) of a freely translating gas molecule, then

$$\begin{aligned} \Delta S_{\mathrm{ad}}^{\mathrm{o}} &= -S_{\mathrm{A}}^{\mathrm{o}}(g) \\ &= -R\ln\left\{\frac{e^{5/2}(2\pi m_{\mathrm{A}} k_B T)^{3/2}}{h^3}\left(\frac{k_B T}{p^{\mathrm{o}}}\right)\right\} \\ &= -R\left[18.1 + \ln\left\{\left(\frac{T}{300}\right)^{5/2}\left(\frac{m_{\mathrm{A}}}{28}\right)^{3/2}\right\}\right] \end{aligned} \tag{5.25}$$

In the absence of specific knowledge about the adsorbed species, the entropy change associated with rotational and vibrational motion is neglected in the above, relative to the change associated with the loss of translational entropy.

For example for CO adsorption (Benziger, 1991), this equation predicts $\Delta S_{\mathrm{ad}}^{\mathrm{o}} = 150\,\mathrm{J/mol\,K}$. Experiments on CO adsorption on Ir and Ru are in the range of $110\,\mathrm{J/mol\,K} - 163\,\mathrm{J/mol\,K}$ (German et al., 2008). The agreement is better at higher coverages. Hydrogen entropy of adsorption of Cu is $\Delta S_1 = -115.78\,\mathrm{J/mol\,K}$ at 1atm, 90 K with 80% coverage (Pritchard and Tompkins, 1960).

Since the entropy of adsorbed species is generally small ($S^{o}_{A\cdot S} \to 0$), the entropy changes in *surface reactions* are often neglected. Thus, only in desorption step there will be significant entropy change, when the transition state would lie between adsorbed species and a gas molecule. Consequently, *surface reaction equilibrium* may be determined by simply estimating *enthalpy change* associated with reaction, obtained from bond energy considerations. Thus the enropy of hydrogen adosped on liquid gallium at 773 K is estimated as $\Delta S^{o}_{1} = -128.6\,\text{J/mol K}$, and $\tilde{\Lambda}_1 = 8.87\times10^{13}\,\text{s}^{-1}$.

5.5 Framework for Hydrogen Interstitial Diffusion in Bulk Liquid Metal

We will follow a quasi-crystalline model of solute diffusion in a liquid metal, although the structure is more loose than that of a solid and, consequently, not as easily described as in a solid crystal, e.g., fcc, bcc, etc. As the simple cubic structure is more open than the others, in the case of absence of better information, we may adopt this as representative of the atomic structure in a liquid metal.

Thus, we adopt Zener's (1951) approach, in which the diffusion coefficient of an atomic solute

$$D = f\frac{1}{6}\sum_{k=1}^{z}\lambda_{D,k}^{2}\nu_k \tag{5.26}$$

where ν_k is rate at which the diffusing element makes a jump of type (direction) *k* in the lattice, and $\lambda_{D,k}$ is the corresponding jump distance, discussed later on for different crystal structures. The summation is over all z_i is the number of nearest neighbor interstitial positions. Sometimes, a factor *f* may be included in the above, which takes into account correlation of subsequent jump directions. For self-diffusion, for simple cubic, *f* = 0.655, for bcc, *f* = 0.721, and for fcc, *f* = 0.781. However, if there are chemical differences, there can be strong vacancy impurity

interactions which lead to large correlation effects. In the absence of better information, we may simply assume *f* to be unity for the liquid metal.

For an isotropic structure, ν_k has a single value, ν. Thus

$$D = f\nu\frac{1}{6}\sum_{k=1}^{z}\lambda_{D,k}^2 \tag{5.27}$$

The individual jump distances to different types of sites may be replaced by λ_D, the mean jump distance defined by

$$\frac{1}{6}\sum_{k=1}^{z}\lambda_{D,k}^2 = \frac{1}{6}(a^2\sum_{k=1}^{z}\alpha^2) = \frac{1}{6}a^2(z_i\alpha^2) \tag{5.28}$$

where, we assume individual jump distance $\lambda_{D,k} = \alpha a$, where *a* is the "lattice" constant, and λ_D is the *mean* jump distance, α is the jumping distance coefficient in metal lattice and γ is geometric factor in interstitial diffusion coefficient. In other words

$$\gamma = \frac{1}{6}z_i\alpha^2 \tag{5.29}$$

For example, for interstitial diffusion in solid fcc, $\alpha = 1/\sqrt{2}$ and $z_i = 12$, so $\gamma = 1$. For interstitial diffusion in solid bcc, on the other hand $\alpha = 1/2$ and $z_i = 4$, so that $\gamma = 1/6$.

As a result

$$D = (f\gamma a^2)\nu \tag{5.30}$$

where from the thermodynamic transition-state theory (Glasstone et al., 1941)

$$\nu = \nu_0 \exp\left(-\frac{\Delta G_D^{\ddagger,o}}{\mathrm{RT}}\right) = \nu_0 \exp\left(-\frac{\Delta S_D^{\ddagger,o}}{\mathrm{R}}\right)\exp\left(-\frac{\Delta H_D^{\ddagger,o}}{\mathrm{RT}}\right) \tag{5.31}$$

where it is assumed that the transmission coefficient $\kappa = 1$, and the tunneling factor is neglected (Glasstone et al. 1941, p. 191). Further the TST provides (Glasstone et al., 1941)

$$\nu_0 = \frac{k_B T}{h} \tag{5.32}$$

Additionally, since diffusion is accompanied by negligible volume, we combine this into the conventional Arrhenius form

$$D_{\mathrm{H}} = D_{\mathrm{H},0} \exp\left(-\frac{E_D}{RT}\right) \tag{5.33}$$

where, the pre-exponential factor

$$D_{\mathrm{H},0} = f\gamma a^2 \frac{k_B T}{h} \exp\left(\frac{\Delta S_D^{\ddagger \mathrm{o}}}{R}\right) = f\gamma a^2 \frac{k_B T}{h} \exp\left(\frac{F^{\ddagger}}{F}\right) = f\gamma a^2 \Lambda_D \tag{5.34}$$

where Λ_D is the jump attempt frequency factor of diffusion step.

5.5.1 Diffusion Pre-exponential Factor

The conventional statistical mechanical transition state theory (TST) formulation relates the equilibrium constant to molecular partition functions. Thus, comparing with TST and assuming $E_D \approx \Delta H_D^{\ddagger,\mathrm{o}}$, in the above

$$\frac{F^{\ddagger}}{F} = \exp\left(\frac{\Delta S_D^{\ddagger,\mathrm{o}}}{R}\right) \tag{5.35}$$

where $F^{\ddagger}$ and F are the partition functions for the transition state and for the initial state, respectively. These include partition functions for each degree of freedom namely, electronic, rotational, vibrational, and translational. Thus (Dumesic et al. 1993) $F = F_{trans} F_{rot} F_{vib}$. For three-dimensional translation, the partition function

$$F_{trans} = F_{tx} F_{ty} F_{tz} \tag{5.36}$$

where the thermal wave length is given by (see also the corresponding entropy for an ideal monatomic gas as given by the Sackur-Tetrode equation in Atkins and de Paula, 2002, p 650)

$$F_{tx} = \frac{\sqrt{2\pi m k_B T}}{h} \tag{5.37}$$

The vibrational partition function

$$F_{vib} = \prod_j \frac{1}{1-\exp(h\nu_j / k_B T)} \tag{5.38}$$

where ν_j is the vibration frequency of each vibrational degree of freedom. And, the rotational partition function

$$F_{rot} = \frac{8\pi^2 I k_B T}{\sigma h^2} \tag{5.39}$$

where σ is symmetry number.

Using rough order-of-magnitude estimates (Dumesic et al., 1993), $k_B T/h = 10^{13}\text{s}^{-1}$, $F_{tx} = 5\times10^8$ cm^{-1} (per degree if translational freedom), $F_r = 10$ (per degree of rotational freedom), and $F_v = 1$ (per degree of vibrational freedom).

The liquid phase is treated by Eyring and coworkers as if its molecules (or atoms in a liquid metal) were free to move around within its "free" volume v_f in an average potential field due to its neighbors. Then partition function of a molecule in liquid (Eyring and Hirschfelder, 1937; Glasstone et al., 1941, p. 478)

$$F_l = F_t^3(v_f) b_l \exp\left(-\frac{E_0}{RT}\right) \tag{5.40}$$

where the first term on the RHS is the translational contribution of a single molecule moving in its free volume v_f. Further, b_l is the combined vibrational and rotational contribution, and E_0 is the difference in energy per mole between molecules in the liquid and in the gas at 0 ºK, and hence is approximately related to ΔU_{vap}. Eq. (5.40) provides the *definition* of the free volume v_f of a molecule in a liquid. We will see how this might be related to volume of liquid per

molecule, $v = V_l / N_{Av}$, where V_l is volume of a mole of the liquid. The free volume $v_f = v_l - v_0$ where v_0 is the molecular volume at absolute zero. It may be estimated from liquid density, and vapor pressure, etc.

For instance, consider the simple cubic packing as above of blue metal atoms, with one solute atom (pink) oscillating about its origin with the nearest metal atoms assumed fixed at their lattice positions along the 3 axes, one of which is shown in Figure 5.8, where *d* is incompressible diameter of the diffusion molecule/atom

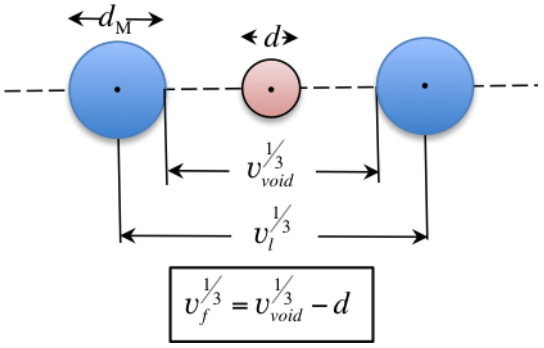

Figure 5.8 Estimation of free volume for an atom from its volume inhabited and exclusion of host metal atoms.

The lattice parameter and unit cell volume

$$a = \left(\frac{N_M A W_M}{N_{Av} \rho_M} \right)^{1/3} \quad ; \quad v_l = \frac{N_M A W_M}{N_{Av} \rho_M} \tag{5.41}$$

where N_M is the total number of atoms in a unit cell. Thus, $N_M = 1 + 3 = 4$ atoms/cell of fcc crystal, $N_M = 2$ in bcc crystal, and $N_M = 1$ in a simple cubic crystal.

Thus, the maximum free volume in a unit cells $v_{void} = v_l (1 - \varepsilon_{PF})$ where ε_{PF} is the volumetric packing fraction. For bcc, $\varepsilon_{PF} = 0.68$, for fcc, $\varepsilon_{PF} = 0.74$, and for simple cubic, $\varepsilon_{PF} = 0.52$.

The distance that the central (pink) atom/molecule is free to move along the shown axis = $v_{void}^{1/3} - d$. Thus, the free volume per molecule

$$v_f \equiv v_l - v_0 = (v_{void}^{1/3} - d)^3 \tag{5.42}$$

Therefore, the free volume may be estimate from density of the liquid.

Now, the chief difference between a molecule in the initial state and one in the activated state for transport is that the latter has one degree of translational freedom less than the former (Glasstone et al., 1941, p. 485, 189). Thus, if the product of F_{rot} and F_{vib} is almost the same in the two states, as it generally would be since the corresponding degrees of freedom are not affected

$$\exp\left(\frac{\Delta S_D^{\ddagger,o}}{R}\right) = \frac{F^{\ddagger}}{F_l} = \frac{1}{F_{tx} v_f^{1/3}} = \left(\frac{h}{\sqrt{2\pi m k_B T}}\right)\frac{1}{v_f^{1/3}} \tag{5.43}$$

Note that this provides $\Delta S_D^{\ddagger,o} < 0$, which implies that in the *liquid the transition state is in fact more ordered* than the initial state. Using in this Eq. (5.7)

$$D_{\mathrm{H},0} = f\gamma a^2 \frac{k_B T}{h}\left(\frac{h}{\sqrt{2\pi m k_B T}}\right)\frac{1}{v_f^{1/3}} \tag{5.44}$$

and simplifying

$$D_{\mathrm{H},0} = f\gamma a^2 \sqrt{\frac{k_B T}{2\pi m}}\,\frac{1}{v_f^{1/3}} \tag{5.45}$$

For a simple cubic structure assumed for liquid metals here estimation of hydrogen interstitial sites follow the methodology of solid sumple cubic structures. Hydrogen diffuses in solid metals through octahedral sites or tetrahedral sites as shown in Figure 5.9 (a) and (b).

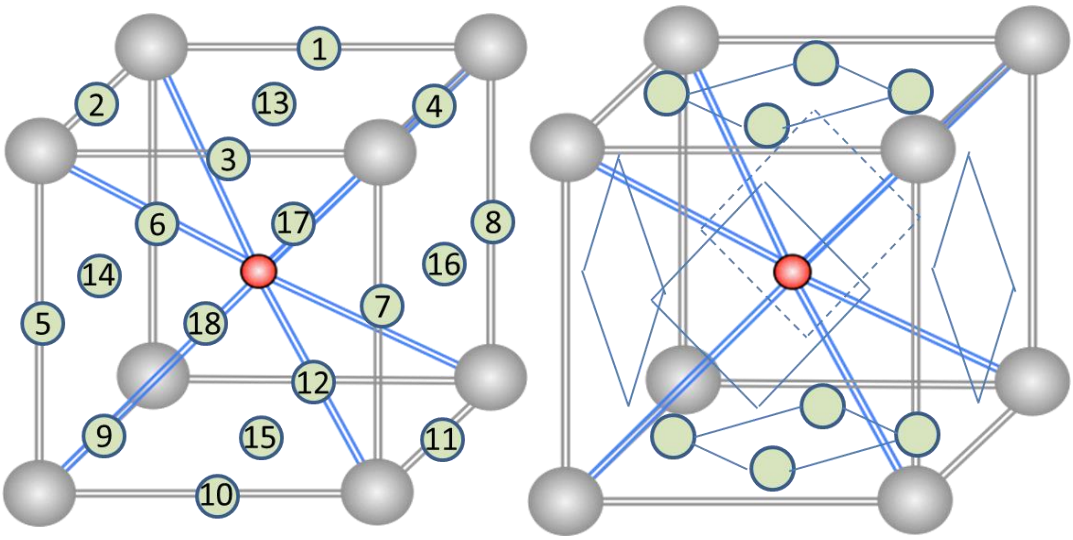

Figure 5.9 Hydrogen interstitial (a) Octahedral (O) sites and (b) Tetrahedral (T) sites for simple cubic structure.

As shown in Figure 5.9, hydrogen atom in the cubic center has 18 nearest octahedral sites jumping $\alpha = \sqrt{2}/2$ (12 in total, for example from center to number 11) and jumping $\alpha = 1/2$ (6 in total, for example from center to number 13). There are 24 nearest tetrahedral sites to jump $\alpha = 0.56$ (for example, from coordinate (0.25, 0, 0.5) to (0. 5, 0.5, 0.5)).

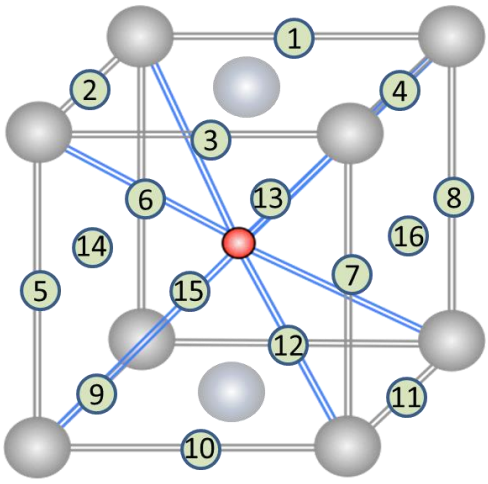

Figure 5.10 Hydrogen interstitial octahedral sites for base-centered orthorhombic unit cell.

Gallium is simple orthorhombic structure as shown in Figure 5.10 and each gallium atom there are 7 nearest gallium atom. Different from simple structure octahedral sites, there are only 16

nearest octahedral sites jumping $\alpha = \sqrt{2}/2$ (12 in total, for example from center to number 11) and jumping $\alpha = 1/2$ (4 in total, for example from center to number 13). The jumping distance and number of tetrahedral interstitial sites are the same as simple structure.

It is noteworthy that mainly liquid density information is needed in this approach to estimate the pre-exponential factor. For the case of H diffusion in liquid Ga, we use the last expression for the pre-exponential factor. For the determination of the unit cell dimension *a* and the free volume v_f, we use the liquid Ga density from Eq. (3.3) $\rho_M = 6077 - 0.611(T - 302.914)\ \mathrm{kg/m^3}$. For instance at 773 K, the density of liquid Ga is 5.79 g/cm^3. Using a packing factor, *PF* = 0.52 for simple cubic structure and a H atomic radius of 0.31 Å (Cordero et al., 2008). The calculated void volume at 350 K is $v_{void} = 9.19 \times 10^{-24}\ \mathrm{cm^3}$ and the free volume $v_f = 3.21 \times 10^{-24}\ \mathrm{cm^3}$ at 350 K. Thus the calculated the pre-exponential factor is $D_{\mathrm{H},0} = 0.0029\ \mathrm{cm^2/s}$ at 350 K using $\alpha = \sqrt{2}/2$, $z_i = 16$ in octahedral jumping and $D_{\mathrm{H},0} = 0.0027\ \mathrm{cm^2/s}$ at 350 K using $\alpha = 0.56$, $z_i = 24$ in tetrahedral jumping. Either of these are compariable to $D_{\mathrm{H},0} = 0.003\ \mathrm{cm^2/s}$ observed from literature (Mazayev and Prokofiev, 1994).

Summerized in Table 5.1, is a comparison of the experimental and hence calculated pre-exponential factor of liquid Ga, Al, Cu, Ni and Fe. The predicted temperature is set to be 50~100 K above its melting point to avoid calculation based on its melting point. Fe fcc structure is selected based on the structure near its melting point (Fe is bcc structure at room temperature). Both octahedral and tetrahedral jumping sites were considered. Results suggest that either gives good predictions. The calculated pre-exponential factor using octahedral sites are always higher than those using tetrahedral sites. Taking Fe for example, the calculated pre-exponential factor is leaning more toward to tetrahedral predicted values while Ni is closer to the predictions with

octahedral sites. In fact, it is commonly observesed that in the diffusion of hydrogen in solid metal, preference of jumping site varies. Hydrogen prefers to diffuse through tetrahedral in bcc V, Nb, Ta, Fe and orctahedral in fcc Pd (Jiang and Carter, 2004).

Further, applying the same approach to estimate solid metal pre-exponential factor gives very good prediction to experimental value as well, as shown in Table 5.2.

Thus, it is seen that the primary determinant of $D_{\mathrm{H},0}$ is the activation entropy for diffusion $\Delta S_D^{\ddagger,\mathrm{o}}/R$, which typically varies between 0 and 4 J/mol.K (Wert and Zener, 1949) for interstitial diffusion in solid metals, increasing with the additional strain exerted in the lattice as a solute passes over the potential energy divide. Thus, $D_{\mathrm{H},0}$ varies between 1 and $10^{-4}\ \mathrm{cm}^2/\mathrm{s}$, which is the experimentally observed range for interstitial diffusion of many small solutes in metals (Wert and Zener, 1949).

Table 5.1 Parameters and the calculated results of hydrogen diffusivity pre-exponential factors of various liquid metals using Eq. (5.45) (Fisher, 1999; Mazayev and Prokofiev, 1994).

	Experiment $D_{\mathrm{H},0}$ (cm^2/s)	Calculated $D_{\mathrm{H},0}$ (cm^2/s)	Packing fraction PF	α	f	Calculated temperature (K)	Nearest interstitial number z_i
Ga	0.003 (Mazayev and Prokofiev, 1994)	0.0029 (O) 0.0027 (T)	0.52	$\sqrt{2}/2$ (O) 0.56 (T)	Simple, 0.655	350	16 (O) 24 (T)
Al	0.038, 0.747, 2.34 (Fisher, 1999)	0.0059 (O) 0.0015 (T)	0.74	$\sqrt{2}/2$ (O) 0.5 (T)	fcc, 0.781	1000	12 (O) 6 (T)
Cu	0.0146, 0.011, 0.0051 (Fisher, 1999)	0.0067 (O) 0.0017 (T)	0.74	$\sqrt{2}/2$ (O) 0.5 (T)	fcc, 0.781	1400	12 (O) 6 (T)
Ni	0.00747, 0.05 (Fisher, 1999)	0.0075 (O) 0.0019 (T)	0.74	$\sqrt{2}/2$ (O) 0.5 (T)	fcc, 0.781	1800	12 (O) 6 (T)
Fe	0.00437, 0.0032, 0.00257, 0.052 (Fisher, 1999)	0.0078 (O) 0.0019 (T)	0.74	$\sqrt{2}/2$ (O) 0.5 (T)	fcc, 0.781	1900	12 (O) 6 (T)

Table 5.2 Parameters and the calculated results of hydrogen diffusivity pre-exponential factors of various solid metals using Eq. (5.45) (Fisher, 1999), * is the preferred jumping orientation from literature (Jiang and Carter, 2004).

	Experiment $D_{H,0}$ (cm^2/s)	Calculated $D_{H,0}$ (cm^2/s)	Packing fraction PF	α	f	Calculated temperature (K)	Nearest interstitial number z_i
Al	0.0486, 0.02, 0.014, 0.12, 0.101	0.004 (O) 0.001 (T)	0.52	$\frac{\sqrt{2}}{2}$ (O) $\frac{1}{2}$ (T)	fcc, 0.781	300	12 (O) 6 (T)
Cu	0.009, 0.00369, 0.00082	0.0038 (O) 0.00095 (T)	0.74	$\frac{\sqrt{2}}{2}$ (O) $\frac{1}{2}$ (T)	fcc, 0.781	300	12 (O) 6 (T)
Ni	0.0058, 0.0075, 0.0019, 0.0047	0.0038 (O) 0.00094 (T)	0.74	$\frac{\sqrt{2}}{2}$ (O) $\frac{1}{2}$ (T)	fcc, 0.781	300	12 (O) 6 (T)
Fe	0.000335, 0.000413, 0.0022, 0.0011, 0.000723	0.00056 (O) 0.00028 (T) *	0.68	$\frac{1}{2}$ (O) $\frac{1}{2\sqrt{2}}$ (T)	bcc, 0.721	300	4 (O) 4 (T)
Pd	0.00518, 0.00283, 0.0029	0.004 (O)* 0.002 (T)	0.74	$\frac{\sqrt{2}}{2}$ (O) $\frac{1}{2}$ (T)	fcc, 0.781	300	12 (O) 6 (T)

5.6 Hydrogen Sub-Surface Penetration

Clearly, the surface of a liquid metal is different from the bulk, both because of dangling bonds and structural differences. Similarly, when an atomic impurity penetrates below the surface toward the bulk, it is not difficult to accept that the energetics of the first sub-surface penetration step (step 2 in assumed mechanism) are different from those of the subsequent bulk diffusion steps, both because of the somewhat different coordination number, and the fact that some of the

coordinating metal atoms have dangling bonds, as shown in Figure 5.11. The corresponding energy landscape for hydrogen permeation through a gallium membrane is shown in Figure 5.12. For step 2 (Eq. 5.1 and Figure 5.1), i.e., for the sub-surface penetration of H atoms adsorbed on the surface, the kinetic parameters are estimated as follows.

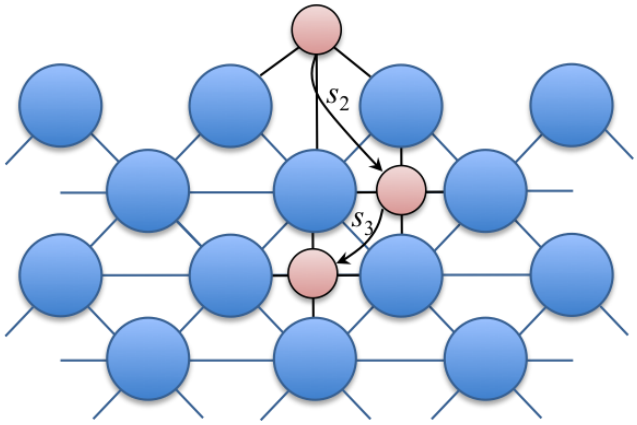

Figure 5.11 Schematic of subs-surface penetration of adsorbed H atom (step s_2) and subsequent diffusion (step s_3) in bulk metal.

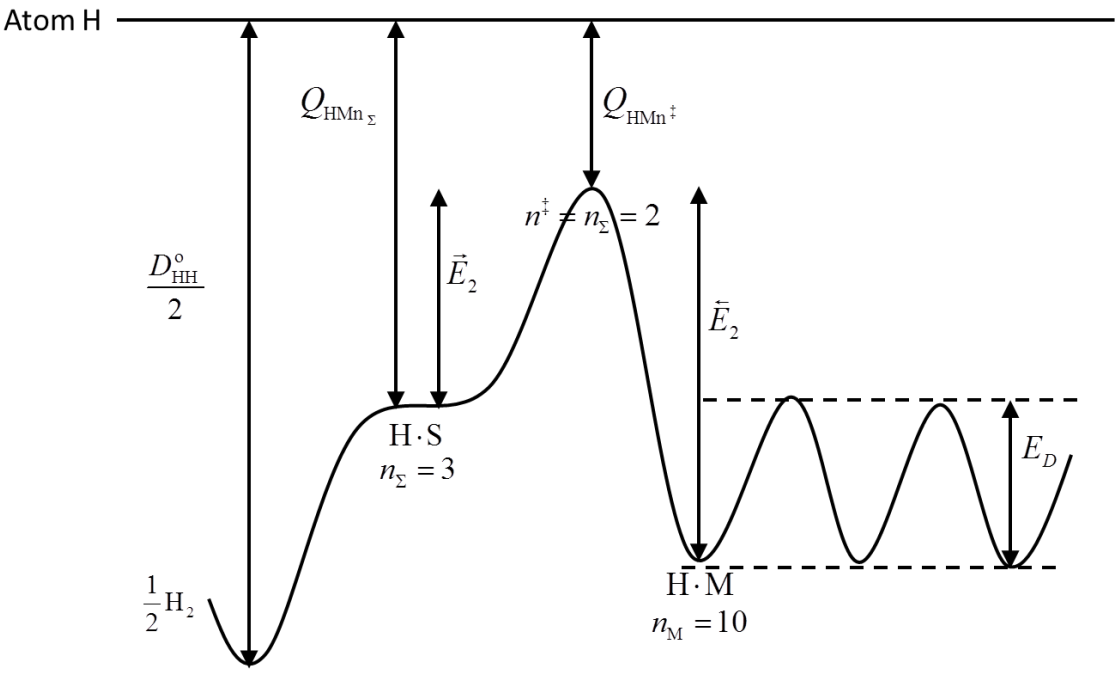

Figure 5.12 Energy landscape for hydrogen permeation through a Ga membrane.

From Figure 5.12

$$\vec{E}_2 = Q_{\mathrm{HMn}_\Sigma} - Q_{\mathrm{HMn}^\ddagger}\,;\ \overleftarrow{E}_2 = Q_{\mathrm{HMn}} - Q_{\mathrm{HMn}^\ddagger} \tag{5.46}$$

where $Q_{\mathrm{HMn}_\Sigma} = D^{\mathrm{o}}_{\mathrm{HM}} - (2 - 1/n_{\mathrm{M}_\Sigma})$, $Q_{\mathrm{HMn}} = D^{\mathrm{o}}_{\mathrm{HM}} - (2 - 1/n_{\mathrm{M}})$ and $Q_{\mathrm{HMn}^\ddagger} = D^{\mathrm{o}}_{\mathrm{HM}} - (2 - 1/n^\ddagger)$.

For liquid gallium $n_{\mathrm{M}_\Sigma} = 3$, $n_{\mathrm{M}} = 10$, $n^\ddagger = 2$ and $D^{\mathrm{o}}_{\mathrm{HM}} = 100.5\,\mathrm{kJ/mol}$ we get $\vec{E}_2 = 16.75\,\mathrm{kJ/mol}$ and $\overleftarrow{E}_2 = 40.2\,\mathrm{kJ/mol}$.

Of course, the frequency factor

$$\overleftarrow{\Lambda}_2 = \Lambda_D / 3 \tag{5.47}$$

i.e., only one-third of the interstitial diffusive jumps from the sub-surface layer go toward the surface ($z_i = 4$ for Pd). Using the pre-exponential factor estimated above for liquid gallium $D_{\mathrm{H},0} = 0.0029\,\mathrm{cm}^2/\mathrm{s}$ we get $\Lambda_D = \dfrac{D_{\mathrm{H},0}}{f\gamma a^2} = 1.7\times10^{13}\,\mathrm{s}^{-1}$ and $\overleftarrow{\Lambda}_2 = 5.66\times10^{12}\,\mathrm{s}^{-1}$.

For the kinetics of the forward step, we invoke the KPL relations for standard entropy and enthalpy change of solution of hydrogen in bulk metal, via a combination of steps 1 and 2, i.e.,

$$\Delta H^{\mathrm{o}}_S = \frac{1}{2}\Delta H^{\mathrm{o}}_1 + \Delta H^{\mathrm{o}}_2 \quad ; \quad \Delta S^{\mathrm{o}}_S = \frac{1}{2}\Delta S^{\mathrm{o}}_1 + \Delta S^{\mathrm{o}}_2 \tag{5.48}$$

For the entropy change in *reverse* step 2, which involves *diffusive* jump of sub-surface hydrogen to the surface, here we accept the argument of Ward and Dao (1999) that its energetic parameters should be similar to those of the interstitial diffusion step considered next, because these are virtually the same phenomena, although in different directions. Thus

$$\Delta\overleftarrow{S}^{\ddagger,\mathrm{o}}_2 = \Delta S^{\ddagger,\mathrm{o}}_D \ ; \ \vec{S}^{\ddagger,\mathrm{o}}_2 = \overleftarrow{S}^{\ddagger,\mathrm{o}}_2 - \frac{1}{2}\Delta S^{o}_1 + \Delta S^{o}_S \tag{5.49}$$

As a result for liquid gallium is $\Delta\overleftarrow{S}^{\ddagger,\mathrm{o}}_2 = -7.26\,\mathrm{J/mol\,K}$ at 773 K.

For $\vec{\Lambda}_2$ we use an alternate form of the second of the above relations, i.e.,

$$\vec{\Lambda}_2 = \overleftarrow{\Lambda}_2 \sqrt{\frac{\overleftarrow{\Lambda}_1}{\vec{\Lambda}_1}} \exp\left(\frac{\Delta S_S^o}{R}\right) \tag{5.50}$$

which e.g. at 773K , yields $\vec{\Lambda}_2 = 3.6\times10^{15}\ \mathrm{s}^{-1}$. These parameters for Ga are summarized in Table 5.3. Estimation of the thermodynamic parameters for H in Ga solution are provided below. The predicted liquid gallium $\Delta H_S^o = 26.95\ \mathrm{kJ/mol}$ and $\Delta S_S^o = -47.34\ \mathrm{kJ/mol}$ is described in section 5.7.1 and 5.7.2. The calculated forward secpnd step enthalpy and jump frequency are

$\vec{S}_2^{\ddagger,o} = -7.26 - \frac{1}{2}(-128) - 47.34 = 9.4\ \mathrm{J/mol\ K}$ and

$\vec{\Lambda}_2 = 5.66\times10^{12}\ \mathrm{s}^{-1}\sqrt{(8.87\times10^{13}/1.7\times10^{7})}\exp(\frac{-47.34}{8.314}) = 4.36\times10^{13}\ \mathrm{s}^{-1}$.

Table 5.3 Estimation of the thermodynamic parameters for H in Ga solution.

Parameter	Value	Units	Comment/reference
ΔH_1^o	100.8	kJ/mol	From Eq. (5.8)
ΔS_1^o	-128.6	J/mol K	From Eq. (5.25)
$\vec{\Lambda}_1$	1.7×10^{7}	$\mathrm{atm^{-1}s^{-1}}$	From Eq. (5.20)
$\overleftarrow{\Lambda}_1$	8.87×10^{13}	$\mathrm{s^{-1}}$	From Eq. (5.21)
$\Delta\vec{S}_2^{\ddagger,o}$	9.4	J/mol K	From Eq. (5.49)
$\Delta\overleftarrow{S}_2^{\ddagger,o}$	-7.26	J/mol K	From Eq. (5.43) and Eq. (5.49)
ΔH_S^o	26.95	kJ/mol	From Eq. (5.57)
ΔS_S^o	-4.64	J/mol K	From Eq. (5.59) and Eq. (5.60)
$\vec{\Lambda}_2$	7.4×10^{15}	$\mathrm{s^{-1}}$	From Eq. (5.50)
$\overleftarrow{\Lambda}_2$	5.66×10^{12}	$\mathrm{s^{-1}}$	From Eq. (5.47)
Λ_D	1.7×10^{13}	$\mathrm{s^{-1}}$	From Eq. (5.34)
$\vec{E}_2$	16.75	kJ/mol	From Eq. (5.46)
$\overleftarrow{E}_2$	40.2	kJ/mol	From Eq. (5.46)

5.7 Hydrogen Solution Thermodynamics

The absorption of hydrogen by a metal, i.e., formation of interstitial hydrogen within the bulk metal phase from the gas phase hydrogen is a two-step process, as described by the steps s_1 and s_2 in Eq. (5.1), i.e., surface adsorption followed by transition of adsorbed H into the bulk phase. We rewrite it here with altered stoichiometric numbers σ_ρ, in order to obtain the standard OR in the literature for solution, i.e., $\tfrac{1}{2}\mathrm{H}_2 + n\mathrm{M} \leftrightarrows \mathrm{H}\cdot\mathrm{M}_n$

$$\begin{array}{lll} \underline{s_\rho} & & \underline{\sigma_\rho} \\ s_1: & \mathrm{H}_2 + 2n_\Sigma \mathrm{M} \leftrightarrows 2\mathrm{H}\cdot\mathrm{M}_{n_\Sigma} & +1/2 \\ s_2: & \mathrm{H}\cdot\mathrm{M}_{n_\Sigma} + n\mathrm{M} \leftrightarrows \mathrm{H}\cdot\mathrm{M}_n + n_\Sigma \mathrm{M} & +1 \\ \hline OR: & \tfrac{1}{2}\mathrm{H}_2 + n\mathrm{M} \leftrightarrows \mathrm{H}\cdot\mathrm{M}_n & \end{array} \tag{5.51}$$

The corresponding dimensionless affinity, in view of KPL, for the solution OR, $\tfrac{1}{2}\mathrm{H}_2 + n\mathrm{M} \leftrightarrows \mathrm{H}\cdot\mathrm{M}_n$, is $\mathcal{A}_S = (+\tfrac{1}{2})\mathcal{A}_1 + (+1)\mathcal{A}_2$. Using expression for dimensionless step affinity in terms of step rates (Deveau et al., 2013), along with the corresponding kinetics given in Eq. (5.4), results, for ideal solution (assumed here), in

$$-\mathcal{A}_S = \frac{\Delta G_S^\circ}{RT} + \ln\left\{\left(\frac{x_{\mathrm{H}\cdot\mathrm{X}}}{1-x_{\mathrm{H}\cdot\mathrm{X}}}\right)\sqrt{\frac{p^\circ}{p_{\mathrm{H}_2}}}\right\} \tag{5.52}$$

where the *standard* Gibbs free energy change for hydrogen solution in bulk metal

$$-\frac{\Delta G_S^\circ}{RT} = \ln(K_S) = \ln\left(\sqrt{\frac{\vec{k}_1}{\overleftarrow{k}_1}\frac{\vec{k}_2}{\overleftarrow{k}_2}}\right) = \ln\left(\sqrt{K_1}K_2\right) \tag{5.53}$$

Here we have used the relation $K_\rho = \vec{k}_\rho / \overleftarrow{k}_\rho$ (Fishtik et al., 2004; Vilekar et al., 2009), $K_S = \sqrt{K_1}K_2$ and of course, the standard Gibbs free energy change for solution, $\Delta G_S^\circ = (+1)\mu_{\mathrm{H}\cdot\mathrm{X}}^\circ + (-1)\mu_{\mathrm{X}}^\circ + (-1/2)\mu_{\mathrm{H}_2}^\circ = \Delta H_S^\circ - T\Delta S_S^\circ$. This further provides the KPL relations as

a consistency check between the rate constants of steps s_1 and s_2 and the absorption equilibrium constant K_S for solution.

5.7.1 Application of the PBV-MPP Method for Solute Solution and Diffusion within a Metal

Although the analog of our model, the UBI-QEP method, has been developed for and applied to surface molecular steps, we use the PBV-MPP method here to evaluate the energetics of atomic solution and diffusion within the bulk of the solid matrix.

The diffusion of a solute atom, e.g., H, B, C, N, and O, in a *solid* metal is via "interstitial" diffusion within a regular crystalline lattice of metal atoms. These smaller-sized solute atoms are incorporated within the interstitial spaces among the host metal atoms (Figure 5.13). Thus, the geometry of the host crystal structure defines the interstitial lattice sites (Figure 5.13) and, hence, the bond-valence as well as the diffusion path and transition-state of the solute atoms.

Furthermore, at a given interstitial site, a solute atom A is coordinated with n host metal atoms. This is 2-3 times that on the metal surface coordination number n_Σ, i.e., typically, n = 8 – 14. For example a solute atom at the center interstitial site of a simple cubic structure, n = 8 (Figure 5.13). On the other hand for an interstitial site at the center of fcc unit cell (Figure 5.13 (a)) n = 6 (or n =14 if including atoms in the same unit cell but in further distance). For bcc structure (Figure 5.13 (b)) there is a metal atom occupy in the center of the unit cell. Therefore the center of solute atom of the interstitial site is on the face of unit cell where it is surrounded by 6 metal atoms, n = 6.

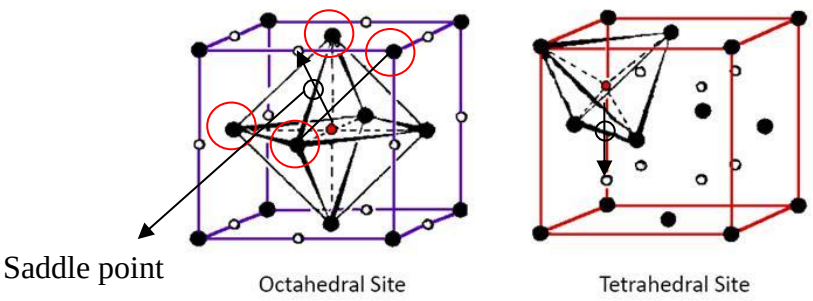

Figure 5.13 (a) A solute at an interstitial site at the center of fcc structure is coordinated to n = 6 metal atoms and saddle point $n^{\ddagger} = 4$ (wikidot.com).

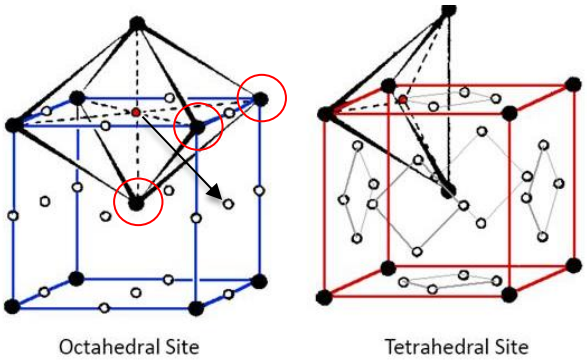

Figure 5.13 (b) A solute at an interstitial site at the center of bcc structure is coordinated to n = 6 metal atoms and saddle point $n^{\ddagger} = 3$ (wikidot.com).

Thus, the average Lewis-Pauling bond-valence of solute (A)-metal (M) bonds, $v_{\mathrm{AM}} = V_{\mathrm{A}} / n$. This n is, of course, not the same as the n_{M}, which is the number of nearest metal atoms to a given metal atom M, not to a solute atom A. Thus, the bond valence v_{AM} is usually fractional. Of course, as before, the solute atom normalized bond x_{AM} sums to unity.

As the solute atom jumps from one interstitial site to one of its neighboring z_i sites, this coordination of solute with metal atoms n changes continuously to $n^{\ddagger}$, corresponding to the saddle point, as shown schematically in Figure 5.6, and then back to n corresponding to the final state at the completion of the jump. Thus, the total energy for the jump first monotonically

increases ($n \rightarrow n^{\ddagger}$), and then monotonically decreases ($n^{\ddagger} \rightarrow n$), assumed limited to the nearest neighbors. In the example of simple cubic structure shown in Figure 5.14, thus $n = 8$ and $n^{\ddagger} = 4$.

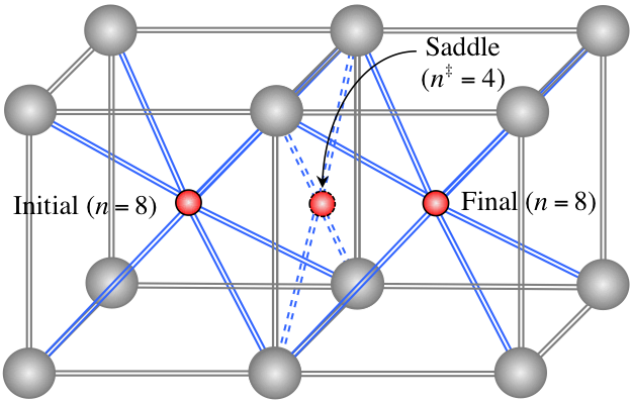

Figure 5.14 Schematic of atomic solute (red) jump in a simple cubic metal $n = 8$ and the corresponding change in bond order from initial state to the saddle point $n^{\ddagger} = 4$.

For fcc structure an interstitial atom in the center of the unit cell (where it is surrounded by 6 metal atoms, $n = 6$) jump to the interstitial site at the edge of the unit cell as arrow indicated in Figure 5.13 (a). The corresponding saddle point surrounds by four atoms (as red circle indicated), thus, $n^{\ddagger} = 4$. Of course, this assumes that bonding is limited only to the nearest neighbors, which is somehat arbitrary. For bcc structure, it is similar to fcc i.e., $n = 6$ and $n^{\ddagger} = 3$. There are two ways in which to treat the energetics of such solute solution and diffusion within a solid metal matrix. One is in which the metal lattice remains frozen during the process, as done in the UBI-QEP method of Shustorovich described above. The other is to assume that metal atoms are movable as well, as done by Benziger (1991; 1994). Let's first follow Shustorovich's approach for solution within the metal bulk, following the above approach for adsorption on the surface. On the metal surface, of course, recall that we assumed that the metal atoms don't reorganize so long at $v_A \leq v_{MF}$.

For the *dilute* solution of single atom, A to form A–M_n within the bulk metal, thus w we neglect any changes in the M–M interactions as a result of solution, along with any A–A interactions that occur at higher concentrations, so that the bond-valence conservation remains limited to nearest neighbor two-center A–M_i (i = 1, 2, …, n) only. Further, we assume that all the n bonds are equivalent. Thus, the total binding energy of the absorbed A for all the n bonds then, using the Morse potential and the bond index x subject to conservation, remains the same as in Eq. (5.9), with of course n for bulk solution being different from that for surface adsorption, n_Σ.

Further, if the solution process of diatomic elements such as A_2 = H_2, O_2, and N_2, $1/2\,\mathrm{A}_2 + n\mathrm{M} \leftrightarrows \mathrm{A}\cdot\mathrm{M}_n$, is written as the thermodynamic Hess cycle

$$\begin{array}{lll} \underline{s_\rho} & & \underline{\Delta H^\circ_\rho} \quad \underline{\sigma_\rho} \\ s_1: & \mathrm{A}_2 \leftrightarrows 2\mathrm{A} & +D^\circ_{\mathrm{A-A}} \quad +1/2 \\ s_2: & \mathrm{A} + \mathrm{M}_n \leftrightarrows \mathrm{A}\cdot\mathrm{M}_n & -Q_{\mathrm{AM}_n} \quad +1 \\ \hline OR: & \tfrac{1}{2}\mathrm{A}_2 + \mathrm{M}_n \leftrightarrows \mathrm{A}\cdot\mathrm{M}_n & \Delta H^\circ_S \end{array} \tag{5.54}$$

Thus

$$\Delta H_S = \frac{D^\circ_{\mathrm{A-A}}}{2} - Q_{\mathrm{AM}_n} \tag{5.55}$$

Thus, we can reimagine the solution OR, $1/2\,\mathrm{H}_2 + n\mathrm{X} \leftrightarrows \mathrm{H}\cdot\mathrm{X}$, where $\mathrm{X} = \mathrm{M}_n$, to occur as follows:

$$\begin{array}{lll} \underline{s_\rho} & & \underline{\Delta H^\circ_\rho} \quad \underline{\sigma_\rho} \\ s_i: & \mathrm{H}_2(g) \leftrightarrows \mathrm{H}(g) + \mathrm{H}(g) & +D^\circ_{\mathrm{H-H}} \quad +\tfrac{1}{2} \\ s_{ii}: & \mathrm{H}(g) + \mathrm{M}_n \leftrightarrows \mathrm{H}\cdot\mathrm{M}_n & -Q_{\mathrm{H}\cdot\mathrm{M}_n} \quad +1 \\ \hline OR: & \tfrac{1}{2}\mathrm{H}_2 + \mathrm{M}_n \leftrightarrows \mathrm{H}\cdot\mathrm{M}_n & \Delta H^\circ_S = D^\circ_{\mathrm{H-H}}/2 - Q_{\mathrm{H}\cdot\mathrm{M}_n} \end{array} \tag{5.56}$$

so that applying KPL (Hess's relation)

$$\Delta H^\circ_S = \frac{D^\circ_{\mathrm{H-H}}}{2} - Q_{\mathrm{H}\cdot\mathrm{M}_n} \tag{5.57}$$

where in analogy with Eq. (5.9) for the surface, we can derive the binding energy in the bulk metal

$$Q_{\mathrm{A{\cdot}M}_n} = D^{\mathrm{o}}_{\mathrm{A{\cdot}M}}\left(2 - \frac{1}{n}\right) \tag{5.58}$$

In a solid metal, $n = 6$ (or $n = 14$ for fcc) is a good approximation for many bcc and fcc structures as shown in Figure 5.13. From section 3.4 we learn that the coordination number of liquid gallium is very close to 10. Coordination number is 9.2 at 838 K from Andrew (2001), 10 at 723 K from Vahvaselkä (1987), 8.7 at 702 K from Holender et al., (1995), 8.5 at 959 K using molecular-dynamics simulation from González and González (2008) and 10.4 at 300K from Tao (2005). And from Figure 5.10 the interstitial site in the center of orthorhombic unit cell is surrounded by 10 atoms (for example, 10 Ga atoms). It is reasonable to make the assumption of $n = 10$ for liquid gallium. For liquid gallium using $n = 10$ in the bulk liquid along with $D^{\mathrm{o}}_{\mathrm{H{\cdot}Ga}} = 100.5\,\mathrm{kJ/g\text{-}atm\,H}$ on Ga, provides the binding energy $Q_{\mathrm{H,\,Ga_n}} = 190.95\,\mathrm{kJ/g\text{-}atm\,H}$ within Ga bulk. Finally, using this in above $H^o_S = 435.8/2 - 190.95 = +26.95\,\mathrm{kJ/g\text{-}atm\,H}$ within Ga. This compares with $H^o_S = 15.76\,\mathrm{kJ/g\text{-}atm\,H}$ obtained from experiments. The two are reasonably close, i.e., within ± 12.54 kJ/mol, or ± 3.0 kcal/mol, which is fairly good accuracy without any fitting, i.e., with literature data and models. This is for dilute solutions. For concentrated solutions, for average heat of solution, we may need to divide by a factor to avoid counting some bonds twice, as done for heat of cohesion.

5.7.2 Entropy of Solution

Based on the above Hess's cycle, the entropy of solution may be written as follows.

$$\Delta S^{\mathrm{o}}_S = S^{\mathrm{o}}_{\mathrm{HM}} - \frac{1}{2} S^{o}_{\mathrm{H_2}(g)} \tag{5.59}$$

where the free volume is estimated above. This is based on the use of Eq. (5.56), whereby, the change in the entropy of solution from a gas into a liquid is given by (Frank, 1945 (a); 1945 (b); 1945 (c))

$$\Delta S_{g,l} = S_g - S_l = R\ln\left(\frac{v_{f,g}}{\omega v_{f,l}}\right) = S^o_{\mathrm{H}(g)} - S^o_{\mathrm{HM}} \tag{5.60}$$

where $v_{f,l}$ is estimated free volume v_f from Eq. (5.42), $v_{f,g}$ is the hydrogen atom volume at gas phase and S^o_{HM} is the standard entropy of hydrogen in liquid metal. $S^o_{\mathrm{H}_2(g)}$ is hydrogen molecule standard entropy in gas phase and $S^o_{\mathrm{H}(g)}$ is the hydrogen atom entropy change in gas phase, could be obtained from NIST chemistry webbook (nist.gov). The discussion of how the free volume $v_{f,l}$ in a liquid metal may be estimated is given above. ω is the correction factor that accounts all the factors including temperature variability, encroachment of the molecules on each other's free volume, occupancy of the physical volume element assigned to, interference in the liquid with the internal motions (rotations, vibrations), geometry of the liquid and the energetic and dynamic interaction of the molecules (Frank, 1945 (a); 1945 (b); 1945 (c)). $\omega = 16$ is found for the ideal liquid, however, for liquid metal ω tends to be higher. For liquid Hg $\omega = 170$ and liquid Cs $\omega = 304$ (Frank, 1945 (b)). $\omega = 170$ is adapted here for preliminary prediction. The predicted theoretical Sieverts' constant with experimental Sieverts' constant at 1 atm is shown in Figure 5.15. The theoretical value is about 5 times lower than experimental value mainly because of the higher heat of solution predicted from Eq. (5.18). Figure 5.15 is the predicted Sieverts' constant using Eq. (5.57), Eq. (5.59), Eq. (5.60) with $Q_{\mathrm{H,Gan}_\Sigma} = 40$ kcal/mol (provides $D^{\mathrm{o}}_{\mathrm{H\cdot Ga}} = 100.5$ kJ/mol) and $Q_{\mathrm{H,Gan}_\Sigma} = 42$ kcal/mol (provides $D^{\mathrm{o}}_{\mathrm{H\cdot Ga}} = 105.6$ kJ/mol). The calculated

K_S is 5 times lower than experimental value using $Q_{\mathrm{H,\,Gan_\Sigma}} = 40\,\mathrm{kcal/mol}$, however, fits accurately with $Q_{\mathrm{H,\,Gan_\Sigma}} = 42\,\mathrm{kcal/mol}$.

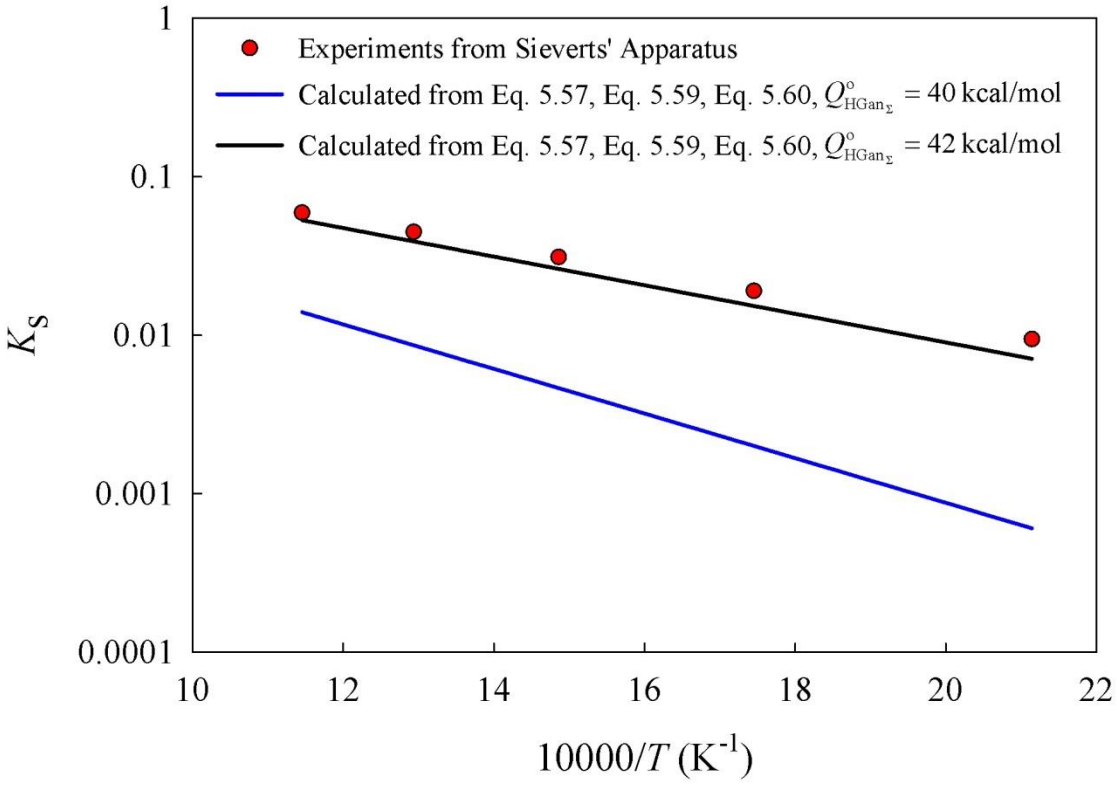

Figure 5.15 Predicted Sieverts' constant using Eq. (5.57), Eq. (5.59), Eq. (5.60) using $Q_{\mathrm{H,\,Gan_\Sigma}} = 40\,\mathrm{kcal/mol}$ (provides $D^{\circ}_{\mathrm{H{\cdot}Ga}} = 100.5\,\mathrm{kJ/mol}$) and $Q_{\mathrm{H,\,Gan_\Sigma}} = 42\,\mathrm{kcal/mol}$ (provides $D^{\circ}_{\mathrm{H{\cdot}Ga}} = 105.6\,\mathrm{kJ/mol}$).vs experimental data.

5.7.3 PBV-MPP Method for Solute Diffusion within a Metal

However, let's first next see if we can estimate the activation energy of diffusion coefficient of atom A in a solid metal. In moving from one interstial site to the adjacent one, the solute atom passes through a saddle point, as shown schematically in Figure 5.14. The saddle point corresponds to the highest energy point along the minimum energy pathway. As mentioned above, when the solute atom jumps from one interstitial site to an adjacent one, this coordination

n changes to $n^{\ddagger}$. Thus, the total energy for the jump first monotonically increases ($n \rightarrow n^{\ddagger}$), and then monotonically decreases ($n^{\ddagger} \rightarrow n$). With reference to the structures shown in Figure 5.14 as an example, $n = 8$ and $n^{\ddagger} = 4$, while for simple cubic structure, $n = 6$ and $n^{\ddagger} = 3$ for bcc, $n = 6$ and $n^{\ddagger} = 4$ for fcc. In other words it is roughly $n / n^{\ddagger} = 1.5 \sim 2.5$. Note that this indicates that for bulk diffusion, $n^{\ddagger} = 3 \sim 4$, while it is 2 for surface diffusion (Shustorovich, 1986).

Thus, the activation barrier for this migration is $E_{n^{\ddagger}} - E_n = Q_{\mathrm{AM}_n} - Q_{\mathrm{AM}_{n^{\ddagger}}} = Q_{\mathrm{AM}_n}(1 - Q_{\mathrm{AM}_{n^{\ddagger}}} / Q_{\mathrm{AM}_n})$. Using Eq. (5.58) in this and rearranging, the activation barrier for migration is

$$E_D = \frac{D^{\mathrm{o}}_{\mathrm{AM}}}{n}\left(\frac{n}{n^{\ddagger}} - 1\right) \tag{5.61}$$

Further, as an *approximation*, if it is assumed that $n / n^{\ddagger} \approx 2$, then

$$E_D \approx \frac{D^{\mathrm{o}}_{\mathrm{AM}}}{n} \tag{5.62}$$

Regardless, however, as for the case of surface diffusion,

$$E_{\mathrm{A},D} = \left(\frac{D^{\mathrm{o}}_{\mathrm{AM}}}{D^{\mathrm{o}}_{\mathrm{BM}}}\right) E_{\mathrm{B},D} \tag{5.63}$$

is applicable to bulk diffusion. In other words, this predicts that if activation enrgy of one solute is known in a metal, that of another solute is simply in a ratio of their binding energies with the metal.

Applying the above approximate formula, Eq. (5.62) and using $D^{o}_{\mathrm{H–Ga}} = 100.5\,\mathrm{kJ/mol}$ for H on Ga, the activation energy for H diffusion in *liquid* Ga $E_D = 100.5/10 = 10.05\,\mathrm{kJ/mol}$ assuming $n = 10$. This compares with $E_D = 9.61\ \mathrm{kJ/mol}$ as reported in the literature (Mazayev and Prokofiev, 1994). This is a very good estimate, especially when considering that it involves no adjustable parameters. Same approach was applied on other liquid and solid metal systems as

shown in Table 5.4 (a) and (b). The results are quite compariable for both liquid and solid metals considered that there was no fitted parameter and purely based on the approximation.

For solid metal calculation it was found that using $n=14$ gives better fitting than $n=6$ possiblly due to shorter lattice distance in solid phase compared to its liquid phase and that gives higher nearest neighbor numbers than liquid phase. The ratio of $n/n^{\ddagger}\approx 2$ is no longer valid thus Eq. (5.61) was used instead of Eq. (5.62) for calculation.

Table 5.4 (a) Approximation of diffusion activation energy of various liquid metals calculated from Eq. (5.62) (Mazayev and Prokofiev, 1994; Fisher, 1999).

	Experiment E_D (kJ/mol)	Calculated E_D (kJ/mol)	n
Ga	9.61 (Mazayev and Prokofiev, 1994)	10.05	10
Al	33, 19.23, 62.7 (Fisher, 1999)	28.42	6
Cu	8.98, 24.6, 18.81 (Fisher, 1999)	27.8	6
Ni	35.8, 40.7 (Fisher, 1999)	26.5	6
Fe	17.3, 13.8, 18.5 (Fisher, 1999)	26.8	6

Table 5.4 (b) Approximation of diffusion activation energy of various solid metals calculated from Eq. (5.61) (Fisher, 1999).

	Experiment E_D (kJ/mol)	Calculated E_D (kJ/mol)	n
Al	50, 35.7, 47.7, 65.7, 50.16 (Fisher, 1999)	30.45	14
Cu	38.37, 43.5, 8.4, 36.82 (Fisher, 1999)	25.1	14
Ni	38.6,40.34, 31.85, 9.2 (Fisher, 1999)	28.39	14
Fe	5.31, 12.21, 12.96, 4.5, 6.7, 9.8, 15.95 (Fisher, 1999)	26.8	6
Ag	59.36, 36.2 (Fisher, 1999)	29.57	14
Pd	27.59, 21.98, 25.7, 21.6 (Fisher, 1999)	28.21	14

Using the pre-exponential factor above, the H diffusion coefficient is plotted in Figure 5.16 as a function of inverse temperature, and is also compared with the experimentally determined diffusion equation reported in the literature. It is seen that the agreement is very good, considering that there are no fitted parameters in our model. Agreement can be improved if the

geometric parameter γ is treated as a fitted parameter with $\gamma = 1$ calculated for the simple cubic structure assumed here for the liquid metal structure.

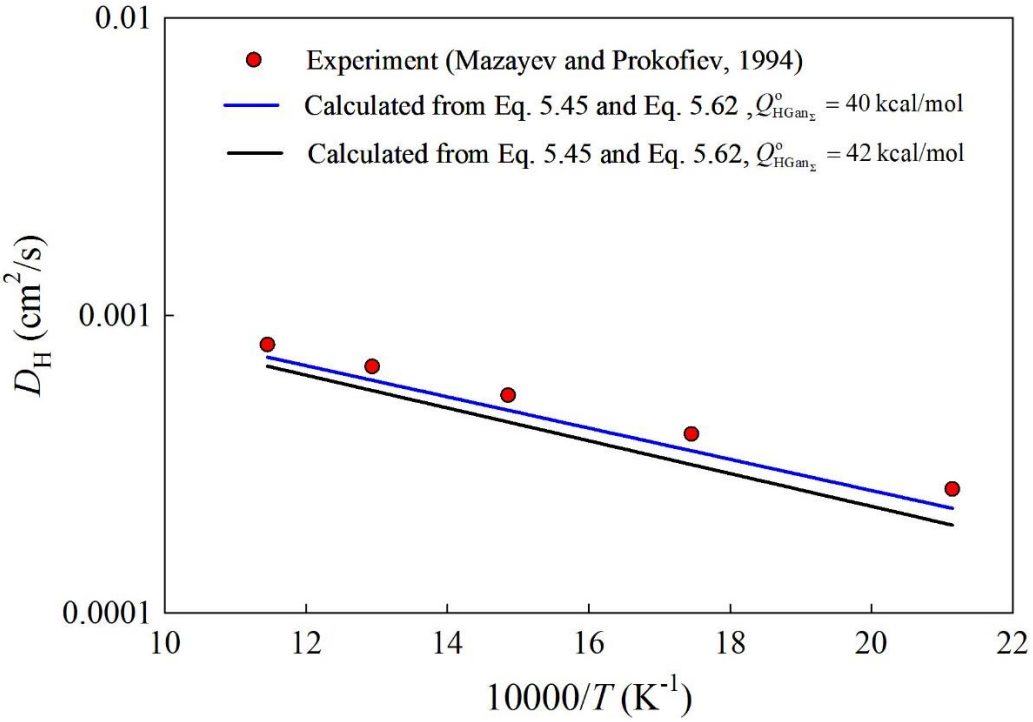

Figure 5.16 Predicted hydrogen diffusion coefficient from Eq. (5.45) and Eq. (5.62) using $Q_{H,\,Gan_{\Sigma}} = 40$ kcal/mol and $Q_{H,\,Gan_{\Sigma}} = 42$ kcal/mol with literature value versus inverse temperature (Mazayev and Prokofiev, 1994).

5.8 Diffusion as Rate Controlling Step in Permeation

It is possible that at high temperatures diffusion step (s_3) has by far the biggest resistance, although at lower temperatures (e.g., at < 350 ºC), this may not be true, and desorption may be rate controlling. Assuming step 3, thus, to be the rate-dtermining step (RDS) with the other four steps at quasi-equilibrium (QE), i.e., $r_1 = 0,\ r_2 = 0,\ r_4 = 0,$ and $r_5 = 0,$ and further assuming ideal solution, i.e., $\Delta G_S^{ex} = 0$ and the activity coefficients are unity because of the low solubility under

these conditions, the from Eq. (5.52) and Eq. (5.53), with $\mathscr{A}_S = 0$ for quasi-equilibrium, there results the ideal absorption isotherm.

$$x_{\mathrm{H\cdot M}} = \frac{K_S\sqrt{p_{\mathrm{H}_2}/p^{\mathrm{o}}}}{1+K_S\sqrt{p_{\mathrm{H}_2}/p^{\mathrm{o}}}} \tag{5.64}$$

Using this in $r_3 \approx \omega_3(x_{\mathrm{H\cdot M},f} - x_{\mathrm{H\cdot M},p})$, along with $N_{\mathrm{H}_2} = r_3/2$, we have

$$N_{\mathrm{H}_2} = \left(\frac{c_t\chi_{\mathrm{H\cdot M},s}K_S D_{\mathrm{H}}}{2\delta}\right)\left\{\frac{\sqrt{p_{\mathrm{H}_2,f}/p^{\mathrm{o}}} - \sqrt{p_{\mathrm{H}_2,p}/p^{\mathrm{o}}}}{\left(1+K_S\sqrt{p_{\mathrm{H}_2,f}/p^{\mathrm{o}}}\right)\left(1+K_S\sqrt{p_{\mathrm{H}_2,p}/p^{\mathrm{o}}}\right)}\right\} \tag{5.65}$$

where $K_S = \exp\left\{\Delta S_S^{\mathrm{o}}/R - (\Delta H_S^{\mathrm{o}}/RT\right\}$. This expression reduces to the common form of Sieverts' law when in the term in the denominator $K_S\sqrt{p_{\mathrm{H}_2,f}/p^{\mathrm{o}}} << 1$, which is valid at high temperatures.

$$N_{\mathrm{H}_2} = P_{\mathrm{H}_2}\left(\sqrt{p_{\mathrm{H}_2,f}} - \sqrt{p_{\mathrm{H}_2,p}}\right) \tag{5.66}$$

where the hydrogen permeance of the membrane

$$P_{\mathrm{H}_2} \equiv \left(\frac{c_t\chi_{\mathrm{H\cdot M},s}K_S D_{\mathrm{H}}}{2\delta p^{\mathrm{o}}}\right) \tag{5.67}$$

For Ga membrane the corresponding effective activation energy may be calculated as $E_a = 10.05 + 26.95 = 37\ \mathrm{kJ/mol}$ while the experimental one is $E_a = 9.61 + 15.76 = 25.37\ \mathrm{kJ/mol}$. The predicted hydrogen flux using parameters from Table 5.3 is compared with SiC-Graphene-15 experimental data as shown in Figure 5.17. The predicted hydrogen flux using $Q_{\mathrm{H,\,Gan}_\Sigma} = 40\ \mathrm{kcal/mol}$ (provides $D^{\mathrm{o}}_{\mathrm{H\cdot Ga}} = 100.5\ \mathrm{kJ/mol}$) is about 4 times lower than experimental value mainly because of the predicted heat of solution $\Delta H_S^o = 26.95\ \mathrm{kJ/mol}$ is higher than $\Delta H_S^o = 15.76\ \mathrm{kJ/mol}$ obtained from Sieverts' experiment. However, using and $Q_{\mathrm{H,\,Gan}_\Sigma} = 42\ \mathrm{kcal/mol}$ (provides $D^{\mathrm{o}}_{\mathrm{H\cdot Ga}} = 105.6\ \mathrm{kJ/mol}$) the calculated $\Delta H_S^o = 17.26\ \mathrm{kJ/mol}$ fits

experimental data from SiC-Graphene-15 data accurately. The entropy of solution $\Delta S_S^o = -4.64$ from Eq. (5.59) and Eq. (5.60) gives very good estimation compared to $\Delta S_S^o = -5.45$ from experiment. Considering $Q_{\mathrm{H,Gan}_\Sigma} = 42$ kcal/mol is within the standard error 40 ± 2 kcal/mol that fitted by Appleby (1983) from experimental data.

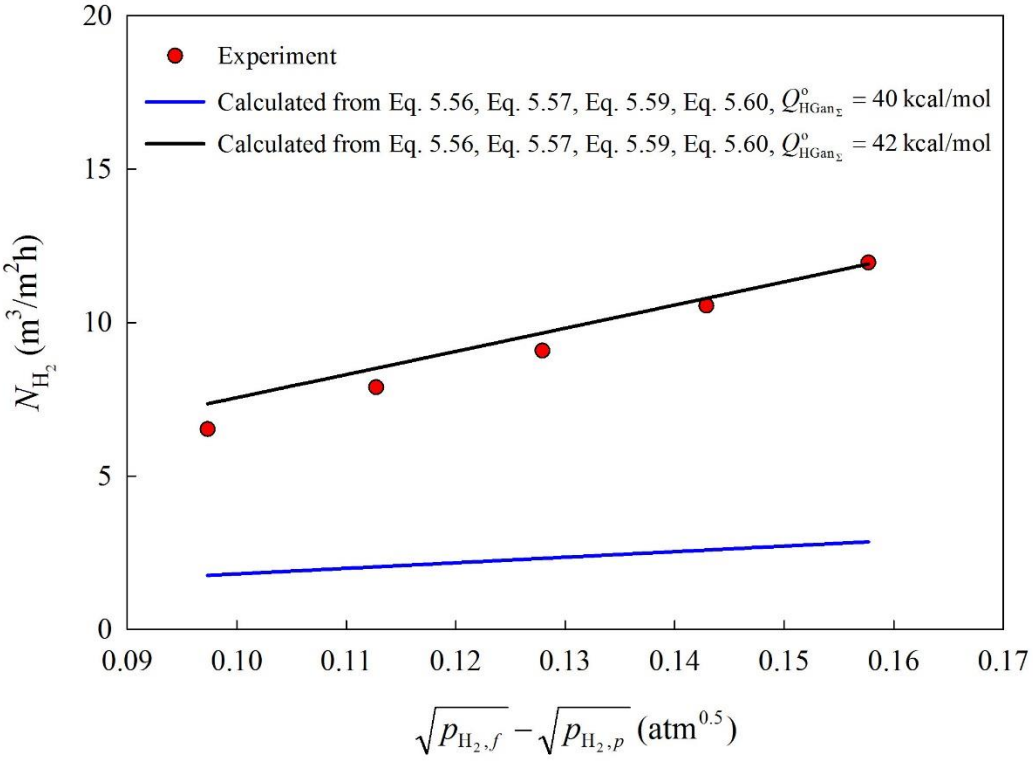

Figure 5.17 Predicted hydrogen flux using Eq. (5.56), Eq. (5.57), Eq. (5.59), Eq. (5.60), with $Q_{\mathrm{H,Gan}_\Sigma} = 40$ kcal/mol and 42 kcal/mol vs SiC-Graphene-15 experimental data at 500 ºC.

5.9 References

Appleby, A. J., Electrocatalysis, In Comprehensive treatise of electrochemistry, *Springer US*, 173-239, (1983).

Atkins, P. and De Paula, J., Physical Chemistry, 7th ed., *W. H. Freeman & Co., New York*, (2002).

Ayturk, M. E., Kazantzis, N. and Ma, Y. H., Modeling and performance assessment of Pd and Pd/Au-Based catalytic membrane reactors for hydrogen production, *Energy and Environmental Science*, 2, (2009), 430-438.

Benziger, J., Thermochemistry of metal catalyzed reactions, *Catalysis Today*, 21, 1, (1994), 211-228.

Benziger, J., Thermochemical methods for reaction energetics on metal surfaces, in Shustorovich, E., Ed., Metal-surface reaction energetics: theory and applications to heterogeneous catalysis, chemisorption, and surface diffusion, *VCH Publishers, New York*, (1991).

Brown, I. D. and Poeppelmeier, K. R., Bond valences, *Springer Berlin Heidelberg*, (2014).

Brown, I. D., Recent developments in the methods and applications of the bond valence model, *Chemical* Reviews, 109, 12, (2009), 6858-6919.

Campbell, J. M., Dulick, M., Klapstein, D., White, J. B., and Bernath, P. F., High resolution infrared emission spectra of GaH and GaD, *The Journal of Chemical Physics*, 99, 11, (1993), 8379-8384.

Cordero, B., Gómez, V., Platero-Prats, A.E., Revés, M., Echeverría, J., Cremades, E., Barragán, F. and Alvarez, S., Covalent radii revisited, *Dalton Transactions*, 2, (2008), 2832-2838.

Darken, L. S., Diffusion of carbon in austenite with a discontinuity in composition, *Transactions AIME*, 180, (1949), 430-438.

Deveau, N. D., Ma, Y. H., and Datta, R. Beyond Sieverts' law: A comprehensive microkinetic model of hydrogen permeation in dense metal membranes, *Journal of Membrane Science*, 437, (2013), 298-311.

Dumesic, J. A., Rudd, D. F., Aparicio, L. M., Rekoske, J. E. and Trevino, A.A., The microkinetics of heterogeneous catalysis, *Washington, DC: American Chemical Society*, (1993).

Emi, T. and Pehlke, R. D., Theoretical calculation of the solubility of hydrogen in liquid metals, *Metallurgical Transactions*, 1, 10, (1970), 2733-2737.

Eyring, H., and Hirschfelder, J., The theory of the liquid state, *Journal of Physical Chemistry*, 41, 2, (1937), 249-257.

Fisher, D. J., Hydrogen diffusion in metals: A 30-year retrospective, *Scitec Publications Ltd, Switzerland*, (1999).

Fishtik, I., Callaghan, C. A., and Datta, R., Reaction route graphs. I. Theory and algorithm, *The Journal of Physical Chemistry B*, 108, 18, (2004), 5671-5682.

Frank, H. S., Free volume and entropy in condensed systems I. General principles. fluctuation entropy and free volume in some monatomic crystals, *The Journal of Chemical Physics*, 13, 11, (1945a), 478-492 .

Frank, H. S., Free Volume and Entropy in condensed systems II. Entropy of vaporization in liquids and the pictorial theory of the liquid state, *The Journal of Chemical Physics*, 13, 11, (1945b), 493-507.

Frank, H. S. and Evans, M. W., Free volume and entropy in condensed systems III. Entropy in binary liquid mixtures; partial molal entropy in dilute solutions; structure and thermodynamics in aqueous electrolytes, *The Journal of Chemical Physics*, 13, 11, (1945), 507-532.

German, E. D., Sheintuch, M. and Kuznetsov, A. M., Diffusion on Metal Surfaces: Formalism and Application to CO Diffusion, *The Journal of Physical Chemistry C*, 112, 39, (2008), 15510-15516.

Glasstone, S., Eyring, H. and Laidler, K. J., The theory of rate processes, *McGraw-Hill, New York*, (1941).

http://electronicstructure.wikidot.com/hydrogen-embrittlement-of-metals

http://webbook.nist.gov/chemistry/

Jiang, D. E. and Carter, E. A., Diffusion of interstitial hydrogen into and through bcc Fe from first principles, *Physical Review B*, 70, 6, (2004), 064102.

Krishtalik, L. I., Hydrogen Overvoltage and Adsorption Phenomena: Part III. Effect of Adsorption Energy of Hydrogen on Overvoltage and the Mechanism of Cathodic Process, in Delahay, P., Tobias, C. W., Eds., Advances in Electrochemistry and Electrochemical Engineering, Vol. 7, *Interscience Pub., New York*, 283-339, (1970).

Maestri, M. and Reuter, K., Semiempirical rate constants for complex chemical kinetics: First-principles assessment and rational refinement, *Angewandte Chemie International Edition*, 50, 5, (2011), 1194-1197.

Mainwood, A. and Stoneham, A. M., Theory of hydrogen in liquid and solid metals, *Joural of the Less Common Metals*, 49, (1976), 271-281.

Mazayev, S. N. and Prokofiev, Yu. G., Hydrogen inventory in gallium, *Journal Nuclear Materials*, 212-215, (1994), 1497-1498.

Morse, P. M., Diatomic molecules according to the wave mechanics II. Vibrational levels, *Physical Review*, 34, 1, (1929), 57-64.

Nachtrieb, N. H., Self-diffusion in liquid metals, *Advances in Physics*, 16, 62, (1967), 309-323.

Nachtrieb, N. H., Atomic transport properties in liquid metals and alloys, *Berichte der Bunsengesellschaft für physikalische Chemie*, 80, 8, (1976), 678-688.

Pauling, L., Atomic radii and interatomic distances in metals, *Journal of the American Chemical Society*, 69, 3, (1947), 542-553.

Pauling, L. and Kamb, B., A revised set of values of single-bond radii derived from the observed interatomic distances in metals by correction for bond number and resonance energy, *Proceedings of the National Academy of Sciences*, 83, 11, (1986), 3569-3571.

Pauling, L., The Nature of the Chemical Bond, Ithaca, *NY: Cornell University Press*, (1960).

Phair, J. W. and Donelson, R., Developments and design of novel (non-palladium-based) metal membranes for hydrogen separation, *Industrial and Engineering Chemistry Research*, 45, (2006), 5657-5674.

Pritchard, J. and Tompkins, F. C., Surface potential measurements - the adsorption of hydrogen by group 1B metals, *Transactions of the Faraday Society*, 560, (1960), 540-550.

Schumacher, R. and Weiss, A., Hydrogen solubility in the liquid alloys lithium-indium, lithium-lead, and lithium-tin, *Berichte der Bunsengesellschaft für physikalische Chemie*, 94, (1990), 684-691.

Shivkumar, S., Wang, L. and Apelian, D., Molten metal processing of advanced cast aluminum alloys, *JOM*, 43, 1, (1991), 26-32.

Shustorovich, E. M., Chemisorption phenomena: analytic modeling based on perturbation theory and bond-order conservation, *Surface Science Reports*, 6, 1, (1986), 1-63.

Shustorovich, E. M. and Sellers, H., The UBI-QEP method: a practical theoretical approach to understanding chemistry on transition metal surfaces, *Surface Science Reports*, 31, 1, (1998), 1-119.

Shustorovich, E. M. and Zeigarnik, A. V., The UBI-QEP method: Basic formalism and applications to chemisorption phenomena on transition metal surfaces. Chemisorption energetics, *Russian Journal of Physical Chemistry*, 80, 1, (2006), 4-30.

Tao, D. P., Prediction of the coordination numbers of liquid metals, *Metallurgical and Materials Transactions A*, 36, 12, (2005), 3495-3497.

Vilekar, S. A., Fishtik, I. and Datta, R., The steady-state kinetics of a catalytic reaction sequence, Chemical Engineering Science, 64, (2009), 1968‑1979.

Ward, T. L. and Dao, T., Model of hydrogen permeation behavior in palladium membranes, *Journal of Membrane Science*, 153, (1999), 211-231.

Wert, C. and Zener, C., Interstitial atomic diffusion coefficients, *Physical Review*, 76, 8, (1949), 1169-1175.

Wimmer, E., Wolf, W., Sticht, J., Saxe, P., Geller, C. B., Najafabadi, R. and Young, G. A., Temperature-dependent diffusion coefficients from ab initio computations: hydrogen, deuterium, and tritium in nickel, *Physical Review B*, 77, 13, (2008), 134305.

Wynblatt, P., Diffusion mechanisms in ordered body-centered cubic alloys, *Acta Metallurgica*, 15, 9, (1967), 1453-1460.

Yang, Q. Q., Yuan, L. I. U. and Li, Y. X., Hydrogen diffusion coefficient in liquid metals evaluated by solid - gas eutectic unidirectional solidification, *Transactions of Nonferrous Metals Society of China*, *24*, 12, (2014), 4030-4037.

Zener, C., Theory of Do for atomic diffusion in metals, *Journal of Applied Physics*, 22, 4, (1951), 372-375.

Chapter VI

Liquid Gallium Membrane Porous Support Screening

6.1 Abstract

The novelty of SLiMM and the consequent lack of guidance in the literature presented significant initial challenges in fabricating a stable liquid metal membrane, specifically in the selection of an appropriate porous support for the liquid metal. As described in chapter III, unlike for Pd (Ayturk et al., 2009; Ma et al., 2004) porous metal supports were found to be unsuitable for SLiMM, as the liquid metals readily react with most metallic substrates at elevated temperatures (~500 ºC) forming intermetallic compounds (Yatsenko, 1970, 2008). Even many ceramic supports were found to be unsuitable as some reacted with the liquid metals at the higher temperatures while others are overly inert and not adequately wetted by the liquid metal to form a thin membrane. Just the right affinity (Gibbs free energy change) is needed between the liquid metal and the porous support to strike a balance between wettability and reactivity to form a free-standing and thin liquid metal layer on top of an inert support. This chapter summarizes the thermodynamic approach of estimating liquid gallium/ceramics wettability and stability at high temperatures. The calculated results were compared with coupon tests to narrow the selection and finalize the material screening process for SLiMM supports. We found that many of the oxide ceramics supports such as Fe_2O_3 and NiO were overly reactive, while others such as Al_2O_3 and ZrO_2 were found to be stable, as were many types of carbide. On the other hand, some ceramics (e.g., Al_2O_3, ZrO_2) were found to be too inert to provide good interfacial wetting, while others were wettable but overly reactive.

6.2 Introduction

From initial experiment and, it was realized that pure metal porous support are going to form intermetallic compound with liquid gallium, and thus they are excluded from the study. However, we did not know the reactivity of in-situ oxide diffusion barrier layer of porous metal support with liquid gallium. Therefore, Fe_2O_3, Cr_2O_3 and NiO (the main components in diffusion barrier of porous stainless steel and Inconel) were included in the screening process.

First in this chapter a thermodynamic reactivity assessment is evaluated and compared with contact angles obtained from several liquid metal/ceramic systems reported in the literature. The purpose of this section is to determine whether the selected ceramics are wettable by liquid gallium. Secondly, the stability of porous ceramic supports with liquid gallium was evaluated via thermodynamic assessment to analyze any potential reaction between liquid gallium and ceramics (oxides, carbides, and nitrides) at 500 ºC. Experimental results confirmed these theoretical predictions, and in this manner we were able to systematically select suitable porous ceramic supports for SLiMM. Through these three steps carbide materials such as SiC and graphite were found to satisfy all the criteria and thus were chosen as supported materials.

6.3 Wettability Assessment between Liquid Gallium and Ceramic Support

Wettability could be influenced physically by support geometry, or chemically by chemical bonding between liquid and solid at the interface, which is a function of temperature and functional groups. Eustathopoulos and Drevet (1994) proposed that there were direct connections between the wettability and the product of liquid metal with ceramic support at high temperatures. If liquid gallium is reactive, the surface reaction between metal and ceramic support surface (e.g., Al_2O_3) could be expressed as Eq. (6.1).

$$2(\mathrm{Ga}) + \mathrm{Al_2O_3} \leftrightarrows \mathrm{Ga_2O_3} + 2(\mathrm{Al}) \tag{6.1}$$

$$\Delta G_R^* = \mu_{\mathrm{Ga_2O_3}} + 2\mu_{\mathrm{All}} - \mu_{\mathrm{Al_2O_3}} - 2\mu_{\mathrm{Ga}} \cong G^o_{f,\mathrm{Ga_2O_3}} - G^o_{f,\mathrm{Al_2O_3}} + RT\ln a^2_{\mathrm{Al}} \tag{6.2}$$

where the activity a_{Al} of Al in liquid Ga is unknown. The activity coefficient $\gamma_{\mathrm{Al}} = a_{\mathrm{Al}} / x_{\mathrm{Al}}$, where x_{Al} is the mole fraction of Al in Ga. By assuming $\gamma_{\mathrm{Al}} = \exp(cx_{\mathrm{Ga}})^2$ (Eustathopoulos and Drevet , 1994), where c is a constant, then

$$\ln\gamma_{\mathrm{Al}} = c(1-x_{\mathrm{Al}})^2;\ RT\ln\gamma_{\mathrm{Al}} = \Delta\overline{H}^{\infty}_{\mathrm{Al(Ga)}} \tag{6.3}$$

$$\frac{\partial\ln\gamma^{\infty}_{\mathrm{Al}}}{\partial(1/T)} = \frac{\Delta\overline{H}^{\infty}_{\mathrm{Al(Ga)}}}{R} \tag{6.4}$$

where $\Delta\overline{H}^{\infty}_{\mathrm{Al(Ga)}}$ is the partial enthalpy of mixing of Al at infinite dilution in Ga.

As the solubility of Al in liquid Ga is small, we assume $x_{Al} \cong 0$, combing Eqs. (6.3) and (6.4) the activity coefficient at infinite dilution of Al in Ga can be expressed as

$$RT\ln\gamma^{\infty}_{Al} = \Delta\overline{H}^{\infty}_{\mathrm{Al(Ga)}}(1-x_{\mathrm{Al}})^2 \cong \Delta\overline{H}^{\infty}_{\mathrm{Al(Ga)}} \tag{6.5}$$

As the result, the simplified Gibbs free energy of reaction thus takes the form:

$$\Delta G^*_{\mathrm{R}} = G^o_{f,\mathrm{Ga_2O_3}} - G^o_{f,\mathrm{Al_2O_3}} + 2\Delta\overline{H}^{\infty}_{\mathrm{Al(Ga)}} \tag{6.6}$$

Due to the lack of experimental data for $\Delta\overline{H}^{\infty}_{\mathrm{Al(Ga)}}$, modeling estimates were used (Miedema, 1977) for the calculation. Ceramic Gibbs free energy of formation data were taken from (Sharafat, 2000).

Figure 6.1 shows the relation between contact angle and Gibbs free energy of reaction of various liquid metal/ceramic systems calculated from Eq. (6.6). The contact angle data were gathered from several literature sources by Eustathopoulos and Drevet (1994). It is observed that if the calculated $\Delta G^*_{\mathrm{R}} / RT$ is greater than 20, the contact angle is most likely to be greater than 120^{o},

which defines a non-reactive system. If the value were smaller than 20, contact angles are mostly located between 60~120°. If $\Delta G_R^* / RT$ is negative, then most of the contact angles are smaller than 60°. A $\Delta G_R^* / RT$ smaller than 20 is, thus, defined as reactive system. Following this methodology, the thermodynamics of Ga/oxide ceramic system (at 500 ºC) were calculated as summarized in the inset table in Figure 6.1. The calculated value of Ga/SiO_2 (23.79) was identical to the value given in the Figure 6.1 (Eustathopoulos and Drevet, 1994).

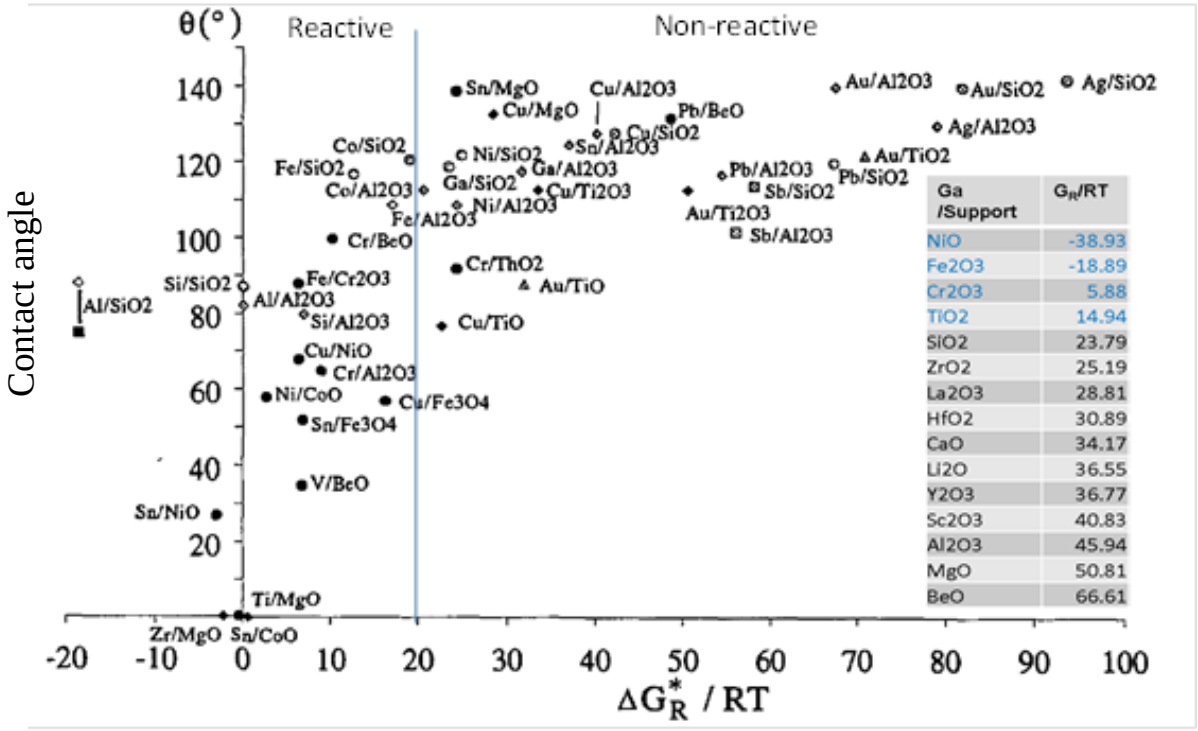

Figure 6.1 Reactivity and contact angle of various liquid metal/ceramic at high temperatures (Eustathopoulos and Drevet, 1994).

The results suggest that liquid gallium has good wetting with NiO (-38.93), Fe_2O_3 (-18.89), Cr_2O_3 (5.88) and but poor wetting with MgO (50.81) and Al_2O_3 (45.94). This means that for Ga/NiO, Ga/Fe_2O_3, and Ga/Cr_2O_3 contact angle would have high possibility to be less than 60º while Ga/MgO, Ga/ Al_2O_3 contact angle would be higher than 120º. As for TiO_2 (14.94), SiO_2

(23.79) and ZrO_2 (25.19) the $\Delta G_R^* / RT$ values were in reactive to non-reactive gray region, so that wettability/inertness cannot be judged *apriori* considering that the calculations are made under several assumptions.

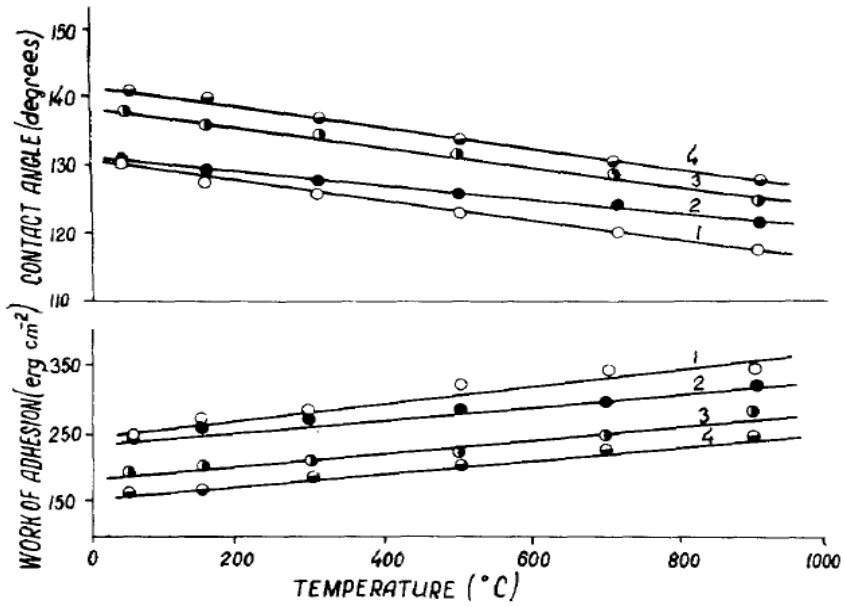

Figure 6.2 Contact angle and work of adhesion for gallium to (1) sapphire, (2) quartz, (3) carbon, (4) graphite as a function of temperature. (Naidich and Chuvashov, 1983).

The above assessment is based on empirical observation and the contact angle data often include scatter, depending on the measurement technique. Therefore, this analysis can only serve as rough guide for reactive wetting and contact angle. As an example, in Figure 6.2 the contact angle of Ga/SiO_2 is higher than that Ga/Al_2O_3, which is opposite to the result indicated in Figure 6.1. Overall, reactive systems tend to have low contact angle and the non-reactive system tend to have high contact angle.

6.4 Thermodynamic Assessment of Ceramic Support–Liquid Gallium Interaction

As described in the previous section, the estimation methodology developed by Eustathopoulos and Drevet (1994) is based on the gallium oxide formation taking place when liquid gallium contacts a ceramic support. The reaction between metal elements from substrate (e.g. Al from Al_2O_3) with liquid gallium was ignored. However, in some cases the solubility of elements from the support in liquid gallium may not reach saturation. Therefore they just dissolve in the melt without any intermetallic compound or gallium oxide formation. In this section, the assessment approach above is improved by calculating chemical potential of all the elements in liquid gallium from experimental data and estimated Gibbs free energy change of the reaction.

A thermodynamic assessment of the support-gallium interaction was made by including the partial Gibbs free energy of the metal (M), oxygen (O), and nitrogen (N) from a ceramic support dissolved in liquid gallium. The potential reaction between liquid Ga and the oxide or nitride ceramic may be represented as

$$\mathrm{Ga} + \mathrm{M}_x\mathrm{O}_y \leftrightarrows y\mathrm{O(Ga)} + x\mathrm{M(Ga)} \tag{6.7}$$

and

$$\mathrm{Ga} + \mathrm{M}_x\mathrm{N}_y \leftrightarrows y\mathrm{N(Ga)} + x\mathrm{M(Ga)} \tag{6.8}$$

The corresponding Gibbs free energy change of these reactions are given by

$$\Delta G_{\mathrm{R}} = y\mu_{\mathrm{O(Ga)}} + x\mu_{\mathrm{M(Ga)}} - G^{\mathrm{o}}_{f,\mathrm{M}_x\mathrm{O}_y} \tag{6.9}$$

and

$$\Delta G_{\mathrm{R}} = y\mu_{\mathrm{N(Ga)}} + x\mu_{\mathrm{M(Ga)}} - G^{\mathrm{o}}_{f,\mathrm{M}_x\mathrm{N}_y} \tag{6.10}$$

where $\mu_{\mathrm{M(Ga)}}$ is the chemical potential of metal in liquid Ga, $\mu_{\mathrm{O(Ga)}}$ is the chemical potential of oxygen in liquid Ga, $\mu_{\mathrm{N(Ga)}}$ is the chemical potential of nitrogen in liquid Ga, and G^{o}_f is the Gibbs free energy of formation of the ceramic, that for liquid Ga being assumed as zero.

Since the concentrations in Ga are low and can be assumed to follow Henry's law, it is assumed that activity is the same as solubility or mole fraction x. This assumption is correct so long as the solubility < 2 at% (Yatsenko et al., 2008; 1970). The chemical potential and partial Gibbs free energy of a metal in liquid gallium could be then calculated.

$$\mu_{\mathrm{M(Ga)}} = \overline{G}_{\mathrm{M(Ga)}} = RT \ln a_{\mathrm{M}} = (\Delta S_{fus} + \Delta S_{\mathrm{M}})T - (\Delta H_{fus} + \Delta H_{\mathrm{M}}) \tag{6.11}$$

where a_{M} is the activity of metal in liquid Ga, ΔH_{fus} is heat of fusion, ΔS_{fus} is entropy of fusion, ΔH_{M} is the excess partial molar heat of solution ΔS_{M} is the excess partial molar entropy of solution. Chemical potential calculated from Eq. (6.11) was then used in Eq. (6.9) and Eq. (6.10). It is assumed in the above that the partial heat of solution does not depend on temperature and that the metal atoms are randomly distributed in gallium. In addition, the metal from ceramics is assumed melted and dissolved in gallium. The solubility data of metals in liquid gallium was obtained from Yatsenko et al. (2008; 1970) as shown in Figure 3.2 in chapter 3. Solubility of silicon in liquid gallium is $x_{Si} = 49\exp(-7601/T)$ from Ogawa et al. (1995). Further details of these calculations are provided in Appendix A. The hence estimated Gibbs free energy of reaction between ceramic supports and liquid gallium at 500 ºC are summarized in Figure 6.3.

From Figure 6.3 it is noticed that Fe_2O_3/Ga, NiO/Ga, Cr_2O_3/Ga, and SiO_2/Ga are reactive ($\Delta G_R < 0$). This indicates that significant interaction of Ga with Fe_2O_3, NiO, Cr_2O_3 and SiO_2 is taking place at 500 ºC. The materials such as ZrO_2 and Al_2O_3 are inert with Ga at 500 ºC. The actual reactivity of materials in gray area such as TiO_2, MgO ($0 < \Delta G_R < 100$) are unknown. These results also match the wettability assessment from section 6.3 in that Fe_2O_3/Ga, NiO/Ga, Cr_2O_3/Ga, are reactive since $\Delta G_R^* / RT \leq 20$ (good wetting). It also implies that the *in-situ* oxidation diffusion barriers on porous stainless steel and Inconel will fail in resisting the reaction between liquid metal and substrates. On the other hand, ZrO_2 and Al_2O_3 will be inert to liquid

gallium; however, from a wettability standpoint Al_2O_3 may not be wetted by liquid gallium ($\Delta G_R^* / RT \geq 20$). ZrO_2 and MgO are uncertain since they are both located in gray region in either assessment.

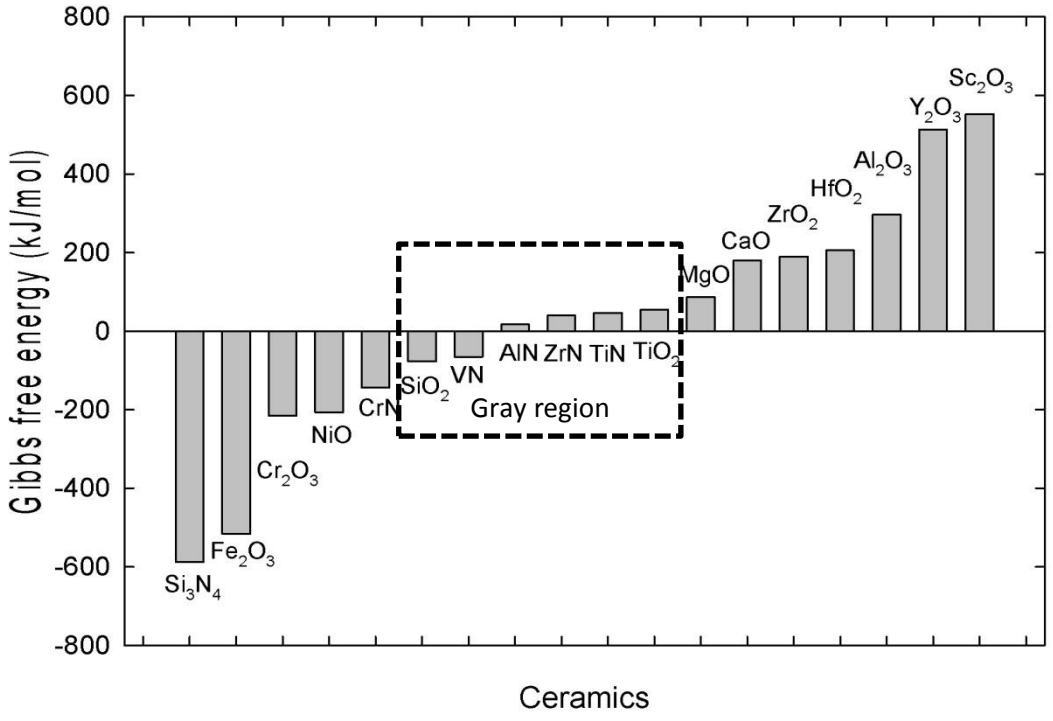

Figure 6.3 Calculated Gibbs free energy of reaction of oxide and nitride ceramic supports with Ga at 500 ºC.

Based on this assessment, most of the nitrides belong to reactive systems and, therefore, may not be suitable candidates as the support for Ga-based membranes. Carbides were excluded in this calculation because of the lack of thermodynamic information on Ga_2C_2 (Samsonov, 1965). The bond Ga-C, like Ga-O, is primarily ionic and is chemically unstable. Hence, the wettability and stability of Ga with carbides remains unknown and must be checked experimentally.

Though the assessment provides some guidelines in selecting support, the kinetics of the reaction are unknown. A reactive material with very slow kinetics may still be eligible as Ga membrane support, although the rather high operating temperature of around 500 ºC would promote

kinetics. Also the reactivity and wettability of several materials such as MgO, ZrO_2 and TiO_2 could not be ascertained by the calculations because of ambiguous results. Therefore, stability coupon tests were performed as described in the next section to further narrow down and select appropriate supports.

6.5 Porous Support and Liquid Gallium Wettability and Stability Experiments

From the thermodynamic assessment described above, it was noticed that some of the oxide supports with moderate wetting with liquid Ga eventually reacted at elevated temperatures, including Fe_2O_3, Cr_2O_3, NiO, which are the main components of *in-situ* oxidation diffusion barrier of porous stainless steel (PSS), the common support used to Pd membrane (Ma et al., 2004). And some of the oxides such as regard to SiO_2, TiO_2, ZrO_2 maybe uncertain in terms of wettability and reactivity. In order to verify the relationship between wettability vs. stability of liquid gallium with promising supports, various coupons were prepared for testing.

Porous supports tested in this part of the study included SiC, Graphite, ZrO_2, TiO_2, NiO, Al_2O_3 (non-porous), SiO_2 (Quartz) and oxidized-PSS. Coupons were plated with a Ga film, followed by heating in ultra-high purity helium or in hydrogen at 500 ºC followed by SEM/XRD testing. This sequence of coupon testing is shown in Figure 6.4. Helium was always purged for at least 30 minutes before heating. Liquid gallium was able to be placed in a small piece of bowl-shaped Al_2O_3, while ZrO_2 coupon was a flat plate, not suitable for holding liquid metal and was thus excluded in the stability test.

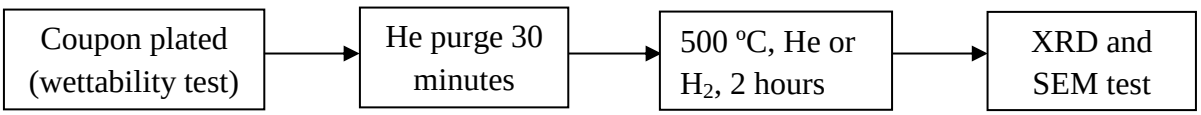

Figure 6.4 Coupon test procedure for support and Ga interaction.

6.5.1 Wettability Results

ZrO_2 and Al_2O_3 were not wetted properly with Ga, so that it was difficult to hold liquid Ga in position while heating in the oven. Rests of the materials were wetted by liquid gallium as shown in Figure 6.5. These results agreed with the wettability assessment, where $\Delta G_R^* / RT$ of Al_2O_3 (45.94) and ZrO_2 (25.19) indicates non-reactivity and would consequently have poor wetting with liquid gallium. This wettability experiment was performed at room temperature and generally as the temperature increased wetting between liquid and solid improved. As indicated in Figure 6.2 e.g. Ga/SiO_2 contact angle decreases from 130º at 200 ºC to 125º at 900 ºC. However, the improvement in wetting is small. The wettability experiment at room temperature is, thus, still considered a good indication of liquid gallium/ceramic wetting behavior at higher temperatures.

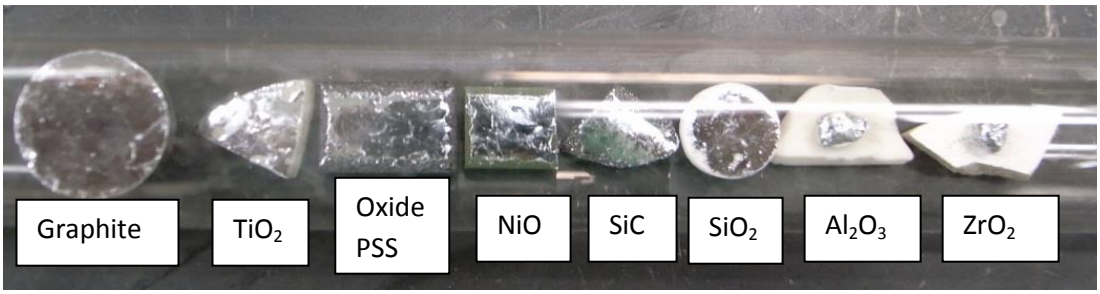

Figure 6.5 Image of various ceramic materials plated with liquid gallium before heating.

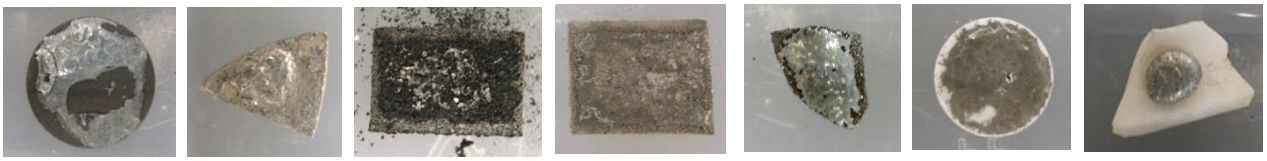

Figure 6.6 Image of various ceramic materials plated with liquid gallium after heating.

After heating in hydrogen for 2 hours coupons were removed from the oven as shown in Figure 6.6. It was clear that Ga/SiC showed no sign of reaction and had proper wetting. Gallium on graphite shrinks in certain area after heating, suggesting that the Ga/Graphite wetting is slightly

poorer than SiC but it is also non-reactive. TiO_2, NiO, oxide-PSS and SiO_2 had good wetting with Ga, and thus the shape remained almost the same before and after heating. However, there are clear signs of interactions and are, thus, considered reactive. The color and morphology of Ga/NiO, Ga/oxidized-PSS changed after heating and they seem to undergo strong reaction at 500 ºC. Gallium on Al_2O_3 formed sphere shape as shown on the picture, suggesting that Ga/Al_2O_3 had poor wetting and is non-reactive. Results from Ga/NiO, Ga/oxidized-PSS and Ga/Al_2O_3 in fact match the wettability predictions from section 6.3. These experiments also confirmed that Ga/TiO_2 Ga/SiO_2 are wettable, reactive systems, while Ga/ZrO_2 is a non-wettable, non-reactive system.

6.5.2 Stability Results

Coupons as shown in Figure 6.6 were analyzed via SEM/EDX and XRD. The microstructure characterization of the membranes were carried out using the Amray 1610 Turbo Scanning Electron Microscope (SEM) equipped with a Princeton Gamma-Tech Avalon EDX light element detector and a RBA-1610 5MC type Robinson Retractable backscattered electron detector for the qualitative and quantitative analysis. The phase identification analysis was conducted by using a Rigaku Geigerflex X-Ray diffractometer (XRD) equipped with a CuKα radiation source (λ = 1.54 Å), and a curved crystal monochromator. A JADE software was utilized for data analysis.

I: NiO support

Figures 6.7 (a) illustrates the SEM image scan and 6.7 (b) EDX of Ga/NiO. The geometry observed from this image demonstrates crystal-like structures and it was clear that Ni had reacted with Ga. XRD result shown in Figure 6.7 (c) confirmed the formation of intermetallic compounds of Ga_3Ni_2 and Ga_3Ni_5. Since coupon was heated in hydrogen it is possible that NiO

was reduced into Ni as observed from XRD. The Pd in Figure 6.7 (b) is from sputtering during sample preparation.

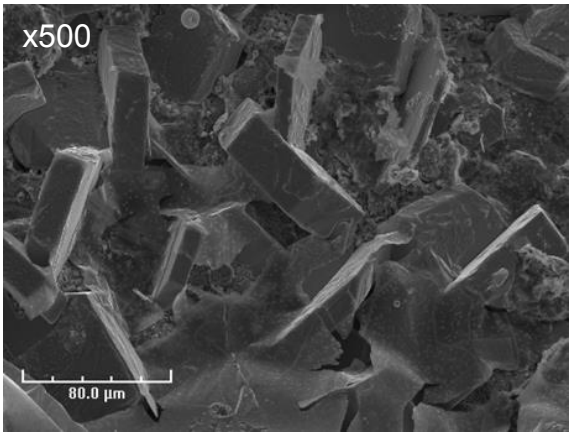

Figure 6.7 (a) SEM image of Ga/NiO.

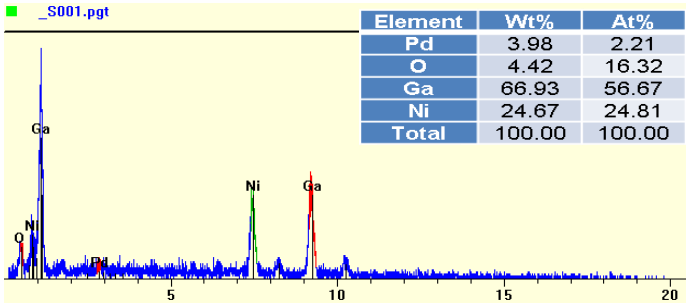

Figure 6.7 (b) Ga/NiO EDX composition analyses.

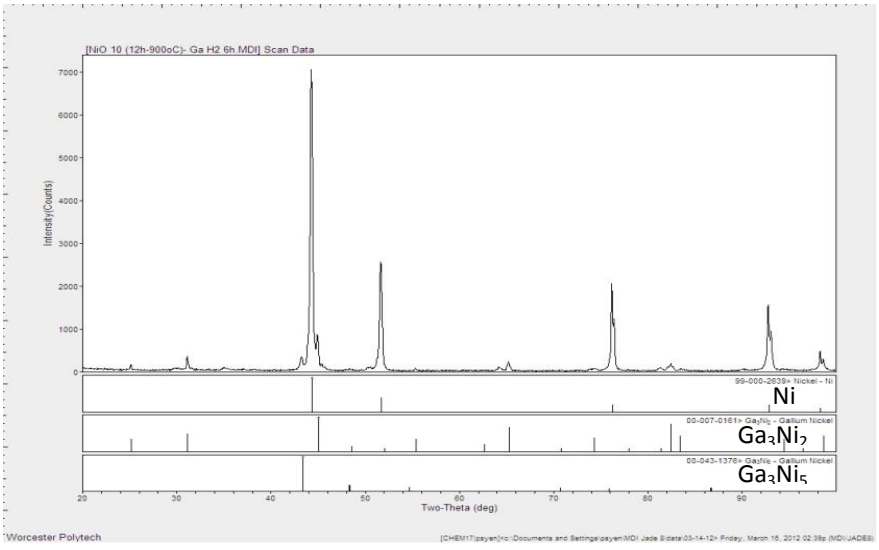

Figure 6.7 (c) XRD of Ga/NiO in hydrogen for 2h, 500 ºC.

II: Oxidized-PSS support

In these experiments, Fe, $FeGa_3$ and Ga_2O_3 peaks were observed from oxide-PSS/Ga XRD results as shown in Figure 6.8. It indicates that even with the *in-situ* oxidation to presumably serve as diffusion barrier as it does for Pd (Ma et al., 2004), oxidized-PSS is clearly not an appropriate candidate for supporting liquid gallium.

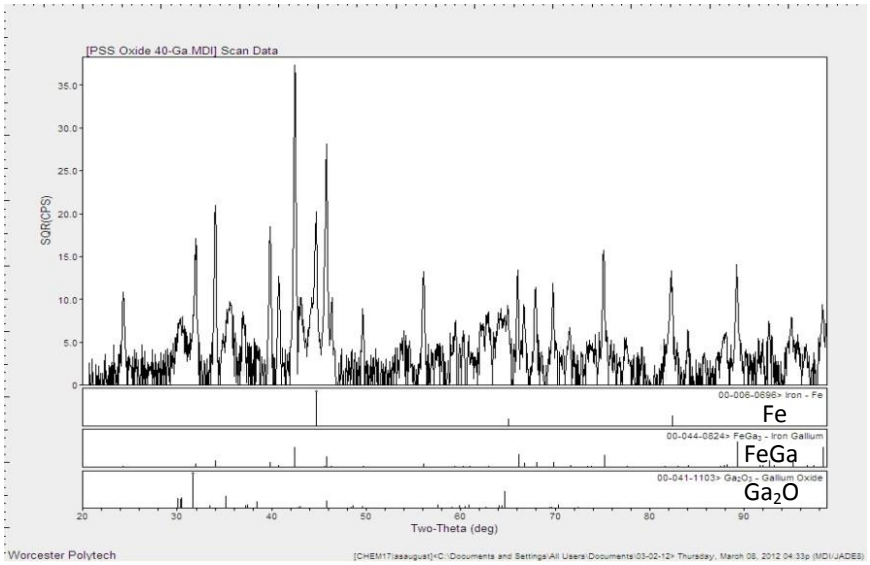

Figure 6.8 XRD of oxidized-PSS/Ga in hydrogen for 2h, 500 ºC.

III: TiO_2 support

The same procedure was applied to TiO_2/Ga. The SEM images and EDX examination of TiO_2/Ga under hydrogen for 2 hours 500 ºC is shown in Figure 6.9 (a) and (b). Unlike NiO coupon having 24.67 wt% of Ni on the surface only 0.44 wt% of Ti was detected at the surface by EDX. Further examination by XRD as given in Figure 6.9 (c) shows that while there was Ga_2O_3 and TiO_2 but there was no evidence of any Ti_xGa_y intermetallic compound. Based on thermodynamic assessment results, the Gibbs free energy of reaction of Ga with TiO_2 is slightly positive, in the gray area. Therefore, the reaction kinetics may also be slower compared to NiO and oxide-PSS. Thus for the same heating period and temperature it is possible that the reaction

of Ni with Ga occurs more rapidly than that of Ti with Ga. The formation of Ga_2O_3 shows that, even in hydrogen, TiO_2 is reacting with Ga at 500 ºC.

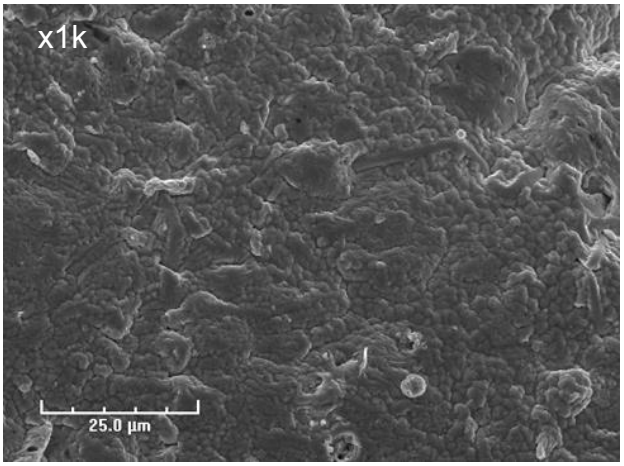

Figure 6.9 (a) SEM image of Ga/ TiO_2.

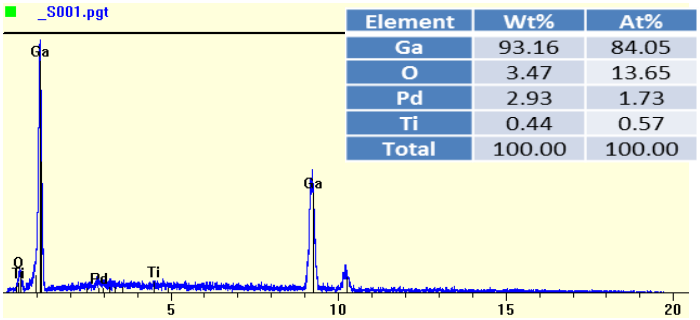

Element	Wt%	At%
Ga	93.16	84.05
O	3.47	13.65
Pd	2.93	1.73
Ti	0.44	0.57
Total	100.00	100.00

Figure 6.9 (b) EDX composition analysis Ga/ TiO_2.

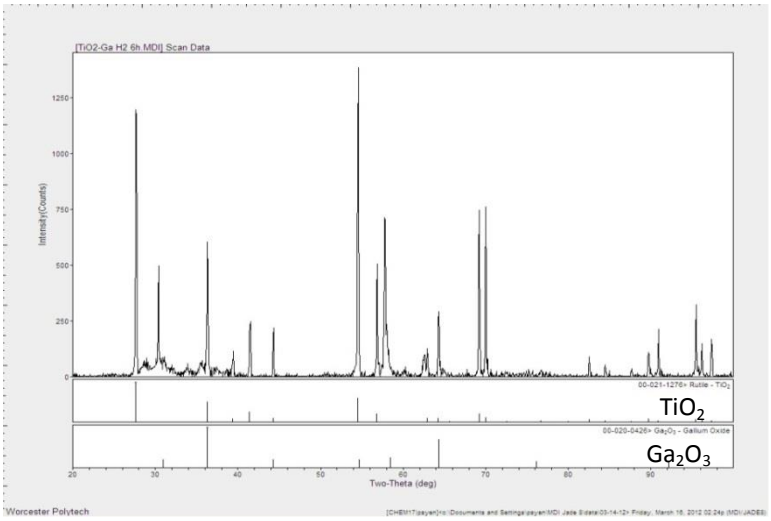

Figure 6.9 (c) XRD of TiO_2/Ga in hydrogen for 2h, 500 ºC.

IV: SiO_2 support

Figures 6.10 (a) and (b) are the SEM and EDX scanning results of (SiO_2)/Ga. Figures 6.10 (c) is the XRD of (SiO_2)/Ga treated in hydrogen for 2 hours. The result reveals that Ga is reacting with SiO_2 at 500 ºC. The strong Ga_2O_3 peak and the broad amorphous peak indicated in Figure 6.10 (b) suggests that Ga remains partially liquid. SiO_2/Ga is considered a reactive system (Figure 6.6) and it is not suitable for supporting liquid gallium membrane.

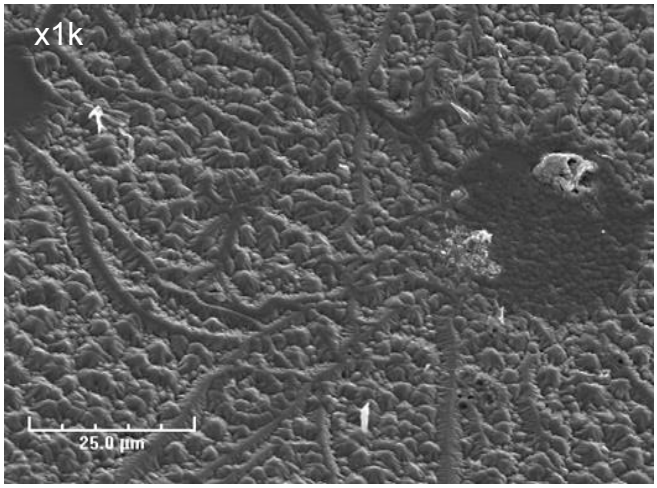

Figure 6.10 (a) SEM image of Ga/ SiO_2.

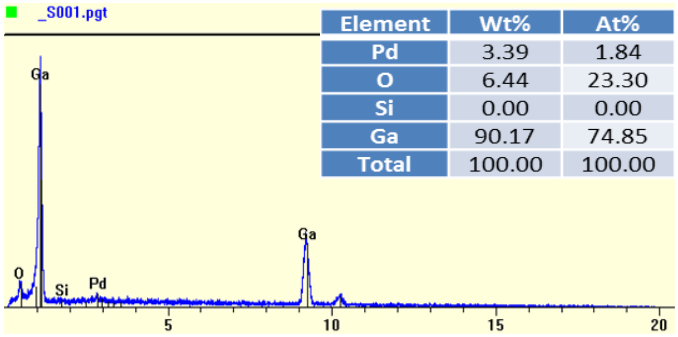

Element	Wt%	At%
Pd	3.39	1.84
O	6.44	23.30
Si	0.00	0.00
Ga	90.17	74.85
Total	100.00	100.00

Figure 6.10 (b) EDX composition analysis of Ga/ SiO_2.

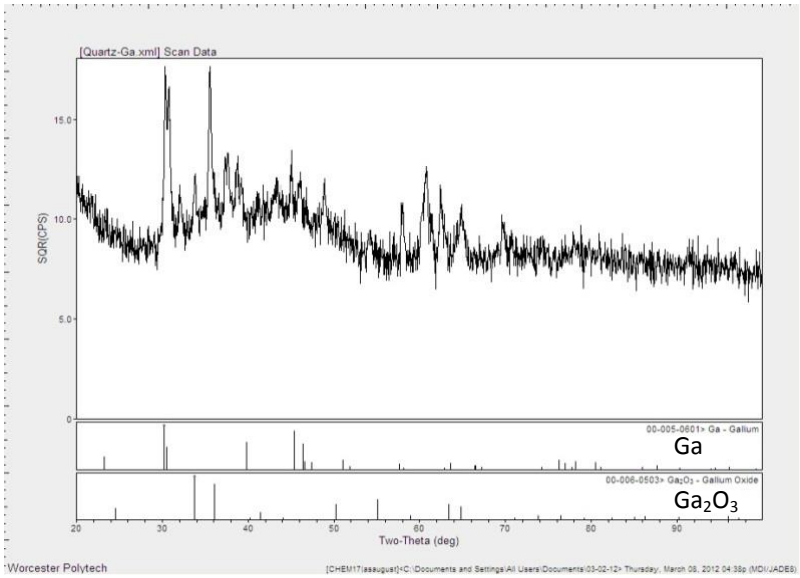

Figure 6.10 (c) XRD of Ga/ SiO_2 in hydrogen for 2h, 500 ºC.

V: SiC and Graphite support

Figure 6.11(a) illustrates SEM and (b) EDX scanning of SiC/Ga. Figure 6.11 (c) and (d) are the XRD results of SiC/Ga and Graphite/Ga in hydrogen for 2 h, 500 ºC. It is noteworthy that only pure Ga was detected with only a trace of Pd coming from sputtering when preparing SEM samples. No sign of oxygen was found in this sample. This provides direct evidence of oxidation reaction between Ga and the oxide supports since all of the coupons discussed here were tested simultaneously. If the oxygen were coming from the gas tank or air leakage, then the oxygen should also be found on SiC and Graphite supported Ga surface. Furthermore, it is now certain that SiC would make a proper candidate in terms of chemical stability. The wettability between Ga/SiC and Ga/Graphite is, however, another matter that needs to be improved.

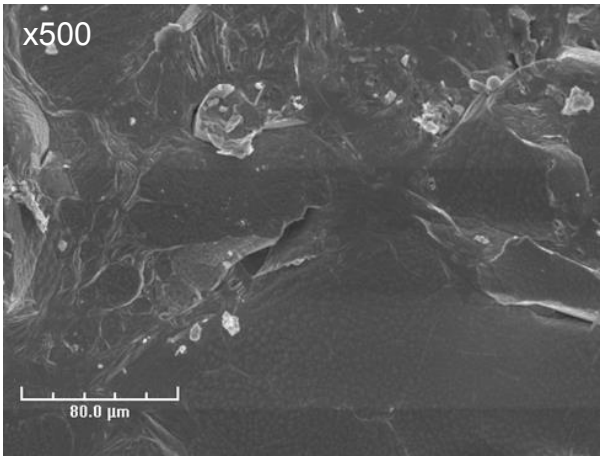

Figure 6.11 (a) SEM image of Ga/ SiC.

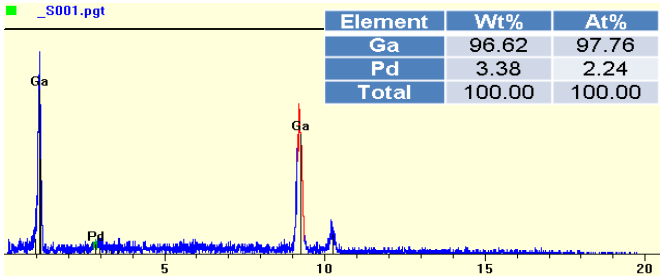

Figure 6.11 (b) EDX composition analysis Ga/ SiC.

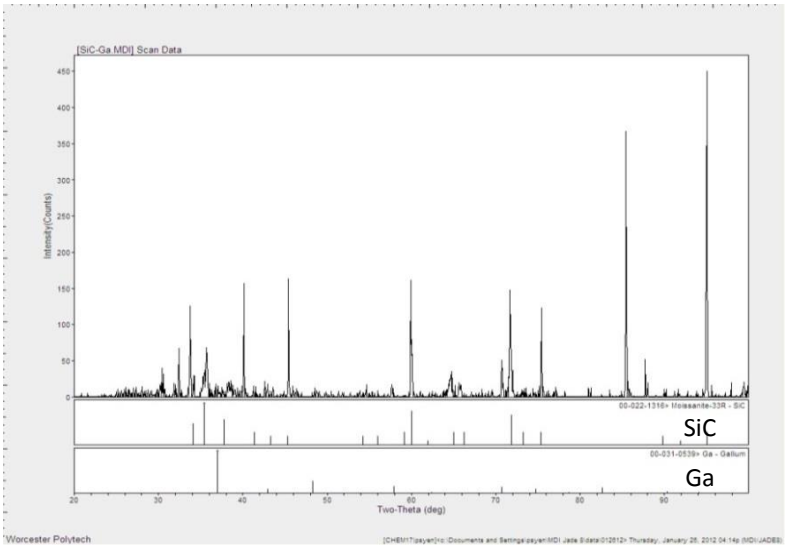

Figure 6.11 (c) XRD of SiC/Ga in hydrogen for 2h, 500 ºC.

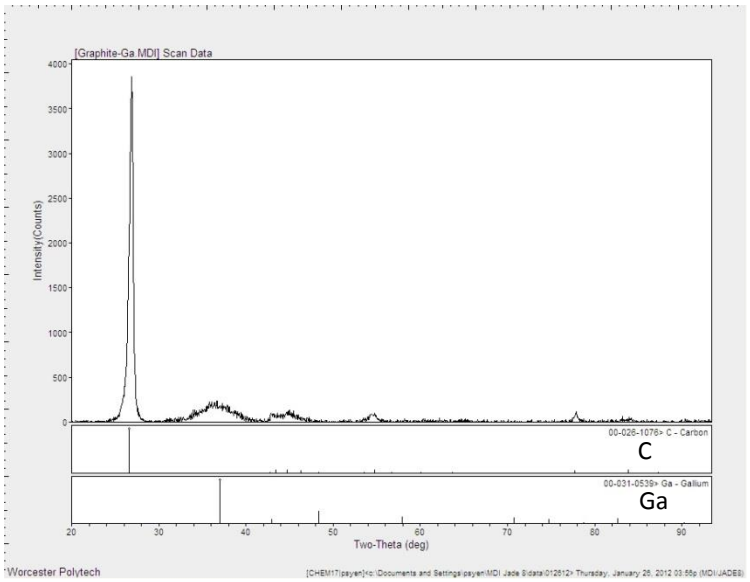

Figure 6.11 (c) XRD of Graphite/Ga in hydrogen for 2h, 500 ºC.

In conclusion, it is realized that most of the substrates with proper wetting have poor stability and react with liquid gallium over time at elevated temperatures. Substrates with poor wetting tend to have good stability as shown in Table 6.1. The lack of chemical reaction on the substrate surface with liquid Ga is one of the reasons for having poor wettability. In terms of making a liquid membrane, it is important to find a support that only has a slight reaction preferably at the liquid metal and support interface to ensure good wetting, but not bulk reaction that potentially would destroy the nature of the membrane and its ability to react with hydrogen. These conclusions are summarized in Table 6.1.

Table 6.1 Experimental positive and negative results of wettability and stability of various materials at 500 ºC.

	TiO_2	SiO_2	SiC	NiO	Al_2O_3	Oxidized -PSS	Graphite
Wettability	√	√	√	√	X	√	√
Stability	X	X	√	X	√	X	√

6.6 References

Ayturk, M. E., Kazantzis, N. and Ma, Y. H., Modeling and performance assessment of Pd and Pd/Au-Based catalytic membrane reactors for hydrogen production, *Energy and Environmental Science*, 2, (2009), 430-438.

Eustathopoulos, N. and Drevet, B., Interfacial bonding, wettability and reactivity in metal/oxide systems, *Journal de Physique III France 4*, (1994), 1865-1881.

Ma, Y. H., Akis, B. C., Ayturk, M. E., Guazzone, F., Engwall, E. E. and Mardilovich, I. P., Characterization of intermetallic diffusion barrier and alloy formation for Pd/Cu and Pd/Ag porous stainless steel composite membranes, *Industrial and Engineering Chemistry Research*, 43, 12, (2004), 2936-2945.

Miedema, A. R., de Boer, F. R. and Boom, R., Model predictions for the enthalpy of formation of transition metal alloys, *Calphad*, 1, 4, (1977), 141-359.

Ogawa, H., Guo, Q. and Ohta, K., Low temperature liquid phase epitaxy of silicon from gallium solution, *Journal of Crystal Growth*, 155, (1995), 193-197.

Samsonov, Q. V., On the problem of the classification of carbides, *Powder Metallurgy and Metal Ceramics*, 4, 1, (1965), 75-81.

Sharafat, S. and Ghoniem, N., Thermodynamic stability assessment of oxides, nitrides, and carbides in liquid Sn-$_{25}$Li, *University of California Los Angeles report*, UCLA-UCMEP-00-32, (2000).

Yatsenko, S. P. Anikin, Yu. A. Khimicheskaya, F. and Materialov, M., Solubility of metals of the fifth period in liquid gallium, *Materials Science*, 6, 3, (1970), 57-62.

Yatsenko, S. P, Sabirzyanov, N. A. and Yatsenko, A. S., Dissolution rates and solubility of some metals in liquid gallium and aluminum, *13th International Conference on Liquid and Amorphous Metals, Journal of Physics: Conference Series*, 98, (2008), 1-7.

Chapter VII

Supported Liquid Metal Membrane (SLiMM) for Hydrogen Purification

7.1 Abstract

Pd membranes are the most advanced for hydrogen separation and are approaching practical application (Ma et al., 2009). However, search for alternative membranes continues trying to lower their cost and susceptibility to poisons. The liquid metals employed here are low-melting, low-cost, non-precious group metals, with an open and fluid lattice that facilitates ready dissolution and diffusion of hydrogen. They can overcome many of the issues with Pd membrane such as sintering, hydrogen embrittlement, and thermal mismatch between the membrane and the support. The overall goal of this study is to develop and test a novel supported liquid metal membranes (SLiMM) for hydrogen separation. To prove the concept we chose Ga as our starting point. We described the methodology and the screening process of choosing ceramic porous substrates in chapter 6, and showed that both liquid metal/substrate wettability as well as stability is crucial for making a stable membrane. The thermodynamic assessment suggested that SiC and graphite materials are the best porous substrate candidates. In this chapter we will discuss the reason for making a sandwich configuration membrane and how to fabricate a seamless connection using SiC tube and disc. A Sieverts' apparatus was also built to measure liquid gallium hydrogen solubility at various temperatures as this is not available in the literature. We describe experimental result of permeance of several leakage-free (no helium flux detected) liquid gallium membranes and their stability. Combining the experimental result of solubility

with literature diffusivity data for hydrogen in liquid gallium, we are able to calculate hydrogen permeance of liquid gallium and compare it with experimental result at various temperatures. This provides the direct proof of the hydrogen permeation ability of liquid gallium and the feasibility as a hydrogen separation membrane. In fact, liquid gallium permeability was found to be higher than most of the hydrogen separation amorphous alloy and metals.

7.2 Introduction

The technologies available for separating H_2 include absorption, membrane separation, pressure-swing adsorption (PSA), and cryogenic distillation (Adhikari and Fernando, 2006; Holladay et al., 2009). The PSA and the cryogenic distillation are the most commonly utilized processes in industry. However, these are energy intensive. This is a key reason for seeking alternate H_2 separation technologies, particularly via dense metal membranes. The most promising current membranes involve Pd and its alloys with Ag and Cu, either as thin foils or as thin membranes supported on porous ceramic or metal supports (Paglieri and Way, 2002; Fukai, 2005; Sholl and Ma, 2006; Nenoff et al., 2006; Adhikari and Fernando, 2006; Ockwig and Nenoff, 2007; Yun and Oyama, 2011). However, these membranes still fall short from the desired cost, chemical and mechanical robustness, and durability targets. Here, we demonstrate the feasibility of a supported *liquid* metal membrane for H_2 purification, using gallium as an example.

As described in this chapter, the measured hydrogen permeance of liquid gallium $72.5\,m^3/m^2h\cdot atm^{0.5}$ at 500 ºC is about 35 times higher than that of Pd foil of similar thickness, i.e., $2\,m^3/m^2h\cdot atm^{0.5}$ (Ayturk et al., 2009), while price is an order of magnitude lower (metal-pages). Development of such high performing and inexpensive membranes could bring the H_2 economy a step closer to reality.

7.3 Membrane Configuration and Fabrication

7.3.1 Membrane Configuration

From research described in Chapter VI, it was discovered that SiC would make a good substrate in terms of its stability with liquid gallium at the operating temperature of around 500 ºC. Liquid gallium wets SiC, but its wettability is barely adequate to make a stable, leakage free membrane with a free surface. Wettability often changes with temperature, pressure, gas environment and gas composition (as discussed in detail in chapter VIII). Free standing liquid gallium films often developed small leakage with time during hydrogen permeation test as described here. Therefore, an appropriate configuration such as a sandwich structure that holds liquid gallium in place between two porous substrate to avoid the wettability change brought by a change of testing conditions such as gas composition or temperature.

Consequently, our so-called sandwiched liquid metal membrane (SLiMM) comprises a thin (~200 μm) film of a liquid metal or alloy, sandwiched between two inert porous ceramic supports (Figure 7.1). The mechanism of hydrogen permeation in liquid metal is assumed to be the same as in Pd and other metals and is described in more detail in section 2.3 and elsewhere.

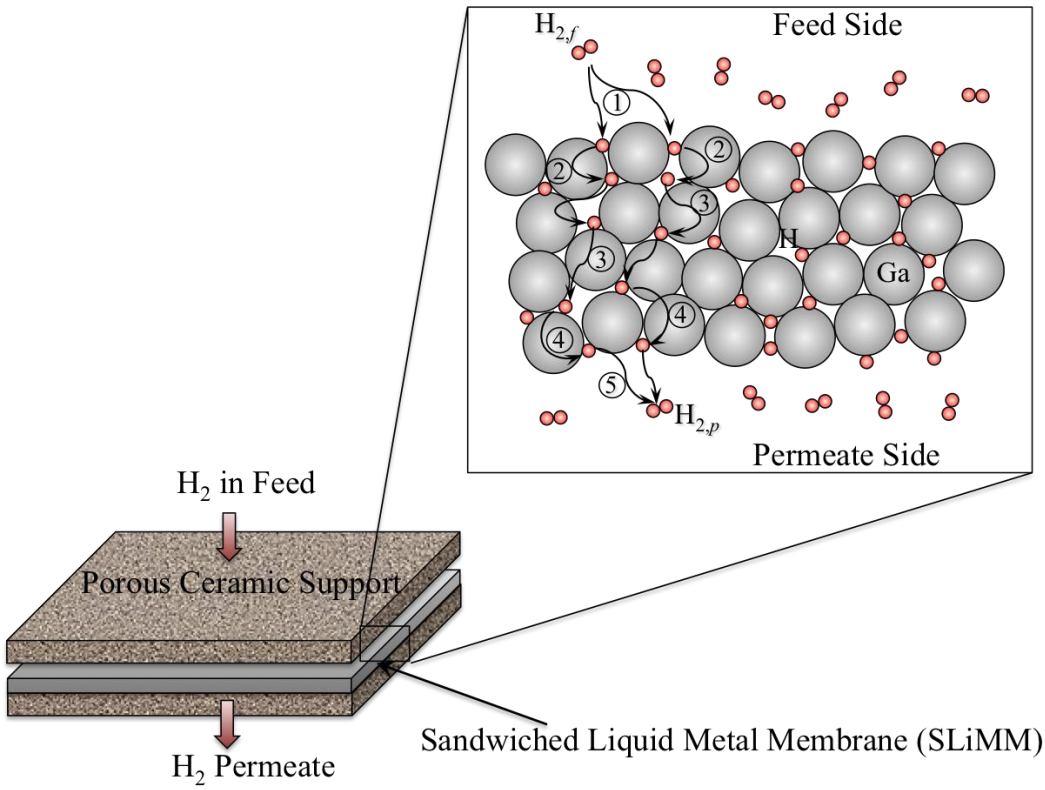

Figure 7.1 A schematic of the H_2 permeation process through a dense liquid metal membrane involving sequential steps of: ① surface dissociative adsorption, ② subsurface penetration, ③ bulk metal diffusion, ④ egression to surface, and ⑤ reassociation of H atoms on the surface to form molecular H_2.

7.3.2 Fabrication of Porous SiC Disc on a Dense SiC Tube

To attach a porous SiC disc supporting the liquid metal membrane at the end of SiC tube, we used ceramic sealant. The gas tight sealing needed for hydrogen separation test is similar to that in SOFC (Solid Oxide Fuel Cell), operating at high temperature for sealing ceramic materials for gas flow separation. The selected sealant, thus, needed to fulfill several requirements as shown in Table 7.1.

Unlike SOFC, however, hydrogen separation membrane operates at a lower temperature, under 600 ºC, but with higher pressure drops and no requirement for electrical conductivity. Therefore,

the ideal sealant for hydrogen separation membrane tubing needs to be: 1) thermally stable with a matching thermal expansion to the SiC support and the tubing; 2) chemically stable with no chemical reaction with H_2 or liquid metal; 3) mechanically stable during high pressure operation; 4) and with the ability to withstand differential pressure up to 14 psi with no helium leakage detected.

Table 7.1 Properties and fabrication requirement of SOFC seal (Mahapatra and Lu, 2010).

Properties	Requirements
Thermal properties	Thermal expansion coefficient at $9.5–12.0 \times 10^{-6}\,°C^{-1}$ Thermally stable for ~5000 h for mobile applications and for ~50,000 h for stationary applications at 650–900 °C cell operating temperatures
Chemical properties	Resistant to vaporization and compositional change in stringent oxidizing and wet reducing atmospheres at 650–900 °C Limited or no reaction with other cell components
Mechanical properties	Withstand external static and dynamic forces during transportation and operation Resistant to thermal cycling failure during start-up and shut-down of cell stacks
Electrical properties	Electrical resistivity $\geq 10^4\,\Omega$ cm at operating temperature Electrical resistivity greater than 500 Ω cm between cells and stacks at nominal stack operating condition (0.7 V at 500–700 mA/cm^2)
Sealing ability	Sealing load <35 kPa Withstand differential pressure up to 14–35 kPa across a cell or stack Total fuel leakage <1% for the duration of the cell life
Fabrication flexibility	Flexible design, low processing cost, and high reliability

There are three types of seals for SOFC: 1) compressive seal; 2) compliant seal and 3) rigidly bonded seal. Both compressive and compliant seals involve mechanical compression on ceramic components and gaskets (Mahapatra and Lu, 2010), which was deemed unsuitable for hydrogen separation membrane setup. Therefore, only rigidly bonded seal was considered appropriate for our purposes.

Rigidly bonded seal glass comprises various oxide materials such as SiO_2, B_2O_3, Li_2O, ZnO, TiO_2, NiO, etc,. for adjusting thermal expansion coefficient, T_g (glass transition temperature) and, T_s (glass softening temperature) temperature, glass viscosity, seal adhesion, and hinders devitrification (Mahapatra and Lu, 2010). Besides the proper proportion of each oxide, the curing profile such as curing time, curing temperature, curing steps, heating speed are also important

factors in making a gas tight seal. Currently, there are several commercial glass products to choose from. After some trail-and-error paste 613 from Aremco, Inc. was chosen for assembling SiC disc and tube. Pastes were selected based on CTE (coefficient of thermal expansion), curing temperature, and material composition.

CTE of 6H-SiC is 4.3×10^{-6} °C (ioffe.ru) and glass is 9×10^{-6} K (engineeringtoolbox.com). Since both porous disc and tube used in this study are SiC, their CTE should be identical thus the only concern is to find the paste material with CTE as close as possible to that of SiC. Heating characteristics of paste 613 are shown in Table 7.2.

Table 7.2 Paste 613 heating characteristic (Supplied by Aremco, Inc.).

Paste	613
Binder	Glass
Max Operation Temperature (ºC)	620
Air Set Before Curing, hour	1
Curing ºF, hour	1150, 0.5

To make a sandwich structure, (Figure 7.1) the first step is to fix the gap between porous SiC disc and SiC tube. Thus, the 0.1 μm grade porous SiC disc (supplied by LiqTech, Denmark) and a dense SiC tube (supplied by Saint Gobain, Worcester) were cleaned via IPA prior sealing. Glass paste was applied to the interface between the tube and the disc multiple times in order to build a wall to contain liquid gallium pool and also to make sure that all the gaps between the tube and the disc were sealed. After air drying for 30 minutes, the tube was then subjected to heat treatment. The glass heating process is listed in Table 7.2. The sealed SiC disc and tube are shown in Figure 7.2 (a).

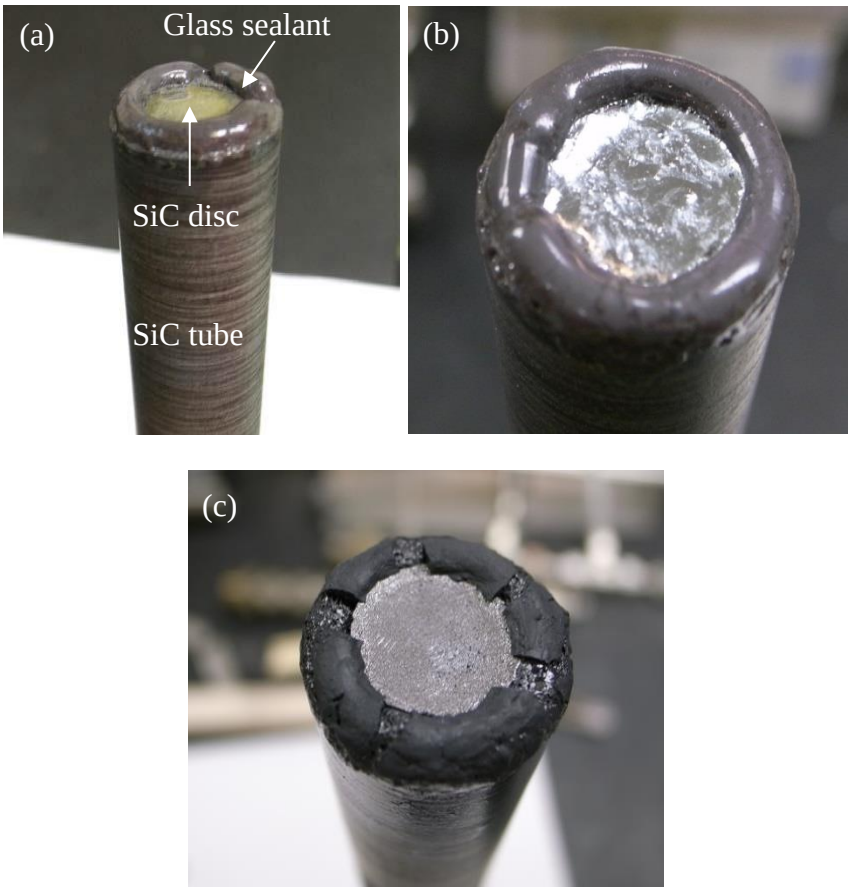

Figure 7.2 (a) SiC disc and SiC tube configuration after glass paste sealing, (b) deposited gallium and (c) sandwiched liquid gallium membrane.

7.3.3 Liquid Gallium Membrane Fabrication

After heat treatment of the sealed assembly, it is ready for membrane deposition. If any visible cracks were spotted on the sealant, extra glass paste would be applied on top, but without further heat treatment step. The additional glass paste would *be in-situ* cured during hydrogen permeation test at high temperatures. A fixed amount of gallium was melted by heating lamp and deposited on the SiC disc using vacuum to improve wetting. A 200~300 μm thick liquid gallium membrane was hence deposited as shown in Figure 7.2 (b). Deposited liquid gallium was then put in a freezer to solidify the membrane. Solid gallium membrane is easier to transport and handle during reactor assembling. To make a sandwich structure (Figure 7.1) a sheet of graphene

was cut to a size slightly larger than the solidified gallium and placed on top of it (Figure 7.2. c). Glass paste was carefully applied only to the interface between the graphene layer and the glass sealant, and to carefully avoid any contact with the solidified gallium. Upon further heating in the setup this graphene layer would become fixed in position by the solidified glasses. This step was to make sure that the graphene protects the liquid gallium surface against any significant morphology change brought about by surface tension change when under helium gas atmosphere.

7.4 Hydrogen Permeation Apparatus Design

The apparatus designed for the hydrogen permeation test is shown in Figure 7.3 (a) and (b). This cell only allowed ¾" OD, 12" L SiC tubes for testing where the porous frit and tube assembly was to be sealed via ceramic paste as described in last section.

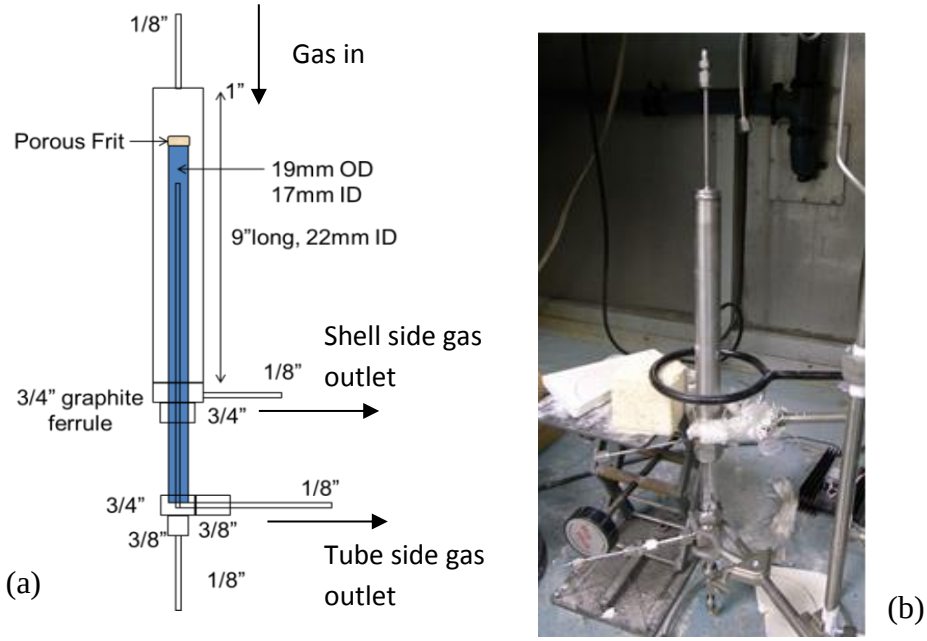

Figure 7.3 (a) Scheme and (b) image of tubular diffusion cell.

Membrane disc/tube assembly was mounted in a 9" L, 1" OD, S.S cell using a ¾"-1" Swagelok adaptor with ¾" graphite and PTFE ferrule. Another 3/4"-3/8"-3/8" adaptor was used to collect

tube side hydrogen flux and provide helium sweep gas. A 1/8" tube was welded to the end of the cell for connecting to shell side hydrogen/helium inlet.

The hydrogen permeation test setup is shown in Figure 7.4. Hydrogen and helium gas share the same pressure regulator (Swagelok, PR Regulator, 0~100 psi) at shell side inlet in order to maintain the same pressure during selectivity test (by switching hydrogen to helium). A needle valve and buffer tank were used to regulate the shell side inlet gas. Ultra-high purity helium (AIMTEK Inc., H_2O < 5 ppm, O_2 < 2 ppm) was used to prevent any potential reaction between liquid gallium and any impurities. Another helium tank was used as sweep gas on the tube side. Moisture trap (Agilent, MT-200) was installed at the regular quality tank to remove moisture before entering the permeation apparatus.

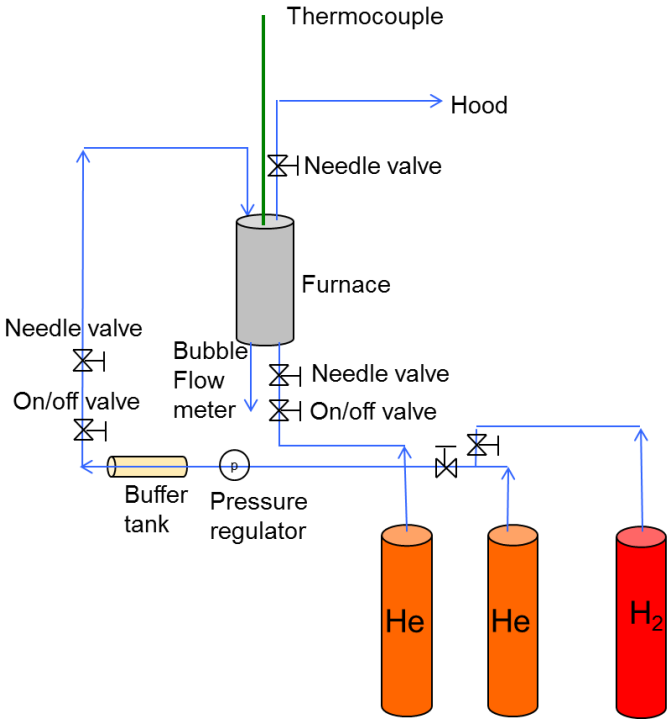

Figure 7.4 Diagram of hydrogen permeation for permeation apparatus.

The cell was mounted vertically in the center of 3-1/2" ID, 12" L, 7-1/2" OD ceramic fiber heater (Watlow, 120V, 900W) with a thermocouple attached to temperature controller

(Eurotherm, 2116) and a relay to control the ceramic heater temperature. The insulation strips were sealed properly at both ends of the ceramic heater. Tube side gas outlet was connected to bubble flow meter and a data acquisition system. A needle valve was used to regulate shell side retentate gas.

The data acquisition system setup consisted of 4 mass flow controllers, a 4 channel readout/power supply (MKS, 247C), 2 pressure transducers (Transducers Direct, 0~10 V DC output, 0~500 psi), 2 data boxes (National Instrument, NI USB 6008) and temperature recorder (Omega Engineering, Inc., UTC- USB to PC Connection). Signals from pressure transducers, mass flow meters, were recorded by LabView program. Signals from the temperature recorder were recorded by TRH Central (Omega Engineering, Inc.) program. And a image of LabView control panel is shown in Figure 7.5. As the program initiated, a file name and file path has to be specified for data recording. The sampling time period has to be specified as well. The LabView coding image is provided in Appendix B.

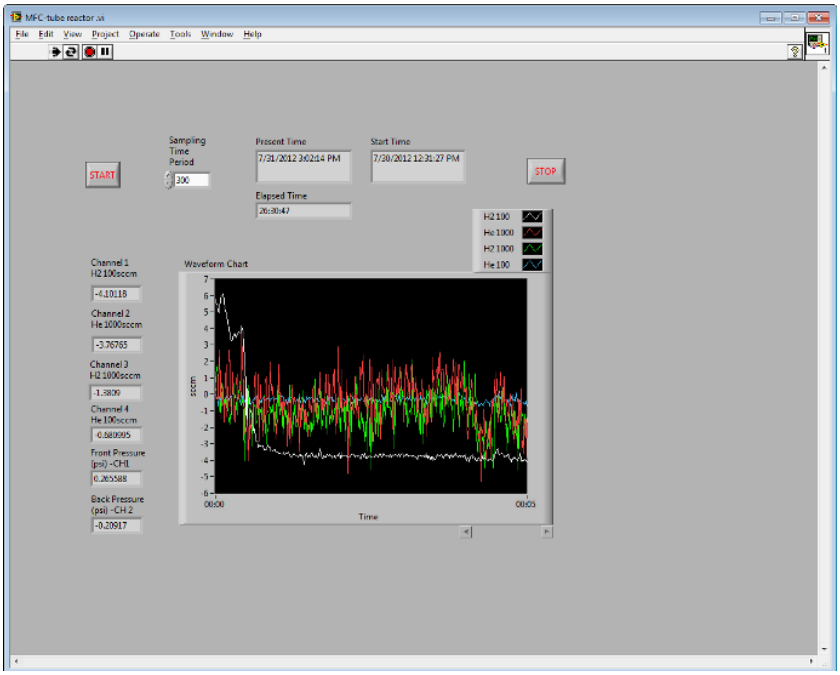

Figure 7.5 An image of LabView control panel.

7.5 Ga Solubility Measurement via Sieverts' Apparatus

Hydrogen permeance can be calculated from hydrogen diffusion coefficient and solubility in liquid metal as described in section 2.3. Hydrogen diffusion coefficient of liquid gallium $D_{\mathrm{H}} = 3\times10^{-3}\exp(-9610/RT)\,\mathrm{cm}^2/\mathrm{s}$ is provided by Mazayev and Prokofive (1994), however, there is no literature report on hydrogen solubility in liquid gallium. Therefore, besides measuring hydrogen flux directly from the membrane permeation apparatus described above, we also determined the solubility of hydrogen in liquid gallium. Hydrogen solubility coefficient was measured via a Sieverts' apparatus (Blach and Gray, 2007) by employing hydrogen at various pressures and temperatures over a pool of gallium. Schematic of the Sieverts' apparatus is shown in Figure 7.6.

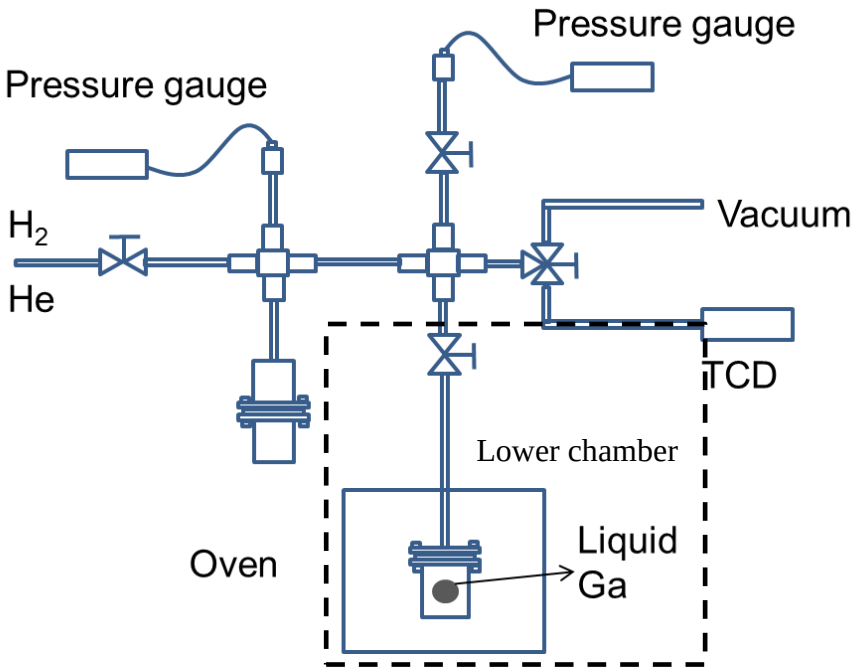

Figure 7.6 Schematic of Sieverts' apparatus.

Thus 7.75 g of gallium was placed in a graphene lined metal chamber to prevent any inter-diffusion and to maintain stability of the liquid metal pool at high temperatures. Highest testing temperature was limited to 550 ºC due to the limitation of the ceramic heater. The Sieverts'

apparatus could be separated into two chambers, namely upper chamber and lower chamber. The lower chamber is enclosed in a temperature controlled oven. The upper chamber at room temperature is the reservoir to store hydrogen during desorption step.

There are two common volumetric measurement methods employed in obtaining hydrogen solubility of a metal. One is to gradually increase hydrogen pressure in steps until hydrogen stops absorption. In each segment, hydrogen and metal reach equilibrium in a set time period. The obtained result is called pressure-composition temperature (PCT) curve, or pressure-composition isotherm (PCI) (Blach and Gray, 2007). The other method is to provide a fixed pressure of hydrogen and monitor hydrogen absorption/desorption behavior (Policicchio et al., 2013). Here we adopt hydrogen adsorption/desorption method by obtain hydrogen solubility to investigating hydrogen uptake and release in liquid gallium at various temperatures (300–550 ºC).

For hydrogen absorption experiment, the lower chamber was first evacuated thoroughly and 1 atm of hydrogen was introduced into the Sieverts' apparatus. The subsequent pressure change because of absorption was recorded via data acquisition system over time.

For hydrogen desorption experiment 1 atm of hydrogen is introduced in both upper and lower chambers overnight to saturate liquid gallium prior to desorption. The overall desorption steps are: 1) close the valve that connects upper and lower chamber; 2) purge upper chamber with helium several times before introducing vacuum. This is a safety precaution to prevent connecting high concentration hydrogen with vacuum pump directly. After finishing evacuation 1 atm helium is introduced again; 3) open the valve that connects upper and lower chamber; 4) record pressure change due to H_2 evolution over elapsed time until it reached equilibrium; 5) steps 1~4 were repeated until all of the hydrogen within the liquid metal had been expunged, in principle requiring an infinite number of such cycles. During one of desorption cycles hydrogen

was sampled and sent to TCD detector to verify the gas composition. This was done to ensure that the released gas from the chamber contains hydrogen, not helium.

The hence measured hydrogen solubility (H/M, the hydrogen/liquid gallium atomic ratio) in liquid gallium versus inverse temperature using hydrogen adsorption as well as desorption methods is shown in Figures 7.7.

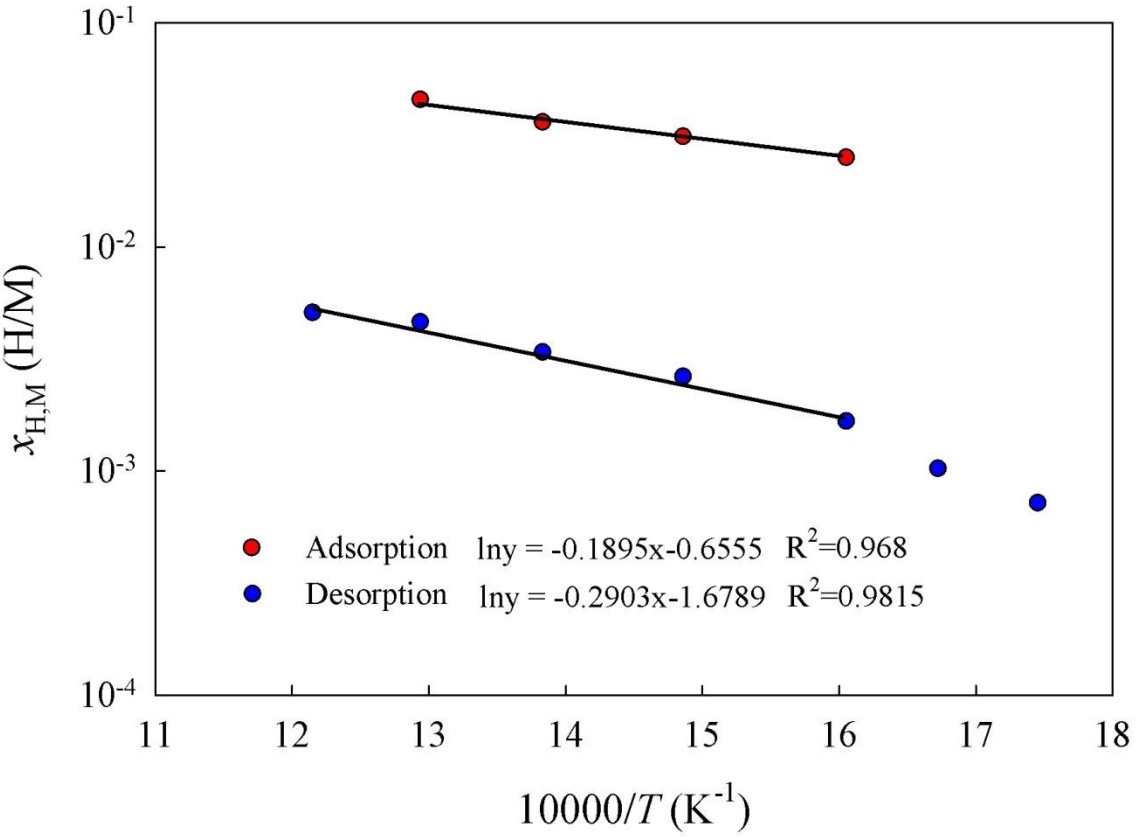

Figure 7.7 Measured adsorption and desorption method of liquid gallium hydrogen solubility versus inverse absolute temperature.

Hydrogen solubility of liquid gallium increases with rising temperature between 300~550 ºC as shown in Figure 7.7. Although the results from absorption and desorption are distinctly different. It was decided to perform desorption experiments first by introducing 1 atm of hydrogen overnight to ensure that the liquid gallium was fully saturated by hydrogen. The experimental

results suggest that below 300 ºC there is no sign of any measurable hydrogen desorption. The calculated heat of solution from desorption in Figure 7.7 provides $\Delta H_S^o = +24.14$ kJ/mol, while the calculated entropy change is $\Delta S_S = -13.67$ J/mol K. The calculated heat of solution from absorption in Figure 7.7 provides $\Delta H_S^o = +15.76$ kJ/mol and the calculated entropy change $\Delta S_S = -5.45$ J/mol K (The Sieverts' constant $K_S = 0.5192 \times \exp(-15758/RT)$).

Overall the desorption process was found to be more complexed than absorption. As mentioned above, interstitial hydrogen in liquid metal and the gas-phase hydrogen reach initial equilibrium by saturating under a set hydrogen pressure. At time t = 0, by opening the valve connecting upper and lower chambers (Figure 7.6), the H_2 in the apparatus is quickly replaced with an inert gas (He), thus, at the start of the experiment, i.e., at time t = 0, the hydrogen partial pressure is zero. As the hydrogen within the metal desorbs, the partial pressure of H_2 gradually increases, which is monitored as a function of time. It is further assumed that the contents of the two gas chambers are well-mixed. If instantaneous equilibrium is further assumed between the gas-phase and the liquid metal surface, the rates of surface desorption and surface association of hydrogen as well as egress from immediately below the surface layer are rapid compared to bulk interstitial H diffusion, we can assume that the concentration of dissolved hydrogen atoms at the surface to be zero at time zero. Due to this concentration gradient in the bulk liquid metal, interstitial hydrogen diffuses toward the surface and evolves into the gas phase. As hydrogen concentration in the chamber increases over time, the hydrogen pressure from desorption levels off and will eventually stop when the concentration in the chamber and in the liquid bulk reach a new equilibrium. For further gas evolution, the system is purged agian by an inert gas and the experiment is repeated a number of times until all of the removable hydrogen in the liquid metal has been exhausted.

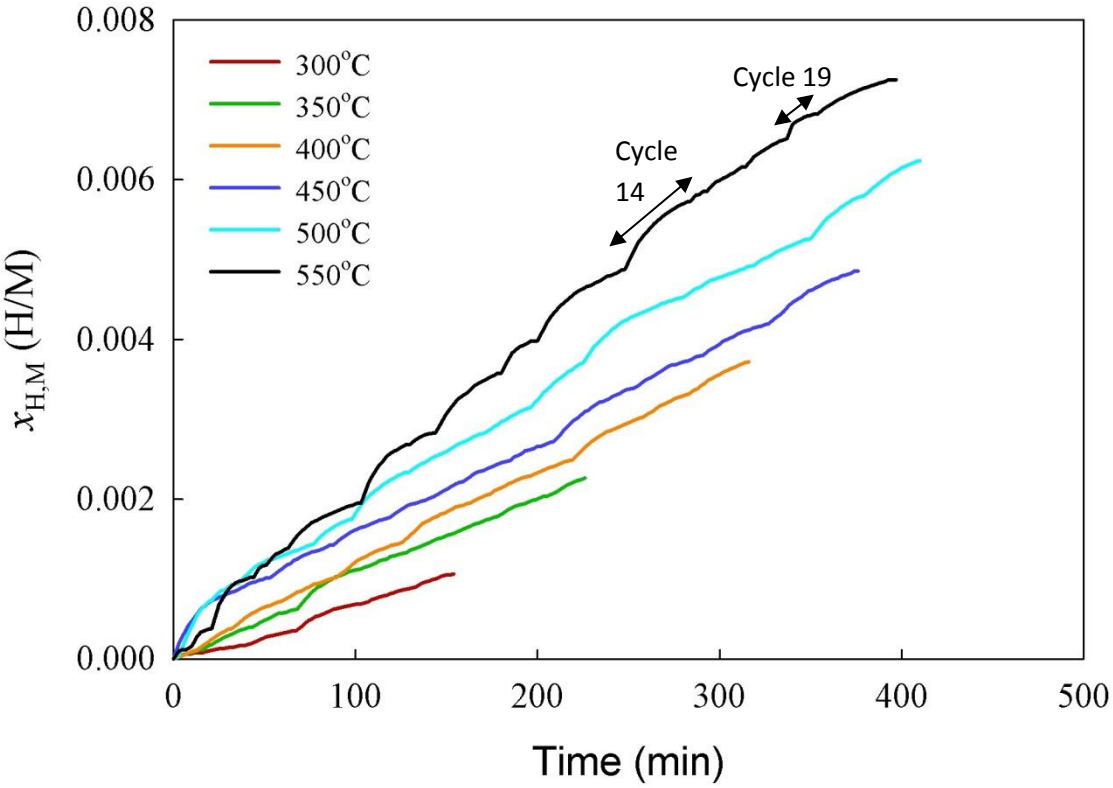

Figure 7.8 Liquid gallium hydrogen solubility calculated from hydrogen desorption pressure at various temperatures over time.

Figure 7.8 demonstrates the hydrogen solubility calculated from hydrogen desorption experiment at various temperatures over time. Each curve comprises multiple desorption cycles as described above. Sometimes there was a long pause between each cycle and required multiple inert gas purging before observing next hydrogen desorption. If the inert gas purging lasted more than four to six times without additional desorption, then the experiment was stopped.

At lower temperatures the overall duration of hydrogen release was shorter and the rate was slower than at high temperatures. It was also observed that the hydrogen desorption frequency and cycle duration of releasing appeared to vary randomly. Any short or long cycle could occur at the beginning or toward the end. All the hydrogen desorption cycles of liquid gallium vs time at 550 ºC are shown in Figure 7.9.

As an example shown in Figure 7.8 and Figure 7.9, at 550 ºC it takes 36 minutes for cycle 14 to reach equilibrium (when pressure levels off) with hydrogen released of 8.5×10^{-4} (H/M) (corresponding to 8.8 torr in Figure 7.9). On the other hand, hydrogen release of 2.7×10^{-4} (H/M) (corresponding to 2.8 torr in Figure 7.9) for cycle 19 occurred in 20 minutes.

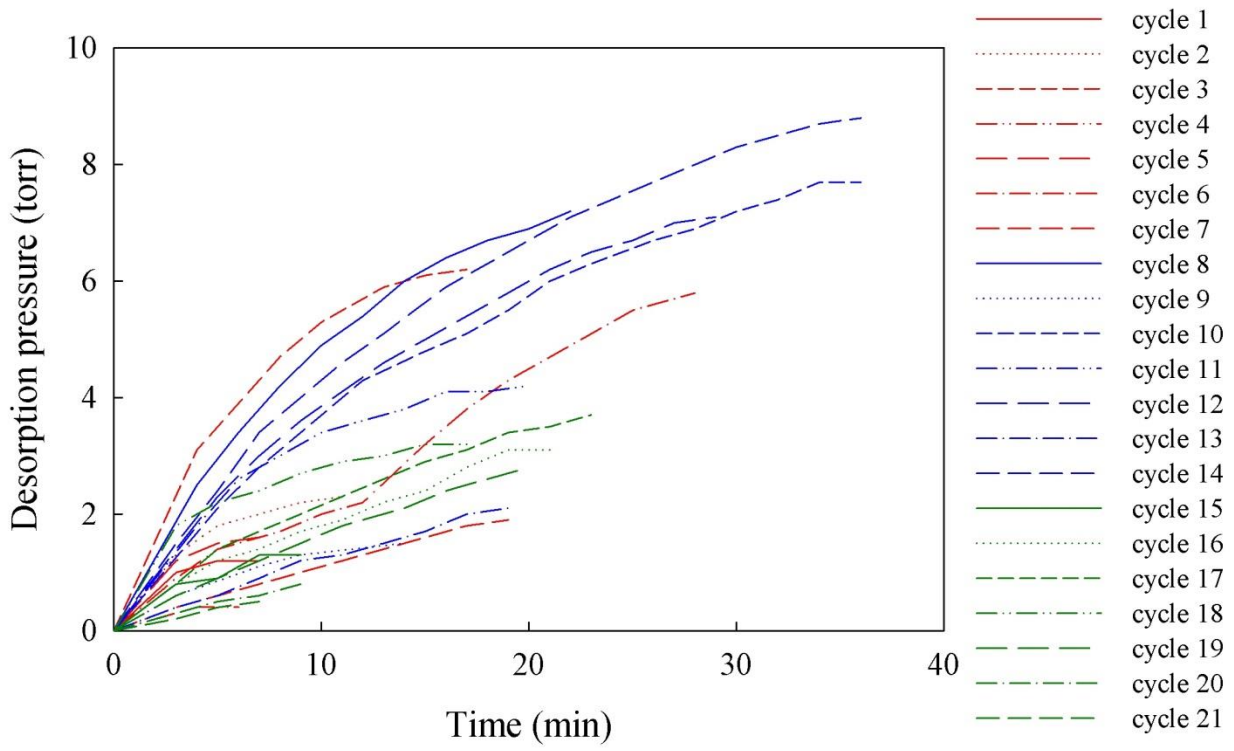

Figure 7.9 Overall hydrogen desorption cycles of liquid gallium vs time at 550 ºC.

This rather erratic hydrogen releasing behavior of liquid gallium was not understood and was the main obstacle in accurately measuring solubility from desorption experiments and could explain why this is an order of magnitude less than absorption solubility method. This strange hydrogen desorption behavior often led to early termination of the experiment. In later experiments, it was discovered that it could take up to 4 days of hydrogen desorption cycles to empty 90% of the adsorbed hydrogen calculated from adsorption experiment. Hysteresis in solid metal/hydrogen system is commonly observed and corresponds to phase transformation (Flanagan et al., 1980). It

is unknown at this point if the liquid metal system exhibits hydrogen hysteresis behavior similar to solid metal, or if it simply takes more time or lower pressure (e.g. by applying vacuum) to complete the hydrogen desorption. Therefore, the hydrogen solubility as determined by the absorption experiments was assumed to be the correct one. (The absorption experiments were conducted with the help of Nicholas Deveau).

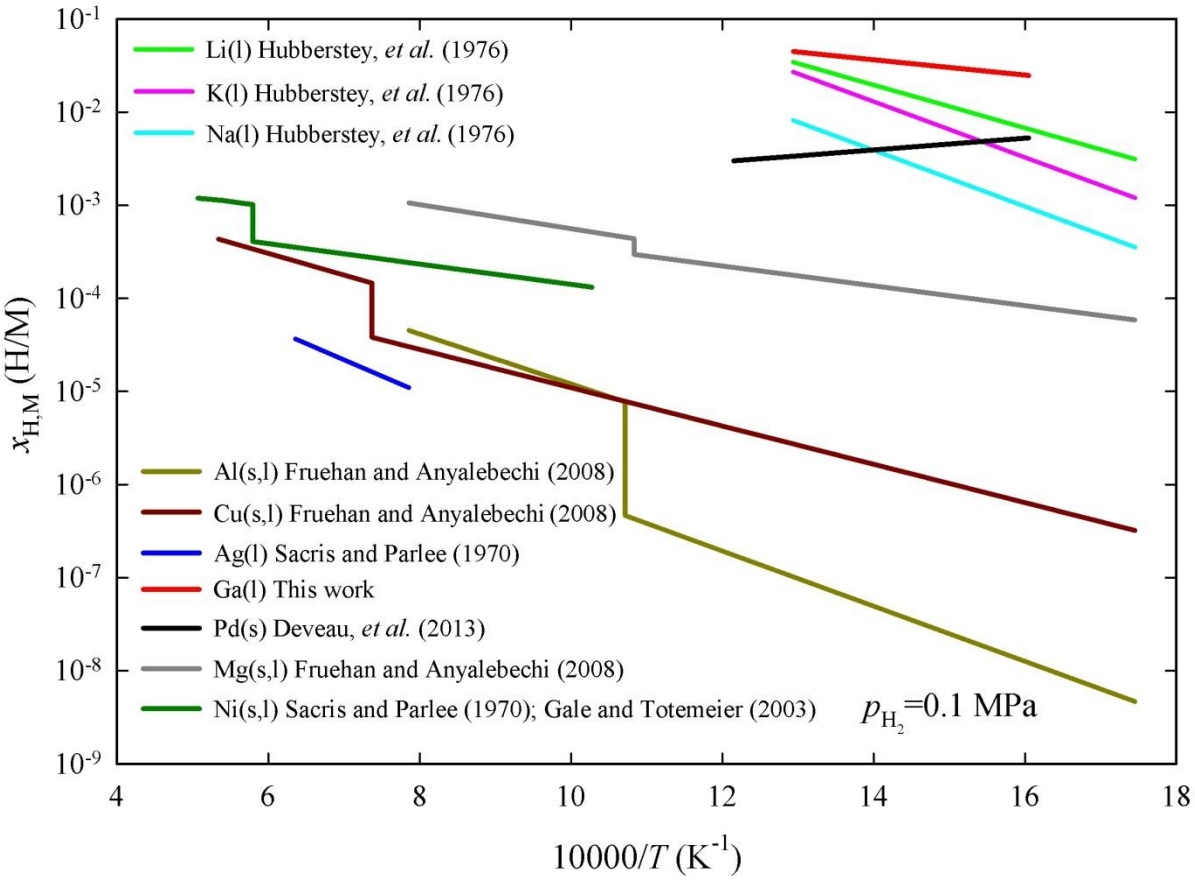

Figure 7.10 Solubility of hydrogen in various liquid and solid metals versus inverse absolute temperature for $p_{H_2} = 0.1$ MPa (Data from Hubberstey et al., 1976; Fruehan and Anaylebechi, 2008; Sacris and Parlee, 1970; Deveau, et al., 2013; Gale and Totemerier, 2003).

Hydrogen solubility of various metals in liquid and solid state is compared with liquid gallium solubility as shown in Figure 7.10 (Hubberstey et al., 1976; Fruehan and Anaylebechi, 2008; Sacris and Parlee, 1970; Deveau, et al., 2013; Gale and Totemerier, 2003). Hydrogen solubility

of metals in their liquid state is higher than that in their solid state as discussed in section 2.8. In fact, a step increase is typically observed at the melting point. This is evidently a result of the increased interstitial space in the bulk metal upon melting. The measured liquid gallium solubility of hydrogen is the highest among all of these metals and it is about 13 times higher than that in Pd at 500 ºC.

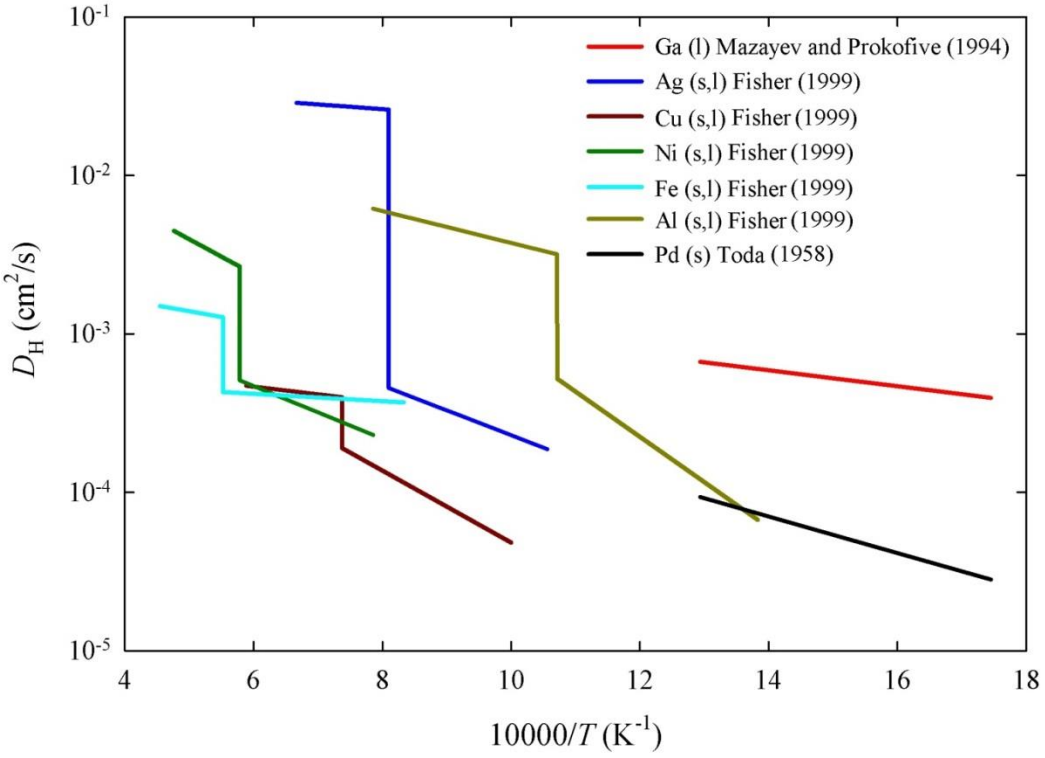

Figure 7.11 Hydrogen diffusion coefficient in some liquid and solid metals as a function of inverse absolute temperature (Mazayev and Prokofive, 1994; Fisher, 1999; Toda, 1958).

Furthermore, even though the diffusion coefficient of H atoms in solid metals is much higher than that of the other atomic impurities such as C or O, which accounts for the extraordinarily high selectivity of Pd membranes for hydrogen permeation, it is typically higher by an order of magnitude or more in liquid metals. Figure 7.11 (see also Figure 2.10) provides examples of H diffusion coefficient in some liquid and solid metals as a function of inverse absolute

temperature (Mazayev and Prokofive, 1994; Fisher, 1999; Toda, 1958), and further shows a step increase in H diffusivity of a metal upon melting. Liquid gallium hydrogen diffusivity (Mazayev and Prokofive, 1994) observed from the literature at 500 ºC is about 7 times higher than that of Pd.

It is, thus, clear from Figures 7.10 and 7.11 that *both* the solubility $x_{H\cdot M}$ and the interstitial H atom diffusion coefficient D_H can be substantially higher. We may thus expect a substantially high permeance, possibly as much as 90 times higher in liquid gallium as compared to solid Pd. This is the central hypothesis behind our proposal for using sandwiched liquid metal films as hydrogen membranes.

7.6 Hydrogen Permeation through Liquid Gallium Membrane

The supported liquid metal membrane configuration (Figure 7.1) was arrived at only after the realization that supported liquid metal membranes with a free surface were not adequately stable. This was found in experiment when hydrogen was switched to helium periodically to check for any leaks. It turns out that the liquid-gas surface tension is dependent on the nature of the gas. Thus, surface tension would increase after switching from hydrogen to an inert gas resulting in poorer wetting of the porous substrate and development of leaks. To avoid this, a minimum of helium was first employed. Finally, however, it was decided to cover the free surface with a graphene layer to avoid these morphological changes. Consequently, the experiments below are described in this temporal sequence.

Described first is free surface (no sandwich) structure with only helium and hydrogen gas. Second set of experiments involves free surface (no sandwich) structure but with H_2/He mixture gas with gas permeated side connected to GC. The third set is to use sandwich structure with pure helium and hydrogen gas.

7.6.1 Free Liquid Metal Surface Membrane

In this section, the permeation tests are divided into two parts. The first part used pure helium for selectivity test. The second part used H_2/He mixture combined with GC at permeation side to detect hydrogen and helium level after permeating through liquid gallium.

Thus, SiC-Ga-8 was about 269 μm (surface area of 0.785 cm^2) and it took over 100 hours to activate this membrane at 500 ºC. After the membrane was activated, helium was used to determine if there was any leakage. Shown in Figure 7.12 (a), (b), and (c) are the helium and hydrogen flow rates of Day 6, Day 7, and Day 8, respectively.

On Day 6 when hydrogen flow rate (blue line) across the membrane was steady at 25.8 ml/min at 6 psi, after switching to helium (red line) there was a sudden peak due to the hydrogen remaining in the system that caused the false reading. Within 1.5 hours of helium test at Day 6, helium flow was undetectable for 10 minutes. However, it rose again. It was suspected that the membrane was unstable under the helium environment. On Day 7 even a longer attempt of leaving membrane in helium for 7 hours was made. No helium flux was measured for the first hour but then it started to oscillate, eventually rising to 10.6 ml/min after 3 hours in helium. No helium flux for 1 hour means the sealing of ceramic tube and porous disc is intact with no leakage on Day 7. On Day 8, another 2 hours of helium purging showed exactly the same behavior, which confirmed that membrane was unstable if exposed to helium for too long. It is possible that the membrane was dense in hydrogen, but helium purging caused wetting behavior and membrane surface morphology change thus creating leaks. Upon exposure to hydrogen, the leaks disappeared. The time required to repair local pleaks could also change from day to day, as shown in Figure 7.12 (c), pinholes developed at the end of Day 7 were still observed on Day 8, but gone on Day 9 as shown in Figure 7.13 (a).

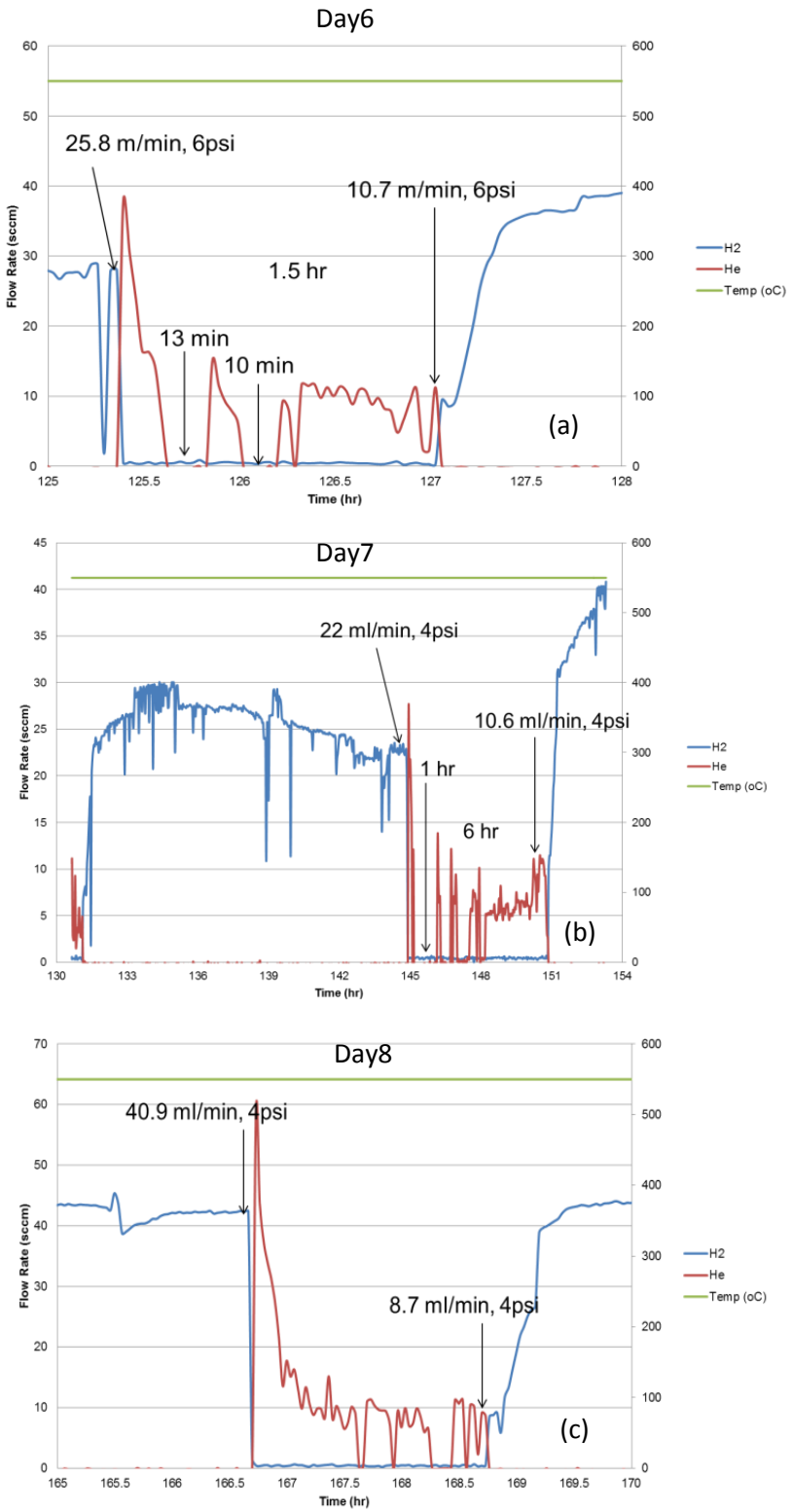

Figure 7.12 SiC-Ga-8 H_2/He flux at (a) Day 6, (b) Day 7 and (c) Day 8. Blue line is H_2, red line He and green line is temperature.

Since membrane was found to be not stable under pure helium after an hour of purging, the usage of helium was limited to a minimum to check its denseness periodically.

On Day 9~11, thus, after hydrogen flow rate measurement, helium was used to predict any leaks for only 1 hour as shown in Figure 7.13 (a), (b), and (c). From 1 hour of no helium leakage it is concluded that sealing between SiC tube and disc is good and the membrane is dense. Hydrogen flow rate across the membrane was also very similar on these days, ranging from 37.5~39.3 ml/min (48.2~50.5 m^3/m^2h or 376~394 $m^3/m^2h\ atm^{0.5}$) at 4 psi. After about 30 minutes in helium, all the hydrogen remaining in the system is removed thus, helium flow dropped to 0 and stayed there for 30 minutes as shown in Figure 7.13. When switching the gas back to hydrogen, there was a lag for solution and diffusion of hydrogen and gallium membrane. It took another 20~30 minutes after introducing hydrogen before the start of flux which is also identical to the time needed for removing hydrogen from system. Hence, it is assumed that membrane was dense from Day 9–11 and possibly dense on Day 6–7 before helium altered the membrane.

From such permeation tests we realized that the liquid metal membrane was unstable under pure helium environment. Thus, leaks developed in pure helium over time that were subsequently recovered after switching to hydrogen. Result supports the notion of wettability changing with gas environment. Thus this topic is explored in great detail in the next chapter.

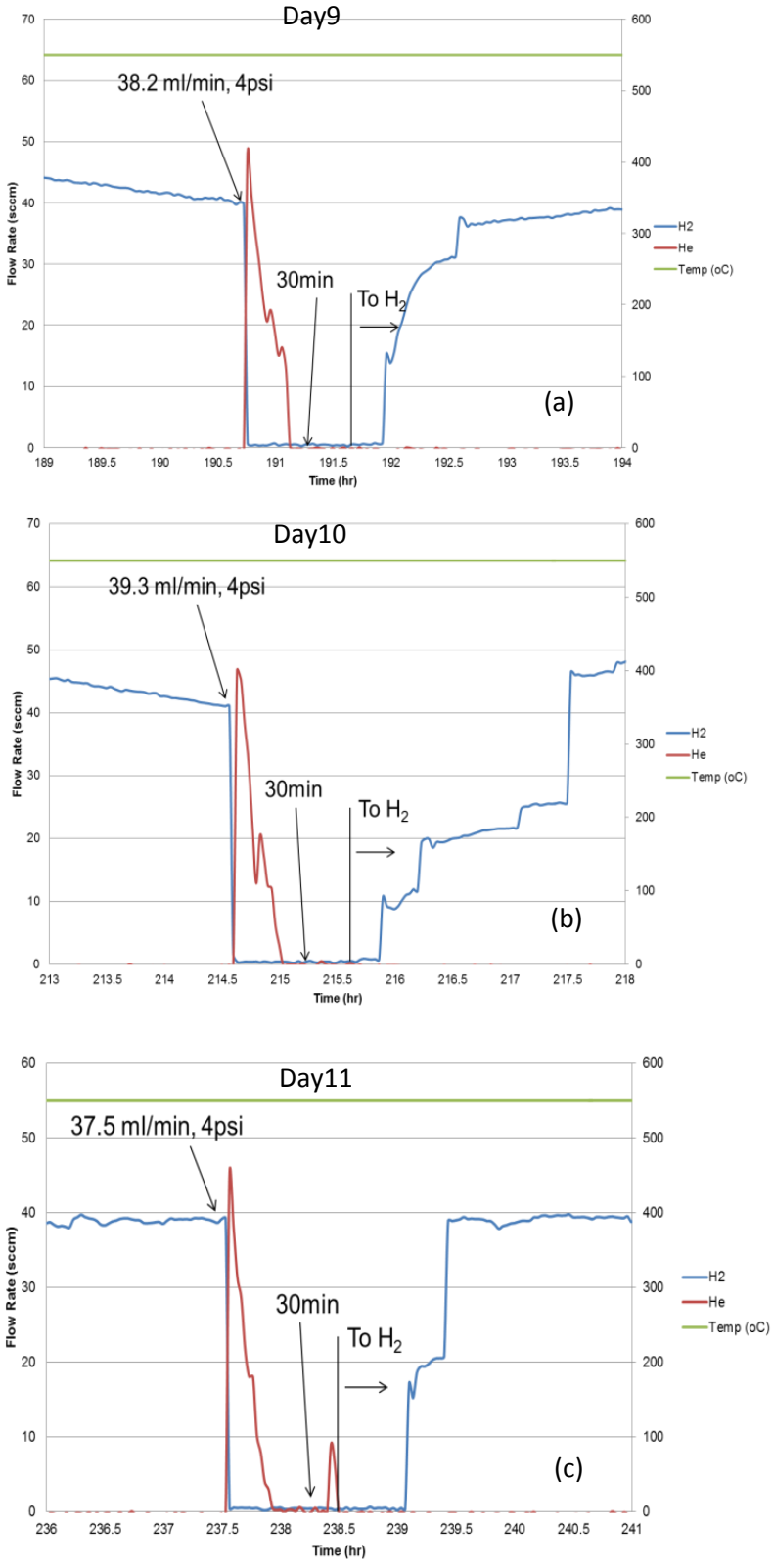

Figure 7.13 SiC-Ga-8 H_2/He flux at (a) Day 9, (b) Day 10 and (c) Day 11.

To reduce helium usage during selectivity tests, thus, we replaced pure helium with a H_2/He (72.5 mole %/27.5 mole %) mixture and connected the membrane permeation to a GC. Retention time and mole concentration of H_2/He (72.5 mole %/27.5 mole %) mixture was corroborated in GC alone with pure helium, hydrogen and a H_2/He (16 mole %/84 mole %) prior to permeation experiments. Thus, a membrane SiC-Ga-16 (257.3 μm) was prepared using the same procedure described above. It was tested between 500–565 ºC at 4 psi in H_2 and H_2/He mixed gas and connected to GC for composition analysis. The tested hydrogen flux versus elapsed time is shown in Figure 7.14.

The overall testing period of this membrane was 20 days. In order to extend the membrane stability, H_2/He mixed gas/GC test was not performed every day. Figure 7.15 demonstrates GC result of helium and hydrogen retention time and peak intensity sampled on Day 6, Day 16 and Day 17. Helium retention time is 1.34 min and hydrogen retention time is 1.65 min (Figure 7.15). Integrated peak represents concentration.

Membrane was heated from 500 ºC on Day 1 to 520 ºC, 535 ºC and 550 ºC on Day 2, Day 3 and Day 4, respectively. Hydrogen flux increased with increasing temperature from Day 1–3 and slightly dropped as temperature reached 550 ºC (Figure 7.14). The temperature remained at 550 ºC thereafter for several days to insure the stability of membrane. On Day 6 and 7, H_2/He mixed gas was introduced to check for any possible leakage from the. No helium peak was detected by GC at the membrane permeate as shown in Figure 7.15 (a), i.e. the membrane was dense. Hydrogen flux increased from 3 to 6 m^3/m^2h on Day 8, and was stable there for the next 8 days. Again, no He peak was observed on Day 10. Since there was no obvious change in hydrogen flux and no He peak was detected with a mixture gas using GC it was assumed that from Day 6 to Day 15 the membrane was dense.

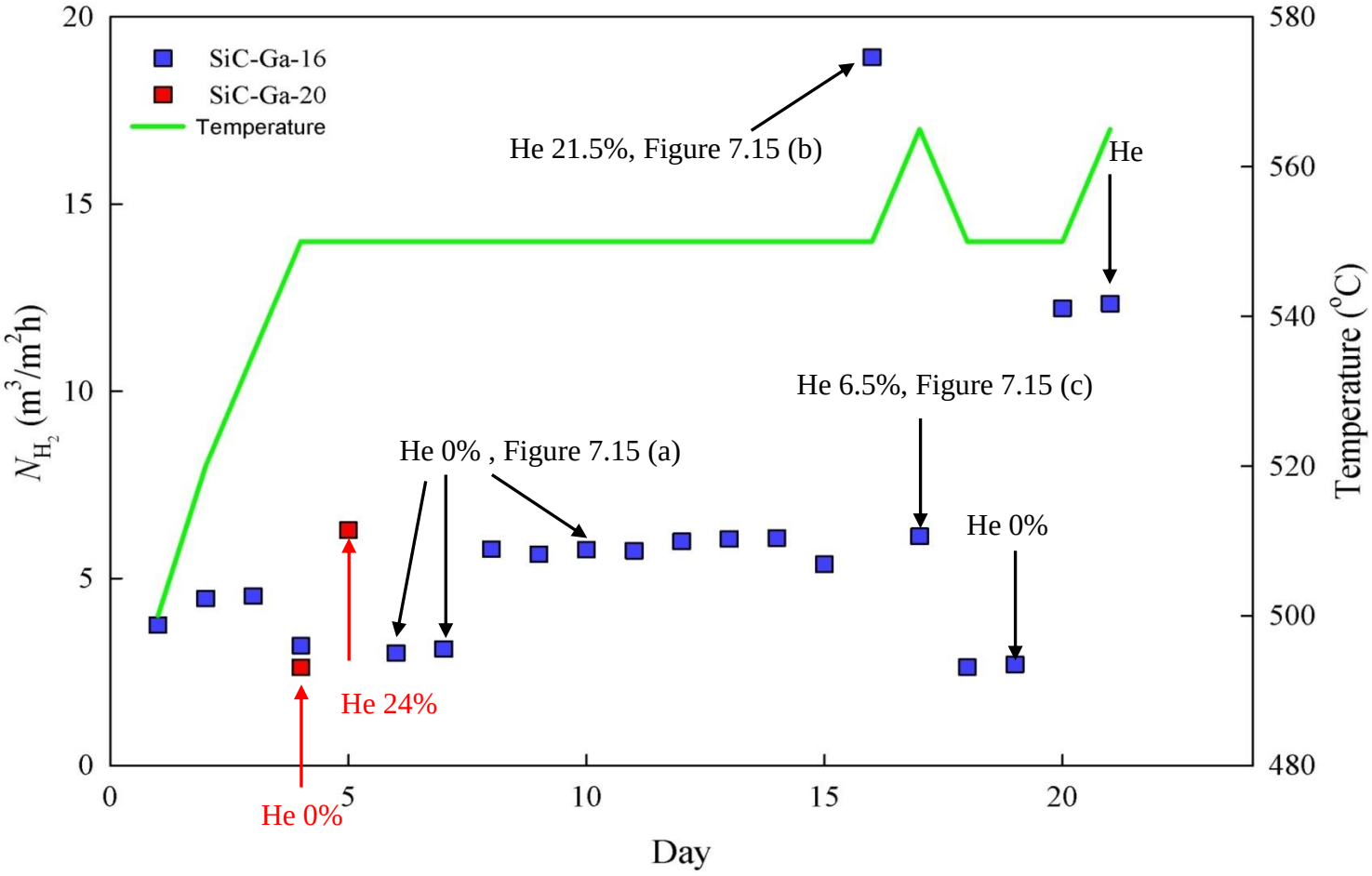

Figure 7.14 SiC-Ga-16 (257 μm) and SiC-Ga-20 (250 μm) hydrogen flux at 4 psi vs elapsed time.

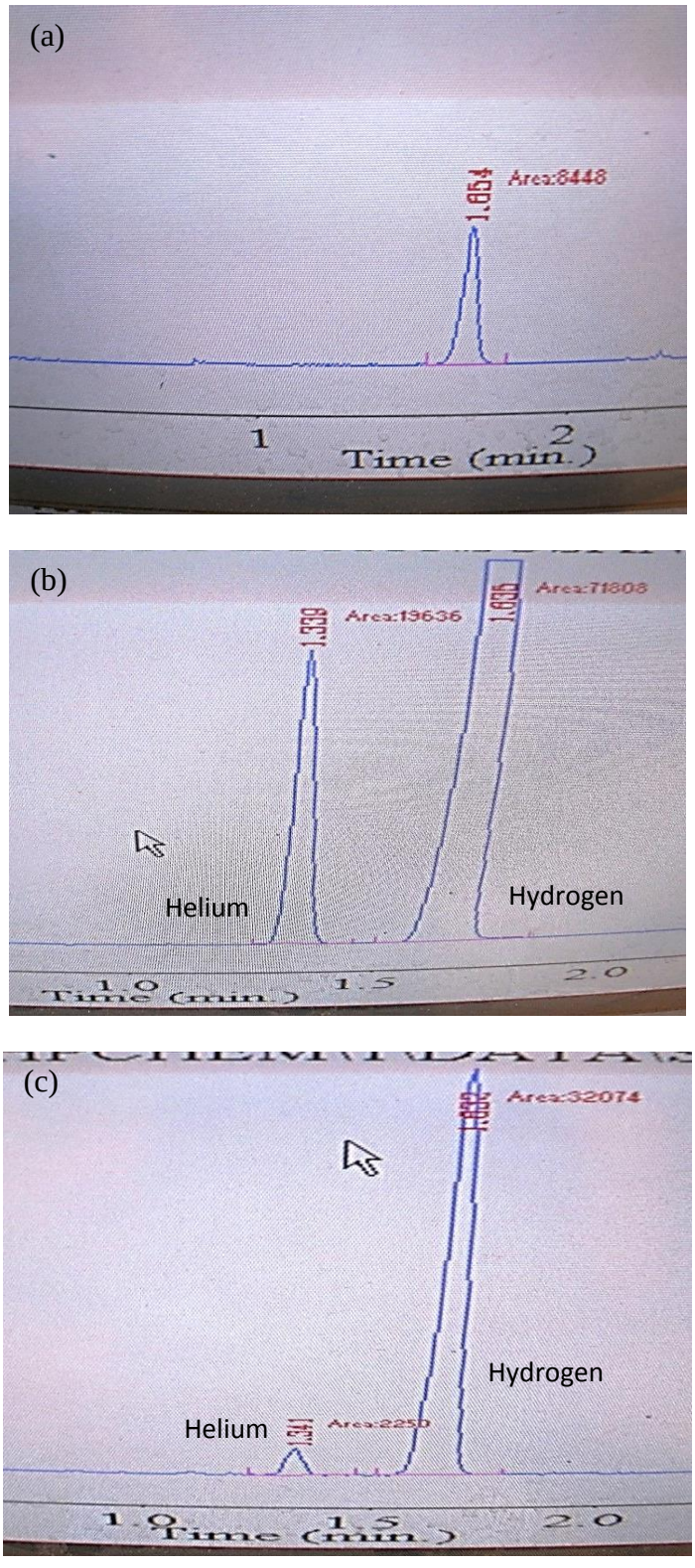

Figure 7.15 SiC-Ga-16 GC test result, (a) pure hydrogen (b) 21.5 mol% helium (c) 6.5 mol% helium.

On Day 16, however, there was a sudden jump of hydrogen flux and 21.5 % He gas in the permeation side was detected by GC, as shown in Figure 7.15 (b). It suggests that a leakage developed at this point. Temperature was increased from 550 ºC to 565 ºC in a bid to repair the membrane. Noticeably hydrogen dropped from 19 to 6 m^3/m^2h and He content dropped from 21.5 % to 6.5 % as indicated in Figure 7.15 (c). Since the wettability of Ga and SiC apparently improved with increasing temperature, therefore small leaks in SLiMM may be repairable temporarily by increasing temperature which reduces surface tension. The decreased hydrogen flux also suggested that the leakage was from membrane and not from the tube sealing. Temperature was decreased from 565 ºC to 550 ºC on Day 18 and the flux remained stable until Day 19. With no He detectable on Day 19 it was concluded that the membrane was dense again. However, on Day 20 hydrogen flux increased from 3 to 12 m^3/m^2h indicating that the membrane had been only temporarily repaired by increasing temperature on Day 16. On Day 21 another attempt for repairing the membrane by increasing temperature from 550 ºC to 565 ºC was performed. However, the hydrogen flux remained the same with 14.5% of He detected in the permeate. The membrane was cooled from 550 ºC to 485 ºC. The activation energy obtained from this temperature range is shown in Figure 7.16 (a) for the case of minor leakage.

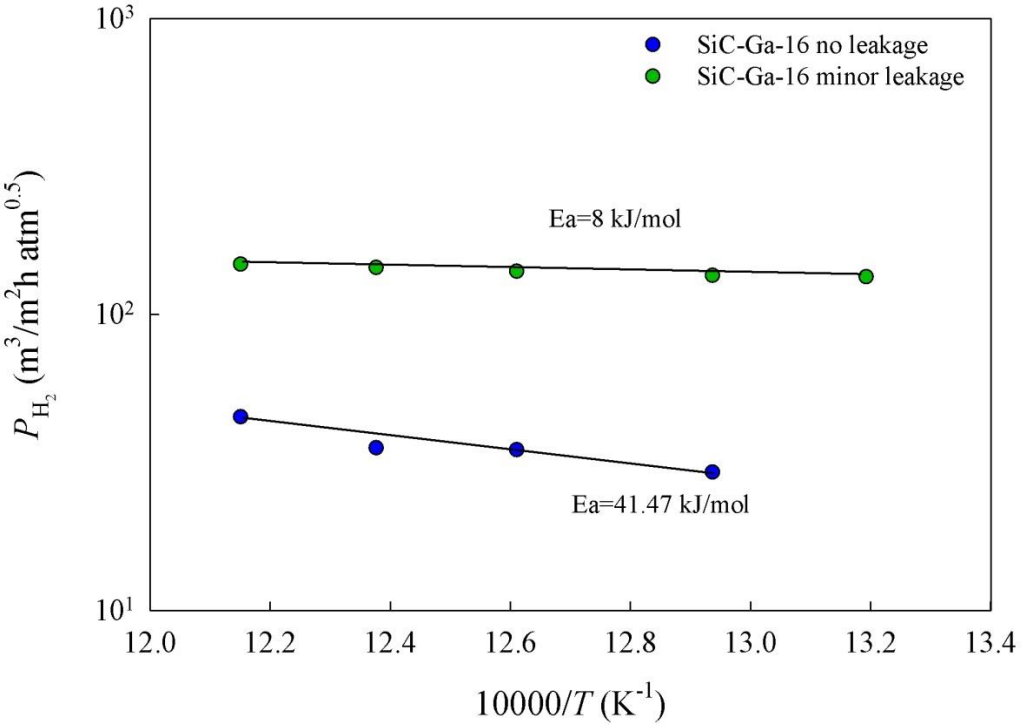

Figure 7.16 (a) Measured SiC-Ga-16 hydrogen flux at various temperatures.

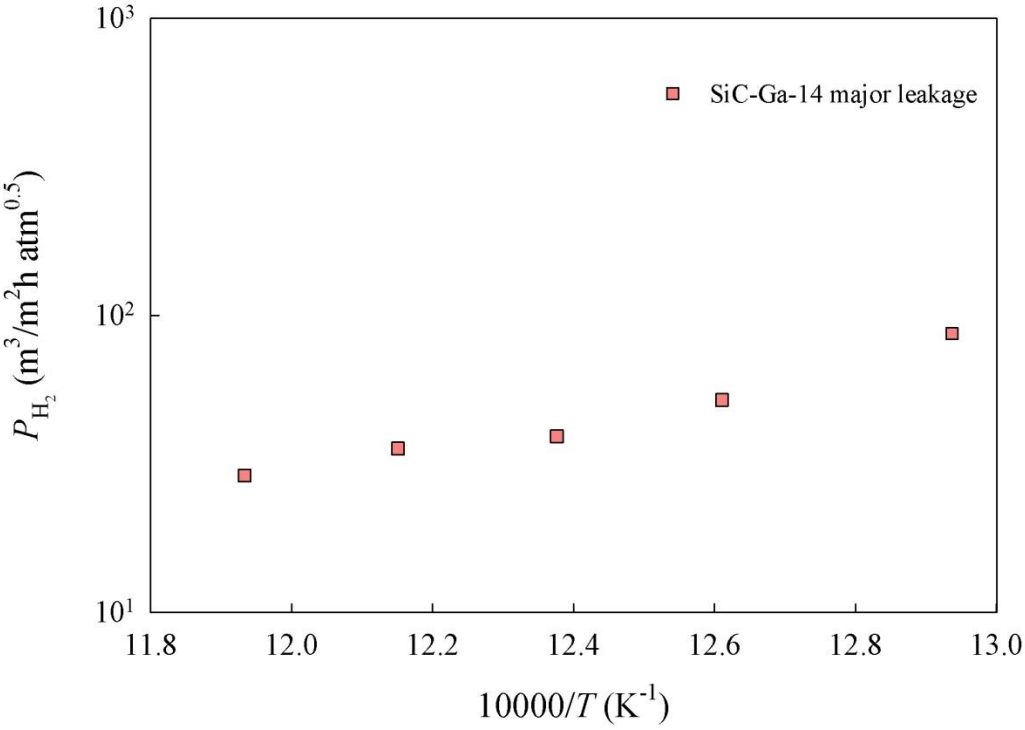

Figure 7.16 (b) Measured SiC-Ga-14 hydrogen flux at various temperatures.

The contribution of hydrogen flux from pin-holes increased the flux permeating from membrane but reduced the activation energy to 8 kJ/mol. This value is much smaller than the activation energy 47 kJ/mol obtained in the beginning of the test when membrane was dense on Days 1–10. The measured hydrogen flux decreased with decreasing temperature clearly showing that the hydrogen flux was permeating through Ga membrane rather than through pin-holes only.

To demonstrate the influence of pin-hole on hydrogen flux and activation energy SiC-Ga-14 is shown in Figure 7.16 (b) as comparison. SiC-Ga-14 was about 270 μm and tested under similar conditions as SiC-Ga-16. GC test result of H_2/He mixed gas showed He at about 22%, indicating that the membrane was not dense with a significant leakage. Measured hydrogen flux increased with decreasing temperature is the case for Knudsen and viscosity flow through pores. Hence, is another indication that there was hydrogen flux permeating through membrane and is not from any pin-hole in SiC-Ga-16 membrane discussed above.

Another attempt of repeating SiC-Ga-16 performance was made. Membrane SiC-Ga-20 (250 μm) was tested under identical condition. On Day 5 the membrane was dense with no He detected. However, on Day 6, 24 % He was found. It is to be noted that on Day 5 the membrane flux of SiC-Ga-16 and SiC-Ga-20 were very similar.

With this set of experiments on membranes with a free liquid surface, thus, we were able to verify that: 1) even with a minimum exposure to pure helium the membrane was not stable. The back and forth pin-hole development and recovery is not a good indication for membrane longevity in real application; 2) pure hydrogen permeation detected via GC with a H_2/He mixture feed provides clear evidence of a leakage-free membrane and high selectivity. It is also a direct proof of hydrogen permeation through the liquid membrane; 3) another proof of hydrogen permeation through the liquid metal membrane is that hydrogen flux increases with increasing

temperature whereas flux of hydrogen permeation through pin-holes decreases with increasing temperature, as discussed in the Appendix. A drawback of H_2/He mixture via GC test is that GC can only verify the helium concentration leaking from the membrane but the selectivity of the membrane is still unknown. In short, small leaks are easily developed with this free surface membrane configuration. Thus, a better configuration is still needed for practical applications of liquid metal membranes. Consequently, we were led to the development of the sandwiched liquid metal membrane, as shown schematically in Figure 7.1

7.6.2 Sandwich Structure, Pure H_2 and He Gas

Sandwiched liquid gallium membranes (200-300 μm) were thus fabricated as described above and tested. With sandwich configuration and the absence of a free liquid metal surface, it obviates the limitation of directly using pure helium during selectivity test. As an example, liquid gallium membrane SiC-Ga-Graphene-15 (~274 μm) was tested between 480–550 ºC, 3-5 psi over two weeks as shown in Figure 7.17.

The membrane was found to be dense and the hydrogen permeation remained stable for roughly the first week. Thus, no helium was detected throughout this period during periodic switching from hydrogen to pure helium. On day 7 of the reported experiment, however, a sudden increase of hydrogen flux was observed and even though helium flux was still not detectable, it was suspected that a small leak had developed. Subsequently, helium flux found to be detectable in the permeate.

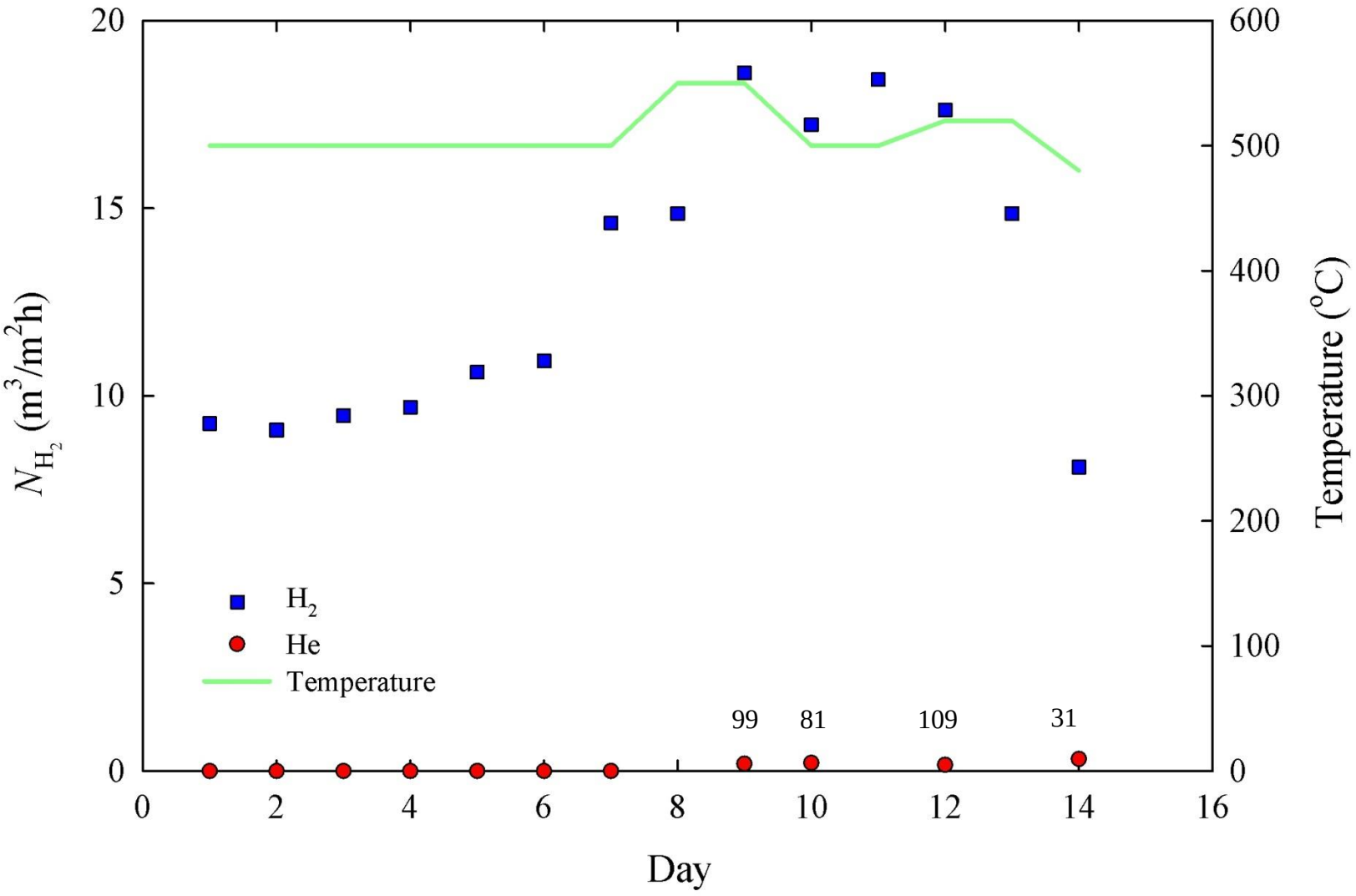

Figure 7.17 SiC-Ga-Graphere-15 (~274 μm) hydrogen permeance vs elapsed time.

The measured hydrogen/helium selectivity $\alpha \equiv N_{H_2} / N_{He}$ was then found to be in the range of 80-110. The test was terminated on Day 14, when H_2/He selectivity dropped to α = 31. This is still substantially higher than that for Knudsen diffusion, i.e., α = 1.44 (Datta et al., 1992) that would be obtained if the flux were entirely through pin-holes, clearly indicating substantial flux through the metal even on Day 14 despite the leak. The completely dense membrane for the first week, however, afforded an essentially infinite selectivity. The measured high hydrogen flux was a clear indication of flux through the metal despite a small leak that developed subsequently.

Hydrogen flux of dense liquid gallium SLiMM measured before pin-hole development for 3-5 psi hydrogen pressure drops at 500 ºC is compared to that with Pd as shown in Figure 7.18. The measured hydrogen permeance of $72.5\,\mathrm{m}^3/\mathrm{m}^2\mathrm{h}\cdot\mathrm{atm}^{0.5}$ is about 35 times higher than that of a Pd foil of similar thickness**,** calculated as $2\,\mathrm{m}^3/\mathrm{m}^2\mathrm{h}\cdot\mathrm{atm}^{0.5}$ (Ayturk et al., 2009).

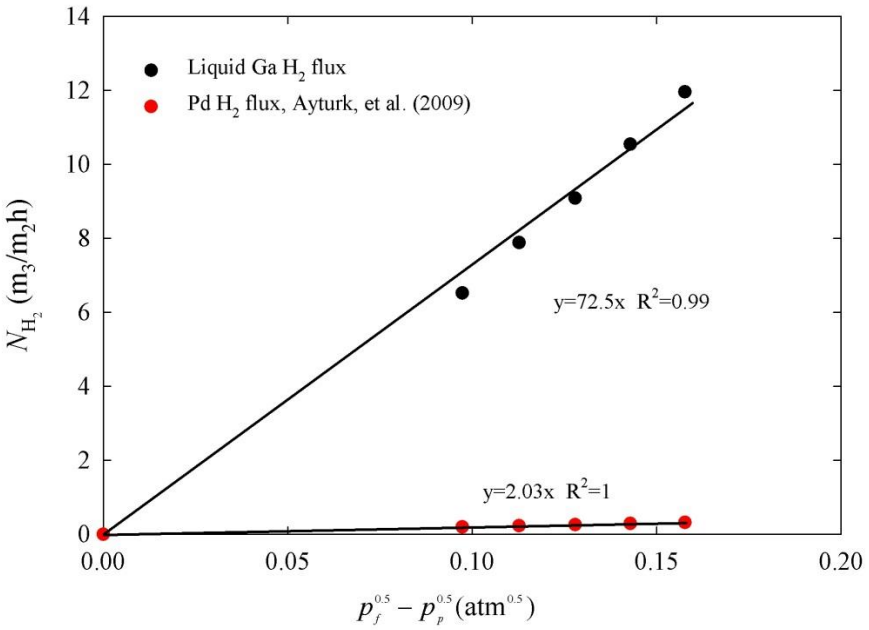

Figure 7.18 Hydrogen permeance of liquid gallium and Pd membrane (calculated based on 274 μm) at 500 ºC.

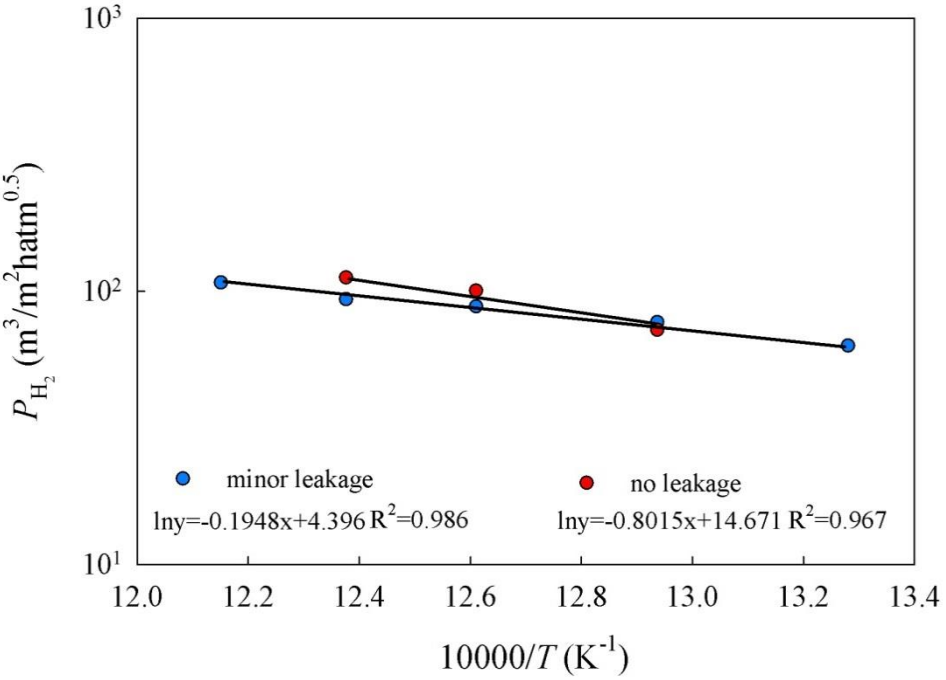

Figure 7.19 Activation energy of permeance of $E_a = 66.6\,\text{kJ/mol}$ with no He leakage, and $E_a = 37.3\,\text{kJ/mol}$ with small He leakage estimated from permeance experiments between 500~550 ºC.

Temperature was also varied between 500~550 ºC at 4 psi pressure drop to obtain an activation energy for permeance of the dense membrane, as shown in Figure 7.19. The results suggest activation energy of $E_a = 66.6\,\text{kJ/mol}$ when there was no helium leakage and activation energy was $E_a = 37.3\,\text{kJ/mol}$ with a small leakage.

The hydrogen flux through Ga SLiMM was further compared with that calculated via Eqs. (2.4) and (2.5) $P_{H_2} \equiv \left(\frac{1}{2V_M\sqrt{p^o}}\right)\frac{K_S D_H}{\delta}$ based on Sieverts' law, and the results are shown in Figure 7.20.

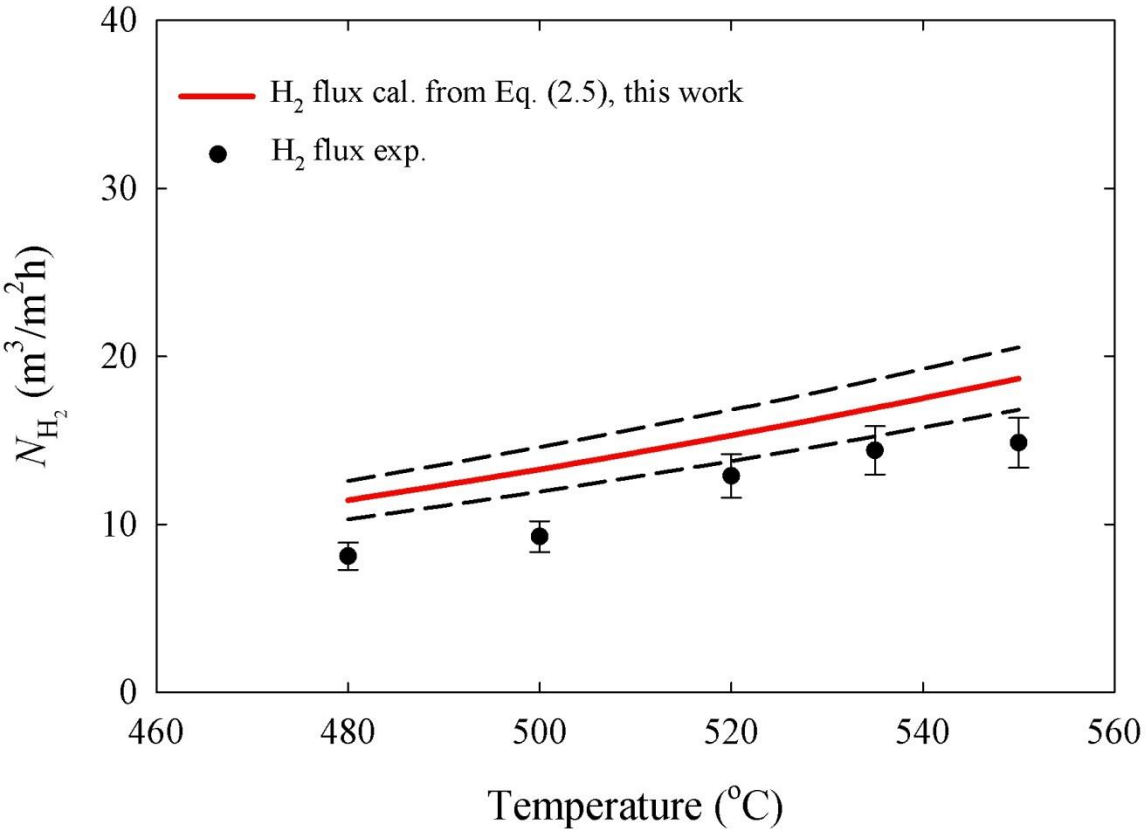

Figure 7.20 Measured SiC-Ga-Graphene-15 hydrogen flux through stability test and calculated hydrogen flux for comparison.

The Sieverts' law constant values used in Eq. (2.5) were measured from Sieverts' experiment as described in section 7.5 and diffusivity values were obtained from Mazayev and Prokofiev (1994). Measured hydrogen flux is about 20 % lower than that calculated from solubility and diffusivity. One of the possible reasons for the deviation is that since it is a sandwiched structure, the hydrogen flux is also affected by the resistance of the porous layers above and below the liquid layers. The other possible reason is that the measured hydrogen flux, solubility or diffusivity contains a certain degree of experimental error. By assuming 10 % of standard error in hydrogen flux measurement during permeation tests, 10% in solubility and another 10 % in diffusivity experiments the results in Figure 7.20 seems to be within the range of experimental

error. Finally, it is possible that diffusion is not the rate controlling step, especially at lower temperatures, as implicit in Eq. (2.4).

Besides SiC-Ga-Graphene-15, there were several other membranes tested under similar conditions with various thicknesses. The corresponding membrane permeability calculated is compared as shown in Figure 7.21.

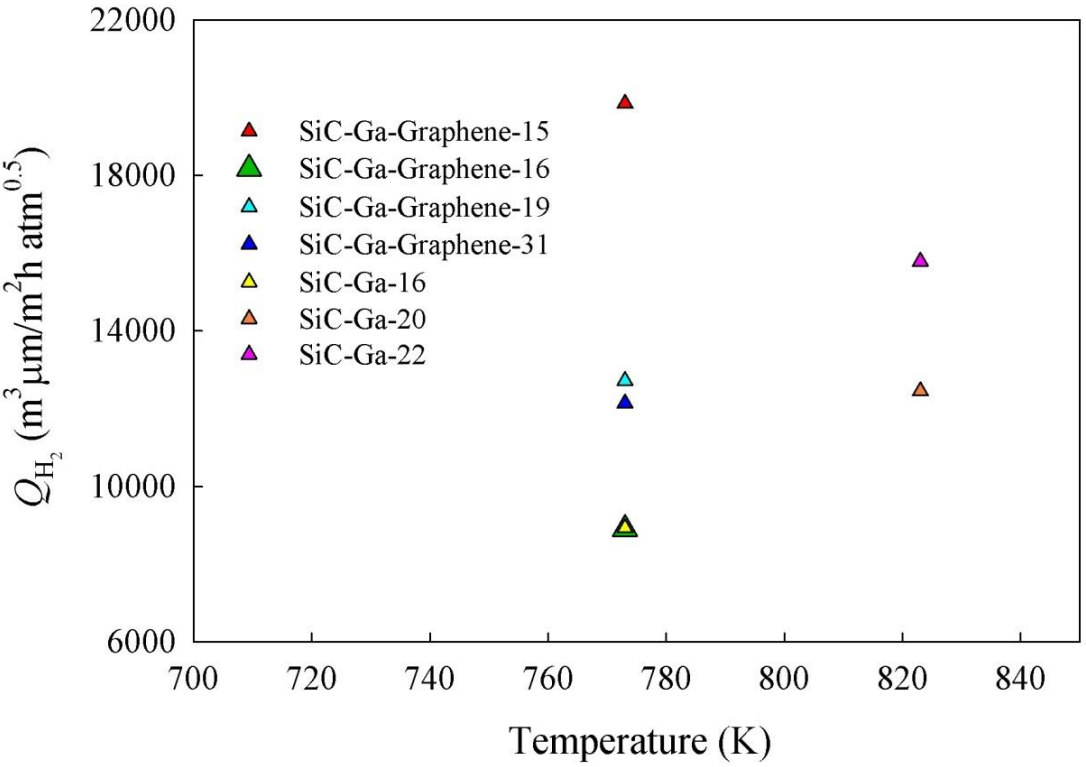

Figure 7.21 Dense liquid gallium membrane hydrogen permeability measured between 773~823K.

All of the membranes compared in Figure 7.21 were essentially *dense* as no helium was detected while testing under various pressure drops. The measured hydrogen permeability of liquid gallium thus ranged between 8900~19850 $m^3\mu m/m^2h\cdot atm^{0.5}$ at 773~823 K (500~550 ºC). Some of these membranes were also tested at various temperatures to obtain activation energy, as shown in Table 7.3. If these membranes developed leakage later on in the experiment, pure

helium or H_2/He were introduced to determine the H_2/He selectivity. Selectivity was calculated using generalized model (combination of effective Knudsen diffusivity, viscosity flow and flux through membrane, see Appendix C) to estimate the leakage through pin-hole (Datta et al., 1992) if the membranes were tested with H_2/He mixed gas.

Table 7.3 Activation energy, selectivity and thickness of various membranes.

Membrane	Thickness (μm)	Test gas	Temperature	Activation Energy	Selectivity $\alpha \equiv N_{H_2}/N_{He}$
SiC-Ga-16	257	H_2/He	485~550	41.47 8	Infinite 11 @550 ºC
SiC-Ga-17	258	H_2/He	435~550	25.39	28 @550 ºC
SiC-Ga-Graphene-2	329	Pure He	480~550	29.11	22@ 480 ºC
SiC-Ga-Graphene-3	598	Pure He	480~550	20.47	119@ 550 ºC 110@ 460 ºC
SiC-Ga-Graphene-10	354	Pure He	520~550	60.49	334@ 500 ºC
SiC-Ga-Graphene-15	274	Pure He	480~550	66.63 37.25	Infinite 30.54@ 480 ºC

From these experimental findings it is clear that membranes with higher selectivity (or infinite selectivity) tend to have higher activation energy as well. As leakage grew the selectivity decreased and the activation energy dropped accordingly. If the leakage continues to grow then eventually hydrogen would permeate through pin-holes via Knudsen flow or viscosity flow instead of permeates through the membrane. In such a case the overall flux would decrease with increasing temperature (as shown in Figure 7.14 SiC-Ga-14) so that there would be a negative activation energy.

Further comparing liquid gallium permeability with various metals and amorphous alloy obtained from literature (Ayturk et al., 2009; Phair and Donelson, 2006; Dolan et al., 2009; Li et al., 2015) it is noticd that liquid gallium has the second highest permeability as shown in Figure 7.22.

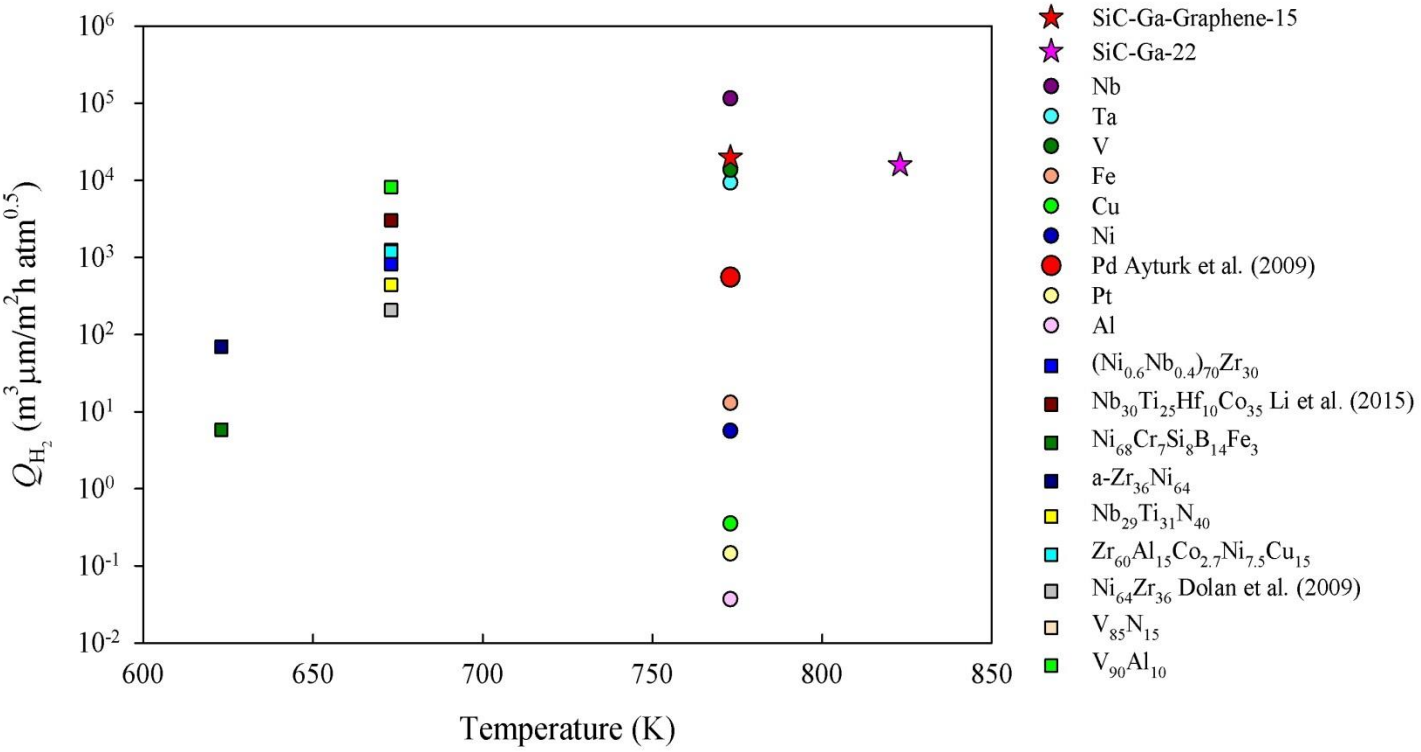

Figure 7.22 A comparison of the hydrogen permeability of dense liquid gallium membrane, metals and amorphous metals between 623~823 K (Pd from Ayturk et al., 2009; $Nb_{30}Ti_{25}Hf_{10}Co_{35}$ from Li et al., 2015; $Ni_{64}Zr_{36}$ from Dolan et al., 2009; all others from Phair and Donelson, 2006).

Many amorphous alloys have high hydrogen permeability comparable to Pd membrane, however, their stability remains an issue. $Ni_{64}Zr_{36}$ permeability (Dolan et al., 2009) at 673K decayed from $173\,m^3\mu m/m^2h\cdot atm^{0.5}$ to $123\,m^3\mu m/m^2h\cdot atm^{0.5}$ (500 nm Pd and 25 nm Cr coated on surface) within 100 hours. Further $Nb_{30}Ti_{25}Hf_{10}Co_{35}$ at 673K with permeability $3037\,m^3\mu m/m^2h\cdot atm^{0.5}$ (190 nm Pd coated on surface) proved to be stable for 120 hours but there is no further information on its stability (Li et al., 2015). The alloy crystallized and needed Pd enhancement (which might form intermetallic compound with alloy). On the other hand SiC-Ga-16 at 773 K with permeability 12136 $m^3\mu m/m^2h\cdot atm^{0.5}$ proved to be stable for 360 hours. Both membranes

were dense with no helium detected during that time. Unlike amorphous alloys that undergo crystallization and resultant permeability decay, the stability of SLiMM has physical reasons (wettability etc.) not chemical. The inherent nature of SLIMM in hydrogen appears stable. Measured liquid gallium hydrogen permeability is about 16~35 time higher than Pd membrane.

7.7 Conclusion

Based on the experimental results presented here, thus, we can conclude that our original hypothesis that liquid metal membranes should have high H_2 permeability because of high solubility and significantly higher diffusion coefficient has been shown to be correct. In fact, both hydrogen diffusivity as well as solubility in liquid gallium was found to be substantially higher than in Pd. This portends the development of non-Pd hydrogen membranes, which has long been elusive (Phair and Donelson, 2006). There are, in fact, numerous other liquid metals and alloys that might be suitable for SLiMM, and need to be tested. Engineering issues such as suitable supports, seals, and good membrane stability still remain to be fully resolved, but the scientific premise is sound.

7.8 References

Adhikari, S. and Fernando, S., Hydrogen membrane separation techniques, *Industrial and Engineering Chemistry Research*, 45, (2006), 875-881.

Ayturk, M. E., Kazantzis, N. and Ma, Y. H., Modeling and performance assessment of Pd and Pd/Au-Based catalytic membrane reactors for hydrogen production, *Energy and Environmental Science*, 2, (2009), 430-438.

Blach, T. P. and Gray, E. M. A., Sieverts apparatus and methodology for accurate determination of hydrogen uptake by light-atom hosts, *Journal of Alloy and Compound*, 446-447, (2007), 692-697.

Datta, R., Dechapanichkul, S., Kim, J.S., Fang, L.Y. and Uehara, H., A generalized model for the transport of gases in porous, non-porous, and leaky membranes. I. Application to single gases, *Journal of Membrane Science*, 75, 3, (1992), 245-263.

Deveau, N. D., Ma, Y. H. and Datta, R., Beyond Sieverts' law: A comprehensive microkinetic model of hydrogen permeation in dense metal membranes, *Journal of Membrane Science*, 437, (2013), 298-311.

Dolan, M., Dave, N., Morpeth, L., Donelson, R., Liang, D., Kellam, M. and Song, S., Ni-based amorphous alloy membranes for hydrogen separation at 400 ºC, *Journal of Membrane Science*, 326, 2, (2009), 549-555.

Fisher, D. J., Hydrogen diffusion in metals: A 30-year retrospective, *Scitec Publications Ltd, Switzerland*, (1999).

Flanagan, T. B., Bowerman, B. S. and Biehl, G. E., Hysteresis in metal/hydrogen systems, *Scripta Metallurgica*, 14, 4, (1980), 443-447.

Fruehan, R. J. and Anyalebechi, P. N., Gases in metals, *ASM Handbook* ,15, 64-73, (2008).

Fukai, Y., The metal-hydrogen system, *Springer-Verlag, Berlin*, (2005).

Gale, W. F. and Totemeier, T. C., Smithells Metals Reference Book Chapter 12, *Elsevier Butterworth-Heinemann, Oxford*, (2003).

Holladay, J. D., J. Hu, D. L. King and Y. Wang, An overview of hydrogen production technologies, *Catalysis Today*, 139, (2009), 244-260.

http://www.engineeringtoolbox.com/linear-expansion-coefficients-d_95.html

http://www.ioffe.ru/SVA/NSM/Semicond/SiC/thermal.html

http://www.metal-pages.com/metalprices/gallium/

Hubberstey, P., Adams, P. F., Pulham, R. J., Down, M. G. and Thunder, A. E., Hydrogen in liquid alkali metals, *Journal of the Less Common Metals*, 49, (1976), 253-269.

Li, X., Liu, D., Liang, X., Chen, R., Rettenmayr, M., Su, Y., Guo, J. and Fu, H., Substantial enhancement of hydrogen permeability and embrittlement resistance of $Nb_{30}Ti_{25}Hf_{10}Co_{35}$ eutectic alloy membranes by directional solidification, *Journal of Membrane Science*, 496, (2015), 165-173.

Ma, Y. H., Kazantzis, N. K., Mardilovich, I. P., Guazzone, F., Augustine, A. S. and Koc, R., Composite Pd and Pd Alloy porous stainless steel membranes for hydrogen production and process intensification, DOE Hydrogen Program, FY 2009 Annual Progress Report, (2009).

Mahapatra, M. K. and Lu, K., Glass-based seals for solid oxide fuel and electrolyzer cells-a review, *Materials Science and Engineering*, 67, (2010), 65-85.

Mazayev, S. N. and Prokofiev, Yu. G., Hydrogen inventory in gallium, *Journal of Nuclear Materials*, 212-215, (1994), 1497-1498.

Nenoff, T. M., Spontak, R. J. and Aberg, C. M., Membranes for hydrogen purification: an important step toward a hydrogen-based economy, *Materials Research Society Bulletin*, 31, (2006), 735-741.

Ockwig, N. W. and Nenoff, T. M., Membranes for hydrogen separation, *Chemical Review*, 107, (2007), 4078-4110.

Paglieri, S. N. and Way, J. D., Innovations in palladium membrane research, *Separation and Purification Methods*, 31, (2002), 1-169.

Phair, J. W. and Donelson, R., Developments and design of novel (non-palladium-based) metal membranes for hydrogen separation, *Industrial and Engineering Chemistry Research*, 45, (2006), 5657-5674.

Policicchio, A., Maccallini, E., Kalantzopoulos, G. N., Cataldi, U., Abate, S., Desiderio, G. and Agostino, R. G., Volumetric apparatus for hydrogen adsorption and diffusion measurements: Sources of systematic error and impact of their experimental resolutions, *Review of Scientific Instruments*, 84, 10, (2013), 103907.

Sacris, E. M. and Parlee, N. A. D., The diffusion of hydrogen in liquid Ni, Cu, Ag, and Sn, *Metallurgical and Materials Transactions B*, 1, (1970), 3377-3382.

Sholl, D. S. and Ma, Y. H., Dense metal membranes for the production of high purity hydrogen, *Materials Research Society Bulletin*, 31, (2006), 770-773.

Steward, S. A., Review of hydrogen isotope permeability through materials; Lawrence Livermore National Laboratory UCRL-53441; National Technical Information Service, *U.S. Department of Commerce: Springfield*, VA, (1983).

Toda, G., Rate of permeation and diffusion coefficient of hydrogen through palladium, *Journal of Research Institute Catalysis Hokkaido University*, 6, (1958), 13-19.

Yun, S. and Oyama, S. T., Correlations in palladium membranes for hydrogen separation: A review, *Journal of Membrane Science*, 375, (2011), 28-45.

Chapter VIII

Butler-Sugimoto Monomolecular Bilayer Interface Model: The Effect of Oxygen on the Surface Tension of a Liquid Metal and its Wetting of a Ceramic

8.1 Abstract

The main purpose of this chapter is to develop a thermodynamic model to predict the change on surface energy brought about by changing temperature, pressure and composition. This is an important step to understand the wetting behavior of liquid gallium in hydrogen and helium. Since there is no literature work on hydrogen/liquid metal/ceramic systems, therefore, the work focus here is on oxygen metal system. The influence of oxygen on liquid-gas surface tension of molten metals has been well-investigated experimentally and modeled theoretically via the Szyszkowski equation, derivable from the Butler molecular monolayer interface model. However, there is no corresponding model describing the experimentally observed profound effect of oxygen partial pressure on solid-liquid surface tension as well as on contact angle of molten metals on ceramic substrates. Here, we utilize the Butler-Sugimoto thermodynamic approach based on a monomolecular *bilayer* interface model to investigate the effect of oxygen partial pressure on liquid-gas as well as solid-liquid surface tension of molten Cu/Al_2O_3 and molten Ag/Al_2O_3 systems. It is shown that both liquid-gas and solid-liquid surface tension are a strong function of oxygen activity in the melt, which, in turn, depends on gas-phase oxygen partial pressure, in conformity with experiments. The change of solid-liquid surface tension and wetting

is also greatly affected by the change of in liquid-gas surface tension. This improved understanding is of practical significance in many applications.

8.2 Introduction

The typical liquid metal and ceramic interface is characterized by weak Van der Waals and electronic interactions, resulting in a contact angle higher than 90 degrees (Gallois, 1997). This poor wetting often needs to be improved as such interfaces find applications in advanced composites, structural joints, microelectronics, catalyst support, solid oxide fuel cells, refractories and thermal barrier coatings (Saiz et al., 2008). Air-brazing is an emerging technique for the production of ceramic-to-ceramic and ceramic-to-metal joints by *in situ* oxidation of the molten metal in air (Bobzin et al., 2010). At high temperatures, oxygen from air adsorbs and dissolves into the molten metal via the liquid-gas interface. The resulting drop in liquid-gas surface tension and the contact angle at various oxygen partial pressures has been extensively investigated, e.g., for the molten Cu/Al_2O_3 (Monma and Suto, 1960; Gallois and Lupis, 1881; O'Brien and Chaklader, 1974; Diemer et al., 1999; Ghetta et al., 1996, Ownby and Liu, 1988; Morita and Kasama, 1976) and Ag/Al_2O_3 (Lee, 2004a; Taimatsu et al., 1985; Mehrotra and Chaklader, 1985; Chatain, 1994; Lee et al., 2004b; Muolo et al., 2008; Sangiorgi et al., 1982; Bernard and Lupis, 1971; Gallois, 1980) systems. The theoretical relation between oxygen concentration in the melt and liquid-gas surface tension was derived independently by Belton (1976) and by March and Tosi in 1976, but was empirically proposed much earlier by von Szyszkowski in 1908 (Ozawa et al., 2010):

$$\sigma_{LG} = \sigma_{LG}^{o} - \Gamma^{o} RT \ln(1 + Ka_{O}) \tag{8.1}$$

where σ_{LG} is the liquid-gas surface tension , σ_{LG}^{o} is the surface tension in the absence of oxygen, Γ^{o} is the saturated oxygen adsorption concentration at the liquid surface ($\mathrm{mol/m^2}$), K is the equilibrium constant for oxygen adsorption, and a_{O} is the activity of oxygen in the liquid metal.

While the effect of oxygen on liquid-gas surface tension is widely discussed in the literature, the effect of oxygen on solid-liquid surface tension is less so. Naidich (1981) proposed that the metal oxide formed in the melt can adsorb strongly at the metal ceramic interface, lowering the liquid-solid surface energy, and hence improving the wetting. The extent of improvement in wetting depends on the interface oxide composition (Eustathopoulos and Drevet, 1994). Density functional theory (DFT) modeling has also been utilized to investigate role of oxygen at the interface in the Ag/O/Al_2O_3 system (Muolo et al., 2008, Passerone et al., 2010). The results suggest that at intermediate oxygen partial pressure (>10^{-11} atm.), O/Ag complex forms at the Al-terminated/O-rich-Ag (111) interface, leading to a strong bonding with the alumina substrate.

Semi-empirical models combining experimental observation and thermodynamic theory have also been proposed for the work of adhesion W_{ad} and surface tension (Chatain et al., 1988). It was found that the bonds in a non-reactive metal/ionocovalent oxide interface are in fact stronger than pure Van der Waals bonds, so that the chemical bonding cannot be ignored. At very low oxygen partial pressure, interaction between molten metal and the substrate is governed by the reactivity between materials, which can be estimated by Gibbs free energy change for the reaction. Thus, Naidich (1981) considered the work of adhesion in such a system as a combination of Van der Waals force and chemical bonds between the melt and the support. Chatain et al. (1988) took into account the chemical bonding energy of oxygen and the metal M in the substrate with the melt Me using enthalpy of mixing at infinite dilution. Thus, the work of adhesion was written as

$$W_{ad} = -\frac{c}{N_{Av}^{1/3} V_{Me}^{2/3}} [\overline{\Delta H}^{\infty}_{\mathrm{O(Me)}} + \frac{1}{n} \overline{\Delta H}^{\infty}_{\mathrm{M(Me)}}] \tag{8.2}$$

where n is the stoichiometric ratio of oxygen (O) and metal ion (M) in the oxide and other variables are described in the Nomenclature. This is, of course, related to the surface tension and the contact angle via the Young-Dupré equation

$$W_{ad} = \sigma_{SG} + \sigma_{LG} - \sigma_{SL} = \sigma_{LG}(1 + \cos\theta) \tag{8.3}$$

For a non-reactive, non-wetting system in the absence of oxygen or at extreme low oxygen partial pressure in so-called plateau region, the work of adhesion is found to essentially remain constant with oxygen partial pressure, the relationship of liquid-solid surface tension being approximately linear with contact angle (Zouvelou et al., 2007)

$$\sigma_{SL} = A\cos\theta + B \tag{8.4}$$

where A and B are constants that are functions of temperature.

As oxygen partial pressure increases, the dissolved oxygen increases and eventually saturates in the melt. Beyond a critical oxygen pressure, the increasing oxygen activity in the melt is found to dramatically alter the surface tension. Even in this regime, Mehrotra and Chaklader (1985) found that the contact angle remains linear with solid- liquid tension, *albeit* with a different slope

$$\theta = m\sigma_{SL} + C \tag{8.5}$$

where m and C are constants.

Further, assuming $\sigma_{SL} = \sigma_{SG}$ at $\theta = 90^{\circ}$, and combining Eqs. (8.1), (8.3) and (8.5), the contact angle and solid-liquid surface tension are predicted by the following for oxygen partial pressure greater than the critical value

$$(\theta - 90\,\text{deg}) = -m\cos\theta\left[\sigma_{LG}^{\circ} - \frac{2.303RT}{2}\cdot\Gamma^{\circ}(\log p_{O_2} - \log^{\circ} p_{O_2})\right] \quad (8.6)$$

where $\log^{\circ} p_{O_2}$ is the logarithm oxygen pressure at which the monolayer formation is complete.

In summary, the presence of oxygen in the melt changes the surface composition and the surface energy at solid-liquid interface. Although empirical models exist, there is no fundamental thermodynamic model that describes the change of solid-liquid surface tension in response to the change of oxygen partial pressure in the gas phase. Thus, the goal in this study is to develop such a theoretical model based on the Butler-Sugimoto thermodynamic approach that imagines the interface region as comprised of a monomolecular bilayer, one for each phase. The model is, in fact, applicable for both liquid-gas and liquid-solid surface tension, and is compared to extensive experimental data for the molten Cu/Al_2O_3 and molten Ag/Al_2O_3 systems.

8.3 Theory

Surface tension represents the excess energy of molecules at the surface compared with those in the bulk, owing to the disruption of the intermolecular forces of attraction in a condensed phase when a surface is created from the bulk. The thermodynamic analysis of this surface energy is conventionally based on the approach developed by Gibbs (1906), which treats the planar interface as a mathematical dividing plane, of zero thickness, separating two bulk phases as shown in Figure 8.1 (a). This is, however, physically implausible (Guggenheim, 1940), as the interface must have a finite thickness. Thus, Butler (1932) assumed the interface layer to be of a monomolecular thickness and further prescribed a chemical potential for a species in the surface layer as being different, and actually higher, from that in the bulk (Tester and Modell, 1997). In fact, the surface tension is simply the difference between the surface and bulk chemical potential of a given species, divided by the partial molar surface area of the species. Butler's model is

well-suited for describing a liquid-gas interface since there is only one monomolecular interfacial layer on liquid side, and is now commonly used in the literature to model this case.

Sugimoto (1996; 1999) extended Butler's model by dividing the interface into *two* sub-layers, each monomolecular in thickness, and influenced primarily by the adjacent bulk-phase as shown in Figure 8.1 (b). This double-layer interfacial phase model is a more realistic representation of the interface between *two condensed* phases and is, thus, used here.

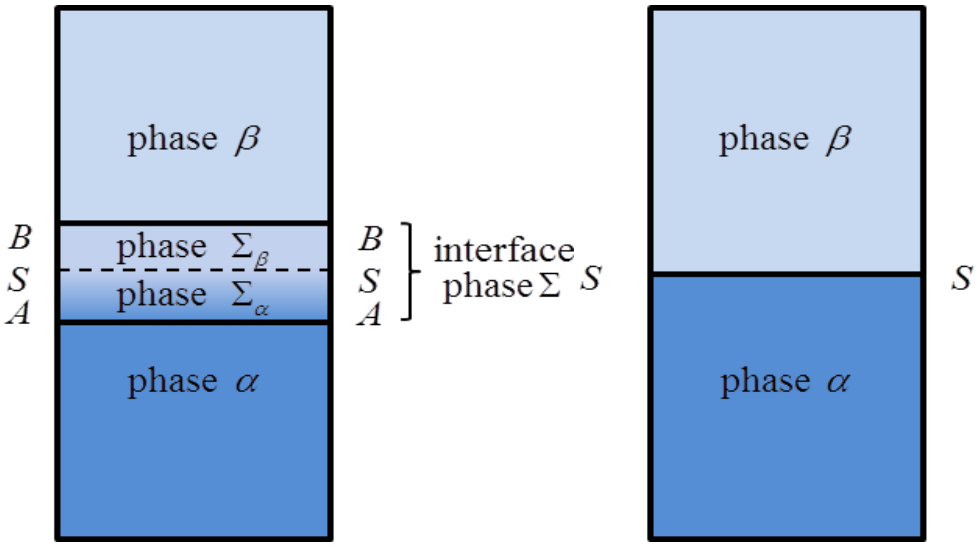

Figure 8.1 (a) A flat Gibbs dividing surface between two bulk phases, and (b) a multicomponent two-phase closed system with a double-layer interfacial phase.

Thus, we consider the closed multicomponent system in Figure 8.1 (b) with a dividing planar surface of area $\underline{A}^{\Sigma}$ between two bulk phases α and β. The matter contained within the control volume is divided into the two bulk phases plus the interface phase of surface energy, or surface tension, $\sigma_{\alpha\beta}$. We neglect any magnetic or gravitational fields, but allow that an electric field could be present (Hsieh and Selman, 2011), so that we consider electrochemical potential $\tilde{\mu}_i^{\alpha}$ of

a species *i* rather than simply its chemical potential μ_i^{α}. The interface phase Σ between the two bulk phases is further sub-divided into two sub-layers Σ_{α} and Σ_{β}, one on either side of the mathematical surface in Figure 8.2, as done by Sugimoto (1996, 1999) who further assumed that these sub-layers were monomolecular in thickness, and influenced primarily by their adjacent bulk-phase. In other words, $\Sigma = \Sigma_{\alpha} + \Sigma_{\beta}$. We further assume that $\underline{A}^{\Sigma_{\alpha}} = \underline{A}^{\Sigma_{\beta}} = \underline{A}^{\Sigma}$.

$$s_i : \quad i(\alpha) \leftrightarrows i(\Sigma_{\alpha})$$
$$s_{\mathrm{A}} : \quad \mathrm{A}(\alpha) \leftrightarrows \mathrm{A}(\Sigma_{\alpha})$$

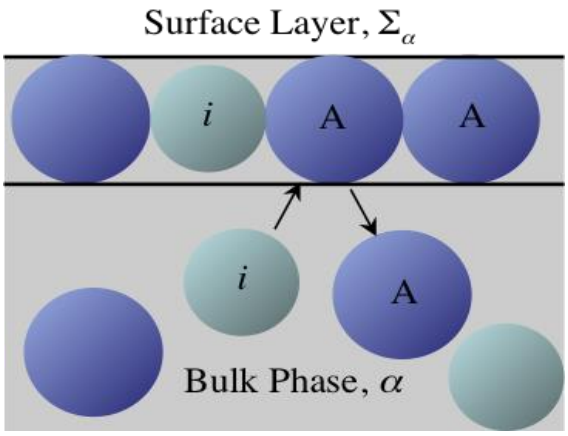

Figure 8.2 Schematic of surface exchange reaction between species bulk species *i* and surface species A.

8.3.1 Thermodynamic Relations

We follow the derivation of Butler (1932), extending his approach to obtain the corresponding relations for the bilayer model of Sugimoto (1996; 1999). The fundamental equation of thermodynamics for the individual phases as well as the overall closed system in differential form is (Aveyard and Haydon, 1973; Tester and Modell, 1997)

$$
\begin{aligned}
d\underline{G}^{\alpha} &= -\underline{S}^{\alpha} dT + \underline{V}^{\alpha} dp + \sum_{i=1}^{n} \tilde{\mu}_i^{\alpha} dn_i^{\alpha} \; ; \\
d\underline{G}^{\beta} &= -\underline{S}^{\beta} dT + \underline{V}^{\beta} dp + \sum_{i=1}^{n} \tilde{\mu}_i^{\beta} dn_i^{\beta} \; ; \\
d\underline{G}^{\Sigma} &= -\underline{S}^{\Sigma} dT + \underline{V}^{\Sigma} dp^{\Sigma} + \sum_{i=1}^{n} \tilde{\mu}_i^{\Sigma} dn_i^{\Sigma} + \sigma_{\alpha\beta} d\underline{A}^{\Sigma} \; ; \\
d\underline{G} &= d\underline{G}^{\alpha} + d\underline{G}^{\beta} + d\underline{G}^{\Sigma}
\end{aligned}
\tag{8.7}
$$

where the underbar denotes extensive properties (Tester and Modell, 1997), and $\tilde{\mu}_i$ is the electrochemical potential of species *i* in a given phase identified by the superscript. For the double-layer interfacial phase assumed here, the thermodynamic properties for the interface may further be written as $\underline{V}^{\Sigma} = \underline{V}^{\Sigma_\alpha} + \underline{V}^{\Sigma_\beta}$, $\underline{G}^{\Sigma} = \underline{G}^{\Sigma_\alpha} + \underline{G}^{\Sigma_\beta}$, and $n_i^{\Sigma} = n_i^{\Sigma_\alpha} + n_i^{\Sigma_\beta}$. By a consideration of the case when the entropy, volume, and composition of the interface layer remain unchanged, i.e., for $d\underline{S}^{\Sigma} = 0$, and $d\underline{V}^{\Sigma} = 0$, it can be shown that in the above, $T^{\alpha} = T^{\beta} = T^{\Sigma} \equiv T$, and $p^{\alpha} = p^{\beta} \equiv p$ (Butler, 1932).

Further this which defines the surface free energy, or surface tension, by

$$
\sigma_{\alpha\beta} \equiv \left(\frac{\partial \underline{G}^{\Sigma}}{\partial \underline{A}^{\Sigma}} \right)_{T,p,n_i^{\Sigma}} = \left(\frac{\partial \underline{G}}{\partial \underline{A}^{\Sigma}} \right)_{T,p,n_i}
\tag{8.8}
$$

Butler (1932) next inquired whether the additional surface free energy $\sigma_{\alpha\beta}$ could simply be regarded as being associated with the individual species within the surface layers. If so, one could then assign a physicochemical potential ψ_i^{Σ} to the species *i* in the surface layer such that (Hsieh and Selman 2011)

$$
d\underline{G}^{\Sigma} = -\underline{S}^{\Sigma} dT + \underline{V}^{\Sigma} dp^{\Sigma} + \sum_{i=1}^{n} \psi_i^{\Sigma} dn_i^{\Sigma}
\tag{8.9}
$$

The constitutive equation for the physicochemical potential of *i* in the interfacial layer, in complete analogy with the usual chemical potential (Sugimoto, 1996; Abu Al-Rub, 1994) may thus be written in the form

$$\psi_i^{\Sigma} \equiv \left(\frac{\partial \underline{G}^{\Sigma}}{\partial n_i^{\Sigma}} \right)_{T,p,n_{j\neq i}^{\Sigma}} = \psi_i^{\mathrm{o},\Sigma}(T,\, p^{\mathrm{o}}) + \int_{p^{\mathrm{o}}}^{p^{\Sigma}} \overline{V}_i^{\Sigma} dp + RT \ln a_i^{\Sigma} \tag{8.10}$$

where a_i^{Σ} is the activity of species *i* in the interfacial layer, and $\psi_i^{\mathrm{o},\Sigma}(T, p^{\mathrm{o}})$ is an standard state physicochemical potential, i.e. at standard pressure p^{o} and unit activity.

The partial molar interfacial area for species *i* in the interface phase

$$\overline{A}_i^{\Sigma} \equiv \left(\frac{\partial \underline{A}^{\Sigma}}{\partial n_i^{\Sigma}} \right)_{T,p,\phi,n_{j\neq i}^{\Sigma}} \approx N_{Av} \left(\frac{\overline{V}_i^{\Sigma}}{N_{Av}} \right)^{2/3} = 1.091 N_{Av}^{1/3} \left(\frac{M_i}{\rho_i^{\alpha}} \right)^{2/3} \left(\frac{\mathrm{m}^2}{\mathrm{mol}} \right) \tag{8.11}$$

Here it is approximated by molar interfacial area A_i^{Σ} for species *i* by assuming that the partial molar volume of *i* in the interfacial phase $\overline{V}_i^{\Sigma}$ is the same as the partial molar volume in the bulk phase $\overline{V}_i^{\alpha}$, i.e., $\overline{V}_i^{\Sigma} \approx \overline{V}_i^{\alpha}$, and further that the partial molar volume of *i* in the bulk phase mixture is the same as the molar volume of the pure species V_i^{α}, i.e., $\overline{V}_i^{\alpha} \approx V_i^{\alpha}$. The factor 1.091 in the above is based on the assumptions (1) the shape of an adsorptive molecule is spherical, (2) the liquid structure of the adsorptive is the close packing structure with 12 nearest neighbors, and (3) the adsorbate molecules are adsorbed on the particle surface with 6 nearest neighbors in close-packed hexagonal structures (Masuda and Higashitani, 2006).

Using the usual relation between partial molar and extensive system quantities

$$\underline{A}^{\Sigma} = \sum_{i=1}^{n} \overline{A}_i^{\Sigma} n_i^{\Sigma} \;\; ; \;\; \sum_{i=1}^{n} \overline{A}_i^{\Sigma} \Gamma_i = 1 \tag{8.12}$$

where the surface concentration of species *i* at interface is $\Gamma_i \equiv n_i^{\Sigma} / \underline{A}^{\Sigma}$.

For the overall system at constant temperature and pressure, thus, including the two bulk phases, i.e., with $\underline{G} = \underline{G}^{\alpha} + \underline{G}^{\beta} + \underline{G}^{\Sigma}$ and with $\Sigma = \Sigma_{\alpha} + \Sigma_{\beta}$ the condition for equilibrium is

$$d\underline{G}_{T,p} = \sum_{i=1}^{n} \tilde{\mu}_i^{\alpha} dn_i^{\alpha} + \sum_{i=1}^{n} \tilde{\mu}_i^{\beta} dn_i^{\beta} + \sum_{i=1}^{n} \psi_i^{\Sigma_{\alpha}} dn_i^{\Sigma_{\alpha}} + \sum_{i=1}^{n} \psi_i^{\Sigma_{\beta}} dn_i^{\Sigma_{\beta}} = 0 \tag{8.13}$$

8.3.2 Partitioning of Solutes Between Bulk Phase and Surface Sub-Layer

First we consider the case when there is partitioning of a species from within a phase to its associated interfacial sub-layer in an effort to minimize the system free energy. Thus, species *i* and A from bulk phase α diffuse in and out of sub-layer Σ_{α} and reach equilibrium. Similarly, species *j* and B from bulk phase β also undergo a similar partitioning step. For the exchange of mass between a bulk-phase and its own surface sub-layer, thus, mass balance provides $dn_i^{\alpha} = -dn_i^{\Sigma_{\alpha}}$; $dn_j^{\beta} = -dn_j^{\Sigma_{\beta}}$ which, when used in Eq. (8.13), provides in the condition for equilibrium

$$d\underline{G}_{T,p} = \sum_{i=1}^{n} \left(\psi_i^{\Sigma_{\alpha}} - \tilde{\mu}_i^{\alpha} \right) dn_i^{\Sigma_{\alpha}} + \sum_{j=1}^{n} \left(\psi_j^{\Sigma_{\beta}} - \tilde{\mu}_j^{\beta} \right) dn_j^{\Sigma_{\beta}} = 0 \tag{8.14}$$

On the other hand, Eq. (8.12) applied to the two interfacial sub-layers, when the interfacial layer area $\underline{A}^{\Sigma}$ is a constant, i.e., when $d\underline{A}^{\Sigma} = d\underline{A}^{\Sigma_{\alpha}} = d\underline{A}^{\Sigma_{\beta}} = 0$, requires

$$\sum_{i=1}^{n} \overline{A}_i^{\Sigma_{\alpha}} dn_i^{\Sigma_{\alpha}} = 0 \quad ; \quad \sum_{j=1}^{n} \overline{A}_j^{\Sigma_{\beta}} dn_j^{\Sigma_{\beta}} = 0 \tag{8.15}$$

Equations (8.14) and (8.15) can only be simultaneously satisfied if (Eriksson, 2007)

$$\begin{cases} \dfrac{\psi_i^{\Sigma_\alpha} - \tilde{\mu}_i^{\alpha}}{\overline{A}_i^{\Sigma_\alpha}} = \text{a constant} = \Omega_\alpha \quad (i = 1, 2, \cdots, n) \\ \dfrac{\psi_j^{\Sigma_\beta} - \tilde{\mu}_j^{\beta}}{\overline{A}_j^{\Sigma_\beta}} = \text{a constant} = \Omega_\beta \quad (j = 1, 2, \cdots, n) \end{cases} \tag{8.16}$$

Next, we apply Eq. (8.14) to the case when the surface area is increased differentially by $d\underline{A}^{\Sigma}$, while the equilibrium composition of the surface is maintained constant. Further, using in Eq. (8.15) the relation $n_i^{\Sigma_\alpha} = \Gamma_i^{\alpha} \underline{A}^{\Sigma}$, or $dn_i^{\Sigma_\alpha} = \Gamma_i^{\alpha} d\underline{A}^{\Sigma} + \underline{A}^{\Sigma} d\Gamma_i^{\alpha} \approx \Gamma_i^{\alpha} d\underline{A}^{\Sigma}$, the corresponding increase in the system Gibbs free energy

$$\sigma_{\alpha\beta} = \frac{d\underline{G}_{T,p}}{d\underline{A}^{\Sigma}} = \sum_{i=1}^{n} \left(\psi_i^{\Sigma_\alpha} - \tilde{\mu}_i^{\alpha}\right) \Gamma_i^{\alpha} + \sum_{j=1}^{n} \left(\psi_j^{\Sigma_\beta} - \tilde{\mu}_j^{\beta}\right) \Gamma_j^{\beta} = \sigma_\alpha + \sigma_\beta \tag{8.17}$$

An alternate form of this is obtained by using Eq. (8.16) in it

$$\sigma_{\alpha\beta} = \Omega_\alpha \sum_{i=1}^{n} \overline{A}_i^{\Sigma_\alpha} \Gamma_i^{\alpha} + \Omega_\beta \sum_{j=1}^{n} \overline{A}_j^{\Sigma_\beta} \Gamma_j^{\beta} \tag{8.18}$$

and further using Eq. (8.12) and again Eq. (8.16)

$$\sigma_{\alpha\beta} = \frac{\psi_i^{\Sigma_\alpha} - \tilde{\mu}_i^{\alpha}}{\overline{A}_i^{\Sigma_\alpha}} + \frac{\psi_j^{\Sigma_\beta} - \tilde{\mu}_j^{\beta}}{\overline{A}_j^{\Sigma_\beta}} \quad (i, j = 1, 2, \cdots, n) \tag{8.19}$$

i.e., the two constants in Eq. (8.16) are simply σ_α and σ_β.

Finally, using the constitutive equation Eq. (8.10) and the corresponding one for the electrochemical potential (Tester and Modell, 1997) along with the standard state potential in Eq. (8.11) $\psi_i^{o,\Sigma_\alpha} = \tilde{\mu}_i^{o,\Sigma_\alpha} + \sigma_i^{o} A_i^{\Sigma_\alpha}$ and with the assumption that $\overline{A}_i^{\Sigma} = A_i^{\Sigma}$

$$\sigma_{\alpha\beta} = \sigma_i^{o,\alpha} + \sigma_j^{o,\beta} - \frac{RT}{A_i^{\Sigma_\alpha}} \ln \frac{a_i^{\alpha}}{a_i^{\Sigma_\alpha}} - \frac{RT}{A_j^{\Sigma_\beta}} \ln \frac{a_j^{\beta}}{a_j^{\Sigma_\beta}} \quad (i, j = 1, 2, \cdots, n) \tag{8.20}$$

which may be written for the matrix components of the two phases along with, $A_{\mathrm{A}}^{\Sigma_\alpha} = 1/\Gamma_{\mathrm{A}}^{\alpha,\mathrm{o}}$ and $A_{\mathrm{B}}^{\Sigma_\beta} = 1/\Gamma_{\mathrm{B}}^{\beta,\mathrm{o}}$, as (Sugimoto, 1999)

$$\sigma_{\alpha\beta} = \sigma_{\alpha\beta}^{\mathrm{o}} - \Gamma_{\mathrm{A}}^{\alpha,\mathrm{o}} RT \ln \frac{a_{\mathrm{A}}^{\alpha}}{a_{\mathrm{A}}^{\Sigma_\alpha}} - \Gamma_{\mathrm{B}}^{\beta,\mathrm{o}} RT \ln \frac{a_{\mathrm{B}}^{\beta}}{a_{\mathrm{B}}^{\Sigma_\beta}} \tag{8.21}$$

where $\sigma_{\alpha\beta}^{\mathrm{o}} = \sigma_{\alpha}^{\mathrm{o}} + \sigma_{\beta}^{\mathrm{o}}$, where $\sigma_{\alpha}^{\mathrm{o}}$ is the Gibbs free energy of formation of unit interfacial area (J/m^2) from pure A in phase α., i.e., for $\mathrm{A}(\alpha) \leftrightarrows \mathrm{A}(\Sigma_\alpha)$.

This extension of the result of Butler (1932) by Sugimoto (1996; 1999) is applicable, e.g., to the interface between two immiscible liquids or between a solid and a liquid. The activity coefficients may be written in terms of activity coefficients or partial molar excess Gibbs free energy.

8.3.3 Solute Partitioning following Langmuir Isotherm

In the partitioning step, solute species *i* from the bulk phase exchanges with the matrix species A on the surface, as shown schematically in Figure 8.2. This is, in fact, a linear combination of the two partitioning steps s_i and s_{A} shown in Figure 8.2, $s_i : i(\alpha) \leftrightarrows i(\Sigma_\alpha)$ and $s_{\mathrm{A}} : \mathrm{A}(\alpha) \leftrightarrows \mathrm{A}(\Sigma_\alpha)$, i.e., $s_i - s_{\mathrm{A}}$, resulting in the overall exchange process $\mathrm{A}(\Sigma_\alpha) + i(\alpha) \leftrightarrows \mathrm{A}(\alpha) + i(\Sigma_\alpha)$.

The standard Gibbs free energy change for this exchange reaction, thus,

$$\Delta G_{\rho}^{\Sigma_\alpha,\mathrm{o}} = \left(\psi_i^{\Sigma_\alpha,\mathrm{o}} + \tilde{\mu}_{\mathrm{A}}^{\alpha,\mathrm{o}}\right) - \left(\tilde{\mu}_i^{\alpha,\mathrm{o}} + \psi_{\mathrm{A}}^{\Sigma_\alpha,\mathrm{o}}\right) = \Delta G_i^{\Sigma_\alpha,\mathrm{o}} - \Delta G_{\mathrm{A}}^{\Sigma_\alpha,\mathrm{o}} \tag{8.22}$$

where $\Delta G_{\mathrm{A}}^{\Sigma_\alpha,\mathrm{o}}$ is the standard state Gibbs free energy change for the partitioning step, $\mathrm{A}(\alpha) \leftrightarrows \mathrm{A}(\Sigma_\alpha)$, and similarly for *i*, so that

$$\left(\frac{a_i^{\Sigma_\alpha}}{a_i^{\alpha}}\right)\left(\frac{a_{\mathrm{A}}^{\alpha}}{a_{\mathrm{A}}^{\Sigma_\alpha}}\right) = \exp\left\{-\frac{\left(\Delta G_i^{\Sigma_\alpha,\mathrm{o}} - \Delta G_{\mathrm{A}}^{\Sigma_\alpha,\mathrm{o}}\right)}{RT}\right\} \equiv K_i^{\Sigma_\alpha} \tag{8.23}$$

where $K_i^{\Sigma_\alpha}$ is the equilibrium constant for the overall surface exchange reaction [34].

Next, it is assumed that: 1) the surface layer is ideal, i.e., $a_i^{\Sigma_\alpha} = \theta_i^{\Sigma_\alpha}$, $a_{\mathrm{A}}^{\Sigma_\alpha} = \theta_{\mathrm{A}}^{\Sigma_\alpha}$, in accord with the Langmuir model, and 2) the bulk mixture is dilute, i.e., $a_{\mathrm{A}}^{\alpha} \to 1$. Finally using surface site balance $\theta_i^{\Sigma_\alpha} + \theta_{\mathrm{A}}^{\Sigma_\alpha} = 1$, provides

$$\theta_{\mathrm{A}}^{\Sigma_\alpha} = \frac{1}{1 + K_i^{\Sigma_\alpha} a_i^{\alpha}};\ \theta_i^{\Sigma_\alpha} = \frac{K_i^{\Sigma_\alpha} a_i^{\alpha}}{1 + K_i^{\Sigma_\alpha} a_i^{\alpha}} \tag{8.24}$$

Under these assumptions, thus, Eq. (8.21) reduces to

$$\sigma_{\alpha\beta} = \sigma_{\alpha\beta}^{\mathrm{o}} - \Gamma_{\mathrm{A}}^{\alpha,\mathrm{o}} RT \ln\left(1 + K_i^{\Sigma_\alpha} a_i^{\alpha}\right) - \Gamma_{\mathrm{B}}^{\beta,\mathrm{o}} RT \ln\left(1 + K_j^{\Sigma_\beta} a_j^{\beta}\right) \tag{8.25}$$

Such relations apply both for the interfacial energy of the liquid-gas interface as well as for the solid-liquid interface. As a result of the change in these interfacial energy terms, the contact angle, work of adhesion, adhesion tension, and the wetting characteristics change.

8.4 Results and Discussion

8.4.1 Liquid Metal-Gas Phase Interface

We consider first the liquid metal-gas interface. Many metals have a strong affinity for oxygen, especially at the higher temperatures. At low partial pressures, oxygen is adsorbed at the surface and thereupon it also dissolves into the liquid metal. This results in a decrease in the surface energy of the liquid metal.

Thus, with $\alpha = L$ as liquid metal phase (e.g., A = liquid Ag, *L*) and $\beta = G$ as gas phase (e.g., B = O_2) we apply Eq. (8.25) to, e.g., the Ag-O_2 system. It is assumed that the partitioning standard state Gibbs free energy change of gas molecules is zero, i.e., in the gas-phase there is no

distinction between the bulk and its surface sub-layer (Sugimoto, 1999). Therefore, the second term of Eq. (8.25) can be ignored resulting in

$$\sigma_{LG} = \sigma_{LG}^{o} - \Gamma_L^{o} RT \ln(1 + K_{\mathrm{O}}^{\Sigma_L} a_{\mathrm{O}}^{L}) \tag{8.26}$$

where Γ_L^{o} is the saturated (maximum) adsorption concentration of liquid-metal-O at liquid-gas interface. This is identical to Eq (8.1), first proposed by von Szyszkowski in 1908, and also subsequently derived independently by Belton (1976) and March and Tosi (1976).

This can further be related to the partial pressure of oxygen as follows. The steps of interface adsorption and the subsequent partitioning of oxygen into liquid Ag are

$$\begin{array}{lcll} \underline{s_\rho} & & \underline{\sigma_\rho} & \\ s_1: & \mathrm{O}_2(G) \leftrightarrows 2\mathrm{O}(\Sigma_L) & +1/2 & K_{ad} \\ s_2: & \mathrm{O}(L) \leftrightarrows \mathrm{O}(\Sigma_L) & -1 & K_O^{\Sigma_L} \\ \hline s_S: & \tfrac{1}{2}\mathrm{O}_2 \leftrightarrows \mathrm{O}(L) & & K_S \end{array} \tag{8.27}$$

where the following linear combination of the above elementary steps provides the overall solution of oxygen into the liquid metal, as does its standard Gibbs free energy change and equilibriums constants

$$s_S = \tfrac{1}{2} s_1 - s_2,\ \Delta G_S^{o} = \tfrac{1}{2}\Delta G_1^{o} - \Delta G_2^{o},\ K_S = \frac{\sqrt{K_{ads}^{L}}}{K_{\mathrm{O}}^{\Sigma_L}} \tag{8.28}$$

For a dilute gaseous component *i* in the liquid metal, e.g., O or H atoms, thus, $a_i^L = K_S\sqrt{p_i / p^{o}}$ $\approx x_i^L$, which is Sieverts' law (Sieverts, 1929). Here K_S is the Sieverts' constant, K_{ads}^{L} is the dissociative adsorption equilibrium constant from the liquid phase, $K_{\mathrm{O}}^{\Sigma_L}$ is the equilibrium constant of oxygen partitioning from the bulk to the surface layer.

Replacing the activity of oxygen in the Szyszkowski relation, Eq. (8.26), using Sieverts' law, along with the use of Eq. (8.28), finally provides

$$\sigma_{LG} = \sigma_{LG}^{o} - \Gamma_{L}^{o} RT \ln\left(1 + \sqrt{K_{ads}^{L}}\sqrt{\frac{p_{O_2}}{p^{o}}}\right) \tag{8.29}$$

8.4.2 Liquid Metal-Gas Interface in Liquid Ag and Liquid Cu Systems

Several parameters need to be estimated to calculate the surface tension for the liquid Ag and liquid Cu systems using Eq. (8.29). The saturation concentration of oxygen adsorption cannot be directly measured; however, it can be evaluated using Gibbs adsorption isotherm if the surface is saturated

$$\Gamma_{L}^{o} = -\frac{1}{RT}\left(\frac{\partial \sigma_{LG}}{\partial \ln a_{O}}\right) = -\frac{2}{RT}\left(\frac{\partial \sigma_{LG}}{\partial \ln p_{O_2}}\right) \tag{8.30}$$

For A = Ag, thus, the reported values of Γ_{Ag}^{o} gathered from the literature are listed in Table 8.1. As evident from this, between 1253K and 1381K, the value of Γ_{Ag}^{o} does not change much, and lies between 4×10^{-6} and 5.8×10^{-6} mol/m^2. Therefore, $\Gamma_{Ag}^{o} = 5\times10^{-6}$ was chosen here for further calculations. The Sieverts' constant K_S of Ag is listed in Table 8.2. The liquid-gas surface tensions were calculated by adjusting $K_{O}^{\Sigma_L}$ and combining with the reported K_S value to estimate K_{ads}^{L}.

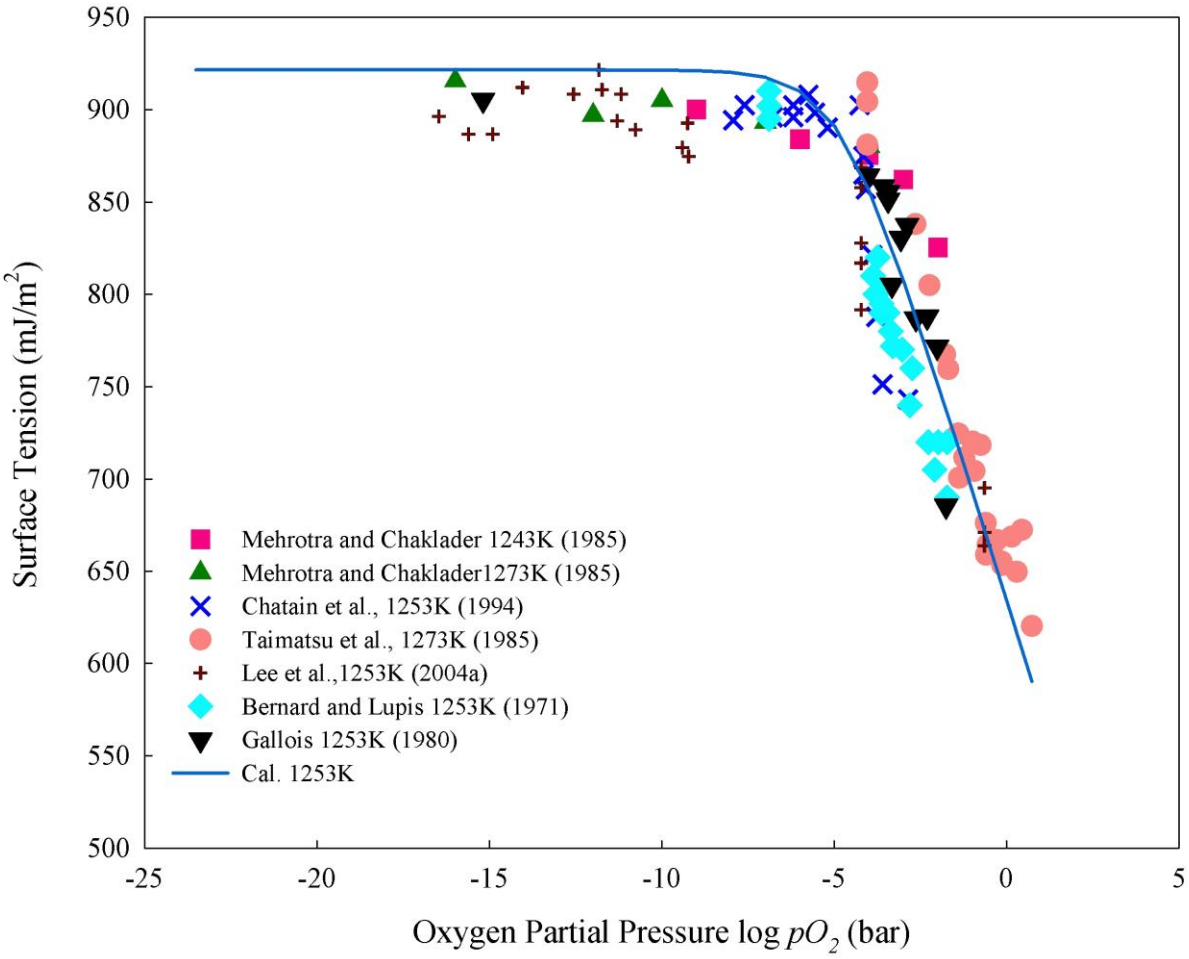

Figure 8.3 (a) Liquid-gas surface tension of Ag estimated from Eq. (8.29) with various of p_{O_2} at 1253K, Mehrota and Chaklader (1985); Chatain et al., (1994); Taimatsu et al., (1985); Lee et al., (2004a); Bernard and Lupis (1971); Gallois (1980).

Experimental data for liquid metal-gas surface tension of Ag/Al_2O_3 as a function of oxygen partial pressure p_{O_2} was gathered from literature and is summarized in Figures 8.3 (a) and (b) for the temperatures of 1253 K, and 1373 K, respectively. The calculated results are in good agreement with experimental data at both temperatures. Thus, surface tension remains essentially constant at both temperatures at very low oxygen partial pressures. As oxygen partial pressure exceeds 10^{-6} bars, the surface tension drops. The slight over prediction of the surface tension in

the plateau region at 1253 K is due to the use of $\sigma_{LG}^{o} = 926$ mJ/m^2 as the pure Ag surface tension at its melting point (Mill and Su, 2006). This value is highly dependent on the experimental methodology, possible oxygen infiltration in the gas environment, and the support substrate used for measurement. Thus, the reported values range from $\sigma_{LG}^{o} = 908 \sim 966$ mJ/m^2 (Ozawa et al., 2010; Mill and Su, 2006).

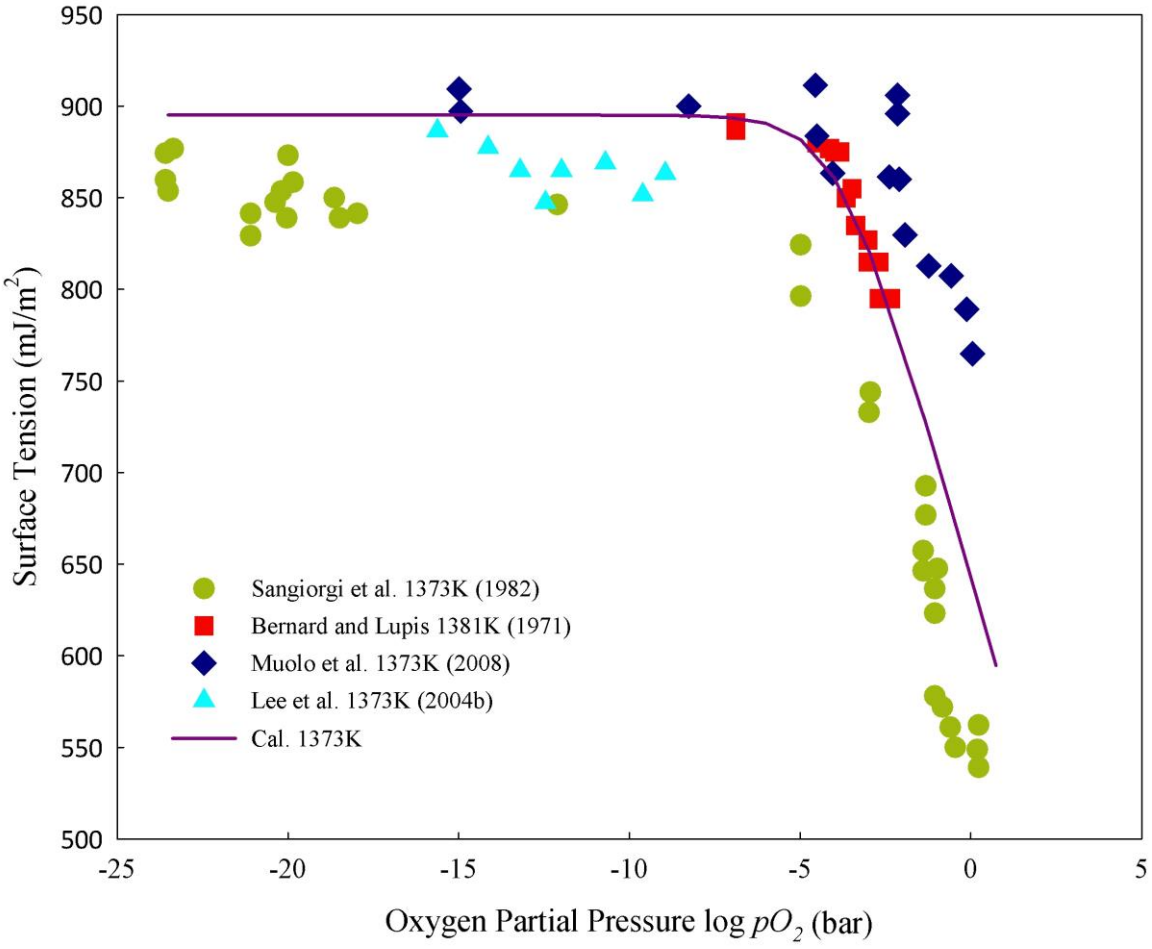

Figure 8.3 (b) Liquid-gas surface tension of Ag estimated from Eq. (8.29) with various p_{O_2} at 1373K, Sangiorgi et al., (1982); Bernard and Lupis (1971); Muolo et al., (2008); Lee et al., (2004b).

The σ_{LG}^{o} value used in this study (Table 8.2), thus, slightly over estimates the pure silver surface tension at 1253 K (Figure 8.3a); however, it fits well the data at 1373K (Figure 8.3b). For the Cu/Al_2O_3 liquid metal-gas phase system, the reported saturation oxygen adsorption concentration of Cu between 1381K and 1473K is also summarized in Table 8.1, while its Sieverts' constant K_S is listed in Table 8.2.

Table 8.1 Reported maximum adsorption concentration at interface.

Temperature (K)	Γ (mole/m^2)	**Reference**
	Silver (Ag)	
1253	$\Gamma_{Ag}^{o} = 4.67 \times 10^{-6}$	Lee et al., 2004a
1273	$\Gamma_{Ag}^{o} = 5.8 \times 10^{-6}$	Taimatsu et al., 1985
1253	$\Gamma_{Ag}^{o} = 4 \times 10^{-6}$	Mehrotra and Chaklader, 1985
1253	$\Gamma_{Ag}^{o} = 4 \times 10^{-6}$	Chatain et al., 1994
1253	$\Gamma_{Ag}^{o} = 4.8 \times 10^{-6}$	Bernard and Lupis, 1971
1373	$\Gamma_{Ag}^{o} = 5 \times 10^{-6}$	Muolo et al., 2008
1381	$\Gamma_{Ag}^{o} = 4.5 \times 10^{-6}$	Bernard and Lupis, 1971
	Copper (Cu)	
1381	$\Gamma_{Cu}^{o} = 5.72 \times 10^{-6}$	Gallois and Lupis, 1981
1365	$\Gamma_{Cu}^{o} = 4.9 \times 10^{-6}$	Ghetta et al., 1996
1373, 1423, 1473	$\Gamma_{Cu}^{o} = 4.8 \times 10^{-6}$	Mehrotra and Chaklader, 1985
1373	$\Gamma_{Cu}^{o} = 5 \times 10^{-6}$	Lee et al., 2004b
1423	$\Gamma_{Cu}^{o} = 9.3 \times 10^{-6}$	Bernard and Lupis, 1971
	Alumina (Al_2O_3)	
1373	$\Gamma_{Al_2O_3}^{o} = 1.14 \times 10^{-5}$	Muolo et al., 2008

The reported Γ_{Cu}^{o} values lie mostly between 4.8×10^{-6} and 5.72×10^{-6} mol/m^2, except one. Thus, the average value $\Gamma_{Cu}^{o}=5.3\times10^{-6}$ was adopted for calculations.

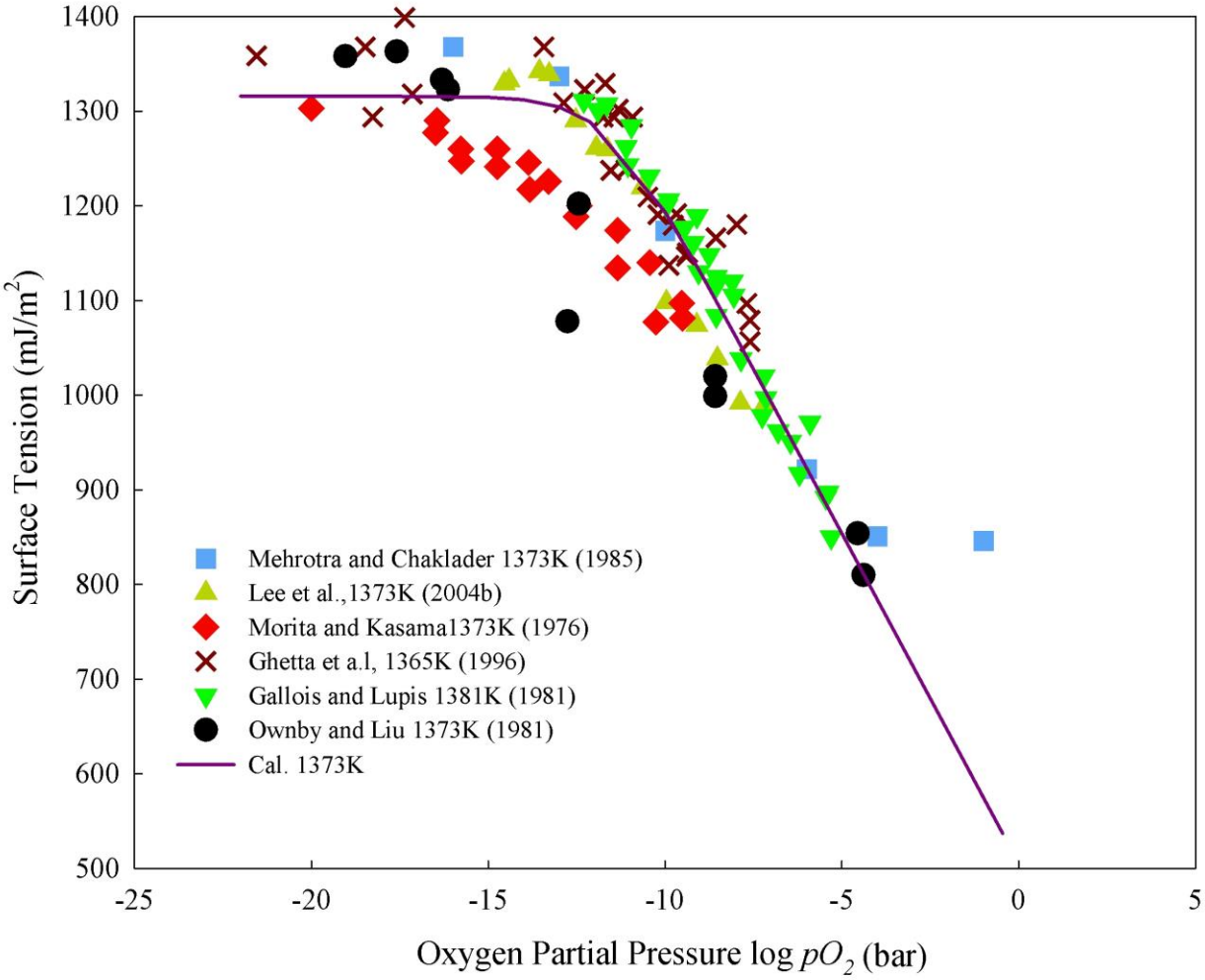

Figure 8.4 (a) Liquid-gas surface tension of Cu estimated from Eq. (8.29) with various of p_{O_2} at 1373K, Mehrotra and Chaklader (1985); Lee et al., (2004b); Morita and Kasama (1976); Ghetta et al., (1996); Gallois and Lupis (1981); Ownby and Liu (1981).

Experimental data for liquid-gas surface tension of Cu/Al_2O_3 were gathered from the literature, and are shown as a function of oxygen partial pressure p_{O_2} at 1373K and 1523K in Figures 8.4 (a) and (b), respectively. The calculated results at 1373K are in good agreement with all

experimental data except those of Morita and Kasama (1976). Experimental data between 1473K~1573K are more scattered; however, the characteristic trend of decreasing with increasing oxygen partial pressure is still evident.

An average temperature of 1523K was used for these calculations in Figure 8.4 (b). Due to the lack of availability of an experimental value of Sieverts' constant at this temperature, the value of Sieverts' constant at 1473K was used. Despite these approximations, the fit of predictions with experiments is reasonable.

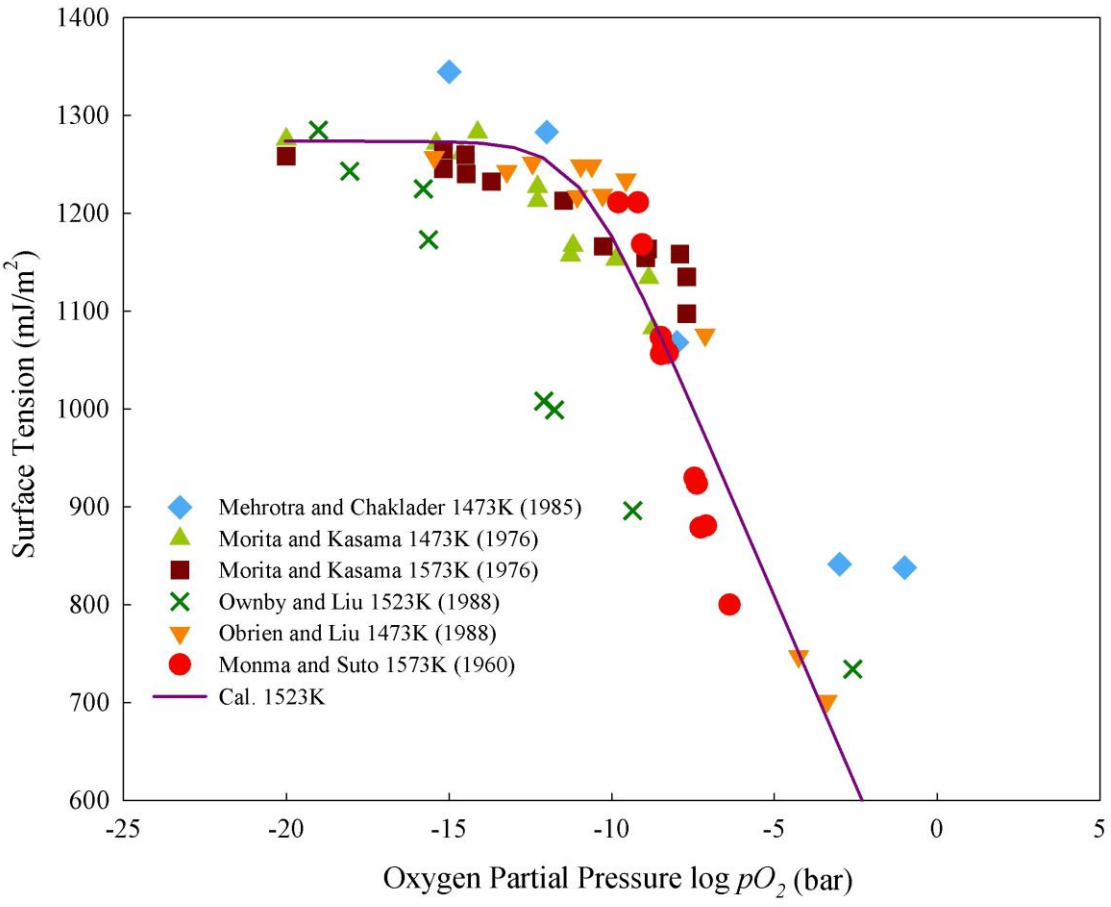

Figure 8.4 (b) Liquid-gas surface tension of Cu estimated from Eq. (8.29) with various of p_{O_2} at 1523K, Mehrotra and Chaklader (1985); Morita and Kasama (1976); Ownby and Liu (1981); Monma and Suto (1960).

Table 8.2 Literature parameters used in calculations.

Elements, Temperature	Parameters	Reference
Cu, 1381K	$x_{\mathrm{O}} = 4.85\sqrt{\mathrm{p}_{\mathrm{O}_2}(\mathrm{bar})}, K_S = 4.85$	Gallois and Lupis, 1981
Cu, 1473K	$x_{\mathrm{O}} = 6.51\sqrt{\mathrm{p}_{\mathrm{O}_2}(\mathrm{bar})}, K_S = 6.51$	Siwiec and Willner, 2009
Ag, 1253K	$x_{\mathrm{O}} = 0.020816\sqrt{\mathrm{p}_{\mathrm{O}_2}(\mathrm{bar})}, K_S = 0.020816$	Bernard and Lupis, 1971
Ag, 1381K	$x_{\mathrm{O}} = 0.0181\sqrt{\mathrm{p}_{\mathrm{O}_2}(\mathrm{bar})}, K_S = 0.0181$	Parlee and Sacris, 1965
sapphire	$\sigma_{SG} = 1.961 - 4.7\cdot 10^{-4} T(^{\circ}C)$ J/m^2, 927-2077°C	Ownby and Liu, 1988
Al_2O_3	$\Gamma^{\mathrm{o}}_{\mathrm{Al_2O_3}} = 1.24\times 10^{-5}$ mole/m^2	
Ag	$\sigma^{\mathrm{o}}_{LG} = 926 - 0.22(T - 1233)(^{\circ}K)$ mJ/m^2	Mill and Su, 2006
Cu	$\sigma^{\mathrm{o}}_{LG} = 1320 - 0.28(T - 1358)(^{\circ}K)$ mJ/m^2	Mill and Su, 2006

8.4.3 Liquid Metal-Solid Ceramic Interface

As an example, we consider the liquid Ag/Al_2O_3 system, with $\alpha = S$ as solid phase (A = Al_2O_3 = *S*) and $\beta = L$ as liquid phase (B = liquid Ag = *L*), which in turn is in contact with gas-phase containing oxygen. Using the liquid-solid surface tension from Eq. (8.25) combines with the use of Sieverts' law

$$\sigma_{SL} = \sigma^{\mathrm{o}}_{SL} - \Gamma^{\mathrm{o}}_S RT \ln\left(1 + \sqrt{K^S_{ads}}\sqrt{\frac{p_{\mathrm{O}_2}}{p^{\mathrm{o}}}}\right) - \Gamma^{\mathrm{o}}_L RT \ln\left(1 + \sqrt{K^L_{ads}}\sqrt{\frac{p_{\mathrm{O}_2}}{p^{\mathrm{o}}}}\right) \tag{8.31}$$

where K^L_{ads} is the oxygen dissociative adsorption equilibrium constant on the liquid phase and K^S_{ads} on the solid-phase, while $K^{\Sigma_S}_{\mathrm{O}}$ is the equilibrium constant for oxygen partitioning from the bulk to the solid surface layer.

8.4.4 Ag/Al_2O_3 Liquid-Solid Phase Interface

Since there are no reported data on pure solid-liquid surface tension σ_{SL}^{o} for this system, it was calculated from the Young-Dupré equation, Eq. (8.3), by using σ_{SG}^{o}, σ_{LG}^{o} and the contact angle obtained at very low oxygen partial pressure. Further, the change of σ_{SL} versus oxygen partial pressure is also calculated from the corresponding contact angle using Eq. (8.3). The solid-gas surface tension of Al_2O_3 is assumed to remain constant at fixed temperature and independent to the change of oxygen partial pressure. Thus, Al_2O_3 solid-gas tension given by $\sigma_{SG} = 1.961 - 4.7 \cdot 10^{-4} T(^{\circ}C)$ J/m^2 (Ownby and Liu, 1988) was used in these calculations. If the σ_{SL} from a literature source was calculated based on different a σ_{SG} value, it was recalculated for consistency. In one or two cases, where only contact angles were listed, the liquid-gas surface tension calculated from Eq. (8.29) was used to estimate σ_{SL}. There is only one reported value of saturation oxygen adsorption concentration on the alumina surface, $\Gamma_{Al_2O_3}^{o} = 1.14 \times 10^{-5}$ mol/m^2 (Muolo et al., 2008) of Al_2O_3-Ag interface at 1373K, which is close to the theoretical value $\Gamma_{Al_2O_3}^{o} = 1.24 \times 10^{-5}$ mol/m^2 calculated from Eq. (8.11). No other report was found for $\Gamma_{Al_2O_3}^{o}$ value at other temperatures and for other liquid metal systems. Thus, it was simply assumed that the variation of $\Gamma_{Al_2O_3}^{o}$ would be small and its theoretical value was used.

Figure 8.5 (a) thus provides a comparison of the calculated solid-liquid surface tension of Ag/Al_2O_3 at 1253 K versus p_{O_2} using Eq. (8.38) with experimental data collected from literature (symbols) as well as with the interface energy obtained from DFT modeling (dashed line). The calculation matches well with the DFT modeling as well as with experimental results, with only a few discrepancies with the data of Taimatsu et al. (1985) and those of Mehrotra and Chaklader (1985) at very low oxygen pressure region. The open circle symbols of Taimatsu et al. (1985)

data are from their experiments using single crystal Ag/Al_2O_3 substrate, while the filled circle symbols represent data using poly crystal Ag/Al_2O_3 substrate. The influence of substrate crystalline structure on Ag/Al_2O_3 solid-liquid surface tension is, of course, not addressed here.

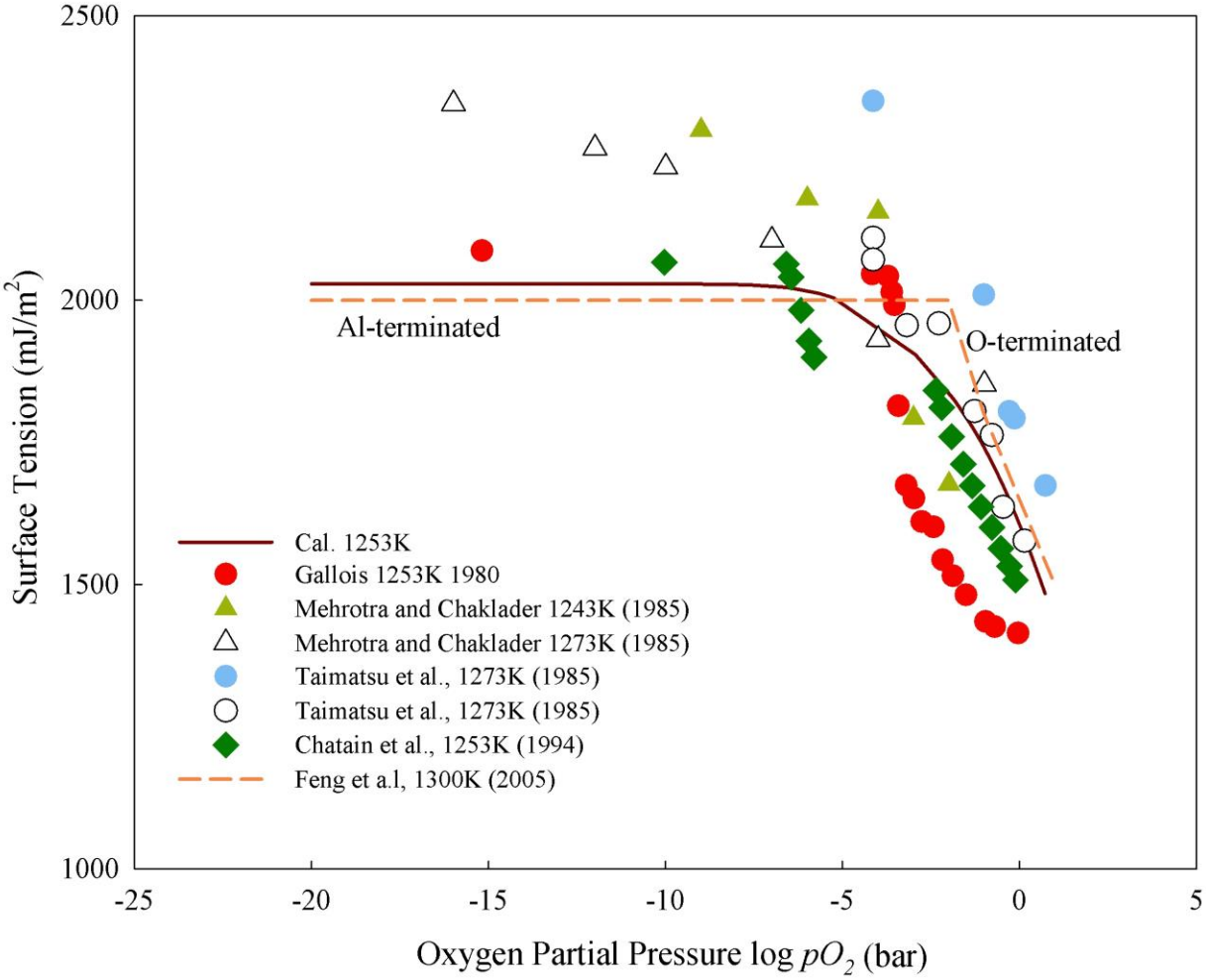

Figure 8.5 (a) Solid-liquid surface tension of Ag estimated from Eq. (8.31) with various p_{O_2} at 1253K, Mehrotra and Chaklader (1985); Taimatsu et al., (1985); Chatain et al., (1994); Feng et al., (2005).

Similar to the case of liquid metal-gas surface tension discussed above, at low oxygen partial pressure region the solid-liquid surface tension remains essentially a constant and then drops

with increasing oxygen partial pressure. Based on the thermodynamic calculations, the equilibrium oxygen pressure of Al_2O_3 to decompose spontaneously into Al and O_2 is 2.12×10^{-31} bar (Sangiorgi et al., 1982). Thus, this is unlikely to occur, since all the testing conditions gathered from literature are above 10^{-23} bar. Equilibrium oxygen pressure for Al_2O_3 to decompose into Al_2O and O_2 is 2.9×10^{-19} bar and 1.04×10^{-16} bar to decompose into AlO and O_2. It may thus be concluded that if any decomposition/formation of Al_2O_3 occurred, it could only occur with oxygen in liquid metal coming from the gas phase, not from O in the bulk solid phase, since both Al and O self-diffusion coefficients in Al_2O_3 are smaller than 2×10^{-16} cm^2/s at 1423 K (Oishi and Kingery, 1960). Therefore, any dissolution of Al and O from Al_2O_3 bulk into liquid metal would be negligible as well.

Feng et.al (2005) concluded from DFT modeling that, at low oxygen partial pressure, Al-terminated surface is the most stable structure of Al_2O_3, where the bonding with Ag at interface is the combination of both metallic interaction and electron polarization. The structure switched at 10^{-2} bar into O-terminated structure, where the bonding at interface is the ionic interaction between Ag and O thus leading to interface energy decrease. In this study, only Ag in the liquid phase was modeled, however, the dissolved oxygen from gas phase adsorption on Al_2O_3 was not considered. Passerone et. al (2010), on the other hand, placed extra oxygen atoms at Al and O terminated interface to simulate the dissolved oxygen from gas phase, and discovered that this Al-terminated/O-rich-Ag is stable at 10^{-10} bar. Therefore, the actual surface tension declining region may be located between 10^{-2} to 10^{-10} bar, which agrees with our calculation of around 10^{-6} bar. The calculated W_{ad} at low oxygen partial pressure region is 0.39 J/m^2, which is close to work of separation W_{sep} 0.33 J/m^2 of Feng et al. (2005), but higher than 0.30 J/m^2 from Muolo et al. (2008).

8.4.5 Cu/Al_2O_3 Liquid-Solid Phase Interface

Figures 8.5 (b) and (c) provide the calculated solid-liquid surface tension with various p_{O_2} of Cu/Al_2O_3 at 1373K and 1523K, respectively, using Eq. (8.31) in comparison with the experimental data collected from literature (symbols) as well as the interfacial energy calculated via DFT modeling (dashed lines). The calculation matches well with the experimental results except with the data of Mehrotra and Chaklader (1985) at both temperatures at low oxygen partial pressures. The contact angle given by Mehrotra and Chaklader is about 160^o which is much higher than $120^o \sim 130^o$ obtained from other sources, thus resulting in high values of calculated σ_{SL}. At both temperatures, the calculated surface tension is also lower than the prediction from DFT modeling. The DFT modeling simulates the Al and O terminated interface with pure Cu rather than combination of Cu and extra O to imitate the dissolved oxygen from gas atmosphere. Thus, the high oxygen solubility in Cu may be the reason for the difference. The trend of surface tension decline at high oxygen pressure is the same as in the Ag/Al_2O_3 system. The extent and nature of species of copper oxide formed at Cu/Al_2O_3 interface depends on the temperature and oxygen partial pressure. A continuous formation of Cu_2O and non-continuous $CuAlO_2$ layer were reported at 1523 K, 10^{-3} bar (Diemer et al., 1999). Scheu et al. (2002) annealed Cu with Al_2O_3 at 1273 K for 96 hours at oxygen partial pressure of 0.02 and 32 Pa and observed a 20-35 nm thick $CuAlO_2$ layer formed at the interface. The layer is also non-continuous and interrupted by Cu pores, resulting in poor wetting behavior. Nonetheless, the experiments show improvement in wetting compared to the pure Cu on Al_2O_3. The contact angle of Cu on Al_2O_3 is 141^o at 1273 K, while that for Cu on $CuAlO_2$ is 110^o for specimen annealed at 32 Pa.

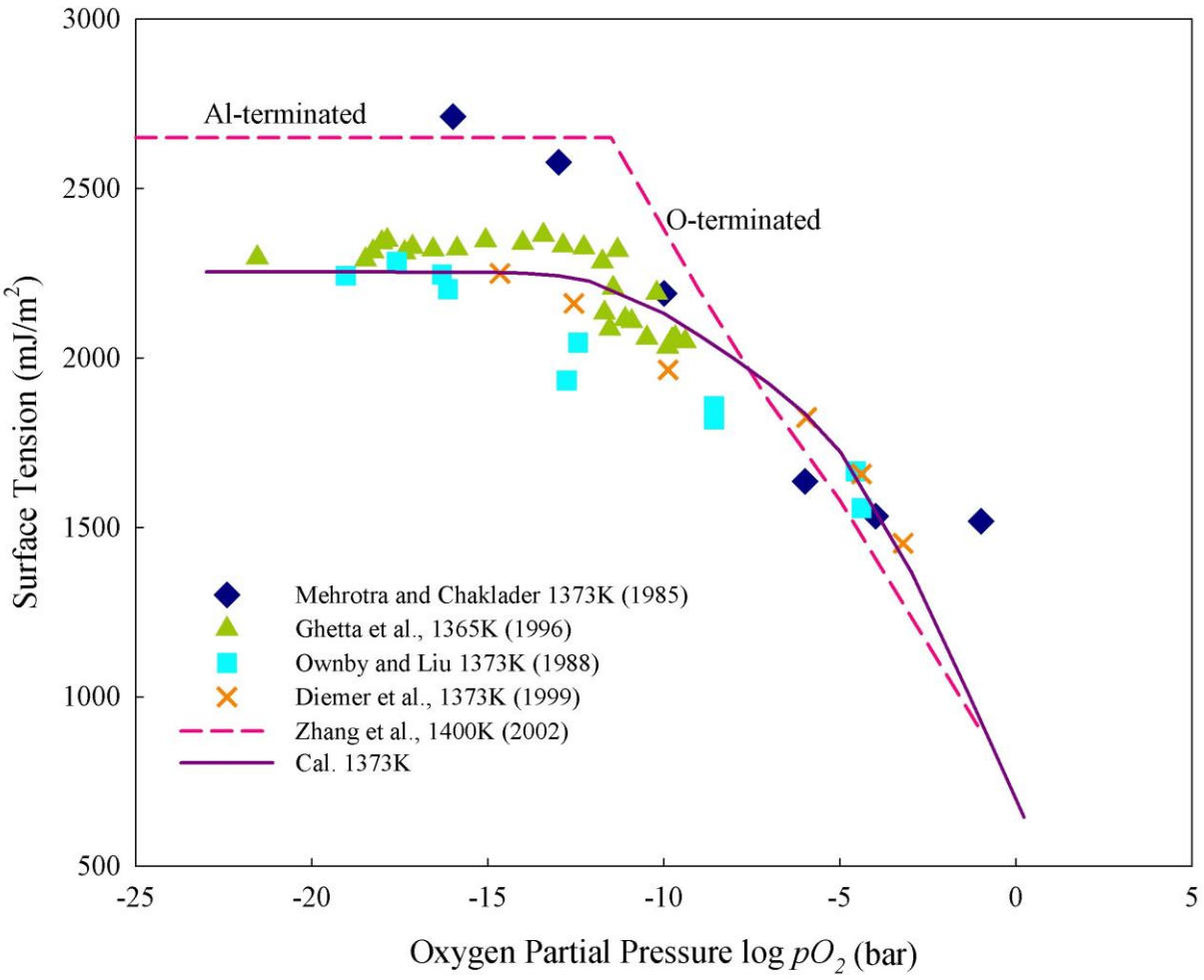

Figure 8.5 (b) Solid-liquid surface tension of Cu estimated from Eq. (8.31) with various p_{O_2} at 1373K, Mehrotra and Chaklader (1985); Ghetta et al., (1996); Ownby and Liu (1988); Diemer et al., (1999); Zhang et al., (2002).

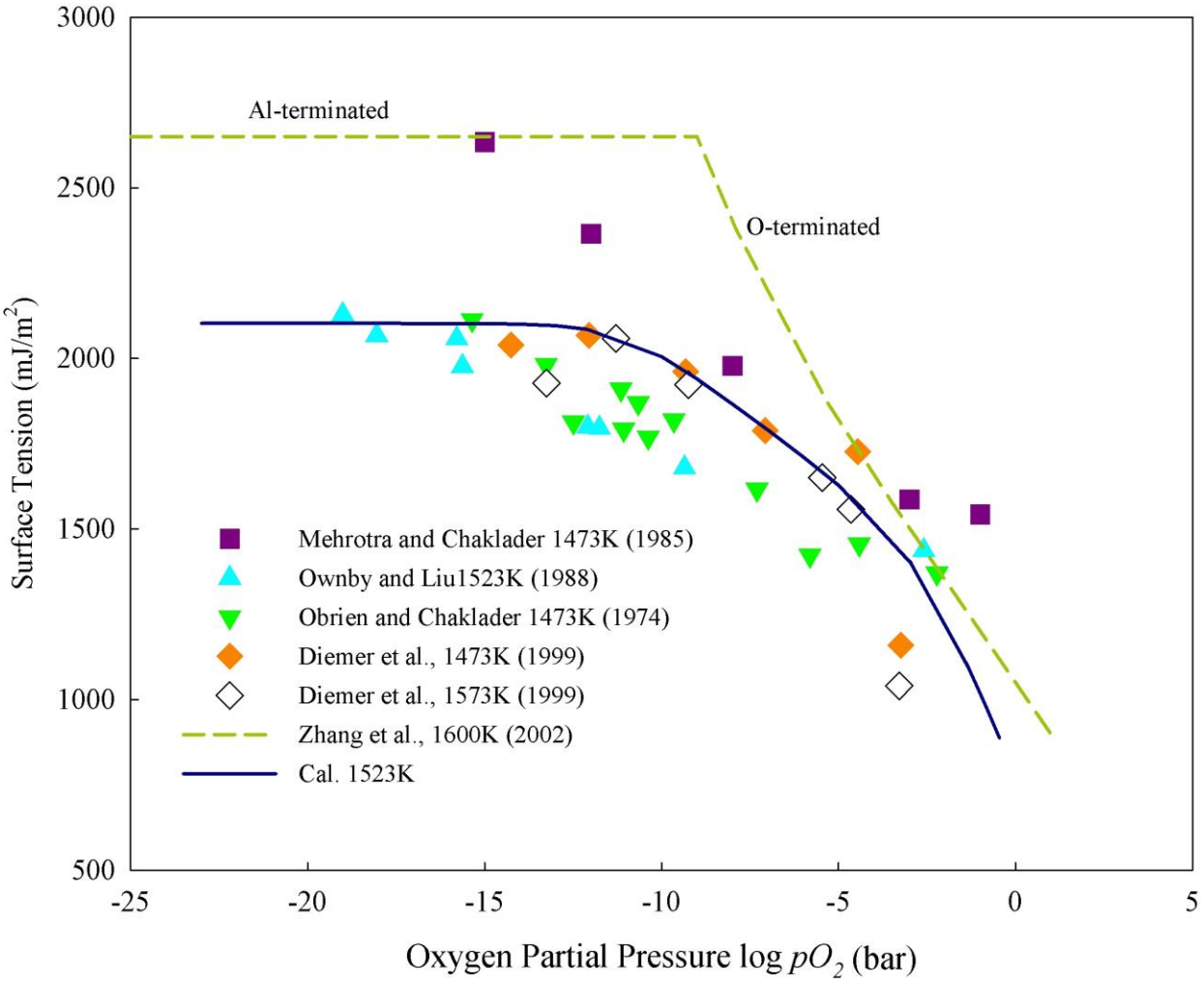

Figure 8.5 (c) Solid-liquid surface tension of Cu estimated from Eq. (8.31) with various p_{O_2} at 1523K, Mehrotra and Chaklader (1985); Ownby and Liu (1988); Obrien and Chaklader (1974); Diemer et al., (1999); Zhang et al., (2002).

8.4.6 Contribution of Solid and Liquid Interfacial Layers to Solid-Liquid Surface Tension

The influence of oxygen on both the liquid metal-gas and solid-liquid metal surface tension is obvious; however, the difference between the two has been difficult to quantify so far. The Butler-Sugimoto bilayer model allows us to do so as described below. Consider the schematic of a drop of liquid metal in contact with solid ceramic, as shown in Figure 8.6. It is clear from this

schematic that the bilayer solid-liquid interface comprises of a solid interface monolayer and a liquid interface monolayer, the latter being the same as the liquid-gas interface layer. In order to quantify the effect of oxygen on these two monolayers, we rewrite Eq. (8.31) as follows.

Recall from Eq. (8.17) that $\sigma_{SL} = \sigma_S + \sigma_L$, which for the case of no oxygen is written as $\sigma^{\circ}_{SL} = \sigma^{\circ}_S + \sigma^{\circ}_L$. Consequently, with $\Delta\sigma_{SL} \equiv \sigma_{SL} - \sigma^{\circ}_{SL}$, $\Delta\sigma_S \equiv \sigma_S - \sigma^{\circ}_S$, and $\Delta\sigma_L \equiv \sigma_L - \sigma^{\circ}_L$, we may write

$$\Delta\sigma_{SL} = \Delta\sigma_S + \Delta\sigma_L \tag{8.32}$$

which when compared with Eq. (8.31) provides

$$\Delta\sigma_S = -\Gamma^{\circ}_S RT \ln\left(1 + \sqrt{K^S_{ads}}\sqrt{\frac{p_{O_2}}{p^{\circ}}}\right);\ \Delta\sigma_L = -\Gamma^{\circ}_L RT \ln\left(1 + \sqrt{K^L_{ads}}\sqrt{\frac{p_{O_2}}{p^{\circ}}}\right) \tag{8.33}$$

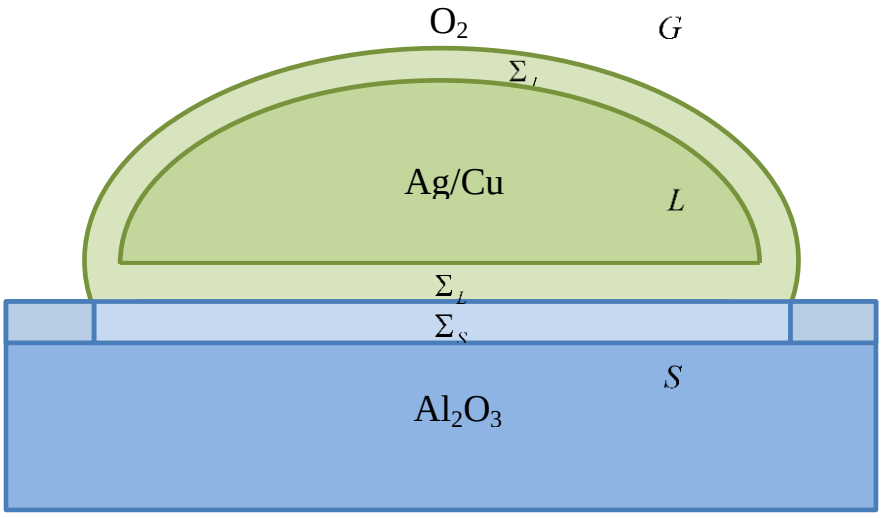

Figure 8.6 Schematic of liquid metal in contact with solid ceramic.

The last of these is, of course, the same as $\Delta\sigma_{LG}$, i.e., $\Delta\sigma_L = \Delta\sigma_{LG}$ the change in the liquid-gas surface tension as a result of the presence of oxygen, as evident from Eq. (8.33) as well as the schematic in Figure 8.6.

Figure 8.7 (a), thus, plots these surface tension changes as a function of oxygen partial pressure as given by the above three relations for both the Ag/Al_2O_3 system at 1253 K and for the Cu/Al_2O_3 at 1373 K using the parameters discussed above. The surface tension change for both liquid and solid-liquid phase is almost zero in region A. Upon entering region B, the surface energy decrease of both Cu and Ag is due entirely to the change in the liquid-gas surface tension, while the change in the solid-liquid phase remains zero. In region C, both liquid monolayer and solid monolayer have strong adsorption at the interface, thus, the energy decreases dramatically due to contribution of both, resulting in a change of slope, as seen in Figure 8.7 (a). Further, the surface energy decrease of Cu system is much higher than Ag system. The higher oxygen solubility in Cu than Ag may be a reason for early surface tension change.

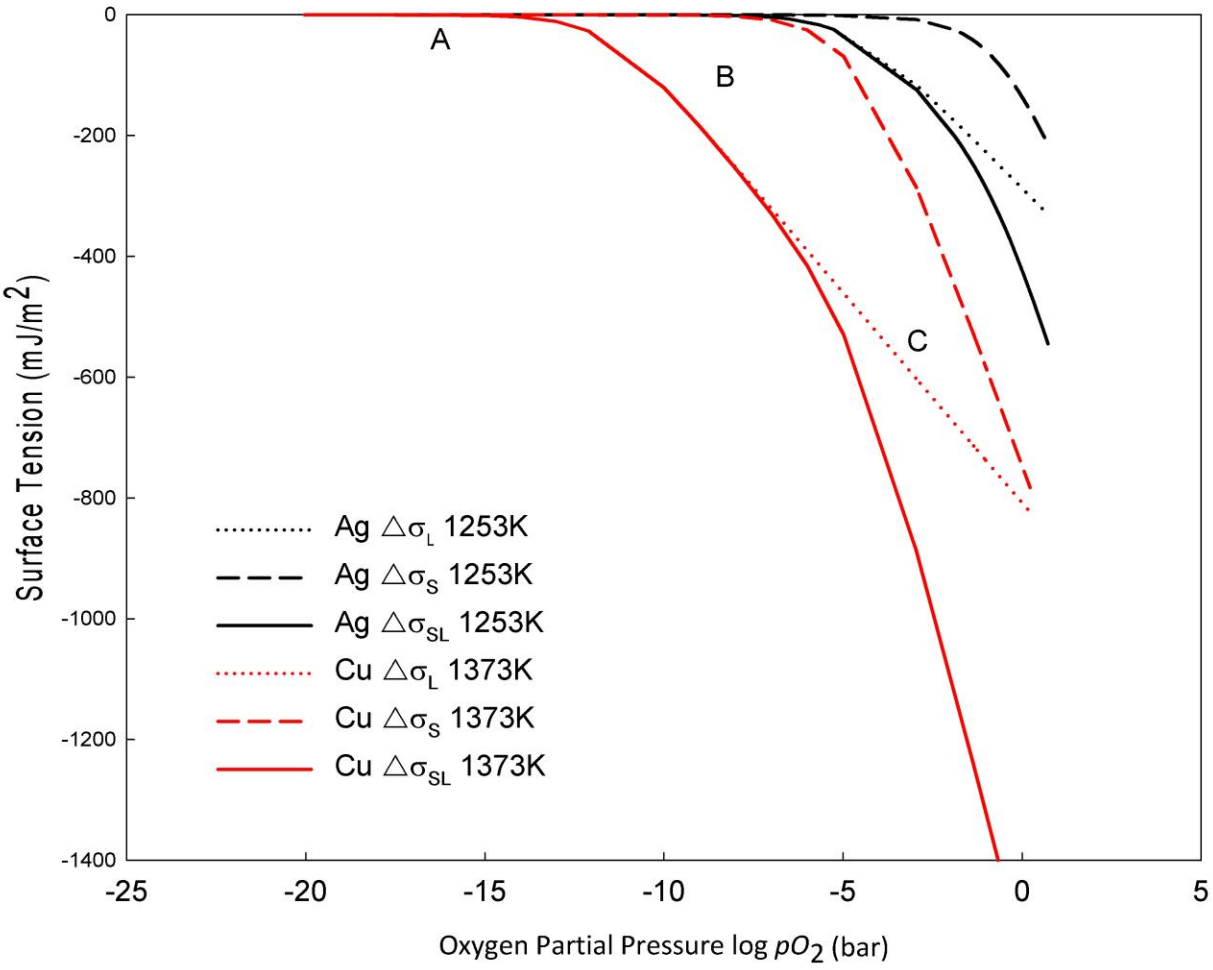

Figure 8.7 (a) Comparison of Ag/Al_2O_3 and Cu/Al_2O_3 the change of $\Delta\sigma_L$, $\Delta\sigma_S$, and $\Delta\sigma_{SL}$ using Eq. (8.32) and Eq. (8.33).

Figure 8.7 (b), thus, plots the overall solid-liquid surface tension of both the Ag/Al_2O_3 system at 1253 K and the Cu/Al_2O_3 at 1373 K. At very low oxygen partial pressure (region A of Cu curve in Figure 8.7 (a), solid-liquid surface tension remains unchanged. As oxygen partial pressure increases, as shown in region B of Cu, the decreased solid-liquid surface tension of both Ag and Cu corresponds with $\Delta\sigma_L$ while there is almost no change contributed by $\Delta\sigma_S$. In region C, the

higher oxygen concentration in liquid metal results in significant change in $\Delta\sigma_S$ as well, resulting in a change in the slope, as seen in Figure 8.7 (b).

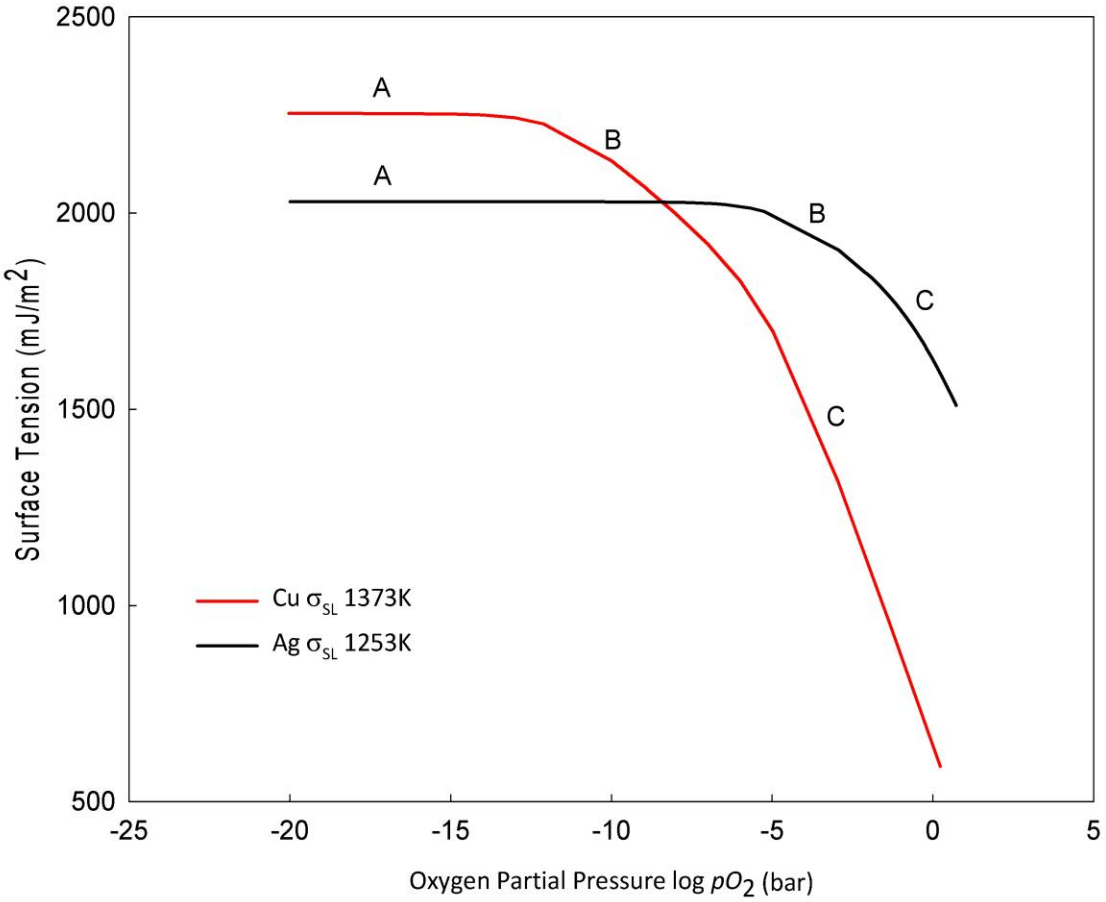

Figure 8.7 (b) Overall solid-liquid surface tension of both the Ag/Al_2O_3 system at 1253 K and the Cu/Al_2O_3 at 1373 K.

8.5 Conclusion

For the first time, the analysis of Butler (1932) based on a single monomolecular interfacial layer and utilized extensively for liquid metal-gas surface tension, as extended by Sugimoto (1996; 1999) to involve two monomolecular interfacial sub-layers, one for each condensed phase, has been utilized in a comprehensive thermodynamic framework to simultaneously investigate the

effect of the presence of oxygen on both the liquid metal-gas surface tension as well as solid-liquid metal surface tension. An extensive comparison with the available experimental data from the literature for both molten Cu/Al_2O_3 and molten Ag/Al_2O_3 shows that the model captures the essence of the change in surface tension and wetting of liquid metal-ceramic systems. It is discovered that the solid-liquid surface tension is influenced by the energy change in liquid-gas phase interface. Both liquid-gas and solid-liquid surface energy remain constant at very low oxygen partial pressure. As oxygen activity increases in the liquid metal, surface tension change at liquid-gas phase starts to show changes at solid-liquid phase. When oxygen pressure passes threshold value both energy changes from liquid-gas and solid-liquid have a strong impact on the solid-liquid interface.

The model predictions have a good fit with experimental results on liquid-gas surface tension, as described by von Szyszkowski equation (Szyszkowski, 1908). The model also gives good predictions and explanation for the change of solid-liquid surface tension at various oxygen partial pressures as noted previously (Muolo et al., 2008; Gallois, 1980), but without any theoretical discussion. The trends are also consistent with the surface energy predicted from DFT modeling. These results should be of value in developing a better understanding of the wetting behavior in the technologically important liquid metal-ceramic-gas-phase system.

Furthermore, this model clearly demonstrates that both liquid-gas, liquid solid interface surface energy will change with elevating temperature, pressure, gas composition and gas concentration change. This conclusion explains why liquid gallium membrane was unstable during gas change from hydrogen into helium. Before improving wettability between liquid gallium and SiC the sandwich structure is the best way to protect and enhance the membrane stability under permeation tests.

8.6 References

Abu Al-Rub, F., Distillation in capillary porous media for separation of biomass ethanol-water mixtures, Ph.D. Thesis, *The University of Iowa, Iowa City*, (1994).

Aveyard, R. and Haydon, D. A., An Introduction to principles of surface chemistry, *Cambridge University Press*, (1973).

Belton, G. R., Langmuir adsorption, the Gibbs adsorption isotherm, and interfacial kinetics in liquid metal systems, *Metallurgical and Materials Transactions B*, 7, (1976), 35-42.

Bernard, G. and Lupis, C. H. P., The surface tension of liquid silver alloys part II. Ag-O alloys, *Metallurgical and Materials Transactions B*, 2, (1971), 2991-2998.

Bobzin, K., Schlaefer, T., Zhao, L., Kopp, N. and Schlegel, A., Brazing of ceramic-to-ceramic and ceramic-to-metal joints in air, *Frontiers of Mechanical Engineering in China*, 5, (2010), 125-129.

Butler, J. A. V., The thermodynamics of the surfaces of solutions, *Proceedings of the Royal Society A*, 135, (1932), 348-375.

Chatain, D., Chabert, F., Ghetta, V. and Fouletier, J., New experimental setup for wettability characterization under monitored oxygen activity wettability of sapphire by silver oxygen melt, *Journal of the American Ceramic Society*, 77, (1994), 197-201.

Chatain, D., Coudurier, L. and Eustathopoulos, N., Wetting and interfacial bonding in ionocovalent oxide-liquid metal systems, *Revue de Physique Appliquée*, 23, (1988), 1055-1064.

Diemer, M., Neubrand, A., Trumble, K. P. and Rödel, J., Influence of oxygen partial pressure and oxygen content on the wettability in the copper–oxygen–alumina system, *Journal of the American Ceramic Society*, 82, (1999), 2825-2832.

Eriksson, J. C., On the thermodynamics of surface systems, in: I. Prigogine, (Eds.), *Advances in Chemical Physics, Vol. 6, John Wiley & Sons, Inc., New Jersey*, p145-174, (2007).

Eustathopoulos, N. and Drevet, B., Interfacial bonding, wettability and reactivity in metal/oxide systems, *Journal de Physique III*, 4, (1994), 1865-1881.

Feng, J., Zhang, W. and Jiang, W., Ab initio study of Ag/Al_2O_3 and Au/Al_2O_3 interfaces, *Physical Review B*, 72, (2005), 115423.

Gallois, B. and Lupis, C. H. P., Effect of oxygen on the surface tension of liquid copper, *Metallurgical and Materials Transactions B*, 12, (1981), 529-557.

Gallois, B. M., Wetting in nonreactive liquid metal-oxide systems, *JOM*, 49, (1997), 48-51.

Gallois, B., Contribution to the physical chemistry of metal-gas and metal-alumina interfaces , Ph.D. thesis, *Carnegie Mellon University, Pittsburgh, USA*, (1980).

Ghetta, V., Fouletier, J. and Chatain, D., Oxygen adsorption isotherms at the surfaces of liquid Cu and Au alloys and their interfaces with Al_2O_3 detected by wetting experiments, *Acta Materialia*, 44, (1996), 1927-1936.

Gibbs, J. W., The Collected Works of J. W. Gibbs, Vol. 1., *Longmans, Green, & Co., New York*, (1906).

Guggenheim, E. A., The thermodynamics of interfaces in systems of several components, *Transactions of the Faraday Society*, 39, (1940), 397-412.

Hsieh, P. H. and Selman, J. R., Electrowetting of molten carbonate electrolytes, *Fuel Cells*, 11, (2011), 626-634.

Lee, J., Tanaka, T., Asano, Y. and Hara, S., Oxygen adsorption behavior on the surface of liquid Cu-Ag alloys, *Materials Transactions*, 45, (2004b), 2719-2722.

Lee, J., Tanaka, T., Yamamoto, M. and Hara, S., Effect of oxygen on surface tension of liquid Ag-Sn alloys, *Materials Transactions*, 45, (2004a), 625-629.

March, N. H. and Tosi, M. P., Atomic dynamics in liquids, *MacMillan, London,* (1976).

Masuda, H., Higashitani, K. and Yoshida, H., Powder technology: Fundamentals of particles, powder beds, and particle, *CRC Press*, (2006).

Mehrotra, S. P. and Chaklader, A. C. D., Interfacial phenomena between molten metals and sapphire substrate, *Metallurgical and Materials Transactions B*, 16, (1985), 567-575.

Mill, K. C. and Su, Y. C., Reviews of surface tension data for metallic elements and alloys: part 1 pure metals, *International Materials Reviews*, 51, (2006), 329-351.

Monma, K. and Suto, H., Effect of dissolved oxygen on the surface tension of liquid copper (fundamental studies on cermet, part 5), *Journal of the Japan Institute of Metals*, 24, (1960), 377-379.

Morita, Z. and Kasama, A., Surface tension of liquid copper in dilute oxygen concentrations, *Journal of the Japan Institute of Metals*, 140, (1976), 787-795.

Muolo, M. L., Valenza, F., Passerone, A. and Passerone, D., Oxygen influence on ceramics wettability by liquid metals: Ag/α-Al_2O_3-experiments and modeling, *Materials Science and Engineering A*, 495, (2008), 153-158.

Naidich, Y. V., The wettability of solids by liquid metals, in: D.A. Cadenhead, J.F. Danielli (Eds.), *Progress in Surface and Membrane Science, Vol. 14, Academic Press, New York,* p353-484, (1981).

O'Brien, T. E. and Chaklader, A. C. D., Effect of oxygen on the reaction between copper and sapphire, *Journal of the American Ceramic Society*, 57, (1974), 329-332.

Oishi, Y. and Kingery, W. D., Self-diffusion of oxygen in single crystal and polycrystalline aluminum oxide, *The Journal of Chemical Physics*, 33, (1960), 480-486.

Ownby, P. D. and Liu, J., Surface energy of liquid copper and single-crystal sapphire and the wetting behavior of copper on sapphire, *Journal of Adhesion Science and Technology*, 2, (1988), 255-269.

Ozawa, S., Morohoshi, K., Hibiya, T. and Fukuyama, H., Influence of oxygen partial pressure on surface tension of molten silver, *Journal of Applied Physics*, 107, (2010), 014910.

Parlee, N. A. D. and Sacris, E. M., The solubility of oxygen in liquid silver, *Transactions of the Metallurgical Society of AIME*, 233, (1965), 1918-1919.

Passerone, D., Pignedoli, C. A., Valenza, F., Muolo, M. L. and Passerone, A., Ab initio simulations of the Ag (111)/Al_2O_3 interface at intermediate oxygen partial pressures, *Journal of Material Science*, 45, (2010), 4265-4270.

Saiz, E., Cannon, R. M. and Tomsia, A. P., High temperature wetting and the work of adhesion in metal/oxide systems, *Annual Review of Materials Research*, 38, (2008), 197-226.

Sangiorgi, R., Muolo, M. L. and Passerone, A., Surface tension and adsorption in liquid silver-oxygen alloys, *Acta Materialia*, 30, (1982), 1597-1604.

Scheu, C., Klein, S., Tomsia, A. P. and Rühle, M., Chemical reactions and morphological stability at the Cu/Al_2O_3 interface, *Journal of Microscopy*, 208, (2002), 11-17.

Sieverts, A., The absorption of gases by metals, *Zeitschrift für Metallkunde*, 21, (1929), 37-46.

Siwiec, G. and Willner, J., The mechanism of liquid copper deoxidation during argon blowing, *Metalurgija -Sisak then Zagreb*, 48, (2009), 75-77.

Sugimoto, T., A new approach to interfacial energy 1. Formulation of interfacial energy, *Journal of Colloid and Interface Science*, 181, (1996), 259-274.

Sugimoto, T., A new approach to interfacial energy 2. Interfacial energies of different interfaces under the influence of adsorption, *The Journal of Physical Chemistry B*, 103, (1999), 3593-3606.

Taimatsu, H., Nakatani, M. Abe, F. and Ogino, K., Effect of soluble oxygen on the wettability of solid oxides by liquid silver, *Journal of the Japan Institute of Metals*, 49, (1985), 523-528.

Tester, J. W. and Modell, M., Thermodynamics and its applications, 3rd Ed., *Prentice-Hall, Upper Saddle River, New Jersey,* (1997).

von Szyszkowski, B., Experimentelle studien uber kapillare eigenschaften der Wasserigen Losungen von Fettsauren, *Zeitschrift für Physikalische Chemie,* 64, (1908), 385-414.

Zhang, W., Smith, J. R. and Evans, A.G., The connection between ab initio calculations and interface adhesion measurements on metal/oxide systems: Ni/Al_2O_3 and Cu/Al_2O_3, *Acta Materialia,* 50, (2002), 3803-3816.

Zouvelou, N., Mantzouris, X. and Nikolopoulos, P., Interfacial energies in oxide/liquid metal systems with limited solubility, *Journal of Adhesion Science and Technology,* 27, (2007), 380-386.

Chapter IX

Conclusions and Recommendations for Future Work

Here we summarize the broad conclusions of this study and make some recommendations for future work.

9.1 Conclusions

◊ The most significant accomplishment of this study is that we were able to successfully prove that the novel concept of using sandwiched liquid metal membrane (SLiMM) for hydrogen purification is meritorious.

◊ Gallium was chosen to be the initial candidate liquid metal to provide the proof of the concept because of its low melting point, large liquidus range, low volatility, low toxicity, and inertness at room environment, which makes it easy to handle and fabricate membrane. The literature reports on heterogeneous catalytic reactions of gallium with hydrogen and the high hydrogen diffusivity in liquid provided further reasons for the choice. The results reported here suggest that liquid gallium was indeed a good starting candidate for proof of SLiMM concept.

◊ Appropriate porous supports for SLiMM were narrowed down after performing a thermodynamic analysis and using an extensive set of coupon tests combined with XRD, EDX, SEM examination to screen for qualified materials in terms of wettability and stability at 500 ºC with liquid gallium.

◊ It was discovered that sintered metal supports used for Pd membrane are not appropriate for supporting SLiMM due to the ready formation of intermetallic compounds with liquid gallium (or other low melting metals, e.g., In or Sn) at elevated temperatures. Most of the

porous oxide and nitride ceramic materials that had good wetting with liquid gallium were also too reactive, while materials with good stability were not wettable. The end result of this screening suggested that porous ceramic carbides and graphites are the most promising substrates.

◊ Sealant material and curing method was repeatedly tested and improved in order to seal SiC porous disc, liquid metal, and dense SiC tube, and consequently, develop a leakproof sandwich structure for hydrogen permeation test.

◊ Solubility of hydrogen in liquid gallium was independently measured via Sieverts' apparatus. Hydrogen solubility of liquid gallium is about 0.0447 H/M at 500 ºC, 1 atm H_2, which is about 13 times higher than Pd solubility of 0.0034 H/M at 500 ºC, 1 atm (Deveau, et al., 2013). The experimental results also provided enthalpy change of solution $\Delta H_S^o = +15.76$ kJ/mol, while entropy change was found to be $\Delta S_S^o = -5.45$ J/mol K.

◊ Hydrogen absorption method via Sieverts' apparatus was found to be more reliable and accurate than the H_2 desorption method, the latter in principle requiring an infinite number of cycles for complete removal of absorbed H_2. Further, the rather erratic hydrogen releasing behavior of liquid gallium was the main obstacle in accuracy and in determining when to terminate the experiment.

◊ Both hydrogen diffusivity in liquid gallium (Mazayev and Prokofiev, 1994) and the hydrogen solubility in liquid gallium are higher than Pd at 500 ºC.

◊ The measured hydrogen permeance of liquid gallium $72.5\,\mathrm{m^3/m^2h\cdot atm^{0.5}}$ at 500 ºC is about 35 times higher than that of Pd foil of similar thickness, i.e., $2\,\mathrm{m^3/m^2h\cdot atm^{0.5}}$ (Ayturk et al., 2009), while price is an order of magnitude lower.

◊ Liquid gallium can operate at higher temperatures than amorphous alloy membranes and it demonstrates higher permeation stability without helium leakage. SiC-Ga-16 at 500 ºC with permeability $12136\,\mathrm{m^3}\mu m/\mathrm{m^2h\cdot atm^{0.5}}$ was stable for 360 hours. It is 4 times higher than 190 nm Pd surface coated amorphous alloy $Nb_{30}Ti_{25}Hf_{10}Co_{35}$ (Li et al., 2015) with permeability $3037\mathrm{m^3}\mu m/\mathrm{m^2h\cdot atm^{0.5}}$ at 450 ºC and stability for 120 hours. Liquid gallium permeability was found to be higher than that of most of the solid metals and amorphous alloys provided in Phair and Donelson review article (2006). Further, unlike amorphous alloys, stability in Ga SLiMM was not of chemical original, but rather physical, which can be resolved through better engineering.

◊ Surface tension of liquid gallium under hydrogen environment is lower than under vacuum or under an inert gas such as He. It suggests that wettability changes as gas switching from helium to hydrogen during selectivity tests. Sandwich structure was, consequently, constructed to avoid a liquid gallium free surface. A thermodynamic model was developed to help us getting better insight into the effect of gas composition on surface tension and wettability.

◊ Butler-Sugimoto thermodynamic approach based on a monomolecular bilayer interface model was developed to investigate the effect of oxygen partial pressure on liquid-gas as well as solid-liquid surface tension of molten Cu/Al_2O_3 and molten Ag/Al_2O_3 systems. This work was focused on oxygen system due to the lack of wettability experiments on hydrogen/liquid metal/ceramic systems. This model clearly demonstrated that both liquid-gas and liquid-solid interface surface energy will change with elevating temperature, pressure, gas composition and gas concentration.

- ◊ A Pauling Bond Valence-Modified Morse Potential (PBV-MMP) model, in which the Pauling's relationship between bond-valence (BV) and bond-length (BL) is incorporated within a modified Morse-Potential (MP) was developed. The model is similar to Shustorovich UBI-QEP approach, however, we further replace the bond-index concept with bond length and bond valence and extend the theory from predicting *surface solid* metal into *bulk liquid* metal.
- ◊ The developed Pauling Bond Valence-Modified Morse Potential (PBV-MMP) approach is a semi-theoretical approach that only needs the M-M bond energy for a specified valence, atom covalent radius, atomic weight and liquid metal density to predict thermophysical properties and, for the first time, those of atomic impurities such as hydrogen in bulk metal of liquid gallium.
- ◊ The PBV-MMP model can accurately predict self-diffusion, viscosity and surface tension properties as a function of temperature for Ga and various other liquid metals.
- ◊ Furthermore, PBV-MMP approach can also model thermodynamic properties of hydrogen in liquid metal such as heat of dissociative adsorption, heat of solution and activation energy of diffusion. The prediction of hydrogen permeation in a liquid gallium membrane gave reliable predictions compared to experimental data.
- ◊ In short, based on the experimental work on solution and permeation of hydrogen coupled with theoretical modeling, we can now say that the concept of SLiMM proposed here has merit, and is worth exploring further.

9.2 Recommendations for Future Works

The stability of SLiMM needs to be further enhanced for industrial application via liquid metal and substrate modification, and its performance under more realistic conditions needs to be

investigated further. Finally, other metals and alloy candidates need to be investigated, These goals may be accomplished as suggested below.

◊ Obtaining both good wettability and stability between liquid gallium and a support is difficult as the two are competing requirements. However, if we select an element that only slightly changes the sub-layer surface Σ_S property of the support without significantly altering the melting point of the liquid metal, it may be possible to improve the wetting without significantly changing liquid gallium characteristics, perhaps even improvingthe hydrogen solubility.

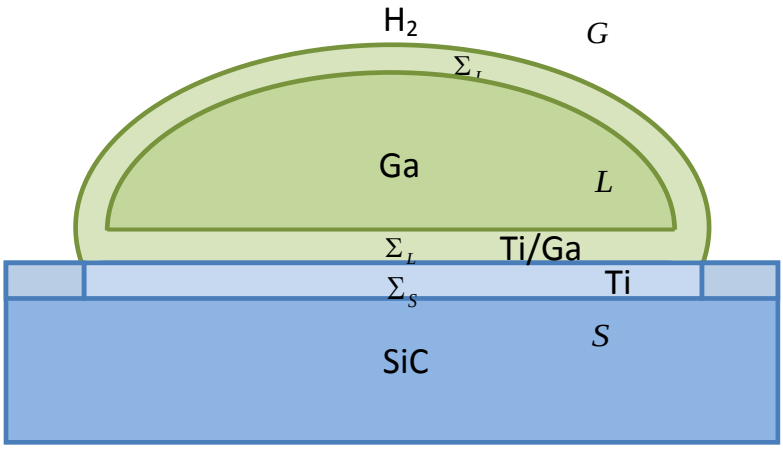

Figure 9.1 Proposed surface modification of SLiMM.

◊ An example of the proposed surface modification of SiC support for SLiMM is shown schematically in Figure 9.1. The idea is to coat a very thin layer (few nano-meter) of a metal using CVD, sputtering, electro-plating or electroless plating that has high affinity with SiC to change Σ_S surface energy. Liquid gallium Σ_L subsurface will form a very thin layer of intermetallic compound with such metal, hence, having good wetting with Σ_S subsurface. Metals such as Ti and V are good candidates as shown in Figure 9.2 (a), their addition greatly improving contact Ga-graphite contact angle.

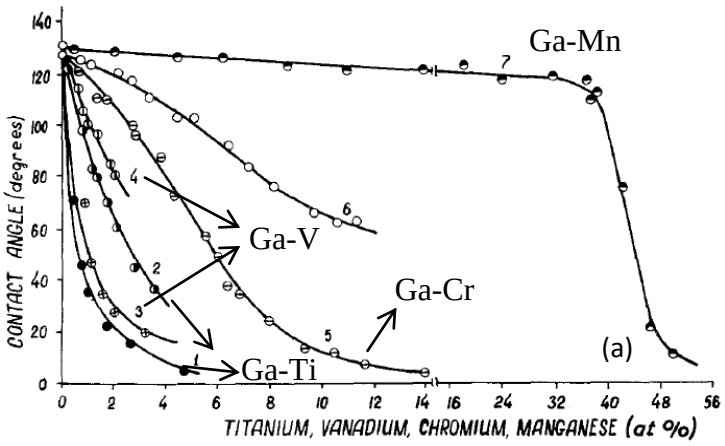

Figure 9.2 (a) Graphite with Ga-Ti, Ga-V, Ga-Cr, Ga-Mn, curves 1, 3 and 5 at 1050 ºC and curves 2, 4, 6 and 7 at 900 ºC (Naidich and Chuvashov, 1983).

◊ Another possible element for improving Ga wetting on SiC might be addition of a small amount of Mg. As shown in Figure 9.2 (b), the contact angle of liquid Al drops 10º with only 2wt% of Mg addition. Ga and Al are in the same group in the periodic table and share some similar characteristics. Further, Mg may not only improve Ga/SiC wetting, it may also help hydrogen dissociation ability.

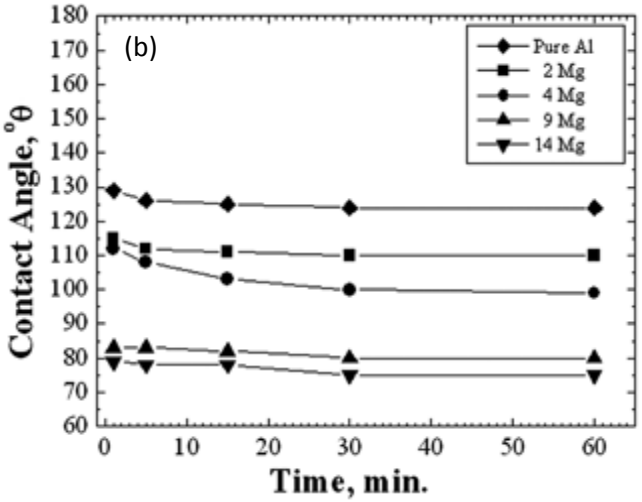

Figure 9.2 (b) Contact angle of molten Al-Mg on SiC at 750 ºC (Candan et al., 2011).

A preliminary test of wetting improvement was performed on coupons. Ga with 1-wt% and 2-wt% Mg were pre-annealed in hydrogen environment for 24 hours at 550 ºC before depositing on SiC. Then, the coupons were heated under hydrogen for 12 hours at 550 ºC. As shown in Figure 9.3, with 1-wt% Mg addition the distribution of Ga on the surface was scattered and parts of the SiC bare substrate are evident.

Figure 9.3 SiC-Ga-1wt%Mg wettability coupon tests before (left) and after heating (right).

However, results shown in Figure 9.4 with 2-wt% Mg addition followed by heating in hydrogen show that SiC wetting by Ga was substantially improved.

Figure 9.4 SiC-Ga-2wt%Mg wettability coupon tests before (left) and after heating (right).

◊ A better SiC disc/tube sealing could also improve the stability for testing. The best way to prepare a seamless SiC disc/tube assembly is to sinter the porous SiC disc and dense tube

simultaneously. Ideally SiC disc should locate at 1 mm or so below the tube opening, as shown in Figure 9.5. This would provide space is for liquid gallium deposition and a second porous layer to rest on top of the liquid gallium. Further, sealing with glass paste could be applied outside of the tube/sandwich cover interface. The advantage of this design is to permanently prevent any leaks in the disc/tube connection. Another advantage is that glass paste would not be in direct contact with liquid gallium since we have learnt that some of the components in the glass paste can react with the liquid metal.

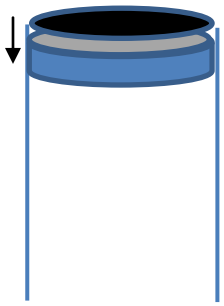

Figure 9.5 Schematic design for porous/dense SiC for SLiMM.

◊ A key consideration in design of practical permeators is sealing. There are, in general, three types of possible seals: 1) compressive seal, 2) compliant seal, and 3) rigidly bonded seal. Both compressive and compliant seal involve mechanical compression on ceramic components and gaskets, while rigidly bonded seal, as we have pursued so far in the test permeation cells, requires careful matching of the thermal coefficient of expansion of the membrane support, substrate, and the sealant glass, to avoid development of leakage during heating and cooling down. Further, the sealant glass has a tendency to react with molten metal. Consequently, we should look into designs that allow compressive/compliant sealing in a sandwich configuration, while avoiding molten metal contact with any material other than a support. These materials are used for both the porous support layers, as well as for seals and as spacers (washers).

◊ A potential sandwich design with compressive sealing in a permeation cell built from Swagelok fittings is shown in Figure 9.6.

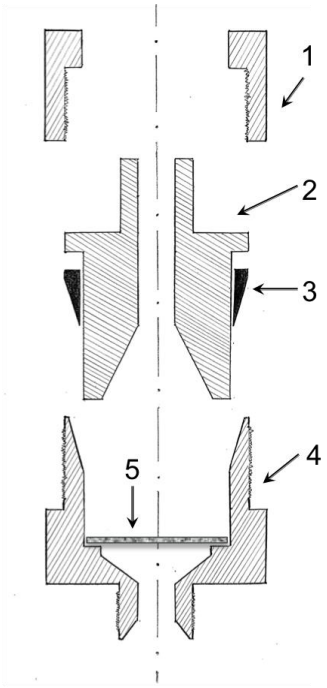

Figure 9.6 Cross section view of the of cell-permeator assembly for 1”OD metal support for a sandwich SMM membrane. 1 – Swagelok 1”OD stainless steel nut; 2 – stainless steel fitting; 3 – graphite ferrules with 1” ID; 4 - Swagelok stainless steel 1” to ¼” union; 5 – I” OD and 0.062” thick porous stainless steel disk.

The key item in this is the specially designed S.S. Swagelok fitting (item 2 Figure 9.6). This fitting provides simultaneous Swagelok sealing of the cell as well as compressive sealing of the membrane support foil/graphite within the cell (Figure 9.6). The porous stainless steel/SiC disk (item 5 on Figure 9.6) provides mechanical support for membrane sandwich supported between two porous layers spaced by a vanadium/carbon paper washer/spacer that determines the membrane thickness and keeps the molten metal from coming in contact with the S.S. housing/porous disk.

◊ Another critical task remaining is to ensure practical feasibility to determine the selectivity and stability of liquid gallium membrane under realistic syngas compositions, including components such as CO, CO_2, CH_4, H_2O and N_2. It is crucial to understand the interaction mechanism and kinetics between liquid gallium and these gaseous components at the relevant temperatures and realistic composition so that we would have a better understanding of practical design and limitations of a SLiMM permeator. The permeability and stability of a Pd membrane is also affected by these components (Gao et al., 2004).

◊ The PBV-MMP model developed here provides a good prediction of energetic parameters of thermodynamics and kinetics based on simple input. The simplicity of this model was based on several reasonable assumptions, which could be further imporved for higher accuracy. For example, free volume model of Eyring was used to determine entropy change and thermal wave-length in condensed phase. To increase the precision of free volume estimation we can include fluctuation factor f (Frank, 1945) i.e., $\upsilon_f = \tilde{V}_f / N_{Av} f$, which accounts for encroachment of other atoms/molecules in each other's free volume. Another free volume model that provides a different approach for estimating fluctuation volume and the accessibility of the empty volume is described by Bondi (1954). The accuracy of the PBV-MMP model could conceivably be further improved by better accounting for the number of nearest neighbor numbers in liquid metal as well as the number of interstitial sites for an impurity (hydrogen atom) in liquid metal. In this study, we assumed that liquid structure is quasi-crystalline and similar to solid. However, this aspect could be further by using approaches such as DFT, MD and X-ray study to get better understanding of liquid structure and its dynamic motions.

In short, while this thesis has provided an early indication and proof of the promise of SLiMM, much scientific and engineering work remains before it can be made practical and understood better.

9.3 References

Ayturk, M. E., Kazantzis, N. and Ma, Y. H., Modeling and performance assessment of Pd and Pd/Au-Based catalytic membrane reactors for hydrogen production, *Energy and Environmental Science*, 2, (2009), 430-438.

Bondi, A., Free volumes and free rotation in simple liquids and liquid saturated hydrocarbons, *The Journal of Physical Chemistry*, 58, 11, (1954), 929-939.

Candan, E., Atkinson, H. V., Turen, Y., Salaoru, I. and Candan, S., Wettability of aluminum-magnesium alloys on silicon carbide substrates, *Journal of the American Ceramic Society*, 94, 3, (2011), 867-874.

Deveau, N. D., Ma, Y. H. and Datta, R., Beyond Sieverts' law: A comprehensive microkinetic model of hydrogen permeation in dense metal membranes, *Journal of Membrane Science*, 437, (2013), 298-311.

Frank, H. S., Free volume and entropy in condensed systems II. Entropy of vaporization in liquids and the pictorial theory of the liquid state, *The Journal of Chemical Physics*, 13, 11, (1945), 493-507.

Gao, H., Lin, Y.S., Li, Y. and Zhang, B., Chemical stability and its improvement of palladium-based metallic membranes, *Industrial and Engineering Chemistry Research*, 43, 22, (2004), 6920-6930.

http://www.metal-pages.com/metalprices/gallium/

Li, X., Liu, D., Liang, X., Chen, R., Rettenmayr, M., Su, Y., Guo, J. and Fu, H., Substantial enhancement of hydrogen permeability and embrittlement resistance of $Nb_{30}Ti_{25}Hf_{10}Co_{35}$ eutectic alloy membranes by directional solidification, *Journal of Membrane Science*, 496, (2015), 165-173.

Mazayev, S. N. and Prokofiev, Yu. G., Hydrogen inventory in gallium, *Journal of Nuclear Materials*, 212-215, (1994), 1497-1498.

Naidich, J. V. and Chuvashov, J. N., Wettability and contact interaction of gallium-containing melts with non-metallic solids, *Journal of Materials Science*, 18, 7, (1983), 2071-2080.

Phair, J. W. and Donelson, R., Developments and design of novel (non-palladium-based) metal membranes for hydrogen separation, *Industrial and Engineering Chemistry* Research, 45, (2006), 5657-5674.

Appendix A

Thermodynamics Analysis of Ga-Al, Ga-Ca, Ga-Sc, Ga-Ti, Ga-V, Ga-Cr, Ga-Ni, Ga-Zr, Ga-Hf, Ga-Si, Ga-Y System

$\overline{G_{\mathrm{M}}}(Ga) = RT\ln a_{\mathrm{M}} = (\Delta S_{\mathrm{melt}} + \Delta S_{\mathrm{M}})T - (\Delta H_{\mathrm{melt}} + \Delta H_{\mathrm{M}})$ (Yatsenko et al., 2008; 1970)

$\ln a_{\mathrm{M}} = (\Delta S_{\mathrm{melt}} + \Delta S_{\mathrm{M}})/R - (\Delta H_{\mathrm{melt}} + \Delta H_{\mathrm{M}})/RT$

$\ln C = A - B/T$

C: solubility

If the solubility is lower than at. 2%

$$2 + \frac{\Delta S_{\mathrm{melt}} + \Delta S_{\mathrm{M}}}{2.3R} = A,\ \Delta S_{\mathrm{melt}} + \Delta S_{\mathrm{M}} = 2.3(A-2)/R$$

$$\frac{\Delta H_{\mathrm{melt}} + \Delta H_{\mathrm{M}}}{2.3R} = B,\ \Delta H_{\mathrm{melt}} + \Delta H_{\mathrm{M}} = 2.3BR$$

$\overline{G_{\mathrm{M}}}(Ga) = RT\ln a_{\mathrm{M}} = 2.3(A-2)RT - 2.3BR$

Ga-Al system

The free energy of liquid Al and Ga solution phases are represented as:

$$G^{i} = F^{i}_{\mathrm{Al}}(1-x) + F^{i}_{\mathrm{Ga}}x + RT(x\ln x + (1-x)\ln(1-x)) + x(1-x)(B^{i} + C^{i}(1-2x) + D^{i}(6x^{2} - 6x + 1))$$

where i: phase, x: atom fraction of Ga, F^{i}: lattice stability, B^{i}, C^{i}, D^{i}: temperature-dependent integrations parameters (Murray, 1983).

$iF_{cub}(Ga) = -5589 + 18.456T, F_L(Ga) = 0$

$iF_{fcc}(Al) = -10795 + 11.5628T, F_L(Al) = 0$

$B_L = 2694 - 1.665T, C_L = 359, D_L = 0$

x_1: atom fraction of Ga, x_2: atom fraction of Al, Ga:1, Al:2, i=liquid

$$G^L = F_2^L x_2 + F_1^L x_1 + RT(x_1 \ln x_1 + x_2 \ln(x_2)) + x_1 x_2 (B^L + C^{Li}(x_2 - x_1))$$

Partial Gibbs free energy of Al in Ga, $\overline{G_2} = (\frac{\partial G}{\partial N_2})_{T,P,N_1}$, N is the total mole

$$\overline{G_2} = \frac{\partial N(G^L)}{\partial N_2} = \frac{\partial N}{\partial N_2}[F_2^L x_2 + F_1^L x_1 + RT(x_1 \ln x_1 + x_2 \ln x_2) + x_1 x_2 (B^L + C^L(x_2 - x_1))]$$

$$= \frac{\partial}{\partial N_2}[F_2^L x_2 + F_1^L x_1 + RT(N_1 \ln \frac{N_1}{N_1 + N_2} + N_2 \ln \frac{N_2}{N_1 + N_2}) + \frac{N_1 N_2}{N_1 + N_2}(B^L + C^L(\frac{N_2}{N_1 + N_2} - \frac{N_1}{N_1 + N_2}))]$$

$$= F_2^L + RT(\frac{-N_1}{N_1 + N_2} + \ln N_2 + \frac{N_2}{N_2} - \ln(N_1 + N_2) - \frac{N_2}{N_1 + N_2}) - \frac{B^L N_1 N_2}{(N_1 + N_2)^2} + \frac{B^L N_1}{N_1 + N_2}$$

$$+ C^L(\frac{2N_1 N_2}{(N_1 + N_2)^2} - \frac{2N_1 N_2^2}{(N_1 + N_2)^3} - \frac{N_1^2}{(N_1 + N_2)^2} - \frac{2N_1^2 N_2}{(N_1 + N_2)^3})$$

$$\overline{G_2} = F_2^L + RT \ln x_2 + B^L x_1 - B^L x_1 x_2 + C^L(2x_1 x_2 - x_1^2 - 2(x_1 x_2^2 + x_1^2 x_2))$$

$\overline{G_2}$ is the partial Gibbs free energy of Al in Ga, by applying the solubility of Al into the equation gives the chemical potential of Al in liquid Ga.

Ga-O system (Zinkevich, 2004)

$$G^{liq}_{(Ga^{3+})_P(\nu^{3-},O^{2-},O)_Q} = y_{\nu^{3-}} Q G^{liq}_{Ga^{3+}:\nu^{3-}} + y_{O^{2-}} G^{liq}_{Ga^{3+}:O^{2-}} + y_O Q G^{liq}_O + G^{liq}_{id} + G^{liq}_{ex}$$

$$G_{id}^{liq} = RTQ(y_{\nu^{3-}} \ln y_{\nu^{3-}} + y_{O^{2-}} \ln y_{O^{2-}} + y_O \ln y_O$$

$$G_{ex}^{liq} = y_{\nu^{3-}} y_{O^{2-}} \sum_{\nu=0}^{n} {}^{\nu}L_{Ga^{3+}:\nu^{3-}:O^{2-}}^{liq} (y_{\nu^{3-}} - y_{O^{2-}})^{\nu} + y_{\nu^{3-}} y_O \sum_{\nu=0}^{n} {}^{\nu}L_{Ga^{3+}:\nu^{3-}:O}^{liq} (y_{\nu^{3-}} - y_O)^{\nu}$$
$$+ y_{O^{2-}} y_O \sum_{\nu=0}^{n} {}^{\nu}L_{Ga^{3+}:O^{2-}:O}^{liq} (y_{O^{2-}} - y_O)^{\nu}$$

$$G_{Ga^{3+}:\nu^{3-}}^{liq} = {}^{O}G_{Ga}^{liq} = 5666.446 - 18.680788T - 1.64554E-23T^{-9} + {}^{O}G_{Ga}^{solid} \quad 4000K$$

$${}^{O}G_{Ga}^{solid} = -7055.646 + 132.7302T - 26.0692906T \ln T + 1.506E-4T^2$$
$$-4.0173E-8T^3 - \frac{118332}{T} + 1.64554E-23R^{-9} \quad 6000K$$

$$G_O^{liq} = -2648 + 31.44T + 0.5\,{}^{O}G_{O_2}^{gas}$$

$${}^{O}G_{O_2}^{gas} = -6960.6927 - 51.1831467T - 22.25862T \ln T - 0.01023867T^2$$
$$+1.339947E-6T^3 - 76749.55/T \quad 900K$$

$${}^{O}L_{Ga^{3+}:\nu^{3-},O^{2-}}^{liq} = 322273.2 - 78.9549T = A \quad 6000K$$

$${}^{O}L_{Ga^{3+}:O^{2-},O}^{liq} = 50000 = B$$

Assume $y_{O^{2-}} = 0$, then it's binary system

$$y_{\nu^{2-}} = y_1, y_O = y_2, G_{Ga}^{liq} = G_1^{liq}, G_O^{liq} = G_2^{liq}$$

$${}^{O}L_{Ga^{3+}:\nu^{3-},O}^{liq} = 0, \nu = 0$$

$$\underline{G}^{liq} = y_1 Q G_1^{liq} + y_2 Q G_2^{liq} + RTQ(y_1 \ln y_1 + y_2 \ln y_2) + y_1 A + y_2 B$$

$$\overline{G_{\mathrm{O}}} = \frac{\partial N(\underline{G}^{liq})}{\partial N_2} = \frac{\partial N}{\partial N_2}(y_1 Q G_1^{liq} + y_2 Q G_2^{liq} + RTQ(y_1 \ln y_1 + y_2 \ln y_2) + y_1 A + y_2 B)$$

$$= \frac{\partial}{\partial N_2}(N_1 Q G_1^{liq} + N_2 Q G_2^{liq} + RTQ(N_1 \ln \frac{N_1}{N_1 + N_2} + N_2 \ln \frac{N_2}{N_1 + N_2}) + N_1 A + N_2 B)$$

$$= QG_2^{liq} - RTQ\frac{N_1}{N_1 + N_2} + RTQ\ln\frac{N_1}{N_1 + N_2} + RTQ\frac{N_2}{N_2} - RTQ\ln(N_1 + N_2) - RTQ\frac{N_2}{N_1 + N_2} + B$$

$$= QG_2^{liq} + B + RTQy_2$$

Ga-N system (Davydov, 1999)

$$G_{\mathrm{GaN}} - H^{ser} = -134869 + 270.578T - 44.377T\ln T - 6.301E-3T^2 + 5.864E5/T$$

Where $C_P = 44.377 + 1.26E-2T - 1.173E6/T^2$

$$H^{ser} = {}^{o}H_{\mathrm{Ga},298} + \frac{1}{2}{}^{o}H_{\mathrm{N}_2,298}, \Delta_f^{o}H_{298} = -111.2kJ/mol,\ {}^{o}S_{298} = 36.5J/molK$$

$$G^{liq} = x_{\mathrm{Ga}}\,{}^{o}G_{\mathrm{Ga}}^{liq} + x_{\mathrm{N}}\,{}^{o}G_{\mathrm{N}}^{liq} + G_{id}^{liq} + G_{ex}^{liq}$$

$$G_{id}^{liq} = RT(x_{\mathrm{Ga}}\ln x_{\mathrm{Ga}} + x_{\mathrm{N}}\ln x_{\mathrm{N}})$$

$$G_{ex}^{liq} = x_{\mathrm{Ga}}x_{\mathrm{N}}\sum_j {}^{j}L_{\mathrm{Ga,N}}^{liq}(x_{\mathrm{Ga}} - x_{\mathrm{N}})^j,\ j = 0...n$$

$$x_{\mathrm{Ga}} = x_1, x_{\mathrm{N}} = x_2$$

$${}^{o}L^{liq} = -35811.5 + 21.74T = A$$

$${}^{o}L^{liq} = -55558.6 + 7.68T = B$$

$$\underline{G}^{liq} = x_1 G_1^{liq} + x_2 G_2^{liq} + RT(x_1 \ln x_1 + x_2 \ln x_2) + x_1 x_2 A(x_1 - x_2)^0 + x_1 x_2 B(x_1 - x_2)^1$$

$$\overline{G_2} = \frac{\partial N(\underline{G}^{liq})}{\partial N_2} = \frac{\partial N}{\partial N_2}(x_1 G_1^{liq} + x_2 G_2^{liq} + RT(x_1 \ln x_1 + x_2 \ln x_2) + x_1 x_2 A(x_1 - x_2)^0 + x_1 x_2 B(x_1 - x_2)^1$$

$$\overline{G_2} = \frac{\partial}{\partial N_2}(N_1 G_1^{liq} + N_2 G_2^{liq} + RT(N_1 \ln \frac{N_1}{N_1 + N_2} + N_2 \ln \frac{N_2}{N_1 + N_2}) + A\frac{N_1 N_2}{N_1 + N_2} + B\frac{N_1 N_2}{N_1 + N_2}(\frac{N_1 - N_2}{N_1 + N_2})$$

$$= G_2^{liq} + RT \ln \frac{N_1}{N_1 + N_2} + A\frac{N_1}{N_1 + N_2} - A\frac{N_1 N_2}{N_1 + N_2} + B\frac{N_1^2}{(N_1 + N_2)^2}$$

$$-3B\frac{N_1^2}{(N_1 + N_2)^3} - 2B\frac{N_1}{(N_1 + N_2)^2} + 3B\frac{N_1 N_2^2}{(N_1 + N_2)^3}$$

$$= G_2^{liq} + RT \ln x_1 + Ax_1 - Ax_1 x_2 + Bx_1^2 - 3Bx_1^2 x_2 - 2Bx_1 x_2 + 3Bx_1 x_2^2$$

Ga-Mg system (Meng, 2010)

$$\underline{G}^{liq} = x_1 G_1^{liq} + x_2 G_2^{liq} + RT(x_1 \ln x_1 + x_2 \ln x_2) + x_1 x_2 A(x_1 - x_2)^0$$
$$+ x_1 x_2 B(x_1 - x_2)^1 + x_1 x_2 C(x_1 - x_2)^2$$

$$x_{\mathrm{Ga}} = x_1, x_{\mathrm{Mg}} = x_2$$

$${}^0L^{liq} = -46077.22 + 16.693T = A$$

$${}^1L^{liq} = 8953.22 - 6.992T = B$$

$${}^2L^{liq} = 5248.59 = C$$

$$\overline{G_2} = \frac{\partial N(\underline{G}^i)}{\partial N_2} = \frac{\partial N}{\partial N_2}[x_1 G_1^{liq} + x_2 G_2^{liq} + RT(x_1 \ln x_1 + x_2 \ln x_2)$$
$$+ x_1 x_2 A(x_1 - x_2)^0 + x_1 x_2 B(x_1 - x_2)^1 + x_1 x_2 C(x_1 - x_2)^2]$$

$$= \frac{\partial}{\partial N_2}[N_1 G_1^{liq} + N_2 G_2^{liq} + RT(N_1 \ln \frac{N_1}{N_1 + N_2} + N_2 \frac{N_1}{N_1 + N_2})$$
$$+ \frac{N_1 N_2}{(N_1 + N_2)^2}(A + B(\frac{N_1}{N_1 + N_2} - \frac{N_2}{N_1 + N_2}) + C(\frac{N_1}{N_1 + N_2} - \frac{N_2}{N_1 + N_2})^2$$

$$= G_2^{liq} + RT(\ln \frac{N_2}{N_1 + N_2}) + \frac{AN_1}{N_1 + N_2} - \frac{AN_1 N_2}{(N_1 + N_2)^2} + \frac{B(N_1^2 - 2N_1 N_2)}{(N_1 + N_2)^2}$$
$$- \frac{2B(N_1^2 N_2 - 2N_1 N_2^2)}{(N_1 + N_2)^3} + \frac{C(N_1^3 + 3N_1 N_2^2)}{(N_1 + N_2)^3} - \frac{3C(N_1^3 N_2 + N_1 N_2^3)}{(N_1 + N_2)^4} - \frac{2C(2N_1^2 N_2)}{(N_1 + N_2)^3} + \frac{6C(N_1^2 N_2^2)}{(N_1 + N_2)^4}$$

$$= G_2^{liq} + RT(\ln x_2) + Ax_1 - x_1 x_2(A + 2B) + Bx_1^2 - (2B + 4C)x_1^2 x_2 + (2B + 3C)x_1 x_2^2$$
$$+ Cx_1^3 - 3Cx_1 x_2^3 - 3Cx_1^3 x_2 + 6Cx_1^2 x_2^2$$

Appendix B

Labview Coding of Hydrogen Permeation Data Acquisition Setup

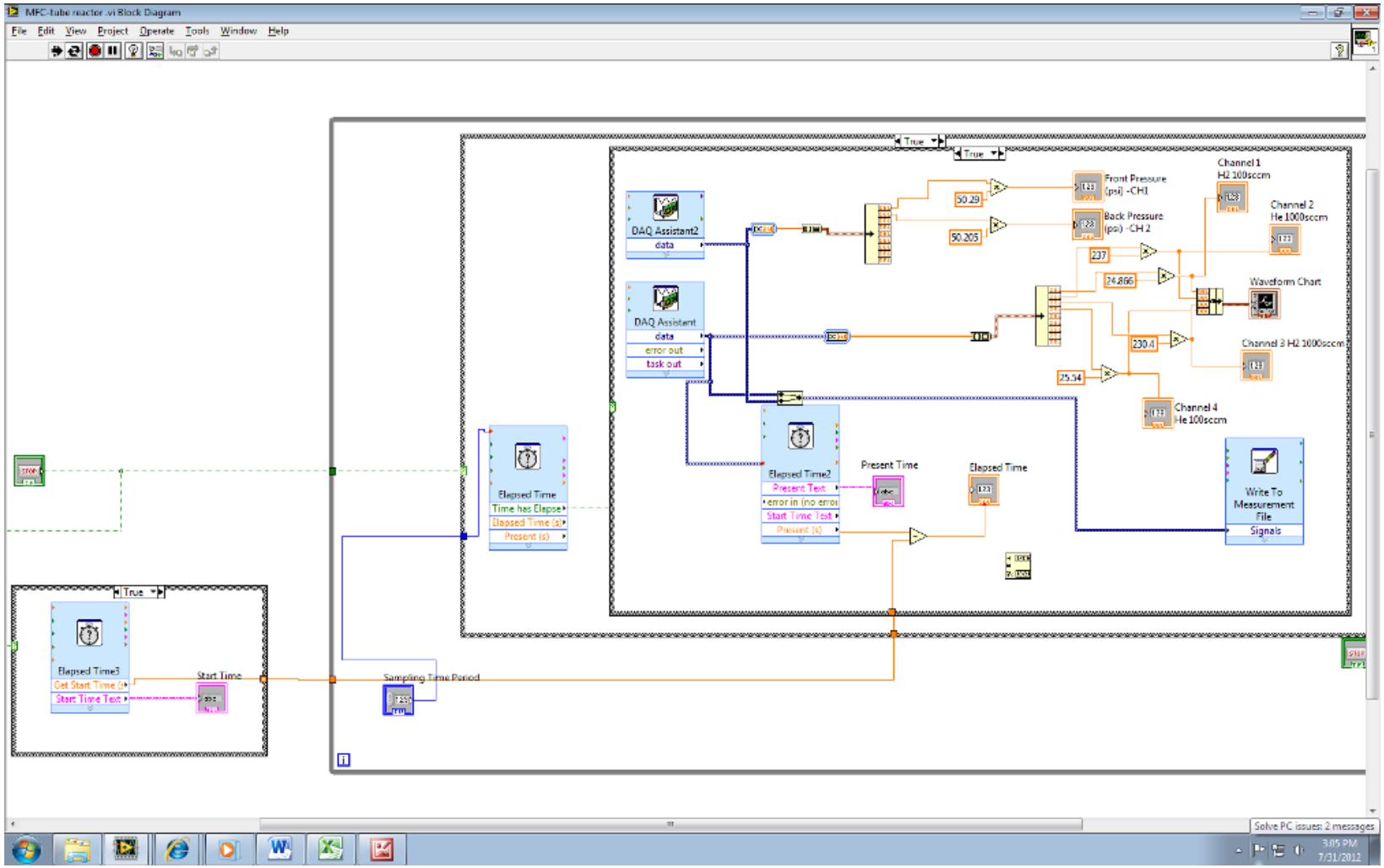

Appendix C

Analysis of Hydrogen Permeation through a Leaky Metal Membrane

Consider the schematic of hydrogen diffusing through a metal (e.g., Pd) membrane with pinholes

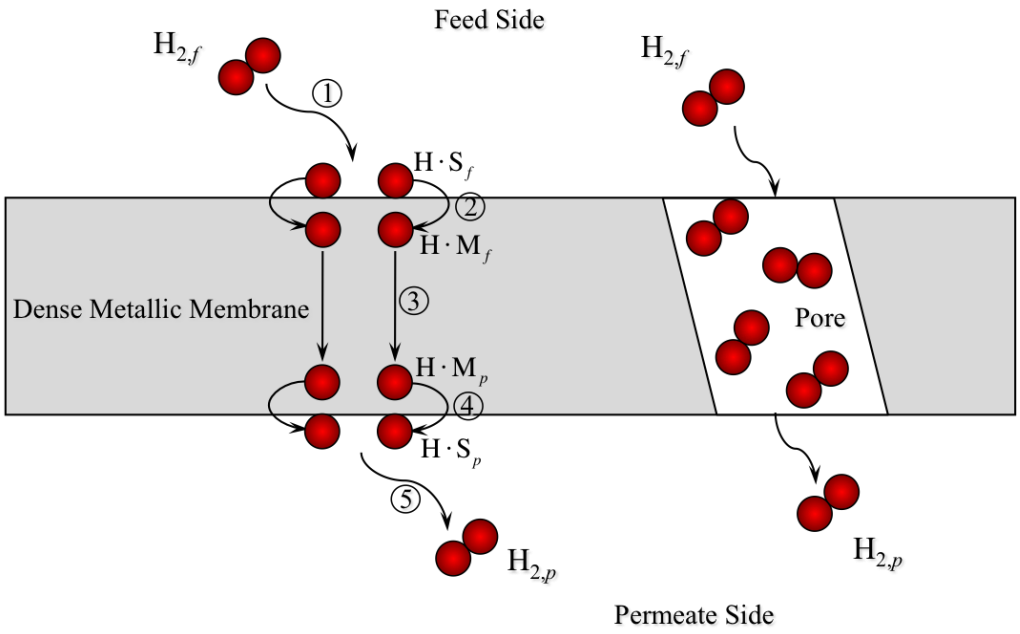

Figure C1. Permeation of H2 through Pd via dissociative adsorption and diffusion plus via Knudsen diffusion and d'Arcy flow in a pinhole (Deveau et al., 2013).

Thus, the combined flux of pure hydrogen through the solid membrane plus through the pinhole (Datta et al., 1992)

$$N_{H_2} = N_{H_2,M} + N_{H_2,K} + N_{H_2,V}$$
$$= -\frac{1}{RT}\frac{c_{H\cdot M} D_H}{2}\frac{d\mu_{H\cdot M}}{dz} - \frac{1}{RT}\left\{D^e_{H_2,K} + \frac{B_0 p_{H_2}}{\eta_{H_2}}\right\}\frac{dp_{H_2}}{dz} \qquad \frac{\text{kmol}}{\text{m}^2\cdot\text{s}} \qquad \text{(C1)}$$

In the above, D_{iK}^{e} is the effective Knudsen diffusivity of species i in a microporous membrane, given for a species i

$$D_{iK}^{e} = K_0 \bar{\upsilon}_i = K_0 \sqrt{\frac{8RT}{\pi M_i}} \tag{C2}$$

where Mi is the molecular mass of the species i, $\bar{\upsilon}_i$ its thermal speed, and the two dusty-gas porous structural parameters, in terms of void fraction, or porosity ε, tortuosity τ, and mean pore radius a are

$$\left.\begin{aligned} K_0 &= \frac{\varepsilon}{\tau}\frac{2a}{3} \\ B_0 &= \frac{\varepsilon}{\tau}\frac{a^2}{8} \end{aligned}\right\} \tag{C3}$$

where K_0 is the dusty-gas constant for Knudsen diffusion, and B_0 is the d'Arcy permeability. The factor 2 in the denominator of the first term on the right-hand side of Eq. (C1) accounts for the fact that for each molecule of hydrogen, two atoms of hydrogen diffuse through the metal.

Further, in the above, the chemical potential is

$$\mu_{\mathrm{H\cdot M}} = \mu_{\mathrm{H\cdot M}}^{\mathrm{o}}(T, p) + RT \ln a_{\mathrm{H\cdot M}} \tag{C4}$$

Combining with Eq. (C1)

$$N_{\mathrm{H_2}} = -\frac{c_{\mathrm{H\cdot M}} D_{\mathrm{H}}}{2}\left(\frac{d \ln a_{\mathrm{H\cdot M}}}{dz}\right) - \frac{1}{RT}\left\{K_0 \bar{\upsilon}_{\mathrm{H_2}} + \frac{B_0 p_{\mathrm{H_2}}}{\eta_{\mathrm{H_2}}}\right\}\frac{dp_{\mathrm{H_2}}}{dz} \tag{C5}$$

Assuming that the activity of interstitial hydrogen is of the form $a_{\mathrm{H{\cdot}M}} = \gamma_{\mathrm{H{\cdot}M}} x_{\mathrm{H{\cdot}M}}$, where $x_{\mathrm{H{\cdot}M}} = \chi_{\mathrm{H{\cdot}M}} / \chi_{\mathrm{H{\cdot}M},s}$ while the atomic ratio, $\chi_{\mathrm{H{\cdot}M}} \equiv c_{\mathrm{H{\cdot}M}} / c_{\mathrm{M},t}$, where $c_{\mathrm{M},t} = 1/\overline{V}_{\mathrm{M}} = \rho_{\mathrm{M}} / AW_{\mathrm{M}}$. Thus, the flux expression becomes

$$N_{\mathrm{H}_2} = -\left\{\frac{(\chi_{\mathrm{H{\cdot}M},s} c_{\mathrm{M},t})\mathscr{D}_{\mathrm{H}}}{2}\right\}\frac{dx_{\mathrm{H{\cdot}M}}}{dz} - \frac{1}{RT}\left\{K_0 \bar{v}_{\mathrm{H}_2} + \frac{B_0 p_{\mathrm{H}_2}}{\eta_{\mathrm{H}_2}}\right\}\frac{dp_{\mathrm{H}_2}}{dz} \tag{C6}$$

where the non-ideal effective diffusion coefficient

$$\mathscr{D}_{\mathrm{H}} \equiv D_{\mathrm{H}}\Gamma_D = D_{\mathrm{H}}\left(\frac{\partial \ln a_{\mathrm{H{\cdot}M}}}{\partial \ln x_{\mathrm{H{\cdot}M}}}\right) = D_{\mathrm{H}}\left(1 + \frac{\partial \ln \gamma_{\mathrm{H{\cdot}M}}}{\partial \ln x_{\mathrm{H{\cdot}M}}}\right) \tag{C7}$$

where $\Gamma_D \equiv 1 + \partial \ln \gamma_{\mathrm{H{\cdot}M}} / \partial \ln x_{\mathrm{H{\cdot}M}}$ is the so-called thermodynamic factor accounting for the non-ideality of hydrogen solubility in the metal due to H-M interaction (Flanagan and Wang, 2010). This is significant in Pd at lower temperatures.

For the ideal case ($\Gamma_D = 1$), assuming dilute metal-hydrogen solution, thus, the flux of hydrogen is

$$N_{\mathrm{H}_2} = -\left\{\frac{(\chi_{\mathrm{H{\cdot}M},s} c_{\mathrm{M},t}) D_{\mathrm{H}}}{2}\right\}\frac{dx_{\mathrm{H{\cdot}M}}}{dz} - \frac{1}{RT}\left\{K_0 \bar{v}_{\mathrm{H}_2} + \frac{B_0}{\eta_{\mathrm{H}_2}} p_{\mathrm{H}_2}\right\}\frac{dp_{\mathrm{H}_2}}{dz} \tag{C8}$$

Integrating

$$N_{\mathrm{H}_2} = \left\{\frac{(\chi_{\mathrm{H\cdot M},s} c_{\mathrm{M},t}) D_{\mathrm{H}}}{2\delta}\right\}\left(x_{\mathrm{H\cdot M},f} - x_{\mathrm{H\cdot M},p}\right) + \frac{1}{RT\delta}\left\{K_0 \bar{v}_{\mathrm{H}_2}\left(p_{\mathrm{H}_2,f} - p_{\mathrm{H}_2,p}\right) + \frac{B_0}{2\eta_{\mathrm{H}_2}}\left(p_{\mathrm{H}_2,f}^2 - p_{\mathrm{H}_2,p}^2\right)\right\} \tag{C9}$$

Using in this Sieverts' law for the solubility of hydrogen under dilute conditions, i.e.,

$$x_{\mathrm{H\cdot M}} = K_S \sqrt{\frac{p_{\mathrm{H}_2}}{p^{\mathrm{o}}}} \tag{C10}$$

where p^{o} is the standard pressure, provides

$$N_{\mathrm{H}_2} = \left\{\frac{\chi_{\mathrm{H\cdot M},s} c_{\mathrm{M},t} D_{\mathrm{H}} K_S}{2\delta\sqrt{p^{\mathrm{o}}}}\right\}\left(\sqrt{p_{\mathrm{H}_2,f}} - \sqrt{p_{\mathrm{H}_2,p}}\right) + \frac{1}{RT\delta}\left\{K_0 \bar{v}_{\mathrm{H}_2}\left(p_{\mathrm{H}_2,f} - p_{\mathrm{H}_2,p}\right) + \frac{B_0}{2\eta_{\mathrm{H}_2}}\left(p_{\mathrm{H}_2,f}^2 - p_{\mathrm{H}_2,p}^2\right)\right\} \tag{C11}$$

which is interesting in terms of the hydrogen partial pressure dependence of the flux. Alternately, Sieverts' law equation could be used in the differential form of the flux equation, as done later.

Writing this as membrane permeance, i.e.,

$$P_{\mathrm{H}_2} \equiv \frac{N_{\mathrm{H}_2}}{\left(\sqrt{p_{\mathrm{H}_2,f}} - \sqrt{p_{\mathrm{H}_2,p}}\right)} \tag{C12}$$

results in the permeance as a function of upstream and downstream hydrogen pressure

$$P_{\mathrm{H}_2} = \left\{\frac{\chi_{\mathrm{H\cdot M},s} c_{\mathrm{M},t} D_{\mathrm{H}} K_S}{2\delta\sqrt{p^{\mathrm{o}}}}\right\} + \frac{1}{RT\delta}\left\{K_0 \bar{v}_{\mathrm{H}_2} + \frac{B_0}{\eta_{\mathrm{H}_2}}\left(\frac{p_{\mathrm{H}_2,f} + p_{\mathrm{H}_2,p}}{2}\right)\right\}\left(\sqrt{p_{\mathrm{H}_2,f}} + \sqrt{p_{\mathrm{H}_2,p}}\right) \tag{C13}$$

which is seen to increase monotonically more than linearly with pressure. Of course, when there are no pinholes, this simply reduces to the usual form of Sieverts' law

$$P_{\mathrm{H}_2} = \left\{ \frac{\chi_{\mathrm{H\cdot M},s} c_{\mathrm{M},t} D_{\mathrm{H}} K_S}{2\delta\sqrt{p^{\mathrm{o}}}} \right\} \tag{C14}$$

In the presence of pinholes, however, there is a complex dependence on hydrogen pressure, partially accounting for the fact that the Sieverts' law is often written in terms of the nth power of the partial pressure, where, n ≥ 1/2.

The definition of permeance depends upon the definition of the driving force. If, for instance, it is assumed to be the pressure difference, i.e.,

$$\Pi_{\mathrm{H}_2} \equiv \frac{N_{\mathrm{H}_2}}{\left(p_{\mathrm{H}_2,f} - p_{\mathrm{H}_2,p}\right)} \tag{C15}$$

then, from Eq. (C11)

$$\Pi_{\mathrm{H}_2} = \left\{ \frac{\chi_{\mathrm{H\cdot M},s} c_{\mathrm{M},t} D_{\mathrm{H}} K_S}{2\delta\sqrt{p^{\mathrm{o}}}} \right\} \frac{1}{\left(\sqrt{p_{\mathrm{H}_2,f}} + \sqrt{p_{\mathrm{H}_2,p}}\right)} + \frac{1}{RT\delta} \left\{ K_0 \bar{v}_{\mathrm{H}_2} + \frac{B_0}{\eta_{\mathrm{H}_2}} \left(\frac{p_{\mathrm{H}_2,f} + p_{\mathrm{H}_2,p}}{2} \right) \right\} \tag{C16}$$

which may be plotted as a function of $p_{\mathrm{H}_2,f}$ for a given downstream pressure $p_{\mathrm{H}_2,p}$. It is seen that this would first decrease and then increase with pressure. The minimum in the middle, thus, for may be useful for parameter estimation and the relative significance of the flux through the metal versus the pinholes.

The DGM parameters K_0 and B_0 may be determined from experiments with an inert gas as follows.

Inert Gas Permeation through a Leaky Membrane as a Function of Temperature

For the case of an inert gas *i*, e.g., He or N_2, the flux through the dense membrane is zero, so that Eq. (C11) reduces to

$$N_i = \frac{1}{RT\delta}\left\{K_0\bar{v}_i\left(p_{i,f} - p_{i,p}\right) + \frac{B_0}{2\eta_i}\left(p_{i,f}^2 - p_{i,p}^2\right)\right\} \tag{C17}$$

which may be written as

$$N_i = \frac{1}{RT\delta}\left\{K_0\bar{v}_i + \frac{B_0}{\eta_i}\,\bar{p}\right\}\Delta p \tag{C18}$$

where the pressure drop $\Delta p = p_{i,f} - p_{i,p}$, and the mean pressure, $\bar{p} = (p_{i,f} + p_{i,p})/2$.

Writing this as STP volumetric flux, $\dot{V}_{0,T} = N_i RT^{\circ}/p^{\circ}$, where T° and p° are standard temperature and pressure (STP), and rearranging

$$\dot{V}_{0,T} = \frac{B_0\bar{p}}{\eta_i\delta}\left(\frac{\Delta p}{p^{\circ}}\right)\left(\frac{T^{\circ}}{T}\right)\left\{1 + \frac{K_0\bar{v}_i\eta_i}{B_0\bar{p}}\right\}\frac{\text{std m}^3}{\text{m}^2\cdot\text{s}} \tag{C19}$$

Further, the viscosity of a pure gas may be given by the kinetic theory relation for monoatomic gases

$$\eta_i = \frac{5}{16}\frac{\sqrt{\pi RM_iT}}{\pi\sigma_i^2\Omega_{\mu}} \tag{C20}$$

where σ_i is the collision diameter of the gas molecule, and Ω_μ is the collision integral of viscosity, of the order of unity, which is a weak function of temperature. When this is accounted for, the temperature variation of hydrogen viscosity is better given by (Guevara et al., 1969)

$$\eta_i = \eta_{i,0}\left(\frac{T}{T^{\circ}}\right)^{2/3} \tag{C21}$$

where $\eta_{i,0}$ is the gas viscosity at ambient temperature.

Thus, the above STP volumetric flux equation may be written in the form

$$\dot{V}_{0,T} = \frac{\beta_i}{3{,}600}\left(\frac{\Delta p}{p^{\circ}}\right)\left\{\left(\frac{T^{\circ}}{T}\right)^{5/3} + \alpha_i\left(\frac{T^{\circ}}{T}\right)^{1/2}\right\} \frac{\text{std m}^3}{\text{m}^2 \cdot \text{h}} \tag{C22}$$

where, the parameters

$$\beta_i = \frac{B_0 \bar{p}}{\eta_{i,0}\delta}\,\frac{\text{m}}{\text{s}} \tag{C23}$$

and

$$\alpha_i = \frac{K_0 \bar{v}_i \eta_{i,0}}{B_0 \bar{p}} = \frac{K_0 \bar{v}_i}{\beta_i \delta} \text{ dimensionless} \tag{C24}$$

Appendix D

References

Datta, R., Dechapanichkul, S., Kim, J. S., Fang, L.-Y., and Uehara, H., A generalized model for the transport of gases in porous, non-porous, and leaky membranes. I. Application to single gases, *Journal of Membrane Science*, 75, (1992), 245-263.

Davydov, A.V. abd Anderson, T. J., Thermodynamic analysis of the Ga-N system, *Proceedings of the Third Symposium on IIIV Nitride Materials and Processes Proceedings of the Third Symposium on IIIV Nitride Materials and Processes*, (1999).

Deveau, N. D., Ma, Y. H. and Datta, R., Beyond Sieverts' law: A comprehensive microkinetic model of hydrogen permeation in dense metal membranes, *Journal of Membrane Science*, 437, (2013), 298-311.

Flanagan, Ted B. and D. Wang. Exponents for the pressure dependence of hydrogen permeation through Pd and Pd-Ag alloy membranes, *The Journal of Physical Chemistry C*, 114, 34, (2010), 14482-14488.

Guevara, F. A., McInteer, B. B., and Wageman, W. E., High-temperature visocsity ratios for hydrogen, helium, argon, and nitrogen, *Physics of Fluids*, 12, (1969), 2493-2505.

Meng, F. G., Wang, J., Rong, M. H., Liu, L. B. and Jin, Z. P., Thermodynamic assessment of Mg-Ga binary system, *Transactions of Nonferrous Metals Society of China*, 20, (2010), 450-457.

Murray, J. L., The AI-Ga (Aluminum-Gallium) system, *Bulletin of Alloy Phase Diagrams*, 4, 2, (1983), 183-190.

Yatsenko, S. P, Sabirzyanov, N. A. and Yatsenko, A. S., Dissolution rates and solubility of some metals in liquid gallium and aluminum, *13th International Conference on Liquid and Amorphous Metals, Journal of Physics: Conference Series*, 98, (2008), 1-7.

Yatsenko, S. P. Anikin, Yu. A. Khimicheskaya, F. and Materialov, M., Solubility of metals of the fifth period in liquid gallium, *Materials Science*, 6, 3, (1970), 57-62.

Zinkevich, M. and Aldinger, F., Thermodynamic assessment of the gallium-oxygen system, *Journal of American Ceramic Society*, 87, 4, (2004), 683-91.